FZD-463

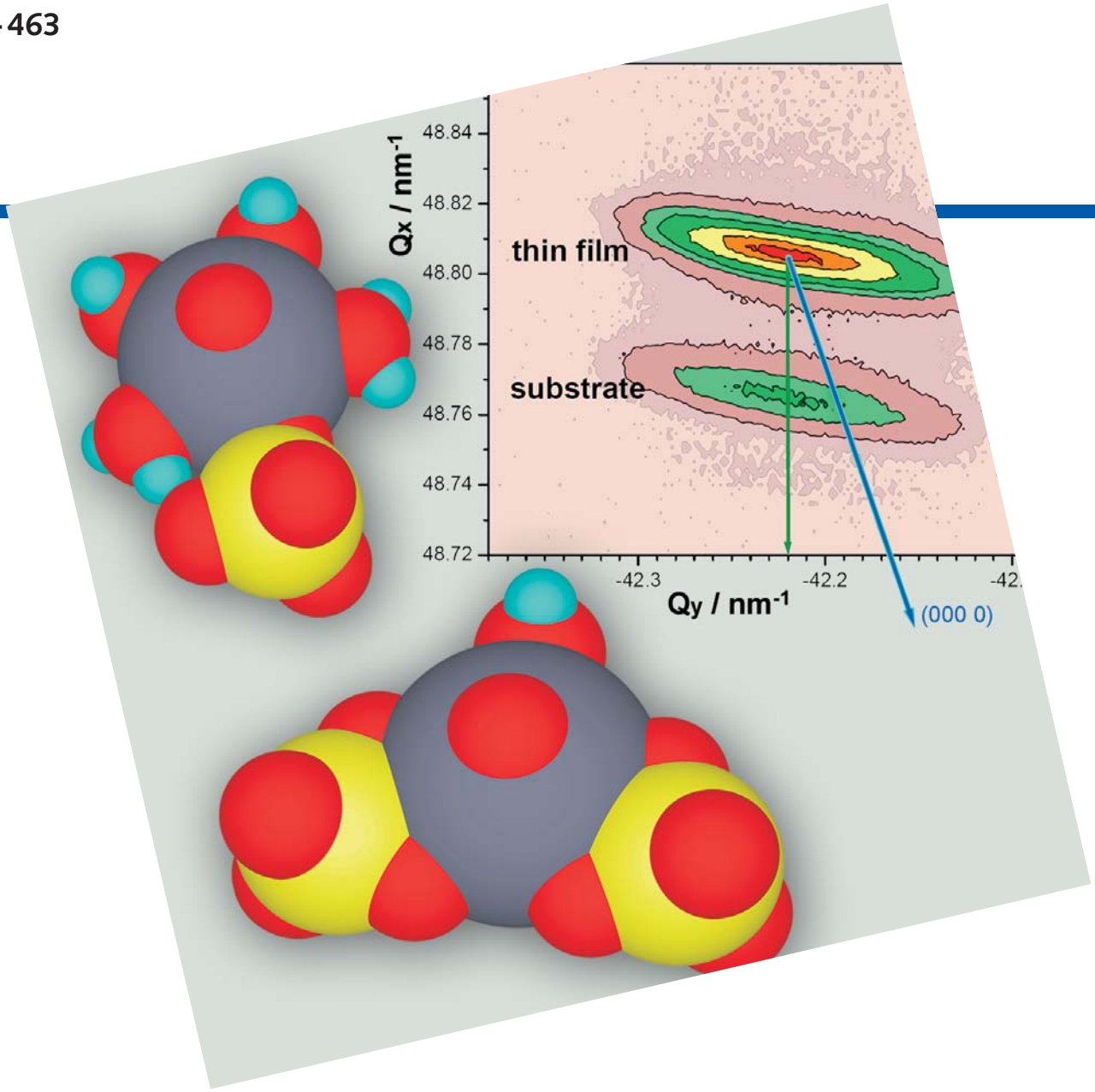


The "teddy bears" depict the monodentate and bidentate ligation of sulfate towards uranyl. While the basic structure has been derived from EXAFS measurements (see experimental report 20-01-618), a further refinement was based on DFT calculations (Courtesy Satoru Tsushima, Humboldt fellow at the Rossendorf Beamline). The combination of spectroscopy and quantum chemical calculations offers new possibilities to decipher structural and energetic aspects of aqueous molecules.

The inset shows a reciprocal space map for an undoped $LiNbO_3$ film epitaxially grown on congruent LiNbO3 substrate (4 -51 0 reflection at 0.154 nm wavelength). The color codes scattering intensity. Using at least two in-plane and out-of-plane reflections, growth mode and precise lattice parameters can be determined. Further details are given in experimental report Si-1346.

Wissenschaftlich-Technische Berichte
FZD-463 2007 · ISSN 1437-322X

# BI-ANNUAL REPORT 2005/06

## ROSSENDORF BEAMLINE AT ESRF (ROBL-CRG)

Forschungszentrum
Dresden Rossendorf

Wissenschaftlich-Technische Berichte
**FZD-463**
2007

# Bi-Annual Report 2005/2006

## The Rossendorf Beamline at ESRF (ROBL-CRG)

Editors:
A. Scheinost; J. v. Borany

Forschungszentrum
Dresden Rossendorf

# Preface

The Rossendorf Beamline (ROBL) - located at BM20 of the European Synchrotron Radiation Facility (ESRF) in Grenoble, France - is in operation since 1998. This 5$^{th}$ report covers the period from January 2005 to December 2006. In these two years, 74 peer-reviewed papers have been published based on experiments done at the beamline, thereby almost doubling the scientific output compared to the previous period. Six exemplary highlight reports on the following pages should demonstrate the scientific strength and diversity of the experiments performed on the two end-stations of the beamline, dedicated to Radiochemistry (RCH) and Materials Research (MRH).

Since July 2004 the beamline is a member of the pooled facilities of ACTINET – European Network of Excellence. RCH has provided 25 % of its inhouse beamtime to perform 12 ACTINET experiments. The high demand for EXAFS spectroscopy of radionuclides is also documented by a large oversubscription of ROBL by ESRF proposals. Consequently. the number of experiments in this biannual period has increased, with 62 on in-house beamtime and 22 experiments on ESRF beamtime. The heavy demand by external users and collaborating institutions may be partly explained by the closure of LURE, where experiments with radionuclides were possible, even though not routinely. At almost the same time, a second dedicated radionuclide beamline became operational in Europe in 2005, the INE beamline at ANKA. The growing demand of beamtime at ROBL-RCH therefore demonstrates the growing need to study radioactive materials with EXAFS on one hand, and the attractiveness of ROBL at the reliable and powerful ESRF on the other hand.

During the reporting period main activities of MRH were focused to *in-situ* x-ray scattering experiments related to the characterization of thin film growth and microstructure development during magnetron sputter deposition. These experiments delivered not only substantial progress in the characterization of shape memory alloys or phase transitions in magnetic thin films, but even led to the synthesis of novel MAX phases (see Highlight Report) for tribological applications. Furthermore, the capability and reliability of ROBL was a prerequisite to extend structural investigations of materials designed for new technologies in micro- and nanoelectronics in a close scientific collaboration with leading manufacturers of processors and memory devices (AMD, Qimonda).

The attractiveness of a beamline depends on a wide range of factors, including reliability, technical state of the art, and user support. The reliability of ROBL is demonstrated by about 500 shifts provided each year for experiments, corresponding to full capacity, matched by only two other CRG beamlines of the ESRF. New technical features and many upgrades have been realized at both endstations in the reporting period. To list just two highlights, MRH has increased its array of techniques by implementing a versatile capillary optics for scattering experiments with a microfocus beam (<100 μm spot size), while RCH has updated detectors and associated components like the cryostat to achieve lower detection limits of a few tenths of parts per million (wppm) for EXAFS spectroscopy.

The ROBL team is currently undergoing major changes. First of all, Norbert Schell, who belonged to the permanent ROBL scientific team since the beginning, left the beamline to take a leading position at the High Energy Materials Science Beamline HEMS at PETRA III, Hamburg. We would like to thank Norbert for his continuous efforts to push the limits of ROBL, among others for developing the in situ x-ray investigations during magnetron sputter deposition. He is replaced by Carsten Bähtz, previously in charge of beamline B2 at HASYLAB. Second, Udo and Manuela Strauch will return to Dresden in 2007. Udo was our onsite beamline scientist from the beginning, and his wife was working as office administrator for the last three years, both at the core of ROBL and essential for

its success. They will be replaced by Marco Hesse from Dresden, and by Marion Glückert, who has been working in the CRG office of the ESRF for many years. Welcome to these new team members.

The beamline has hosted several international visitors in the past two years. Prof. Roberto Colella, Dept. of Physics, Purdue University (USA), an expert on diffraction phenomena in crystals, has spent 4 weeks in spring 2005 at ROBL to help find better solutions for our DCM crystal. An expert on quantum chemical calculations, Prof. Satoru Tsushima, Department of Nuclear Engineering, Nagoya University (Japan), used his Alexander-von-Humboldt fellowship to join ROBL for one year to support the XAS analysis of actinides with DFT. Dr. Marina Chukalina, Institute of Microelectronics Technology at the Russian Academy of Sciences, visited ROBL seven times and a total of four months in the framework of a NATO project on the development of wavelets for XAS analysis. We would like to thank these visitors for their interest in our work and for their highly appreciated contributions.

In fall 2007, ROBL will be reviewed by a review panel on behalf of the ESRF. This early review was granted by the ESRF to support the subsequent review of ROBL's home institution, the Forschungszentrum Dresden-Rossendorf (FZD). We are confident that both ROBL and the FZD will receive very positive reviews, and we envision a major upgrade of ROBL, parallel to the upgrade of the ESRF, to keep ROBL competitive for many years to come.

We thank all partners, research groups and organizations who supported the beamline during the last 24 months. Special thanks to the FZD management, the CRG office of the ESRF with Axel Kaprolat as liaison officer, and to the ESRF safety group headed by Paul Berkvens.

Andreas Scheinost and Johannes von Borany

# Contents

# 1. Scientific Highlights

# Protactinium (V): an actinide without the actinyl moiety

C. Le Naour[1], C. Den Auwer[2], D. Trubert[1], M.V. Di Giandomenico[1], C. Fillaux[2], P. Moisy[2], Ch. Hennig[3,4]

[1] CNRS/Université Paris-Sud, Institut de Physique Nucléaire, 91406 Orsay cedex, France

[2] CEA-Valrhô, DEN/DRCP/SCPS, Bagnols sur Cèze Cedex, France

[3] The Rossendorf Beamline (BM20), ESRF, 38043 Grenoble, France

[4] Institute of Radiochemistry, Forschungszentrum Dresden-Rossendorf, 01314 Dresden, Germany

### *Introduction*

Protactinium is experiencing a renewal of interest, because the $^{233}$Pa isotope is involved as intermediate in the nuclear reaction $^{232}$Th $\rightarrow$ $^{233}$U that occurs in thorium fuel reactors. The isotope $^{231}$Pa is also produced in secondary reaction ($^{232}$Th(n,2n)$^{231}$Pa) and from now on, it has to be considered as a nuclear waste [1]. Modelling the behaviour of this element in the geosphere requires therefore thermodynamics and structural data relevant to environmental conditions. Moreover, protactinium (Z=91) occupies a key position in the actinide series since it is the first actinide with 5f electrons involved in bonding. The 5f electrons of light actinides (from Pa to Pu) can be described as itinerant or in some intermediate configuration, whereas heavy actinides have localised 5f states. Studies on protactinium may therefore provide additional information about the coordination chemistry of actinides.

At the pentavalent oxidation state, which it's the most stable oxidation state in solution as well as in the solid state, Pa(V) corresponds to a formal $5f^0$ electronic configuration like U(VI). U(VI) exists most often as the dioxocation form $UO_2^{2+}$. Np(V) is also often encountered as $NpO_2^+$. In contrast, the $PaO_2^+$ form is highly improbable both in solution and in solid state [2-4]. The chemical behaviour of Pa(V) bears only little resemblance to that of group 5 elements (Nb, Ta) and even less to the pentavalent actinides U, Np and Pu. The main feature of Pa(V) aqueous chemistry is its strong tendency towards hydrolysis, polymerisation and sorption on any solid, leading to irreproducible results, especially in absence of strong complexing ligands [3,5-6].

The scarce thermodynamic data available in the literature have been obtained with the element at tracer scale ($C_{Pa} < 10^{-10}$M) using partition methods (like liquid-liquid extraction) that allows only the determination of the mean charge and the mean ligand number of the species [7]. No information about the ion structure can be derived and species differing by one molecule of $H_2O$ cannot be distinguished. In acidic non complexing media ($HClO_4$), the assumed species are $PaO(OH)^{2+}$, $PaO(OH)_2^+$ and $Pa(OH)_5$. In HCl, HF and $H_2SO_4$, oxo- or hydroxo-complexes, have been proposed, depending on the acidity and the ligand concentration [2-3].

Some spectrophotometric studies performed with weighable amounts of Pa are described in the literature: in concentrated mineral acids (HCl, $HClO_4$, $H_2SO_4$) the large absorption band in the UV region (~200-210 nm) of colourless Pa complexes has been associated to the presence of a Pa-O bond . However strong absorption of the medium itself in this region may interfere [3,5], as illustrated in Fig. 1. Moreover, in perchloric, hydrochloric and nitric acid, polymerisation is known to occur with erratic induction time [2,6]. This capricious behaviour, even at high proton concentration, results in scarce reliable absorption data for Pa(V) in the literature. Up to now X ray Absorption Spectroscopy (XAS) has never been used to characterize the coordination of protactinium species, contrarily to other actinides, that have been extensively studied with this

technique in various oxidation states and chemical environments, in solution, in solid state as well as at surfaces.

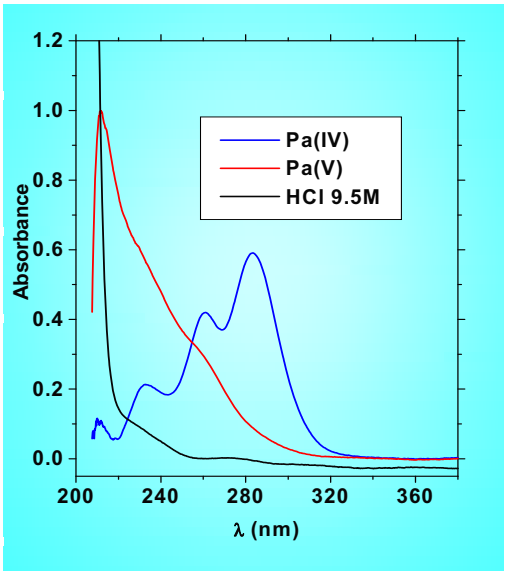


**Fig. 1.**
UV-vis absorption spectra of protactinium (IV) and (V) in con-centrated HCl ($C_{Pa}$ = 9 x $10^{-3}$ M)

The present report describes our work on Pa(V) in both acidic and complexing media (HF and $H_2SO_4$) using both regimes of absorption coefficients: XANES and EXAFS. These spectra are compared with those of U(VI) and Np(V) aqua ions.

### *Results and discussion*

Protactinium $L_{III}$-edge XANES spectra of two samples of Pa(V) (sample **I** in 0.5 M HF and sample **II** in 13 M $H_2SO_4$ are illustrated in Figure 2 (bottom set) and compared to U(VI) and Np(V) in perchloric acid. The actinide elements from U to Am at their higher oxidation states form trans-dioxo species [2]. The linear (or quasi-linear) actinyl moiety O-An-O is characterized by short An-O multiple bonds (1.7 to 1.9 Å) and leads to the observation of specific spectral features in the edge region of the absorption spectrum. $L_{III}$-edge XANES spectra of the actinyl species $U^{VI}O_2^{2+}{}_{aq}$ and $Np^{V}O_2^{+}{}_{aq}$ in $HClO_4$ (Fig. 2, bottom set) present usually 3 features. Feature A (white line) is associated with the dipolar $2p^6 6d^0$-$2p^5 6d^1$ electronic transition. The broadening of the edge white line as compared to lanthanides is mainly due to the short lifetime of core hole states at the actinide $L_{III}$ edge, and due to the 6d character of the final state. The shoulder B originates from the multiple scattering paths along the linear trans-dioxo unit. Feature C is a shape resonance attributed to scattering from the equatorially coordinated ligands; its position and width is therefore predominantly related to equatorial bond length [8-10].

For XANES simulations, we employed the FDMNES code [11], starting from the well-known bipyramidal pentagonal cluster of $UO_2(H_2O)_5$ (with U-$O_{ax}$ = 1.77 Å and U-$O_{eq}$ = 2.42 Å) [9]. Successive removal of one and two axial oxygens in the oxocation and replacement by $H_2O$ at 2.42 Å was performed, leading to the two virtual clusters $UO(H_2O)_6$, and $U(H_2O)_7$. A dramatic decrease of feature B intensity in the first step and disappearance in the second step is observed upon breaking the transdioxo geometry. The comparison between the simulations and experimental spectra of **I** and **II** confirms the absence of two linear Pa-O oxo bonds in the Pa(V) samples. However, due to the broadening of the white line no distinction between one oxo bond and a pure $H_2O$ coordination can be achieved by considering the XANES spectra. On the other hand, the shift of feature C (C') to higher energy in the experimental spectra of **I** and **II** can be correlated to a global shortening of the equatorial bond length: the distances between Pa and the equatorial oxygen ($O_{eq}$) should be shorter than the U-$O_{eq}$ distances of 2.42 Å observed in $UO_2(H_2O)_5$.

An additional XANES simulation has been carried out for sample **I**, using a cluster of one Pa atom surrounded by seven F atoms at a distance of 2.16 Å (*cf* EXAFS results in the next section). The agreement between simulated and experimental spectra of sample **I** is good: all the features are well reproduced in position and amplitude.

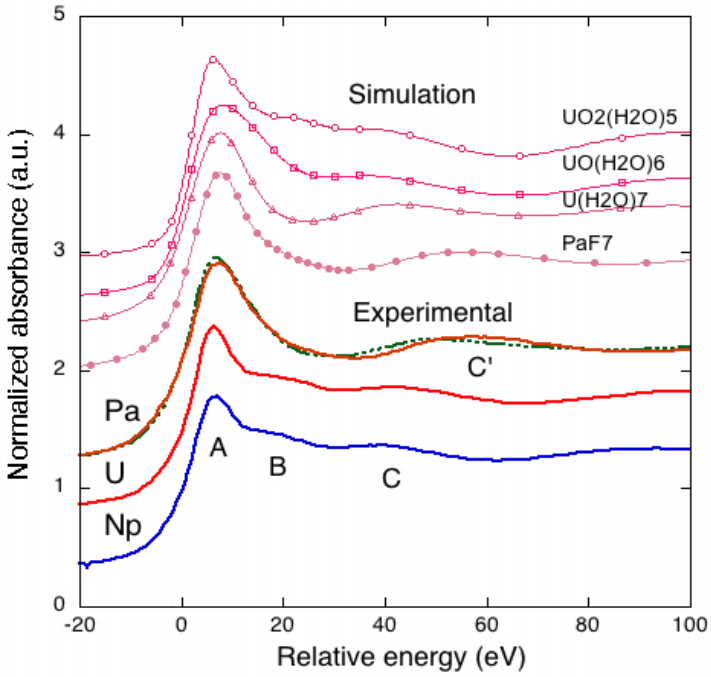


**Fig. 2.**
Experimental and simulated $L_{III}$ edge XANES spectra of Pa(V), U(VI) and Np(V) species. All spectra are normalized and shifted with respect to the inflexion point energy.

*Bottom set* : experimental spectra of Pa(V), U(VI) and Np(V) species in aqueous solution. ——— sample **I** (Pa(V) in hydrofluoric solution); --- — --- sample **II** (Pa(V) in sulfuric solution) ; —— — $UO_2^{2+}$ in 0.1 M perchloric solution; ——— $NpO_2^{+}$ in 0.01M perchloric solution.

*Top set* : simulated spectra of aqueous uranyl with successive removal of oxo-oxygen atoms. $UO_2(H_2O)_5$: see [9] for details on the cluster used for simulation; $UO(H_2O)_6$ ; $U(H_2O)_7$. Note that no atom charge or cluster charge have been included in the simulation. The simulation of a cluster of $PaF_7$ using the Pa-F distances determined by EXAFS is also presented.

Figure 3 presents the Pa $L_{III}$ edge EXAFS spectra of samples **I** and **II** and Figure 4 illustrates the modulus part of the corresponding Fourier transforms (FT). Although attribution of the FT features in terms of atomic scatters can be ambiguous because of the intricate constructive and destructive interferences, it will be used here for sake of clarity.

The FT of sample **I** exhibits a single peak, H, related to a monotonic sinusoidal EXAFS signal without any interference features, indicating that only one type of backscatterer contributes to the signal. According to the literature, seven to nine fluoride ligands have been assumed to be in the first coordination sphere [3,6]. Best fit parameters given in Table 1 have been obtained with 7 fluoride ligands positioned at 2.16(2) Å. Note that in the absence of model compound, coordination numbers are difficult to estimate. A similar fit can be obtained with CN=8 suggesting that the Pa coordination numbers falls in the 7-8 range. Note also that due to their similar atomic number F and O give very similar EXAFS signals and therefore the results of the EXAFS experiment do not exclude the presence of water molecules in the Pa first coordination sphere.

For HF concentrations ranging from $10^{-3}$ to 4 M, the complex $PaF_7^{2-}$ is expected to be predominant [3,6]. At solid state, $K_2PaF_7$ has been characterized by Brown *et al.* [12]. The Pa-F distances obtained by EXAFS can hardly be compared to distances obtained for solid structures as in $RbPaF_6$ (2.09 + 2.34 Å) [13], $K_2PaF_7$ (2.22 + 2.46 Å) [12] $Na_3PaF_8$

(2.21 Å) [14], in which the Pa coordination sphere is highly distorted due to lattice constraints. On the other hand, a simple bond distance estimation using Shannon's ionic [15] radii indicates that 6-coordinate Pa(V) yields a Pa-F distance of 2.11 Å, and 8-coordinate Pa(V) yields a Pa-F distance of 2.24 Å. The EXAFS result of 2.16 Å falls in this range.

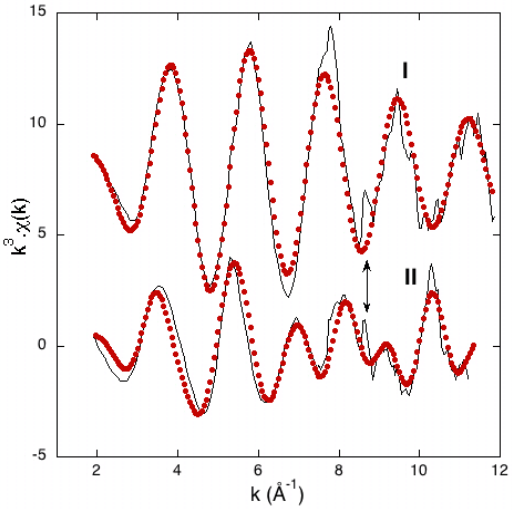


**Fig. 3.**
Experimental $L_{III}$ edge EXAFS spectra (—) of samples **I** (hydrofluoric solution) and **II** and fit (••••). The arrow indicates a glitch in the spectra.

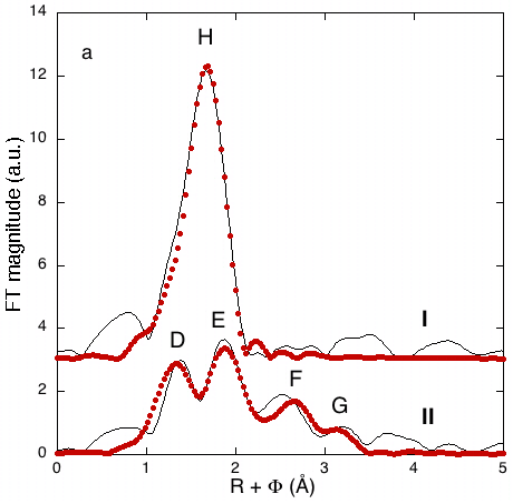


**Fig. 4.**
Fourier transform of the $L_{III}$ edge EXAFS spectra of samples **I** (hydrofluoric solution) and **II** (sulfuric solution). a) Experimental modulus of the FT (—— uncorrected for phase-shift) and fit (•••••).

For sample **II**, peak D in Figure 4 is attributed to a short Pa-ligand bond. This result agrees with the XANES experimental data and simulations of Figure 2 and is interpreted as strong evidence for the existence of a single short Pa-O bond in a monooxo form. Peak E reflects second sphere O ligands and peak F originates from third sphere S ligands. In this scheme, peak G would correspond to single and multiple scattering contributions from the monodentate sulfate ligands. Adjustment of the EXAFS spectrum was carried out according to the general formula $PaO(SO_4)^{bid}_n(SO_4)^{mon}_p$ (bid = bidentate, mon = monodentate) from n = 0 to 3, p = 0 to 7. Because the coordination number in the equatorial plane of actinyls falls essentially between 5 and 6, between 6 and 7 ligands are estimated to be coordinated to the Pa-O moiety (2n+p = 6, 7).

In the fits, sulfate groups were considered as rigid tetrahedra according to the crystal structure of $Na_{10}[(UO_2)(SO_4)_4](SO_4)_2.3H_2O$ [16].Therefore only the Pa-O distances were allowed to vary and the corresponding Pa-S distances and associated multiple scattering paths were linked to the corresponding Pa-O.

Fits with only bidentate or only monodentate sulfate ligands did not reproduce the experimental spectrum. Fits with n = 1, p = 4 or n = 3, p = 1 lead to a poor agreement. The optimum number for n was found to be 2 (four oxygen atoms coming from two bidentate sulfate ligands). Within the uncertainty associated with the amplitude estimation in EXAFS, the fit is more sensitive to number n than to number p because n contributes for two oxygen atoms and one sulfur atom. Backscattering from the sulfur atom also contributed to the determination of n. The value of p was then fixed to 3 according to the assumption that 2n+p = 6 and 7. However the uncertainty is about ± 1. Best fit structural parameters presented in Table 1 were obtained with one Pa-O bond at 1.72(2), two bidentate sulfate ligands at 2.41(2) Å with corresponding S atoms at 3.09 Å, and three monodentate sulfate ligands at 2.31(2) Å with corresponding S atoms at 3.72 Å. The high Debye Waller values of the $O(SO_4)$ contributions may indicate that water molecules can also contribute to the

Pa coordination sphere. The R factor is only equal to 6.5% because peak F is poorly reproduced in the fit. The poor agreement obtained on peak F is due to a discrepancy in the amplitude factors although the imaginary parts of the FT are in very good agreement[4]. The presence of a glitch in the EXAFS curves (arrow in Figure 3) may also contribute to an increase of the R factor.

In conclusion, the results indicate unambiguously the presence of one oxo bond for Pa(V) species in $H_2SO_4$ 13 M medium, as postulated for more dilute media where the species $PaOSO_4^+$ and $PaO(SO_4)_2^-$ have been proposed[3,6]. Furthermore, the number of mono- and bi-dentate sulfate ligands deduced from EXAFS agrees with one of the formulations of the oxo-trisulfato- protactinate (V) proposed by Bagnall *et al.* [17]. A recent theoretical study based on DFT calculations tend to support this experimental result [18].

**Table 1**. Best fit parameters obtained from the EXAFS data adjustment. Multiple scattering paths included in the fit of II are not reported in the table. Number in italics were fixed or linked to variables during the fit.

| Sample | Coordination shell | |
|---|---|---|
| **I**<br>hydrofluoric solution | *7* F at 2.16(2) Å, $\sigma^2$ = 0.0050 Å$^2$ | $S_0^2$ = 0.83<br>$\Delta E_0$ = 3.6<br>R factor = 2.6 % |
| **II**<br>sulfuric solution | *1* O at 1.72(2) Å, $\sigma^2$ = 0.0030 Å$^2$<br>*4* $O(SO_4)^{bid}$ at 2.41(2) Å, $\sigma^2$ = 0.0102 Å$^2$<br>*2* $S(SO_4)^{bid}$ at *3.09* Å, $\sigma^2$ = 0.0023 Å$^2$<br>*3* $O(SO_4)^{mon}$ at 2.31(2) Å, $\sigma^2$ = 0.0120 Å$^2$<br>*2* $S(SO_4)^{mon}$ at *3.72* Å, $\sigma^2$ = 0.0077 Å$^2$ | $S_0^2$ = 0.80<br>$\Delta E_0$ = 8.3<br>R factor = 6.5 % |

### *Conclusion*

XAS experiments on protactinium(V) in HF and concentrated $H_2SO_4$ solutions have demonstrated the absence of the transdioxo bond in Pa(V) species unlike other actinides like U and Np at their higher oxidation states. For the first time, the existence of a single Pa-O oxo bond in aqueous solution (sulfuric acid) has been proven unambiguously. However, in 0.5 M HF, XAS measurements have confirmed the predominance of a pure fluoro-complexe in agreement with the literature data on protactinium(V) in solution and at solid state.

### *Experimental details*

### *Sample preparation*

The isotope $^{231}$Pa was isolated from its daughters $^{227}$Ac, $^{227}$Th and $^{223}$Ra using the ion exchange chromatography technique: a small volume of a solution containing around 15 mg of $^{231}$Pa in concentrated HCl was percolated slowly onto a column filled with the anion exchange resin AG-MP1 (Bio-Rad). In these conditions, protactinium(V) is quantitatively retained whereas its decay products passed through. The elution of Pa was performed with 0.1M HF/8M HCl, leaving iron, if present, on the column [3-5]. The eluted Pa fraction were evaporated to dryness in a teflon crucible, and the residue taken up in concentrated HCl. The procedure was repeated at least 8 times to ensure the elimination of fluoride. The last evaporation was performed in perchloric acid before taking up the residue in the medium under study ($H_2SO_4$ or HF). The $^{231}$Pa concentration was determined by $\gamma$-spectroscopy at 283 keV. The Pa concentrations deduced from these measurements are $6.8\times10^{-3}$ M for sample in 0.5 M HF (sample **I**) and $1.1\times10^{-2}$ M for sample in 13 M $H_2SO_4$ (sample **II**).

### *XAFS data acquisition and treatment*

Protactinium $L_{III}$ edge XAS spectra were collected at the Rossendorf Beamline (BM20) at the ESRF in fluorescence mode. Energy calibration was carried out with a Y foil (17052 eV at the absorption maximum). Data treatment (AUTOBK normalization) was done with the Athena code [19]. Data fitting was carried out with the Artemis code [19] in R space between 1.0 and 3.5 Å. Phases and amplitudes were calculated with Feff82 [20] from the crystal structure of $RbPaF_6$ [13] for sample **I,** and from the crystal structure of $Na_{10}[(UO_2)(SO_4)_4](SO_4)_2.3H_2O$ [16] (with Z=92 replaced by Z=91 in the Feff input file) for sample **II**. The following multiple scattering paths were included in the fit of **II**: the triangular paths originating from the bidentate sulfates and the colinear triple and quadruple paths originating from the monodentate sulfates.


### *Acknowledgements*

Support for this research was provided by the ACTINET program (JRP-02-19), a European network for actinide sciences and GdR PARIS (French organization). XAS measurements were carried out at the Rossendorf Beamline, ESRF (Pa, U) and at the Stanford Synchrotron Radiation Laboratory (Np, U), a national user facility operated by Stanford University on behalf of the U.S. Department of Energy, Office of Basic Energy Sciences. The authors would like to thank for their help A. Scheinost, H. Funke and A. Roßberg (ESRF/ROBL) and J. Bargar, J. Rogers (SSRL/11-2), S. D. Conradson (LANL).


### *References*


[1] A. Nuttin, D. Heuer, A. Billebaud, R. Brissot, C. Le Brun, E. Liatard, J.M. Loiseaux, L. Mathieu, O. Meplan, E. Merle-Lucotte, H. Nifenecker, F. Perdu and S. David, Prog. Nucl. Energy **46** (2005) 77-99

[2] L.R. Morss, N.M. Edelstein and J. Fuger, The Chemistry of the Actinide and Transactinide Elements, 3rd edition, Springer Verlag, Netherlands, 2006

[3] R. Muxart and R. Guillaumont, Compléments au Nouveau Traité de Chimie Minérale, Masson, Paris, 1974.

[4] C. Le Naour, D. Trubert, M.V. Di Giandomenico, C. Fillaux, C. Den Auwer, P. Moisy and C. Hennig, Inorg. Chem. **44** (2005) 9542-9546.

[5] D. Brown and A.G. Maddock, Quart. Rev., **XVII** (1963) 289-341.

[6] R. Guillaumont, G. Bouissières and R. Muxart, Actinides Rev. **1** (1968) 135-163.

[7] J.P. Adloff and R. Guillaumont, Fundamentals in Radiochemistry, CRC Press Boca Raton, Florida, 1993.

[8] E.A. Hudson, J.J.Rehr and J.J. Bucher, Phys. Rev. B **52** (1995) 13815-13826

[9] C. Den Auwer, D. Guillaumont, P. Guilbaud, S.D. Conrdadson, J.J. Rehr, A. Ankudinov and E. Simoni, New J. Chem. **28** (2004) 929-939

[10] C. Den Auwer, E. Simoni, S. Conradson and C. Madic, Eur. J. Inorg. Chem. **21** (2003) 3843-3859

[11] Y. Joly, Phys. Rev. B **63** (2001) 125120-125130.

[12] D. Brown and A.J. Smith Chem. Comm. **21** (1965) 554-555.

[13] J.H. Burns, H.A. Levy and O.L. Keller Jr., Acta Cryst. B **24** (1968) 1675-1680.

[14] D. Brown, J.F. Easey and C.E. Rickard, C. E. J. Chem. Soc. A **7** (1969) 1161-1164.

[15] R.D. Shannon Acta Cryst. A **32** (1976), 751-767.

[16] P.C. Burns and L.A Hayden, Acta Cryst. C **58** (2002) i121-i123.

[17] K.W. Bagnall, D. Brown and P.J. Jones, J. Chem. Soc. **27** (1965) 176-181.

[18] T. Toraishi, T. Tsuneda and S. Tanaka, J. Phys. Chem. A **110** (2006) 13303-13309.

[19] B. Ravel, M. Newville J. Synchrotron Rad. **12** (2005), 537-541.

[20] J.J. Rehr and R.C. Albers, Rev. Mod. Phys. **72** (2000) 621-654.

# Carbonate and pH effects on surface speciation of uranyl at the ferrihydrite-water interface: New insights by factor analysis of EXAFS spectra

A. Rossberg[1], A.C. Scheinost[1], S. Tsushima[1], K.-U. Ulrich[2]

[1] Institute of Radiochemistry, Forschungszentrum Dresden-Rossendorf, 01314 Dresden, Germany
[2] Department of Environmental Engineering, Washington University, St. Louis, MO 63130-4899

## *Introduction*

Due to their high surface area and high concentration in many soils (up to 10 %), as well as due to their capability to form inner- and outer-sphere sorption complexes with uranium, iron(hydr)oxides may influence the migration behaviour of uranium more than other minerals [1]. For the structural investigation of these sorption complexes, X-ray Absorption Spectroscopy (XAS) is the method of choice. There is a general agreement on the structure of inner-sphere U(VI)-iron(hydr)oxide sorption complexes, with U(VI) coordinating to edges or corners of $Fe(OH)_6$ octahedra. Binary or ternary complexes are formed depending on the absence or presence of $CO_2$. As a function of pH and the partial pressure of $CO_2$ ($pCO_2$) the following U(VI) coordination structures have been proposed: a binary edge sharing complex [2-5], a ternary bis-carbonato complex with double corner sharing linkage [6], a ternary mono-carbonato complex with edge sharing linkage [7], a ternary bis-carbonato complex with edge sharing linkage [7], and a dimeric ternary complex with edge sharing linkage [7]. Under atmospheric conditions the sorption of U(VI) is most efficient in the pH range 5-9 [2, 8]. If the partial pressure of $CO_2$ is increased from its value in air (~0.037 %-vol) to 1%-vol, however, U(VI) starts to desorb already at pH <8 [9], while the adsorption edge at around pH 4 to 5 remains unaffected. In the pH range ~4-8, the binary complex with edge sharing linkage was suggested by several authors [2-5]. However, Bargar et al. [7] proposed the formation of ternary mono- and bis-carbonato complexes at pH values as low as 4.6. To clarify the structures of the sorption complexes, and to resolve the substantial inconsistencies in the interpretation of the XAS data. we investigated a series of sorption samples with variable pH and $pCO_2$ by factor analysis.

## *Experimental*

We prepared acidic solutions (pH ~3) of 1 mM $Fe(NO_3)_3 \cdot 9H_2O$ and 12 µM $UO_2(NO_3)_2 \cdot 6H_2O$ under the following conditions: (i) $CO_2$-free atmosphere ($pCO_2$ <0.2 Pa), (ii) air with $pCO_2$ = 35.5 Pa (0.037 %-vol), and (iii) air with an increased $pCO_2$ = 1014 Pa (1.0 %-vol). After 24 h of equilibration, sodium hydroxide (0.1 or 1 M NaOH) was added under vigorous stirring to adjust a pH of either 5.5, 7.0, or 8.0, initiating the precipitation of ferrihydrite (Fh) and adsorption of U(VI). For (i), dissolved carbonate was excluded by preparing all reagents with de-aerated de-ionized Milli-Q water in a glovebox purged with $N_{2(g)}$. The pH of all U(VI) sorption batches was controlled after 6, 12, and 24 h and readjusted if necessary. After 24 h of equilibration, stirring was stopped and the precipitates were allowed to settle for 65-70 h. The coagulated colloids were concentrated to wet pastes by ultra-centrifugation and placed into polyethylene vials. These vials were immediately shock-frozen and stored in liquid $N_2$ to avoid sample alterations and to exclude contact with atmospheric $CO_{2(g)}$. Table 1 summarizes the experimental conditions.

The EXAFS measurements were carried out on the Rossendorf Beamline at the European Synchrotron Radiation Facility. Uranium $L_{III}$-edge spectra were collected in fluorescence mode using a 13-element germanium detector and a closed-cycle helium cryostat at 30 K. The aqueous $UO_2(CO_3)_3^{4-}$ complex was measured at room temperature in transmission mode (sample 10). The EXAFS spectra were analyzed according to standard procedures

including statistical weighting of the 13 fluorescence channels and dead-time correction using the suite of programs EXAFSPAK [10]. The theoretical scattering phases and amplitudes were calculated with the scattering code FEFF802 by using the structural model (Fig. 1) for the sorption samples. For the aqueous $UO_2(CO_3)_3^{4-}$ complex we calculated theoretical phase and amplitude functions basing on the XRD data of swartzite [11]. The EXAFS spectra of the sorption samples were investigated with factor analysis using the ITFA [12] software package. We applied Monte Carlo simulation of EXAFS spectra for the structural analysis of the binary U(VI) sorption complex with edge sharing linkage [13]. This method, Monte Carlo Simulation Target Transformation Factor Analysis (MCTFA), is described in detail in [14].

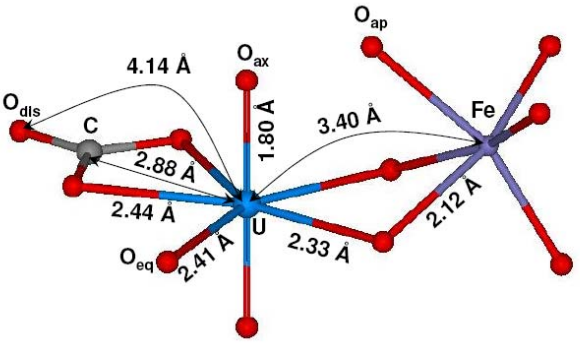


**Fig. 1.**
Structural model for the calculation of theoretical scattering phases and amplitudes for the modelling of the EXAFS spectra of the sorption samples. $O_{ax}$ – axial oxygen, $O_{eq}$ – equatorial oxygen, $O_{dis}$ – distal oxygen, $O_{ap}$ – apical oxygen.

**Table 1.** Experimental conditions of the U(VI) adsorption experiments ($[U]_T$ = 0.012 mM, $[Fe]_T$ = 1 mM, [solids] = 0.096 ± 0.002 g/L)

| XAFS spectrum | $pCO_2$ (Pa) | $pCO_2$ (%vol) | Matrix anions added | Final pH | U up-take (%) |
|---|---|---|---|---|---|
| 1 | <0.2 | 0 | 0.003 M $NO_3^-$ | 8.0 | 99.9 |
| 2 | <0.2 | 0 | 0.015 M $NO_3^-$ | 5.6 | 99.4 |
| ~~3~~ | <0.2 | 0 | 0.010 M $NO_3^-$ | 5.5 | 99.2 |
| 4 | 35.5 | 0.038 | 0.015 M $NO_3^-$, 0.042 mM $HCO_3^-$ | 5.8 | 99.9 |
| 5 | 35.5 | 0.038 | 0.015 M $NO_3^-$ | 5.5 | 99.4 |
| 6 | 35.5 | 0.038 | 0.003 M $NO_3^-$, 0.67 mM $HCO_3^-$ | 7.9 | 98.7 |
| 7 | 1014 | 1.0 | 0.015 M $NO_3^-$ | 5.5 | 99.3 |
| 8[#] | 1014 | 1.0 | 0.015 M $NO_3^-$ | 5.5 | 99.3 |
| 9 | 1014 | 1.0 | 0.015 M $NO_3^-$, 1.0 mM $HCO_3^-$ | 7.0 | 98.8 |
| aqueous $UO_2CO_3^{4-}$ complex: | | | | | |
| 10 | 1.0 M $CO_3^{2-}$, 50 mM U(VI), pH 11.8 | | | | |

[#] Fh precipitate was equilibrated with $CO_{2(g)}$ before U(VI) was added

### *Factor analysis of EXAFS spectra of U(VI)-Fh sorption samples*

The U(VI) sorption complex structure is expected to change as a function of the varied physicochemical parameters pH and $pCO_2$, leading to a correspoding variation of the EXAFS spectra (Fig. 3). In the first step, the principal component analysis, the number of structurally different species (i.e. components) is determined. For this purpose we use the common theoretical error functions RE (real error), IE (imbedded error), XE (extracted error) and the semi empirical indicator function IND developed by Malinowski [15]. Table 2 contains the error functions for the first four components.

**Table 2.** Principal component analysis of spectrum 1-10. Theoretical error functions and indicator function.

| n | RE(n) | IE(n) | XE(n) | IND(n)·10$^3$ |
|---|---|---|---|---|
| 1 | 0.464 | 0.147 | 0.440 | 5.73 |
| **2** | **0.273** | **0.122** | **0.244** | **4.27** |
| 3 | 0.250 | 0.137 | 0.209 | 5.10 |
| 4 | 0.221 | 0.140 | 0.171 | 6.14 |

n-number of component, RE(n) - real error, IE(n) - imbedded error, XE(n) - extracted error, IND(n) - indicator function

Both IND(n) and IE(n) functions reach a minimum for two factors. From this we conclude that the minimum number of components necessary for the data reproduction is two. Since the aqueous $UO_2(CO_3)_3^{4-}$ complex was included in the data analysis, it is necessarily a component of the sorption samples, representing an outer-sphere $UO_2(CO_3)_3^{4-}$ sorption complex. The error in the data is RE(2) ~ 0.27 and the error in the reproduced data is IE(2) ~ 0.12 (Tab. 2). Therefore the data quality is improved by factor RE(2)/IE(2)= 2.2 due to the removal of the experimental error contained in component 3-10. Only components 1 and 2 show an EXAFS-like signal in Fig. 2, while the remaining components contain only experimental error (i.e. noise). The linear combinations of the abstract spectra of components 1 and 2 (Fig. 2) give an excellent reproduction of all spectra (Fig. 3). Especially the FT of the second component gives important insights in the varying atomic environment of U(VI). In the FT-range ~1.5-4.0 Å the largest variation is visible (Fig. 2). Assuming for a light element like O or C a phase shift of ~0.5 Å, the range of the varying local atomic environment of U(VI) is ~2.0-4.5 Å. This R-range starts with the O-atoms in the equatorial plane of U(VI) and ends at the distance of distal O-atoms from bidentate coordinated $CO_3^{2-}$ groups.

For the determination of relative concentrations of the two components we used the VARIMAX procedure [12, 16] and the iterative target test (ITT) [12]. The model independent VARIMAX procedure calculates a qualitative concentration profile for each component, while the ITT uses information about relative concentrations for the calculation of the composition for each spectral mixture. Figure 4 shows the qualitative concentration profile and the relative concentrations for component 1 and 2.

As input information for the ITT we used the result of the VARIMAX procedure that most of component 1 is contained in spectrum 1 and that the component 2 is the spectrum of the aqueous $UO_2(CO_3)_3^{4-}$ complex (spectrum 10). The samples in table 1 are sorted according to the VARIMAX result (Fig. 4). Sample 1-3 were prepared in absence of $CO_2$ and can be used for the estimation of the error in the determination of the relative concentrations (Fig. 4). In these samples the maximum amount of component 2 is 7% (sample 3). Component 2 cannot be present in these samples and therefore 7% is a rough estimate for the error in concentration determination. In the samples prepared without $CO_2$ (sample 1-3) and in air atmosphere (sample 4-6) component 1 is predominant. In the samples 4-6 only 15% of the outer-sphere $UO_2(CO_3)_3^{4-}$ sorption complex is present (Fig. 4). If the $pCO_2$ is increased from 35.5 to 1014 Pa then the relative concentration of the outer-sphere $UO_2(CO_3)_3^{4-}$ sorption complex increases significant (Fig. 4). The pH influences the speciation of the two components more at elevated $pCO_2$ than at low $pCO_2$. At $pCO_2$=35.5 Pa and between pH 5.5 and pH 7.9 (sample 4 and 6) the relative concentration of the $UO_2(CO_3)_3^{4-}$ outer-sphere $UO_2(CO_3)_3^{4-}$ sorption complex increases from 6% to 15%, while at $pCO_2$=1014 Pa and between pH 5.5 and pH 7.0 (sample 7,9) the relative concentration of the $UO_2(CO_3)_3^{4-}$ increases from 32% to 53%.

***Structural investigation of components 1 and 2***

We isolated the spectrum of component 1 and 2 by using ITT from the EXAFS spectral mixtures (Fig. 5). The structure of the inner-sphere sorption complex (component 1) was determined by using MCTFA [13]. In this sorption complex U(VI) coordinates in a bidentate arrangement to the edge of an $FeO_6$ octahedron. The structure of the aqueous $UO_2(CO_3)_3^{4-}$ complex is found to be similar to those of solid U(VI)-carbonates like swartzite [11] (Fig. 11) or Liebigite [17, 18] in which U(VI) is surrounded by three bidentate coordinated $CO_3^{2-}$ groups. Table 3 contains the structural parameter for the inner-sphere and the outer-sphere $UO_2(CO_3)_3^{4-}$ sorption complex and the aqueous $UO_2(CO_3)_3^{4-}$ complex determined by shell fitting. In all shell fits the 2-fold degenerated 4-legged multiple-scattering path $U\text{-}O_{ax1}\text{-}U\text{-}O_{ax2}$ was included in the curve fit

by constraining its effective path length and its Debye-Waller factor to twice the values of the corresponding, freely fitted U-$O_{ax}$ single-scattering path.

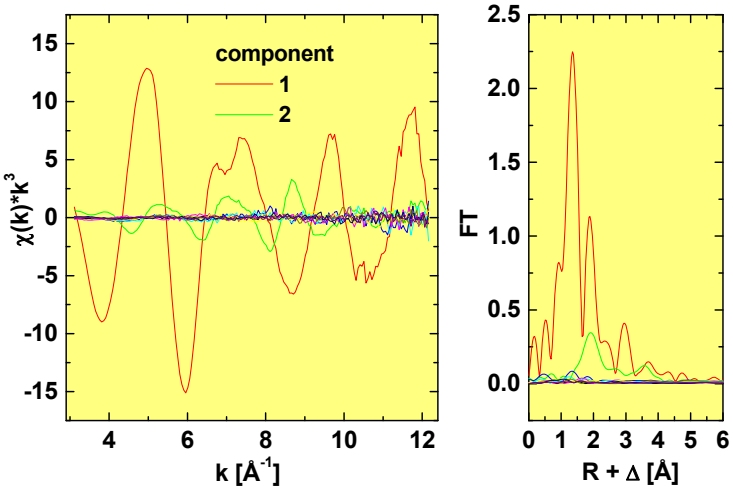


**Fig. 2.**
Abstract spectra of components 1-10 and corresponding Fourier transforms.

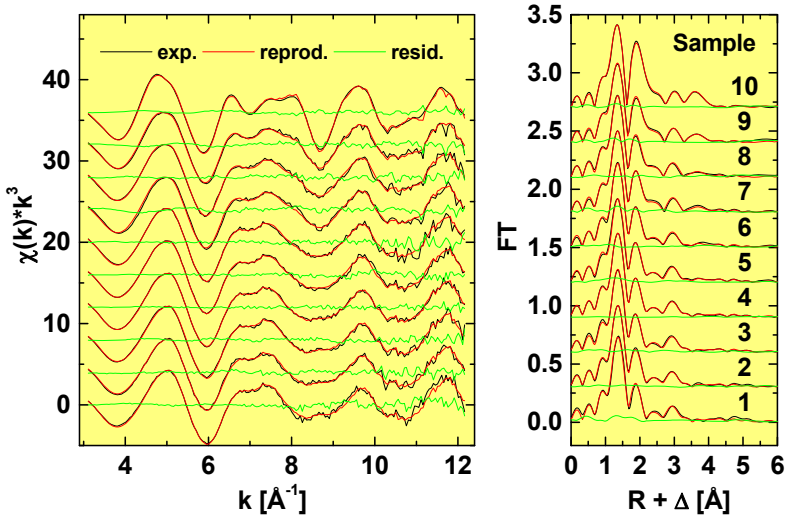


**Fig. 3.**
Abstract reproduction (re-prod.) of the experimental (exp.) data and residual (resid.) by using two com-ponents.

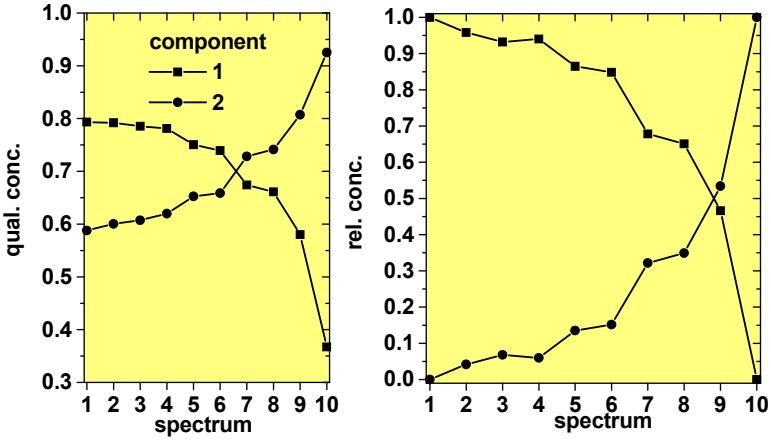


**Fig. 4.**
Qualitative concentration pro-file of component 1 and 2 determined by VARIMAX (left) and relative concentrations determined by ITT (right).

In the case of the inner-sphere sorption complex, the U-Fe interaction at 3.41 Å suggests a bidentate coordination (Tab. 3, Fig. 5). Due to the large structural disorder in the equatorial plane a relatively high Debye-Waller factor of $\sigma^2$=0.011Å$^2$ is found for $O_{eq}$ (Tab. 3). The average U-$O_{eq}$ distance of 2.36 Å is significantly smaller than the U-$O_{eq}$ distance of 2.41 Å found for U(VI)-hydrate ($UO_2(H_2O)_5^{2+}$) [19]. The structural parameters of the outer-sphere $UO_2(CO_3)_3^{4-}$ sorption complex are very close to those of aqueous

$UO_2(CO_3)_3^{4-}$ (Tab. 3). The large amplitude of the peak at 3 Å in the FT is due to the 24-fold degenerated 3-legged U-$O_{ax}$-$O_{eq}$ path (Fig. 5). In the case of the inner-sphere sorption complex the peak at 3 Å in the FT is mainly stemming from the backscattering of the Fe atoms (Fig. 5).

**Table 3:** EXAFS structural parameters for components 1 and 2, the aqueous $UO_2(CO_3)_3^{4-}$ complex at different k-ranges and m-autunite.

| Spectrum | Shell | *CN* | *R* [Å] | $\sigma^2$ [Å$^2$] | $\Delta E_0$ (eV) |
|---|---|---|---|---|---|
| Component 1: inner-sphere sorption complex k: 3.1-12.2Å$^{-1}$ | U=O | 2* | 1.801(2) | 0.0018(2) | 3.1(6) |
| | U-$O_{eq}$ | 4.5(4) | 2.355(6) | 0.011(1) | / |
| | U-Fe | 1.0(3) | 3.407(9) | 0.007(2) | / |
| Component 2: outer-sphere sorption complex ($UO_2(CO_3)_3^{4-}$) k: 3.1-12.2Å$^{-1}$ | U=O | 2* | 1.794(1) | 0.0018(1) | -7.5(3) |
| | U-$O_{eq}$ | 6* | 2.443(2) | 0.0064(2) | / |
| | U-C | 3* | 2.904(4) | 0.0015(4) | / |
| | U-C-$O_{eq}$ | 12* | 3.33(2) | 0.004(3) | / |
| | U-$O_{ax}$-$O_{eq}$ | 24* | 3.75(2) | 0.006(2) | / |
| | U-$O_{dis}$ | 3* | 4.19(1) | 0.003(3) | / |
| | U-C-$O_{dis}$ | 6* | /4.19 | /0.0055(5) | / |
| | U-C-$O_{dis}$-C | 3* | /4.19 | /0.0055 | / |
| Aqueous $UO_2(CO_3)_3^{4-}$ complex (sample 10, Tab.1) k: 3.1-12.2 Å$^{-1}$ | U=O | 2* | 1.796(1) | 0.0016(1) | -7.7(3) |
| | U-$O_{eq}$ | 6* | 2.442(2) | 0.0060(2) | / |
| | U-C | 3* | 2.904(4) | 0.0018(4) | / |
| | U-C-$O_{eq}$ | 12* | 3.32(2) | 0.003(2) | / |
| | U-$O_{ax}$-$O_{eq}$ | 24* | 3.74(2) | 0.006(2) | / |
| | U-$O_{dis}$ | 3* | 4.18(1) | 0.003(3) | / |
| | U-C-$O_{dis}$ | 6* | /4.18 | 0.0056(5) | / |
| | U-C-$O_{dis}$-C | 3* | /4.18 | /0.0056 | / |

CN - Coordination number, R - atomic distance, σ - Debye-Waller factor, $\Delta E_0$ energy shift parameter linked for all paths, * - fixed parameter, / - linked parameter. Standard deviations estimated by EXAFSPACK are given in parenthesis.

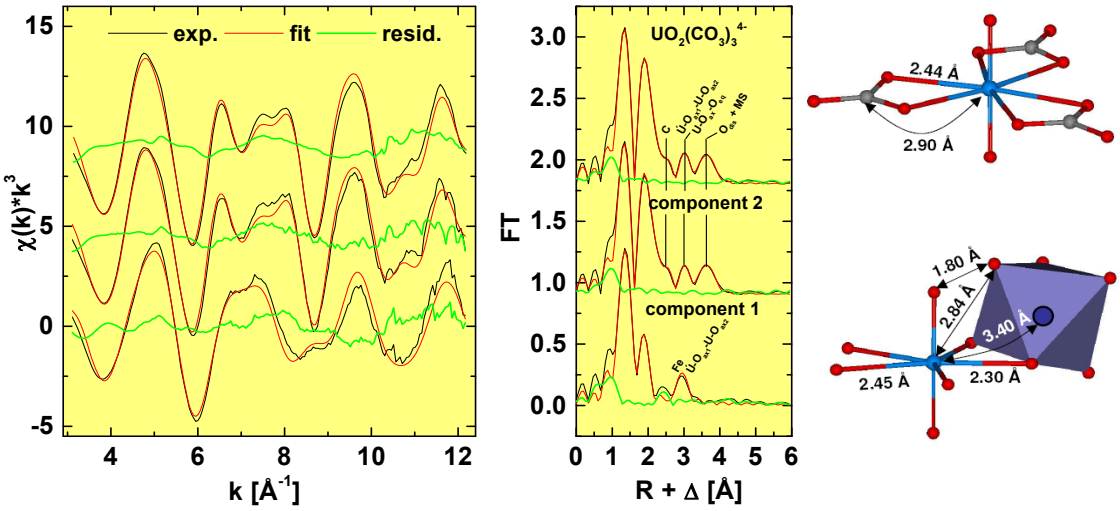


**Fig. 5.** Shell fits of component 1 and 2 and of the aqueous $UO_2(CO_3)_3^{4-}$ complex. Structures of the inner-sphere sorption complex (component 1) determined by MCTFA [13], the outer-sphere sorption complex (component 2) and the aqueous $UO_2(CO_3)_3^{4-}$ complex.

The *2.4 Å* peak is visible in the residual of the inner-sphere sorption complex (Fig. 5), which contains no carbonato ligands. This peak was misinterpreted in the literature [6, 7] as C atoms stemming from bidentate coordinated $CO_3^{2-}$ groups even at a pH as low as 4.6, where carbonato species are highly unlikely. According to the results of MCTFA, a $O_{ap}$ atom with a radial U-$O_{ap}$ distance of 2.84 Å (Fig. 5), was identified as the origin of the

*2.4 Å peak* [13]. In this steric arrangement the $O_{ax}$ – $O_{ap}$ distance would be ~1.80 Å [13] and is much smaller than the O-O distance of 2.831 Å in a hydrogen bond $O_{ax}\cdots HO_{ap}$ [20]. On the other hand, the U-$O_{ap}$ interaction and the small $O_{ax}$ – $O_{ap}$ distance is supported by the measured U-Fe and U-$O_{eq}$ distances. According to these two distances the position of U(VI) at the $FeO_6$ octahedron can be determined and the distance of the U-$O_{ap}$ interaction and the $O_{ax}$ – $O_{ap}$ distance results directly from the geometry. If one assumes that the origin of the *2.4 Å peak* is not the $O_{ap}$ atom of the $FeO_6$ than the geometry of the $FeO_6$ octahedron must be significantly changed during the sorption of U(VI).

### *Summary*

The influence of pH and $pCO_2$ on the sorption of U(VI) on ferrihydrite was investigated by factor analysis and Monte Carlo simulation of EXAFS spectra. Two sorption complexes were identified: a inner-sphere binary U(VI) sorption complex, in which U(VI) shares an edge of an $FeO_6$ octahedron and an outer-sphere sorption complex. The structure of the outer-sphere sorption complex agrees with the structure of the aqueous $UO_2(CO_3)_3^{4-}$ complex. The inner-sphere U(VI) sorption complex is the predominant species between pH 5.5-8.0, without $CO_2$ and under air ($pCO_2$=35.5 Pa). Only at elevated $pCO_2$=1014 Pa, the outer sphere sorption complex contributes significantly to the U(VI) speciation. Ternary sorption complexes, as proposed by Bargar et al. [7], were not present.

### *References*

[1] R.M. Cornell and U. Schwertmann, The Iron Oxides: Structure, Properties, Reactions, Occurence and Uses, VCH Publishers, New York, 1996.
[2] T.D. Waite, J.A. Davis, T.E. Payne, G.A. Waychunas and N. Xu, Geochimica Et Cosmochimica Acta **58** (1994) 5465-5478.
[3] M.A. Denecke, T. Reich, M. Bubner, S. Pompe, K.H. Heise, H. Nitsche, P.G. Allen, J.J. Bucher, N.M. Edelstein and D.K. Shuh, Journal of Alloys and Compounds **271** (1998) 123-127.
[4] M. Walter, T. Arnold, T. Reich and G. Bernhard, Environmental Science & Technology **37** (2003) 2898-2904.
[5] G. Redden, J. Bargar and R. Bencheikh-Latmar, Journal of Colloid and Interface Science **244** (2001) 211-219.
[6] J.G. Catalano, T.P. Trainor, P.J. Eng, G.A. Waychunas and G.E. Brown, Geochimica Et Cosmochimica Acta **69** (2005) 3555-3572.
[7] J.R. Bargar, R. Reitmeyer, J.J. Lenhart and J.A. Davis, Geochimica Et Cosmochimica Acta **64** (2000) 2737-2749.
[8] J.J. Lenhart and B.D. Honeyman, Geochimica Et Cosmochimica Acta **63** (1999) 2891-2901.
[9] J.A. Davis, D.E. Meece, M. Kohler and G.P. Curtis, Geochimica Et Cosmochimica Acta **68** (2004) 3621-3641.
[10] G.N. George and I.J. Pickering. Stanford Synchrotron Radiation Laboratory, Stanford, CA. USA. 1995.
[11] K. Mereiter, Neues Jahrbuch Fur Mineralogie-Monatshefte (1986) 481-492.
[12] A. Rossberg, T. Reich and G. Bernhard, Analytical and Bioanalytical Chemistry **376** (2003) 631-638.
[13] K.U. Ulrich, A. Rossberg, H. Foerstendorf, H. Zanker and A.C. Scheinost, Geochimica Et Cosmochimica Acta **70** (2006) 5469-5487.
[14] A. Rossberg and A.C. Scheinost, Analytical and Bioanalytical Chemistry **383(1)** (2005) 56-66.
[15] E.R. Malinowski, Factor Analysis in Chemistry, 2 ed., John Wiley & Sons, New York, 1991.
[16] H.F. Kaiser, Psychometrika **23** (1958) 187-200.
[17] G. Bernhard, G. Geipel, T. Reich, V. Brendler, S. Amayri and H. Nitsche, Radiochimica Acta **89** (2001) 511-518.
[18] S. Amayri, T. Reich, T. Arnold, G. Geipel and G. Bernhard, Journal of Solid State Chemistry **178** (2005) 567-577.
[19] L. Semon, C. Boehme, I. Billard, C. Hennig, K. Lutzenkirchen, T. Reich, A. Rossberg, I. Rossini and G. Wipff, Chemphyschem **2** (2001) 591-598.
[20] R. Kannappan, S. Tanase, D.M. Tooke, A.L. Spek, I. Mutikainen, U. Turpeinen and J. Reedijk, Polyhedron **23** (2004) 2285-2291.

# The interaction of *Desulfovibrio äspöensis* cells with plutonium in different oxidation states

H. Moll[1], M.L. Merroun[1], C. Hennig[1,2], A. Rossberg[1,2], S. Selenska-Pobell[1], G. Bernhard[1]

[1] Institute of Radiochemistry, Forschungszentrum Dresden-Rossendorf eV, 01314 Dresden, Germany

[2] The Rossendorf Beamline (BM20), ESRF, 38043 Grenoble, France

## *Introduction*

During the last years the interest in interaction processes involving actinides and bacteria has increased markedly. In a recent review the research on plutonium-bacteria interactions is summarized [1]. The plutonium speciation can be affected by environmental bacteria in many ways such as internal accumulation or uptake (Pu internal to cells), external accumulation (Pu associated with cells), metal reduction and oxidation, and biomineralization. Which pathway influences the plutonium speciation depends mostly on the local conditions (organic and inorganic ligands in the aquifer system, pH, Eh etc.) and the nature of the microorganism. To consider the influence of microbes on migration processes of actinides in risk assessment estimations of potential high level nuclear waste disposal sites one has to determine the indigenous microbial diversity to identify dominating bacterial strains. The Äspö HRL, established in Sweden in a granite rock formation for *in-situ* experiments with radionuclides, is one example for a facility to examine which methods are most suitable for research in the bedrock, to develop and demonstrate methods for deciding in which way a deep repository can be planned and constructed. Investigations of the microbial diversity at the Äspö site were performed and published by Pedersen et al. [2-4]. The total number of microorganisms measured at Äspö ranged from $1x10^3$ to $5x10^6$ cells $mL^{-1}$, whereas the number of SRB was between $10^1$ to $2x10^4$ cells $mL^{-1}$. The SRB strain *D. äspöensis* was isolated from the Äspö site, [5] and its unknown interaction behavior with plutonium is the subject of this paper.

The interaction process between microbes and actinides depends amongst others on the nature of the actinide element and the nature of the microbes. Plutonium exhibits a complicated chemistry because it can coexist in several oxidation states, i.e., +3, +4, +5 and +6, in aqueous solution under environmental conditions [1]. For instance, Pu(VI) dominates in marine and saline environments and in environments of high radionuclide concentrations [1] and possesses a high potential to be transported from contaminated areas due to its high solubility. For a better understanding of the migration process of plutonium, knowledge about the speciation and oxidation state distribution of this radionuclide is necessary. A detailed analysis of Pu(VI) interactions with the soil bacteria *Pseudomonas stutzeri* and *Bacillus sphaericus* was performed by Panak and Nitsche [6]. The authors found that 33% of Pu(VI) was reduced to Pu(V) after a contact time with the biomass of 24 h. They divided the interaction process into three sub processes: a) complexation of Pu(VI) with phosphate groups of the cell membrane, b) reduction of Pu(VI) to Pu(V) followed by a dissolution of Pu(V), and c) disproportionation of Pu(V) to Pu(VI) and Pu(IV) and complexation of the latter with the biomass (observed after 1 month). The formation of surface complexes of Pu(VI) with phosphate groups of the cell membrane of *B. sphaericus* was confirmed by X-ray absorption spectroscopy (XAS) [7].

Our research was focused on the interaction of plutonium in mixed oxidation states, 48 % as Pu(VI) and 31 % as Pu(IV)-polymers, with cells of the obligatory anaerobic SRB *D. äspöensis*. The accumulation of $^{242}Pu$ by the bacteria was investigated in dependence on the contact time and the initial plutonium concentration, $[^{242}Pu]_{initial}$, at pH 5 at strict anaerobic conditions due to the physiological needs of the studied bacterium. Solvent extractions and absorption spectroscopy were applied to explore the $^{242}Pu$ oxidation state

distribution a) in the blanks, b) the supernatants after separating the cells and c) of the Pu bound to the bacteria. XAS is a powerful tool to characterize the speciation of heavy metals in a broad range of experimental systems. This technique consists of two spectroscopic parts, X-ray absorption near edge structure (XANES) and extended X-ray ab-sorption fine structure (EXAFS). XANES was used to verify the plutonium oxidation states determined with the methods mentioned above, and EXAFS was applied to characterize the structure of the Pu accumulated by the cells of *D. äspöensis*.

### *Materials and methods*

The details concerning the biomass preparation, biosorption experiments, and experiments determining the Pu oxidation state distribution (absorption spectroscopy and solvent extractions) are given in [8].

XAS. The spectrum from the Pu(VI) reference sample (0.05 M in 1 M $HNO_3$) was taken from earlier measurements [9]. The Pu(IV) reference sample (0.08 M in 1 M $HClO_4$) was prepared as described in [10]. To get measurable amounts of *D. äspöensis* DSM 10631$^T$ biomass the concentration was enhanced to 9.2 ± 0.9 g/L. 1 mL of the bacterial suspension in 0.9 % NaCl was incubated with 5 mL of $^{242}$Pu, 127 mg/L, at pH 5. The amount of accumulated plutonium was 7.16 mg/$g_{dry\ weight}$. After shaking the samples for 96 h under nitrogen atmosphere, the biomass was separated by centrifugation, washed with 0.154 M NaCl solution, and sealed in a polyethylene cuvette. The bacterial sample was measured as wet past. The samples were measured 8 days after preparation. The Pu XAS data were recorded at the Rossendorf Beamline (ROBL, BM20) at the ESRF in Grenoble, France. The Pu $L_{III}$-edge X-ray absorption spectra were collected at room temperature either in fluorescence mode using a 13-element Ge solid-state detector or in transmission mode using Ar filled ionization chambers. A water-cooled Si(111) double-crystal mono-chromator was used in cannel cut mode (E = 5 - 35 keV). The higher harmonics were rejected by two Pt coated mirrors. Several EXAFS scans were collected from each sample and averaged. The fluorescence signal was corrected for dead time. For energy calibration of the sample spectra, the K-edge spectrum (17998 eV) from a Zr foil was recorded simultaneously. The ionization energy of the Pu $L_{III}$ electron, $E_0$, was arbitrarily defined as 18 077 eV. Data analysis was performed according to standard procedures [11] using EXAFSPAK software [12]. The amplitude reduction factor, $S_0^2$, was held constant at 0.9 for all the fits. The program FEFF7 [13] was used to calculate theoretical scattering amplitudes and phase-shift functions.

### *Results and discussion*

Figure 1 shows the main results of the Pu oxidation state distribution measurements obtained for the blanks, the supernatants after separating the cells and the biomass samples by solvent extraction. The Pu oxidation state distribution of the blanks remains relatively unchanged as 44 ± 6 % Pu(VI) and 29 ± 3 % Pu(IV)-polymers. 77 ± 5 % of the Pu occurs in the pentavalent oxidation state in the supernatant. The cell-bound $^{242}$Pu consist of 49 ± 7 % Pu(IV)-polymers and a certain amount of Pu, 37 ± 6 %, which is not accessible by solvent extraction. The observed processes cause changes of the oxidation state of Pu which have an impact on its migration behavior. The reduction of the Pu(VI) to Pu(V) by the bacteria leads to an increased dissolution of the cell bound plutonium. In contrast to the release of Pu(V) from the cell surface into the surrounding solution, we observed an immobilization of Pu as Pu(IV)-polymers by the biomass.

Pu $L_{III}$ edge XANES spectroscopy is a sensitive technique to identify changes in the electronic and molecular structure of Pu samples due to the energy position and shape of the spectra. Fig. 1A shows the results of the XANES measurements. The low intensity of the white line (WL) and the feature near 18080 eV are indicating dominating plutonyl

species in the blank, the supernatant and in the Pu(VI) reference. This shoulder above the WL, results from multiple scattering processes of the photo electron wave between the central Pu atom and the two axial oxygens.

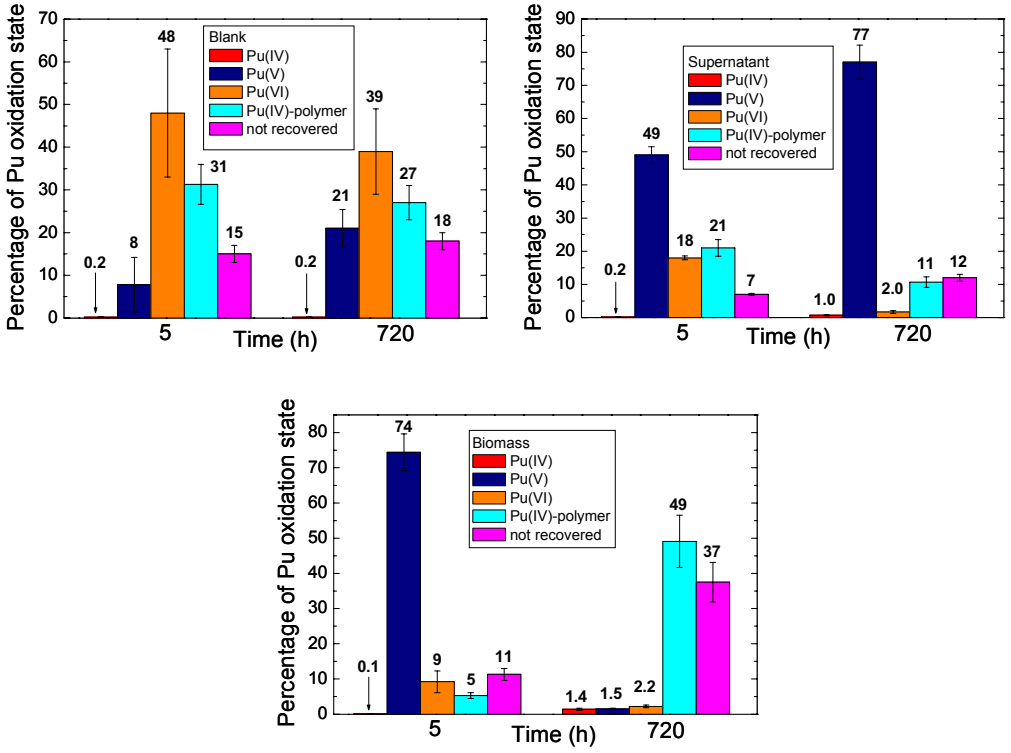


**Fig. 1.**
Summary of the solvent extraction experiments showing the change of the $^{242}$Pu oxidation state distribution in the samples (a) blank, (b) supernatant and (c) biomass over the time.

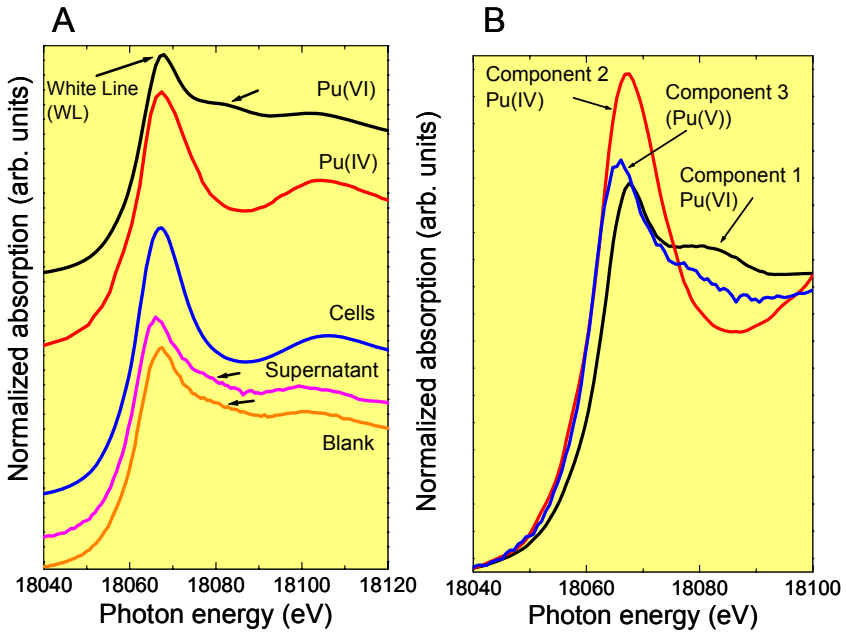


**Fig. 2.**
(A) XAS data of the blank solution, the supernatant, the biomass and from the Pu(IV) and Pu(VI) reference samples at the Pu $L_{III}$-edge. (B) Single component XANES spectra as a result from the iterative transformation factor analysis (FA).

From the shift of the first inflection point of the Pu $L_{III}$ absorption edge of the supernatant of 1.2 eV to lower energies compared to the Pu(VI) reference one can conclude that presumably Pu(V) dominates the Pu oxidation state distribution. In contrast to these samples, in the biomass sample and the Pu(IV) reference the WL is more pronounced and the Pu-Oax multiple scattering contribution is missing. It follows that the Pu accumulated by *D. äspöensis* occurs in the tetravalent oxidation state. These characteristic changes in the absorption spectra between 18000 and 18120 eV were used to determine the relative concentrations of the Pu species by applying the iterative transformation factor analysis (FA) as described in [14]. The calculations showed that every spectrum in Fig. 2A can be described by a combination of three independent components (see Fig. 2B). The main Pu oxidation states are Pu(VI), component 1, Pu(IV), component 2 and presumably Pu(V) for component 3. The analysis of the XANES spectrum of the biomass sample shows that the tetravalent Pu dominates besides 14 % of Pu(V) the oxidation state distribution of the biosorbed plutonium. Moreover, we can conclude that the plutonium which is not accessible by solvent extraction occurs as Pu(IV), presumably incorporated Pu(IV)-polymeric species, and as Pu(V), residuals of the reduction process of Pu(VI). In general a fair agreement between the results of the plutonium oxidation state distribution by solvent extraction as described in [8] and by FA of the XANES spectra was observed.

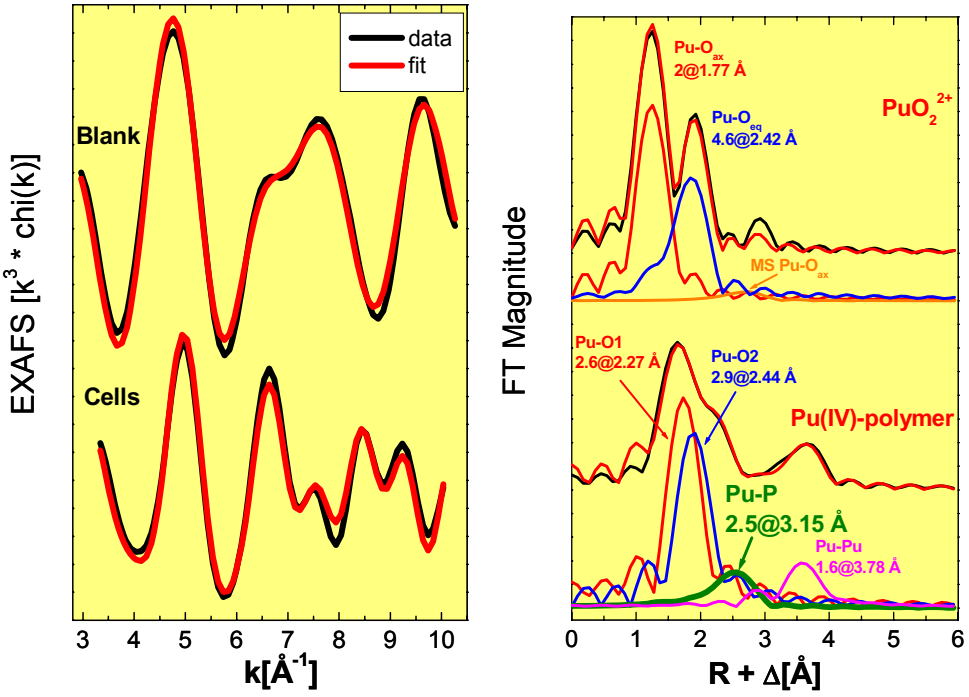


**Fig. 3.**
Pu $L_{III}$-edge $k^3$-weighted EXAFS spectra (left) and the corresponding Fourier transforms (right) of the blank and the biomass sample and the theoretical fits (dotted line). The transform range is 2.9 – 10.3 $Å^{-1}$ and the data were FT filtered using a Gaussian window (0.3 $Å^{-1}$).

The isolated and Fourier-filtered EXAFS oscillations and the corresponding Fourier transforms (FT) of the blank and biomass sample are shown in Figure 3. The FTs are not corrected for the EXAFS phase shift, so peaks appear at shorter distances (R + Δ) than the true near-neighbor distances (R). Ideally every peak shown in the FT corresponds to a special backscatter atom around the absorbing Pu atom. The amplitude of the EXAFS oscillation gives information concerning the coordination number of the individual atoms around the plutonium. The Pu in the blank is surrounded by two close axial oxygens at 1.77 Å and approximately 5 equatorial oxygens at 2.42 Å (see Fig. 3). These values are in

very good agreement with the literature [7]. Unfortunately, we cannot present structural parameter of Pu in the supernatant solution. Changes in the XANES from scan to scan showed that the sample was not stable in the synchrotron beam. The EXAFS oscillation of the cell-bound Pu shows close similarities to the spectra of colloidal Pu(IV) species published in [15]. The presence of an additional symmetric EXAFS oscillation giving a FT peak at R+Δ of app. 2.8 Å gives evidence for an interaction of the Pu(IV)-polymers with light atoms of the biomass. The best fit result could be obtained using phosphorus which points to an interaction with organic phosphate groups of the cell membrane structure as postulated for Cm(III) in [16]. The relatively short Pu-P distance of 3.15 Å indicates a bidentate coordination of the phosphate group to plutonium.

### *Conclusion*

This study demonstrates that there is a strong interaction of the two main Pu species, Pu(VI) and Pu(IV)-polymers, with the cells of *D. äspöensis*. On the basis of our results and taking into consideration the work of Panak and Nitsche [6], we developed a model which describes the ongoing processes (see Fig. 4) in the system Pu – *D. äspöensis*. The interaction with plutonium includes five processes which have different time scales. Interestingly, we have noticed close similarities, processes A to C in Fig. 4, between Pu – *D. äspöensis* interactions and those observed for Pu(VI) with the physiologically very different soil bacteria *P. stutzeri* and *B. sphaericus* published in [6].

**Process A and D:**
Simultaneous complexation of Pu(VI) and Pu(IV) Polymers by functional groups of the cell surface (e.g. phosphate groups)

**Process B:**
Fast reduction of Pu(VI) to Pu(V) and dissolution
of Pu(V)

**Process C:**
Disproportionation of Pu(V) to Pu(IV) and Pu(VI)

**Process E:**
Indications for
a) penetration of pu inside the cells
b) association / uptake of Pu
with / by degraded cells

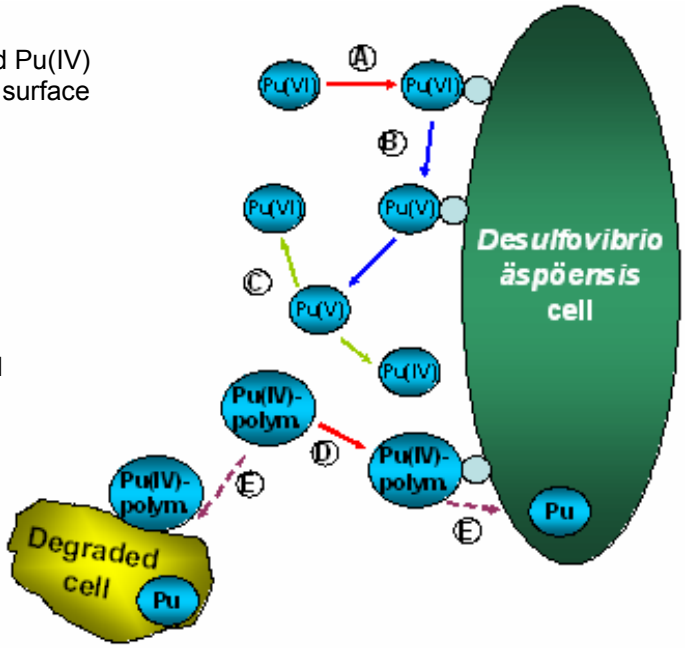


**Fig. 4.**
Illustration of the different processes describing the interaction of Pu with *Desulfovibrio äspöensis* based on the schema developed by Panak and Nitsche in [6].

In the first step, the Pu(VI) and Pu(IV)-polymers are bound to the biomass. However, in contrast to the results in [6], where one third of the initial Pu(VI) was reduced to Pu(V) after 24 h, we observed that 97 % of the Pu(VI) was reduced to Pu(V) due to the activity of the *D. äspöensis* cells in the same time range. The electron donors for such a process can be released from the dead part of the treated *D. äspöensis* culture. Most of the formed Pu(V) dissolves back to the aqueous solution due to the weak complexing properties of plutonium in this oxidation state. The dissolved Pu(V) disproportionates to Pu(IV) and Pu(VI). As already described for uranium in [17], we assume also for Pu a

damage of the cell membrane structure caused by the metal stress. Therefore, we conclude from the increased Pu amount which is strongly bound and not accessible for solvent extractions a penetration of Pu species (e.g., Pu(IV)-polymers) inside the bacterial cell. On the basis of the presented results we can not exclude additional interaction processes such as association of Pu(IV) polymeric species with released cell compo-nents and/or uptake of Pu(IV)-polymers by degraded cells. The EXAFS investigation of the Pu accumulated by *D. äspöensis* showed that Pu(IV)-polymeric species are bound to the cells. The XAS analysis gave no evidence for a precipitation of amorphous $Pu(OH)_4$ on the biomass. An interaction of the Pu(IV)-polymeric species with phosphate groups of the biomass were indicated by isolation of a Pu-P distance at 3.15 Å.

By characterizing the individual processes between *D. äspöensis* cells and pluto-nium, this study contribute to a more realistic description of the influence of microbial actions on the migration behavior of plutonium in the environment and are helpful for an improved risk assessment for potential underground nuclear waste repositories.

### *Acknowledgements*

This work was funded by the BMWi under contract number: 02E9491. The authors thank A. Scheinost and H. Funke for their help and support during the XAS experiments at ROBL. We would like to thank Ch. Den Auwer (CEA Marcoule, France) for providing us with the Pu(IV) reference sample.

### *References*

[1] M.P. Neu, G.A. Icopini, H. Boukhalfa, Radiochim. Acta **93** (2005) 705, and references therein.

[2] K. Pedersen, J. Arlinger, S. Ekendahl, L. Hallbeck, FEMS Microbiol. Ecol. **19** (1996) 249.

[3] S. Kotelnikova, K. Pedersen, FEMS Microbiol. Ecol. **26** (1998) 121.

[4] K. Pedersen, Engineer. Geol. **52** (1999) 163.

[5] M. Motamedi, K. Pedersen, Int. Syst. Bacteriol. **48** (1998) 311.

[6] P.J. Panak, H. Nitsche, Radiochim. Acta **89** (2001) 499.

[7] P.J. Panak, C.H. Booth, D.L. Clauder, J.J. Bucher, D.K. Shuh, H. Nitsche, Radiochim. Acta **90** (2002) 315.

[8] H. Moll, M.L. Merroun, C. Hennig, A. Rossberg, S. Selenska-Pobell, G. Bernhard, Radiochim. Acta **94** (2006) 815.

[9] T. Reich, G. Geipel, H. Funke, C. Hennig, A. Rossberg, G. Bernhard, Project-Group ESRF-Beamline (ROBL-CRG) Bi-Annual Report 1999/2000, FZR-322 (2001) 27.

[10] N. Charrin, Ph. Moisy, P. Blanc, Radiochim. Acta **88** (2000) 25.

[11] C.D. Koningsberger, R. Prins (eds): X-ray Absorption: Principles, Application, Techniques of EXAFS, SEXAFS and XANES. Wiley, New York, USA, 1988.

[12] G.N. George, I.J. Pickering: EXAFSPAK: A Suite of Computer Programs for Analysis of X-ray Absorption Spectra. Stanford Synchrotron Radiation Laboratory, Stanford, USA, 1995.

[13] S.I. Zabinsky, J.J. Rehr, A. Ankudinov, R.C. Albers, M.J. Eller, Phys. Rev. B **52** (1995) 2995.

[14] A. Roßberg, T. Reich, G. Bernhard, Anal. Bioanal. Chem. **376** (2003) 631.

[15] J. Rothe, C. Walther, M.A. Denecke, Th. Fanghänel, Inorg. Chem. **43** (2004) 4708.

[16] H. Moll, Th. Stumpf, M. Merroun, A. Roßberg, S. Selenska-Pobell, G. Bernhard, Environ. Sci. Technol. **38** (2004) 1455.

[17] H. Moll, M. Merroun, Th. Stumpf, A. Roßberg, G. Geipel, S. Selenska-Pobell, G. Bernhard: Interaction of actinides with the predominant indigenous bacteria in Äspö aquifer – Inter-actions of selected actinides U(VI), Cm(III), Np(V) and Pu(VI) with *Desulfovibrio äspöensis*. Wissenschaftlich-Technische Berichte FZR-422 (2005), and references therein.

# *In situ* x-ray studies of $M_{n+1}AX_n$-phase $Ti_2AlN$ thin film growth

M. Beckers[1,2], N. Schell[3,4], A. Mücklich[2], R.M.S. Martins[2,4], and C. Höglund[1]

[1] Thin Film Physics Division, IFM, Linköping University, SE-581 83 Linköping, Sweden

[2] Institute of Ion Beam Physics and Materials Research, Forschungszentrum Dresden-Rossendorf, 01314 Dresden, Germany

[3] GKSS Research Center Geesthacht, Max-Planck-Str. 1, 22502 Geesthacht, Germany

[4] The Rossendorf Beamline (BM20), ESRF, 38043 Grenoble, France

## *Introduction*

The $M_{n+1}AX_n$ (n = 1–3, or short MAX) phases constitute a family of about 60 nanolaminated ternary carbides and nitrides with M being an early transition metal, A an A -group element, and X being carbon or nitrogen [1]. The interest in these compounds was stimulated by the remarkable material $Ti_3SiC_2$, combining ceramic properties as temperature stability and oxidation resistance with metallic properties as good thermal and electrical conductivity, ductility, and ease of machinability. These properties are based on the MAX phase hexagonal crystal structure of $M_{n+1}X_n$ slabs interleaved by A-element layers. Alternating strong covalent-ionic M-X bonds within the slabs, and weak metallic M-A bonds in between yield low plasticity and kink band formation, in contrast to the hard yet brittle binary MX phases. These properties can be further designed by the number of M layers separating the A layers, which is, two, three, and four in the $M_2AX$, $M_3AX_2$ and $M_4AX_3$ compounds, respectively.

The MAX phases' unique mechanical properties could also be profitable for nano-scale applications, and consequently the feasibility of MAX phase thin film synthesis in the Ti-Si-C system was recently demonstrated by Palmquist *et al.* [3]. Using DC magnetron sputtering, they reported deposition temperatures of 900°C, far below bulks synthesis temperatures. Results on $Ti_2AlC$ and $Ti_3AlC_2$ as well as on $Ti_{n+}1GeC_n$ followed [4, 5]. The reactive sputter deposition of nitride $M_{n+1}AN_n$ thin films is more challenging, since nitrogen has to be introduced via the gas phase within a narrow partial pressure window. As a consequence, only recently Joelsson *et al*. [6] reported the deposition of $Ti_2AlN$ thin films. They used reactive sputtering from a compound 2Ti:Al target at temperatures of 830°C, leading to single crystal films with parallel basal plane $Ti_2AlN$ growth.

The present work reports on *in situ* x-ray diffraction studies during $Ti_2AlN$ formation by reactive cosputtering using elemental Ti and Al targets [7, 8, 9], as well as by solid-state-reaction from AlN and Ti bilayers [10].

## *Experimental*

The *in situ* experiments were facilitated by a deposition chamber that is equipped with x-ray windows and mounted into the goniometer of the ROBL beamline [11]. Two one inch magnetrons with pneumatically controlled shutters and Ti, respectively Al targets were used for the thin film deposition. The substrate temperature during deposition was measured by using a K-type thermocouple, which was re-checked by pyrometry. The base pressure was ~ $8\times10^{-5}$ Pa. Single crystal MgO(111) and $Al_2O_3$(0001) wafers were used as substrates.

Monochromatized x-rays with $\lambda$ = 0.961 Å and $\lambda$ = 1.051 Å were employed to study the film growth *in situ.* Each sequential deposition step was characterized in two different scattering geometries: (1) low angle time-resolved x-ray scattering at a fixed incidence angle to characterize growth mode and roughening by the observed intensity oscillations, or angle-resolved x-ray reflectivity (XRR) for the determination of the film thickness; (2)

symmetric $\theta$–$2\theta$ large angle x-ray diffraction (XRD) in order to determine included phases, off-plane lattice parameters and preferred orientation. The microstructure and texture of the films were investigated using a combination of pole figure measurements and cross-sectional transmission electron microscopy (TEM). The film composition was examined by Rutherford backscattering spectroscopy (RBS), using a 1.7 MeV $He^+$ beam.

### *Results and discussion for $Ti_2AlN$ formation by reactive cosputtering*

The first route of $Ti_2AlN$ formation described here is setting the magnetron powers and the nitrogen partial pressure to appropriate parameters to obtain the correct stoichiometry. To avoid interdiffusion into the MgO(111) substrate, and to account for eventual deviation from composition, a $(Ti_{0.67}Al_{0.33})N$ seed layer was deposited prior to $Ti_2AlN$ at a working pressure of 0.35 Pa and powers according to previous work [7]. For stable $Ti_2AlN$ growth conditions, the pressure was increased to 0.8 Pa at $Ar/N_2$ fluxes of 7.94/0.48 sccm, with changed Ti/Al powers of 80/26 W. The deposition temperature was kept at 630°C, 200°C below previously reported values for $Ti_2AlN$ deposition [6].

Figure 1 shows the time-resolved growth oscillations for (a) the seed layer and (b) the subsequent $Ti_2AlN$ deposition. The amplitude of the intensity oscillations for the seed layer does not diminish during deposition, suggesting a smooth layer-by-layer growth. Each oscillation can be attributed to one lattice constant of $(Ti_{0.63}Al_{0.37})N$, hence a perfect cube-on-cube heteroepitaxial relation $(Ti_{0.63}Al_{0.37})N\{100\}<100>$ // $MgO\{100\}<100>$ can be deduced. On the contrary, the exponential decay of the $Ti_2AlN$ growth oscillations, shown in Fig. 1(b), points towards a pronounced kinetic roughening. Hence the $Ti_2AlN$ grows via a Stranski-Krastanov-like mode, which is in clear contrast to the seed layer.

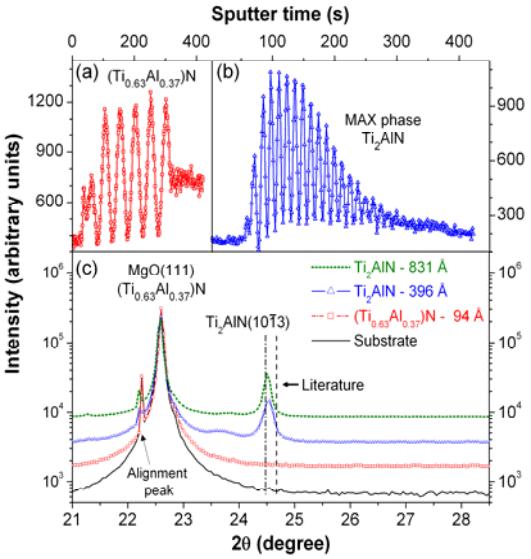


**Fig. 1.**
Time-dependent *in situ* XRR data for (a) the fcc $(Ti_{0.63}Al_{0.37})N$ seed layer and (b) the $Ti_2AlN$ deposited onto MgO(111). (c) shows *in situ* XRD data recorded after the deposition of the seed layer and two $Ti_2AlN$ deposition steps of approximately 400 Å.

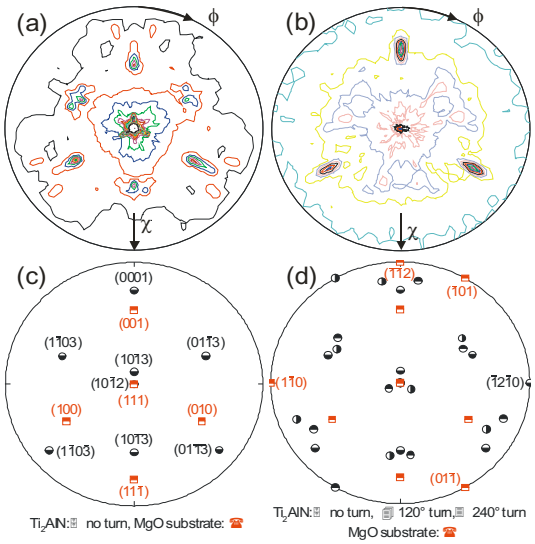


**Fig. 2.**
Pole figures of $Ti_2AlN$ grown onto MgO(111), nominally measured on (a) $Ti_2AlN(10\bar{1}3)$ and (b) $Ti_2AlN(0002)$. The stereographic projection (c) shows the theoretical poles of $Ti_2AlN\{10\bar{1}3\}$, $\{10\bar{1}2\}$, $\{0001\}$, $\{\bar{2}1\bar{1}0\}$ and $MgO\{111\}$, $\{1\bar{1}0\}$, $\{\bar{1}\bar{1}2\}$. (d): The experimental pole figures in (a) and (b) can be obtained by turning (c) for 120°, as indicated by the symbols.

The corresponding $\theta$–$2\theta$ XRD scans are shown in Fig. 1(c). After deposition of the seed layer the intensity distribution remains undistinguishable due to the perfect epitaxial nature of the seed layer growth. After the first deposition of ~ 400 Å $Ti_2AlN$, only the

$Ti_2AlN(10\bar{1}3)$ peak can be identified. A mix-up with $Ti_2AlN(0006)$ can be excluded due to the lack of other order $Ti_2AlN(000\ell)$ peaks at lower scattering angles (not shown here). For later discussions it should be noted that the lattice spacing of the $Ti_2AlN(10\bar{1}3)$ peak is larger compared to literature values, as indicated by the dashed vertical line.

Figure 2 shows the experimental pole figure for $Ti_2AlN$ on MgO(111), recorded for the $Ti_2AlN(10\bar{1}3)$ peak. Due to the immediate vicinity of the $Ti_2AlN(0006)$ and MgO(111) as well as MgO(100) peaks, the pole figure comprises orientation distributions of all these four lattice planes. The $\theta$-$2\theta$ scans of all cluster points within the experimental pole figure in Fig. 2(a) showed only substrate and $Ti_2AlN(10\bar{1}3)$ Bragg peaks, except for the ones at $\chi \sim 60°$. Here, a peak at $2\theta = 13°$ was observed, which is close to $Ti_2AlN(0002)$. The pole figure on that peak in Fig. 2(b) clearly shows three distinct cluster points at $\chi \sim 60°$ and $\phi = 0°$, 120° and 240°. Thus, the $Ti_2AlN(000\ell)$ basal planes are tilted ~60° away from the surface normal with threefold in-plane symmetry.

Figure 2(c) displays the stereographic projection of the $Ti_2AlN$ and MgO lattice. Assuming single-crystal $Ti_2AlN$ and MgO(111), we obtain a central MgO(111) pole and three MgO{100} poles at $\chi = 54.7°$ with azimuth angles $\phi = 0°$, 120° and 240°. As seen in Fig. 2(b), the $Ti_2AlN(0001)$ pole lies in close vicinity at $\chi = 60°$. As a consequence, the $Ti_2AlN(10\bar{1}3)$ pole does not lie in the center, but at $\chi = 9°$ and $\phi = 0°$ and accordingly, the $Ti_2AlN(10\bar{1}2)$ pole lies at the center. Hence, one can denote MgO(111) // $Ti_2AlN(10\bar{1}2)$. Within Fig. 2(a), permutation of the first three Miller indices yields five additional $Ti_2AlN\{10\bar{1}3\}$ poles, positioned as indicated by the indices and the symbol (5). Additionally, this figure must also be turned around by 120° and 240° due to the threefold symmetry of the $Ti_2AlN(0002)$ peak. This makes up for another fourteen [2 times (6+1)] cluster points. For clarity, the indexing of these collective points in Fig. 2(d) has been omitted. Each turn of 120° is indicated by the symbols (4) and (3). The picture obtained describes all the features of the experimental pole figures in Figs. 2(a) and 2(b).

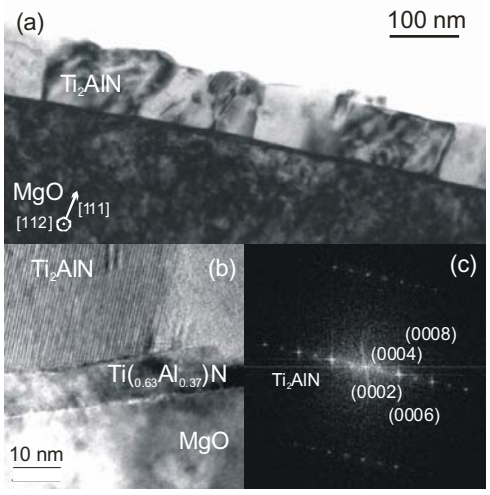


**Fig. 3.**
XTEM micrographs of $Ti_2AlN$ grown on MgO(111) along the MgO[112] zone axis. (a) shows the film morphology consisting of large crystal regions. (b) shows a high resolution micrograph at the interface with the typical MAX phase 2-1-1 layered structure. It is made up by the (000 ) pla nes as confirmed from the d-spacing calculation by Fast Fourier Transformation in (c).

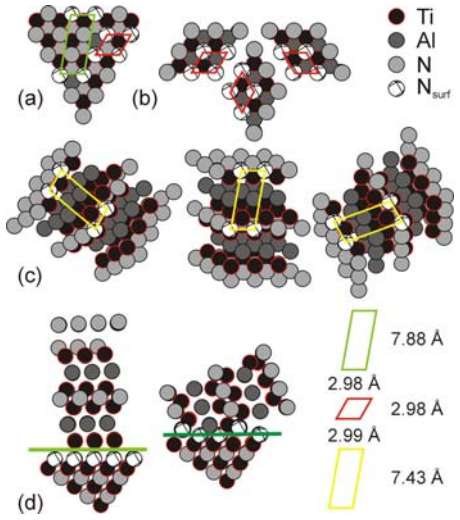


**Fig. 4.**
Atomic illustration of $(Ti_{0.63}Al_{0.37})N$ and $Ti_2AlN$ planes and directions (a) shows the $(Ti_{0.63}Al_{0.37})N(111)$ surface and (b) the three different $Ti_2AlN\{0001\}$ orientations along $(Ti_{0.63}Al_{0.37})N<110>$. (c) shows the same threefold orientation for the $Ti_2AlN\{10\bar{1}2\}$ planes. (d) shows cross-sectional views of the $Ti_2AlN/(Ti_{0.63}Al_{0.37})N$ interface for basal-plane and *non* basal-plane growth.

The azimuthal orientation relationship can be found by looking at the poles for

$\chi = 90°$, where the MgO($1\bar{1}0$) and $Ti_2AlN$($1\bar{2}\bar{1}0$) poles overlap. For the cubic MgO the corresponding direction is [$1\bar{1}0$] and for the $Ti_2AlN$ it is [$1\bar{2}\bar{1}0$]. Since there are three possible MgO<110> directions on the MgO(111) surface, the threefold in-plane symmetry of the $Ti_2AlN$ can thus be described by the full orientation relation MgO{111}<110> // $Ti_2AlN${$10\bar{1}2$}<$1\bar{2}\bar{1}0$>.

Figure 3(a) depicts an XTEM micrograph from the $Ti_2AlN$ film described above, recorded along the MgO[112] zone axis. The layer is not single-crystalline, but exhibits equiaxed morphology with individual epitaxial grains oriented corresponding to Fig. 2. Their sizes are in the dimension of the film thickness. Individual grains show strong diffraction contrast, which is due to the threefold in-plane symmetry described above. In accordance with the exponential decay of the growth oscillations, the layer displays high surface roughness, caused by the tilted *non* basal-plane growth. In a higher magnification of the interface shown in Fig. 3(b), the tilted $Ti_2AlN$ basal-planes can be depicted from the typical layered 2-1-1 MAX phase structure. The lattice plane spacing calculations by Fast Fourier Transformation shown in Fig. 3(c) confirm multiple $Ti_2AlN(000\ell)$ planes. The basal plane tilt angle is ~ 70°, in agreement with pole figure measurements. Hence, each grain in Fig. 3(a) represents one possible $Ti_2AlN(000\ell)$ in-plane orientation.

To conclude, both pole figures and XTEM show that for the current low temperature deposition at 630°C the orientation relationship between MgO and $Ti_2AlN$ is MgO{111}<110> // $Ti_2AlN${$10\bar{1}2$}<$1\bar{2}\bar{1}0$>. This is in contrast to the $Ti_2AlN$ basal-plane growth for a high-temperature deposition, with MgO{111}<110> // $Ti_2AlN${0001}<$1\bar{2}\bar{1}0$> [6, 8]. This orientation relation is to be expected due to the low 0.77% lattice mismatch between the $Ti_2AlN$(0001) and MgO(111) surfaces, as indicated in Figs. 4(a-d). During initial growth, three different types of $Ti_2AlN$(0001) nuclei along the MgO<110> directions may nucleate as illustrated in Fig. 4(b). These orientations allow for grain-boundary free coalescence in later stages, resulting in single-crystal film morphology [6, 8].

For the described low-temperature process, we find the MgO(111) to be parallel to the $Ti_2AlN$($10\bar{1}2$) plane, which is indicated by the polygons in Fig. 4(c). As can be taken from the polygons a low lattice mismatch of 0.77% along one MgO<110> direction is possible. However, single-crystalline epitaxial growth is prevented. Firstly, an initial threefold rotated $Ti_2AlN$($10\bar{1}2$) nucleation does *not* allow grain-boundary free coalescence. This is in agreement with the polycrystalline equiaxed morphology observed in XTEM, and the pole figure results. Secondly, the adaptation to the other MgO<110> directions can only be achieved when taking also next-nearest surface nitrogen atoms into account, as shown by the polygon in Fig. 4(a). Still, the reconstruction exhibits a large lattice misfit of 6%. Besides, the cross-sectional view in Fig. 4(d) demonstrates that the interface cannot be configured only by Ti-N bondings, as it would be the case for basal-plane grown $Ti_2AlN$(0001) // MgO(111). In fact, a ternary Ti-Al-N atomic reconfiguration of more than nearest-neighbor-atoms is necessary.

This rather complicated and strained interfacial bonding could be attributed to the following: When depositing on the $(Ti_{0.63}Al_{0.37})N$ seed layer, its (111) surface tends to be N-terminated. Comparing with Fig. 4(d), this implies that the initial atomic layer of $Ti_2AlN$(0001) has to consist purely of Ti atoms. However, the employed co-sputtering process provides an incoming flux of *both* Ti and Al atoms, so the initial elementary composition would need to be reconfigured. This reconfiguration will be hindered, since the $(Ti_{0.63}Al_{0.37})N$(111) surface is one with a relatively high adatom bonding energy and thus low mobility [7]. Moreover, the low substrate temperatures will aggravate this deficiency of adatom mobility. Hence, a texture evolution with maximum thermodynamic stability, e.g. parallel basal-plane orientation is hampered by kinetics. A deposition on MgO substrates at higher temperatures from 675°C [8] to 830°C [6] allows for the correct partitioning of the elements at the substrate-film interface and consequently induces parallel basal plane growth.

### *Results and Discussion for $Ti_2AlN$ formation by solid-state reaction*

An alternative route for $Ti_2AlN$ formation is a solid-state-reaction from appropriate diffusion couples. Here we concentrate on the couple AlN and Ti, deposited at low temperatures and subsequently annealed. The AlN and Ti multilayers were deposited onto $Al_2O_3(0001)$ at 200°C and working pressures of 0.33 and 0.48 Pa. The AlN was grown at $N_2$/Ar fluxes of 0.66/2.16 sccm at an Al power of 27 W, the Ti at an Ar flux of 3.4 sccm with the magnetron set to 20 W. Figs. 5 and 6 show the *in situ* data obtained for a stack of 26 nm AlN / 10 nm Ti / 11 nm AlN / 20 nm Ti / 11 nm AlN that was subsequently annealed between 400–500°C for about 2 h.

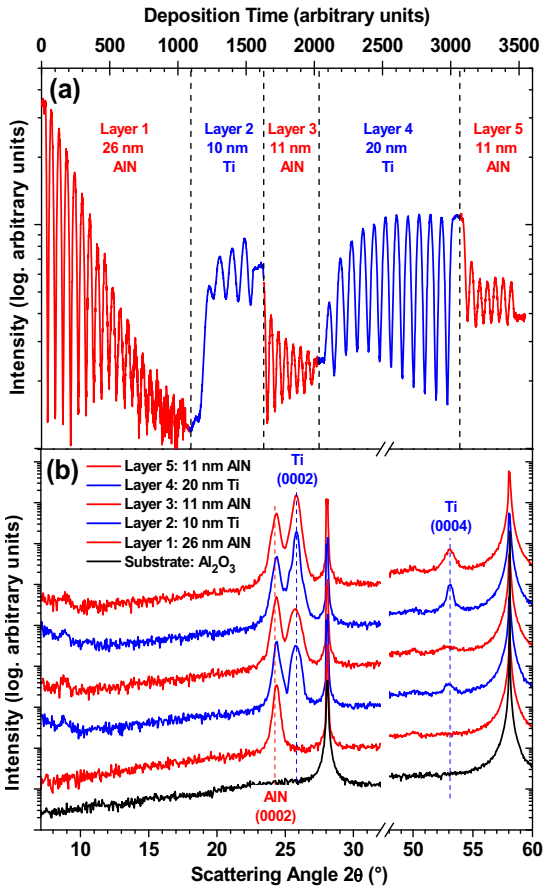


**Fig. 5.**
(a) shows *in situ* time-resolved x-ray reflectivity taken during sequential deposition steps of epitaxial AlN and Ti on $Al_2O_3(0001)$ and (b) shows the corresponding XRD patterns recorded after each deposition step.

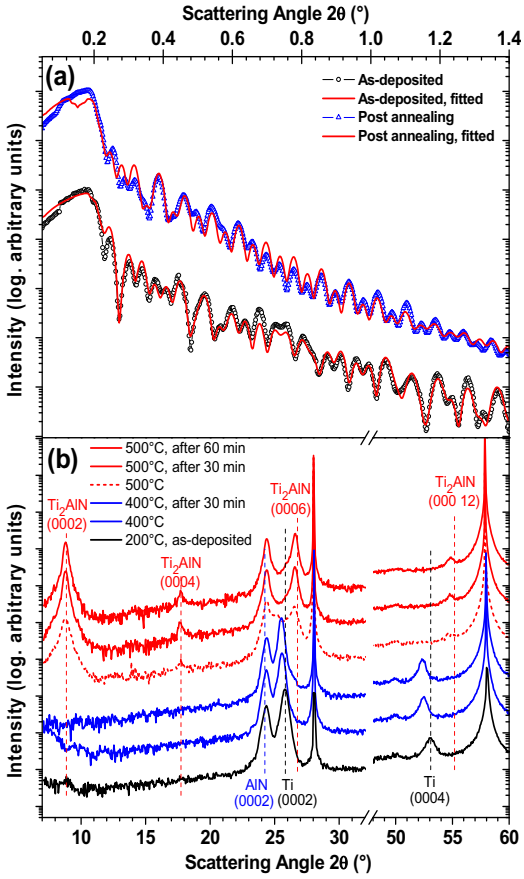


**Fig 6.**
(a) shows experimental and fitted *in situ* angular resolved x-ray reflectivity of the as-deposited and annealed film, and (b) shows the large angle XRD data recorded every 30 minutes during annealing between 400–500ºC.

Figure 5(b) depicts the XRD data obtained after each sequential deposition step. It reveals basal-plane heteroepitaxial growth of AlN(0001) and Ti(0001) onto the $Al_2O_3(0001)$ substrate. Pole figure measurements (not shown here) demonstrated multiple domains though, due to the relatively large lattice mismatch of 5 % (AlN-Ti) and 16 % (AlN-$Al_2O_3$). Each AlN(0002) signal exhibits lower intensity when compared to the Ti(0002) intensity of the yet thinner Ti layer. This can be understood by the x-ray growth oscillations displayed in Fig. 5(a). Since the adatom mobility on AlN at 200°C is considerably low, the growth surface roughens and correspondingly the intensity oscillations for each AlN deposition show rapid exponential decay. Ti on the contrary possesses a higher electron density than AlN plus increased adatom mobility, hence already during initial growth stages the reflectivity signal is increased, amplified by a significant surface smoothing, as can be

deduced from the exponential growth of the intensity oscillations, in clear contrast to the AlN signal. Also the fits to the angle-resolved XRR of the final film resulted in AlN surface roughnesses in the order of 5 Å, while the Ti roughnesses were in the sub-Å region. In accordance to the smoother growth front a lower mosaicity of the Ti can be expected, and hence also an increased XRD signal. The growth oscillations were not recorded at the anti-Bragg ½*$Q_d$ value, but could easily be fitted with a layer-by-layer growth model when taking the $Q_{meas}/Q_d$ value into account, where $Q_d$ denotes the $Q$ value corresponding to the c-axis value of Ti and AlN, respectively.

The XRD data during annealing of this multilayer stack, shown in Fig. 6(b) imply that the first stage of interfacial reaction at 400°C seems to be AlN decomposition and nitrogen diffusion into Ti to form a $TiN_x$ compound as can be deduced from the shifting Ti peak, pointing towards lattice expansion. No further reaction takes place after holding 400°C for another 30 minutes. When increasing the temperature to 500°C, however, already after the ramping period of approx. 5 minutes $Ti_2AlN$ formation is evident by a $Ti_2AlN$(0002) peak. Accordingly the Ti(0002) intensity diminishes beyond the detection limit after a holding time of 60 minutes. The interfacial reaction can also be deduced from the XRR data illustrated in Fig. 5(a), where the single layer beating after annealing has vanished. Also RBS data (not shown here) proves a complete transformation of Ti in $Ti_2AlN$ with superfluous AlN residues.

This parallel basal plane-oriented $Ti_2AlN$ formation at 500°C is about 170°C lower than temperatures reported in [8] and may open up low temperature $Ti_2AlN$ applications as well as MAX phase formation by other AN-M diffusion couples.

### *Summary*

We have demonstrated the formation of $Ti_2AlN$ by both-reactive magnetron cosputtering from elemental targets and solid-state reaction from AlN-Ti diffusion couples. While sputter deposition at 630°C leads to a tilted basal plane growth due to a kinetically hampered nucleation, parallel basal plane oriented $Ti_2AlN$ can be achieved at temperatures down to 500°C when using templates of comparable as the desired texture state.

### *Acknowledgments*

We gratefully acknowledge assistance by U. Strauch during experiments and financial support from the Deutsche Forschungsgemeinschaft under contract SCHE 682.

### *References*

[1] M.W. Barsoum, Prog. Solid St. Chem. **28** (2000) 201.
[2] W. Jeitschko, H. Novotny, F. Benesovsky, Monatshefte der Chem. **94** (1963) 1198.
[3] J.-P. Palmquist, U. Jansson, T. Seppänen, P.O.Å. Persson, L. Hultman, P. Isberg, Appl. Phys. Lett. **81** (2002) 835.
[4] O. Wilhelmsson, J.-P. Palmquist, T. Nyberg, U. Jansson, Appl. Phys. Lett. **85** (2004) 1066.
[5] H. Högberg, P. Eklund, J. Emmerlich, J. Birch, L. Hultman, J. Mater. Res. **20** (2005) 779.
[6] T. Joelsson, A. Hörling, J. Birch, L. Hultman, Appl. Phys. Lett. **86** (2005) 111913
[7] M. Beckers, N. Schell, R.M.S. Martins, A. Mücklich, W. Möller, L. Hultman, J. Appl. Phys. **99** (2006) 034902.
[8] M. Beckers, N. Schell, R.M.S. Martins, A. Mücklich, W. Möller, Appl. Phys. Lett. **89** (2006) 074101.
[9] M. Beckers, N. Schell, R.M.S. Martins, A. Mücklich, W. Möller, L. Hultman, J. Appl. Phys., accepted.
[10] C. Höglund, M. Beckers, N. Schell, J. Birch, J. v. Borany, L. Hultman, Appl. Phys. Lett., submitted.
[11] W. Matz, N. Schell, W. Neumann, J. Bøttiger, J. Chevallier, Rev. Sci. Instrum. **72** (2001) 3344.

# Metastability of $CuInS_2$ and its implications on thin film growth

T. Hahn[1], J. Cieslak[1], H. Metzner[1], J. Eberhardt[1], U. Reislöhner[1], M. Gossla[1], W. Witthuhn[1] and J. Kräußlich[2]

[1] Institute of Solid State Physics, Friedrich-Schiller-University of Jena, Max-Wien-Platz 1, 07743 Jena, Germany

[2] Institute for Optics and Quantum Electronics, Friedrich-Schiller-University of Jena, Max-Wien-Platz, 07743 Jena, Germany

### *Introduction*

Due to their advantages Cu-based Chalcopyrite semiconductors are nowadays used as absorber layers in thin-film photovoltaic devices. They combine high conversion efficiencies with an extraordinary resilience against radiation damage and the possibility for economic large area depositions by well established thin-film technologies [1]. A special feature of these materials has attracted some attention in recent years: the easy formation of polytypes. Here, apart from the ground-state chalcopyrite ordering, the metastable CuAu-type ordering is of high importance, especially in epitaxial and polycrystalline thin layers of the ternary semiconductor $CuInS_2$ (CIS). As a result of theoretical calculations, Wei *et al.* [2, 3, 4] pointed out, that this metastable phase has an exceptionally low formation energy for CIS and most related compounds, so that the coexistence of chalcopyrite and CuAu-type ordering in thin-films grown at low deposition temperatures is very likely to occur. High-resolution transmission electron microscopy investigations on epitaxial CIS-layers on Si-substrates confirmed these predictions [4-6].

Since then, it turned out, that the metastable CuAu-structure of CIS is essential for the growth of CIS-based solar cells: on one hand absorber material consisting mainly of the CuAu-polytype shows low performance [7] as compared to the chalcopyrite ground state. On the other hand, the phase formation of chalcopyrite CIS in polycrystalline layers formed by the sulphurization of metallic precursors was found to occur via the preceding nucleation of the CuAu-type structure [8]. As a consequence, we now have quite a profound knowledge about the CuAu-type structure of CIS as far as transmission electron microscopy, Raman scattering and photoluminescence are concerned [6, 9, 10]. However, with respect to the lattice constants of this important polytype, only few results are reported in literature. Alvarez-Garcia *et al.* [9] assumed similar lattice constants for both orderings, while Hahn *et al.* [11] reported the CuAu-phase of CIS to be nearly cubic with a lattice constant of $a$ = 0.549(6)nm. Keeping in mind the anisotropic nature of the CuAu-type structure, it becomes clear, that measurements of higher accuracy are necessary in order to specify its crystallographic properties.

### *Experiments and discussion*

Hence, we have performed x-ray diffraction (XRD) measurements on epitaxial CIS thin-films on Si(001) substrates at the ROBL beamline (BM-20) at the ESRF synchrotron facility in Grenoble (France) [12]. CIS was grown on sulphur-terminated Si(001) substrates without off-cut via molecular beam epitaxy (MBE) from elemental sources in a deposition process described previously [13]. The (001)-orientation of the substrates was chosen, since we found that it promotes the growth of the CuAu-polytype with its $c$-axis perpendicular to the surface [11]. The chalcopyrite and CuAu-type structures are shown in Fig. 1. These orderings can easily be distinguished in XRD if the proper reflections are chosen. Considering the selection rules for the chalcopyrite structure ($h+k+l = 2n$ and if $h = k$, then $2h+l = 4n$) and the CuAu-type structure ($h+k = 2n$, $l$ arbitrary), it follows that the appearance of a reflection like $(001)_{ca}$ is unique for the CuAu-type structure, since the

corresponding $(002)_{ch}$ reflection is forbidden for the chalcopyrite structure. Here, we have introduced subscripts in order to distinguish a labeling of the reflections according to the chalcopyrite (ca) or CuAu-type (ca) structure.

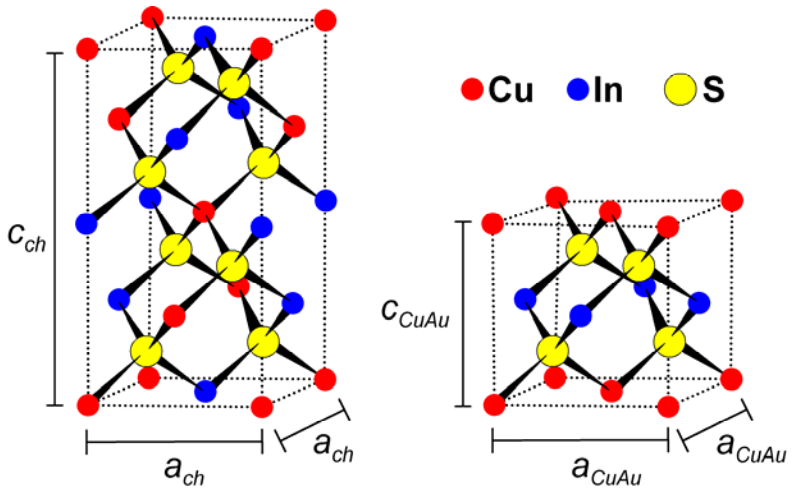


**Fig. 1.**
Crystal structures of the chal-copyrite (left, subscript "ch") and CuAu-type (right, subscript "ca") phase of CIS. For the CuAu-type structure a conventional unit cell is shown, which is used throughout this work for indexing CuAu-type reflections and evaluation of the lattice parameters. The tetragonal primitive unit cell for the CuAu-type structure differs from the depicted unit cell by a rotation of 45° in the *x*-*y*-plane and by being half as large [16].

The high intensity of the synchrotron source provides the opportunity to investigate in-plane (00*l*)-reflections as well as perpendicular (0*k*0)-reflections by utilizing a reflection or a transmission geometry setup, respectively. The diffraction patterns were taken in a standard Bragg-Brentano geometry and an X-ray wavelength of $\lambda$ = 0.1032 nm was chosen. All lattice parameters given within this work were calculated as mean values from the respective series of measurements. The volume fractions of the chalcopyrite and CuAu-type phase were calculated as mean values from those diffraction patterns showing both types of ordering. The errors for the lattice parameters as well as the volume fractions were derived from the fitting errors, which were found to be larger as compared to the dispersion of the individual values.

The composition, homogeneity, and morphology of the samples were investigated by means of Rutherford backscattering spectroscopy (RBS). Figure 2 depicts a typical spectrum. Here, a completely homogeneous, 430 nm thick film of the slightly Cu-rich composition $Cu_{1.06}In_{0.94}S_{2.0}$ with a surface roughness of 47 nm (half-width at half maximum - HWHM - of the height distribution) is visible. From RBS, there is no evidence for any phase segregations or the inclusion of minor phases within the sample.

The series of XRD measurements on the (00l) reflections as shown in Fig. 3 reveals unambiguously the coexistence of two phases. The appearance of the $(001)_{ca}$ and $(003)_{ca}$ reflections reveals the presence of the CuAu-type ordering in the sample, while the double- peak structure of the $(004)_{ch}$ / $(002)_{ca}$ and $(008)_{ch}$ / $(004)_{ca}$ reflections is due to the coexistence of CuAu-type with the chalcopyrite ordering. The assignment of the double-peak structures being due to the simultaneous growth of *c*-axis and *a*-axis oriented chalcopyrite grains is less likely, since a different peak-splitting is observed within the (0*k*0)-series of diffraction patterns as depicted in Fig. 4.

From the peak positions within the series of (00*l*)-reflections we derived the *c*-axis parameters of the CuAu-type and the chalcopyrite ordering to be $c_{ca}$ = 0.5503(3) nm and $c_{ch}$ = 1.1078(7) nm, respectively. The ratio of the intensities of the reflections allows the direct determination of the volume fractions of the two orderings since their structure

factors are equal [9]. In the present case, the CuAu-ordering accounts for 67(3)% of the sample, while 33(3)% of the sample exhibits the chalcopyrite structure. A third net plane parallel to the surface appears in the diffraction pattern taken between $2\theta$ = 43° and 45° by a weak shoulder at $2\theta$ = 44.51(1)°. However, the derived lattice parameter of $c$ = 0.5468(2) nm does neither match the chalcopyrite, nor the CuAu-type ordering. Therefore, it presumably stems from a small inclusion of a third phase such as the disordered zincblende structure.

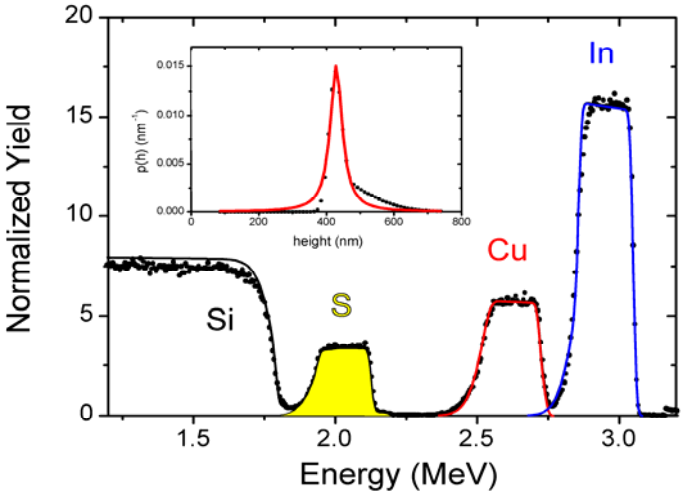


**Fig. 2.**
RBS-spectrum of an epitaxial CIS-thin-film on Si(001). The contributions of the individual elements to the spectrum are indicated. The inset shows the normalized height distribution of the sample as derived from the RBS-spectrum. The spectrum was recorded with an incident α-energy of 3.5MeV.

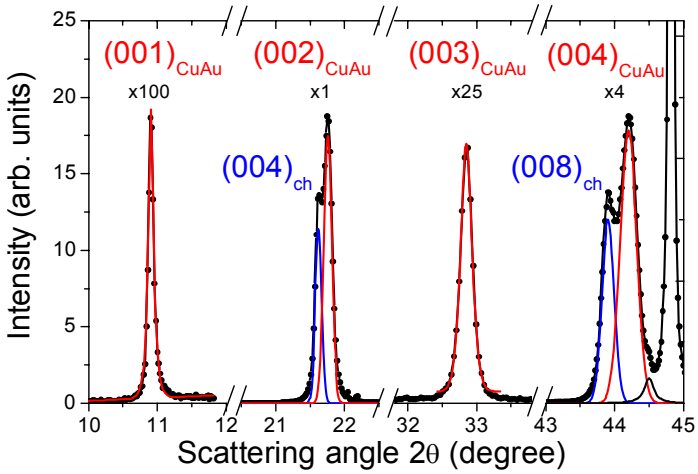


**Fig. 3.**
XRD-spectra of the (00l) in-plane reflections. Mixed Lorentz / Gauß-profiles (solid lines) were fitted to the spectra. The high diffraction intensity around $2\theta$ = 44.8° is due to the Si-substrate.

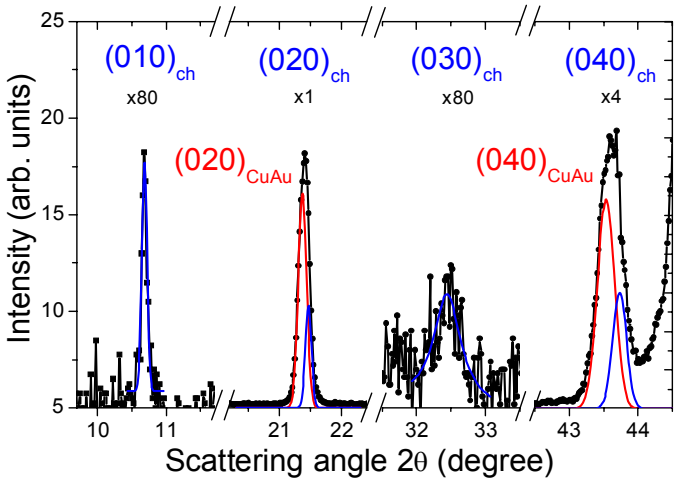


**Fig. 4.**
XRD-spectra of the (0$k$0) out-of-plane reflections as measured in transmission geometry.

Figure 4 depicts the series of (0*k*0)-reflections taken in transmission. The (010)- and (030)-reflections shown are forbidden for all known CIS orderings. Nevertheless, faint but sharp reflections are visible at $2\theta$ = 10.687(4)° and 32.45(4)°. One first might suggest a small amount of *a*-axis oriented growth within the sample to be responsible for the occurrence of these two reflections. However, the associated lattice parameter does not match the *c*-axis for the CuAu-type ordering and for the chalcopyrite ordering the $(002)_{ch}$ and $(006)_{ch}$ reflections are forbidden. So, the explanation of the reflections being due to *a*-axis oriented grains has to be ruled out. More likely is the occurrence of these otherwise forbidden reflections due to deviations from the ideal crystal structure for one of the present phases. The assignment of the (010)- and (030)-reflections to one of the two orderings contemplable follows from a deconvolution of the (020) and (040)-reflections. These reflections with even *k* are allowed for the CuAu-type as well as the chalcopyrite structure. Accordingly, two different net planes contribute to the respective diffraction patterns. The smaller net plane distance, with Bragg angles of $2\theta$ = 21.47(1)° and 43.74(15)° matches perfectly with the lattice parameter derived from the forbidden reflections. From the ratio of the intensities in the diffraction patterns, the volume fraction of the ordering exhibiting the smaller net plane distance is calculated to be 35(5)%. This finding points directly towards the chalcopyrite ordering, when the results on the (00*l*)-diffraction series are considered. Hence, the larger net plane distance, solely showing up at Bragg angles of $2\theta$ = 21.37(3)° and 43.54(8)°, is due to the CuAu-type ordering. Thus, we conclude, that the *a*-axis of the chalcopyrite structure amounts to $a_{ch}$ = 0.5541(5)nm, while the CuAu-type ordering has a lattice parameter of $a_{ca}$ = 0.5565(5) nm. As a consequence, the CuAu-type structure of CIS turns out to be tetragonal with a distinct positive tetragonal distortion of $\delta_{ca} = 1 - (c_{ca} / a_{ca})$ = 0.02228(3). Contrary to this result, the tetragonal distortion practically vanishes for the chalcopyrite inclusions within the epitaxial layer investigated ($\delta_{CH} = 2 - (c_{ch} / a_{ch})$ = 0.0006(7)).

It must be noted here, that the lattice values obtained for the chalcopyrite structure deviate considerably from the values given by Abrahams and Bernstein for CIS [14]. They report a much smaller value for the a-axis ($a_{CIS}$ = 0.552279nm), a much larger *c*-axis ($c_{CIS}$ = 1.113295 nm), and a significant negative tetragonal distortion $\delta_{CIS} = 2 - (c_{CIS} / a_{CIS})$ = -0.01582. However, if we calculate the volume of a chalcopyrite unit cell from our data, the obtained value ($V_{ch}$ = 0.3401(1) $nm^3$) matches the value derived from Abrahams and Bernstein's results ($V_{CIS}$ = 0.3396 $nm^3$). So, it seems that the chalcopyrite inclusions in the epitaxial layers are highly distorted in order to adjust their lattice constants to the tetragonal CuAu-type majority of the sample. Hence, the observed behavior, where otherwise forbidden diffraction peaks appear for the chalcopyrite structure, while the CuAu-type fraction of the film obeys the selection rules for kinematic scattering. The lattice mismatch as well as the difference in thermal expansion coefficients between film and substrate are less likely to be responsible for the observed deformation of the chalcopyrite phase. From the lattice mismatch between CIS and Si, one would expect a compressive stress state for the epitaxial layer instead of the found tensile one. Furthermore, epitaxial CIS on Si(001) is found to form misfit dislocations at the substrate-film interface and an essentially relaxed growth of the CIS layer is reported in literature instead of pseudomorphic growth [6]. The differences in the thermal expansion coefficients between CIS and Si would introduce a tensile stress in the film upon cooling down from the deposition temperature. However, the resulting strains are too small by a factor of 5 to account for the observed distortion of the chalcopyrite phase [15]. Therefore it seems that external stresses are less likely to be responsible for the deformation of the chalcopyrite phase. More likely is the presence of internal stresses introduced into the chalcopyrite phase during growth. A major source for these stresses may be the recrystallization of the chalcopyrite phase from the CuAu-type phase. Here, the incongruent lattices could lead to a significant distortion of the chalcopyrite phase, thus hindering the recrystallization process and stabilizing the otherwise metastable CuAu-type structure.

### *Conclusions*

Epitaxial CIS thin films on Si(001) substrates were grown by MBE and investigated by means of XRD. A coexistence of the ground state chalcopyrite phase and the metastable CuAu-type phase was ascertained. The lattice parameters of the CuAu-type phase were determined and a significant positive tetragonal distortion is deduced. Since in the ground-state chalcopyrite structure the tetragonal distortion is found to be negative, the transformation of the CuAu-type into the chalcopyrite phase apparently is accompanied by deformations of the latter. The observed coexistence of a relaxed metastable and an highly distorted ground-state structure might hold the key for understanding the poor performance of CIS-based solar cells, if a significant amount of CuAu-type ordering is still present.

### *Acknowledgements*

Ms. Valentina Cantelli (Institute of Ion Beam Physics and Materials Research, Forschungszentrum Dresden-Rossendorf, Dresden, Germany and ROBL-CRG, Grenoble, France) is thanked for her support of the XRD measurements. The Deutsche Forschungsgemeinschaft and the European Synchrotron Radiation Facility are thanked for financial support.

The presented results have been recently published as T. Hahn *et al.*; Appl. Phys. Lett. **88**, 171915 (2006).

### *References*

[1] A. Goetzberger, C. Hebling, and H.-W. Schock, Materials Science and Engineering R: Reports **40**, 1 (2003).

[2] Su-Huai Wei, L.G. Ferreira, and A. Zunger, Phys. Rev. B **45**, 2533 (1992).

[3] Su-Huai Wei, S.B. Zhang, and A. Zunger, Phys. Rev. B **59**, R2478 (1999).

[4] D.S. Su and Su-Huai Wei, Appl. Phys. Lett. **74**, 2483 (1999).

[5] D.S. Su, W. Neumann, R. Hunger, P. Schubert-Bischoff, M. Giersig, H.J. Lewerenz, R. Scheer, and E. Zeitler, Appl. Phys. Lett. **73**, 785 (1998).

[6] T. Hahn, H. Metzner, B. Plikat, and M. Seibt, Appl. Phys. Lett **72**, 2733 (1998).

[7] J. Alvarez-Garcia, E. Rudigier, N. Rega, B. Barcones, R. Scheer, A. Pérez-Rodríguez, A. Romano-Rodríguez, and J.R. Morante, Thin Solid Films **431-432**, 122 (2003).

[8] E. Rudigier, B. Barcones, I. Luck, T. Jawhari-Colin, A. Pérez-Rodríguez, and R. Scheer, J. Appl. Phys. **95**, 5153 (2004).

[9] J. Alvarez-García, A. Pérez-Rodríguez, B. Barcones, A. Romano-Rodríguez, J.R. Morante, A. Janotti, Su-Huai Wei, and R. Scheer, Appl. Phys. Lett. **80**, 562 (2002).

[10] J. Eberhardt, H. Metzner, R. Goldhahn, F. Hudert, U. Reislöhner, C. Hülsen, J. Cieslak, Th. Hahn, M. Gossla, A. Dietz, G. Gobsch, and W. Witthuhn, Thin Solid Films **480-481**, 415 (2005).

[11] T. Hahn, H. Metzner, B. Plikat, and M. Seibt, Thin Solid Films **387**, 83 (2001).

[12] W. Matz, N. Schell, G. Bernhard, F. Prokert, T. Reich, J. Claußner, W. Oehme, R. Schlenk, S. Dienel, H. Funke, F. Eichhorn, M. Betzl, D. Pröhl, U. Strauch, G. Hüttig, H. Krug, W. Neumann, V. Brendler, P. Reichel, M.A. Denecke, and H. Nitsche, J. Synchrotron Rad. **6**, 1076 (1999).

[13] H. Metzner, J. Cieslak, J. Eberhardt, Th. Hahn, M. Müller, U. Kaiser, A. Chuvilin, U. Reislöhner, F. Hudert, and J. Kräußlich, Appl. Phys. Lett. **83**, 1563 (2003)..

[14] S.C. Abrahams and J.L. Bernstein, J. Chem. Phys. **59**, 5415 (1973).

[15] G.C. Bahr and L.K. Samanta, Phys. Rev. B **26**, 2275 (1982).

[16] B.J. Stanbery, S. Kincal, S.Kim, C.H. Chang, S.P. Ahrenkiel, G. Lippold, H. Neumann, T.J. Anderson, and O.D. Crisalle, J. Appl. Phys. **91**, 3598 (2002).

# Two-dimensional x-ray waveguides and waveguide gratings

C. Ollinger[1], C. Fuhse[1], T. Salditt[1], and N. Schell[2,3]

[1] Institute of X-ray Physics, University of Göttingen, Friedrich-Hund-Platz 1, D-37077 Göttingen, Germany

[2] Institute of Ion Beam Physics and Materials Research, Forschungszentrum Dresden-Rossendorf, 01314 Dresden, Germany

[3] now at GKSS Research Center Geesthacht, Max-Planck-Str. 1, 22502 Geesthacht, Germany

### *Introduction*

Making use of third generation synchrotron radiation, channel waveguide structures produce highly coherent and slightly divergent x-rays with a size on the order of a few 10 nm - 100 nm [1]. These waveguide structures are made of a low electron density guiding layer (e.g. a polymer) embedded in a high electron density cladding (e.g. silicon). Coupling an x-ray beam into these waveguide structures leads to the propagation of only a discrete number of modes, resulting in a coherent and slightly divergent beam in the waveguide far-field. Using these optical elements, objects can be illuminated, magnified and imaged in holographic geometry [2]. In order to characterize these waveguide structures, several experiments were carried out at the Rossendorf Beamline (ROBL) at ESRF, Grenoble.

### *Experimental*

The waveguide structures were prepared by spin-coating an e-beam resist (e.g. polymethylmathacrylate (PMMA, a positive resist) or calixaren (a negative resist)) onto a cleaned silicon wafer [4]. The resist material was subsequently structured using a 5 keV LION LV I (Leica, Germany) electron beam system. After developing the resist, the cladding material (here silicon) of about 200 nm was evaporated on top (see Fig. 1A). The resulting two-dimensionally (2*D*) confined waveguide structures had lateral dimensions of approx. $90 \times 90$ nm$^2$ (see electron micrograph of comparable structure in Fig. 1B).

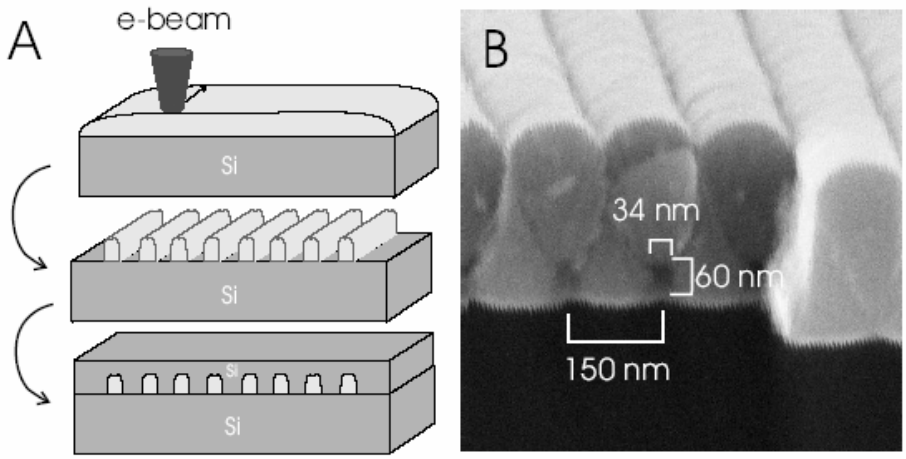


**Fig. 1.**
(A) sketch of the fabrication process for single channel waveguides. (B) Scanning electron micrograph of a calixarene grating after evaporation of silicon.

Finally, samples were cut to a length of approx. 4 mm which suppresses the transmission of x-rays outside the waveguides ($T \cong 10^{-8}$ at 12 keV). Onto the top cladding layer an additional stripe of lead was glued with conductive silver to block the primary beam passing above the wafer.

The experiments were carried out with an x-ray beam of 12 keV at ROBL (BM-20, ESRF), yielding a flux of about $10^{10}$ photons / s mm$^2$ (for 200 mA ring current) at the sample position. The waveguides were carefully positioned and aligned to the beam. The incident x-ray beam was coupled into the waveguide grating from the front side, as described in detail elsewhere [1].

### *Results*

Since the 90 × 90 nm$^2$ waveguide channels work with a transmission efficiency of approx. 5 - 10 %, the detection of single channel waveguide far-fields becomes time-consuming. In Fig. 2 the integrated intensity in the waveguide far-field is plotted while scanning the wafer along the different waveguides. Each peak can be clearly attributed to a single channel waveguide structure on the wafer. It is obvious from this graph that a detailed analysis of a single channel waveguide far-field would be very time-consuming.

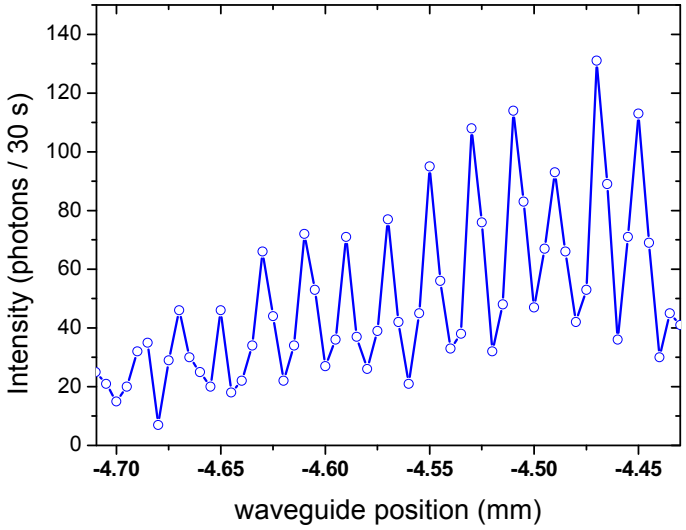


**Fig. 2.**
Translational x-ray scan along a *2D* waveguide structure. Each peak corresponds to the transmission through a single waveguide.

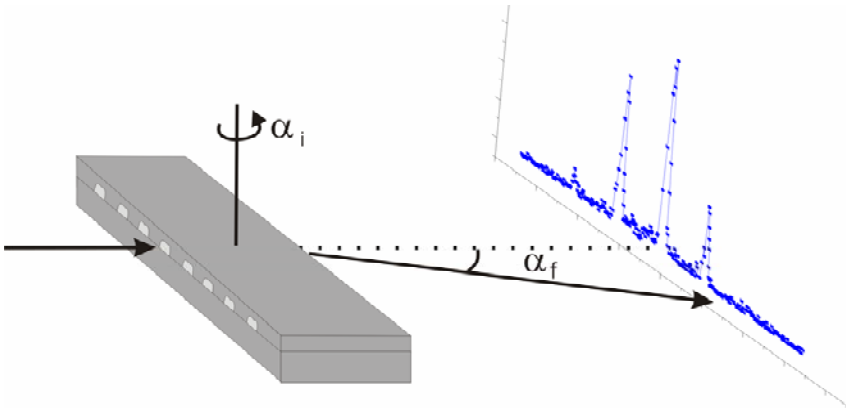


**Fig. 3.**
Sketch of the setup used for analysing the waveguide grating structures.
Depending on the incidence angle $\alpha_i$ several peaks are detected at discrete $\alpha_f$ positions. The envelope of this far-field repre-sents the averaged single channel far-field.

In order to facilitate a detailed analysis of an (averaged) single channel waveguide, the channel guides can be structured on a lateral lattice to enhance the flux in the far-field (see Fig. 3). These grating-structures were fabricated with a lateral periodicity of $d$ = 150 nm.As described in [3] the far-field for such structures can be

analysed by modeling the field distributions at the waveguide exit as follows: The field consists of a Gaussian beam emitter with a width $w$, representing the individual waveguide, convolved with a sum of Dirac δ-functions at positions $m \times d$, representing the one-dimensional lattice. We further assume that a change in the incident angle $\alpha_i$ leads to a phase shift between the single channels corresponding to their respective lateral position. An additional factor is implemented to model the lateral coherence length $N \times d$ of the incoming beam. (Note that $2\theta = \alpha_i + \alpha_f$.)

$$I(\alpha_f, \alpha_i) = \left| \int E(x, \alpha_i)\, e^{\frac{ix 2\pi \sin \alpha_i}{\lambda}}\, dx \right|^2$$

$$= A^2(\alpha_i) \left| \frac{w}{2} e^{-\frac{1}{8} w^2 (\frac{2\pi}{\lambda} \sin(2\theta - \alpha_i))^2} \right|^2 \left| \sum_m e^{idm(\frac{2\pi}{\lambda} \sin(2\theta))} e^{-\frac{2m^2}{N^2}} \right|^2$$

The averaged single channel waveguide far-field is thus the envelope function of the detected intensity peaked at discrete angular positions $2\theta = 2 \cdot \arcsin(n \cdot \lambda / d_L)$ (see Fig. 4). By changing the incidence angle $\Delta\alpha_i$ the center of the envelope of the far field pattern is shifted correspondingly $\Delta\alpha_i = -\Delta\alpha_f$. A series of two dimensional CCD images of these waveguide lattice far-fields were recorded. A typical pattern is shown in Fig. 4 (right). From these far-field patterns it is possible to reconstruct the *E*-field distribution at the exit of a single *2D* waveguide and thus obtain information about efficiency of the optics. This work is currently in progress.

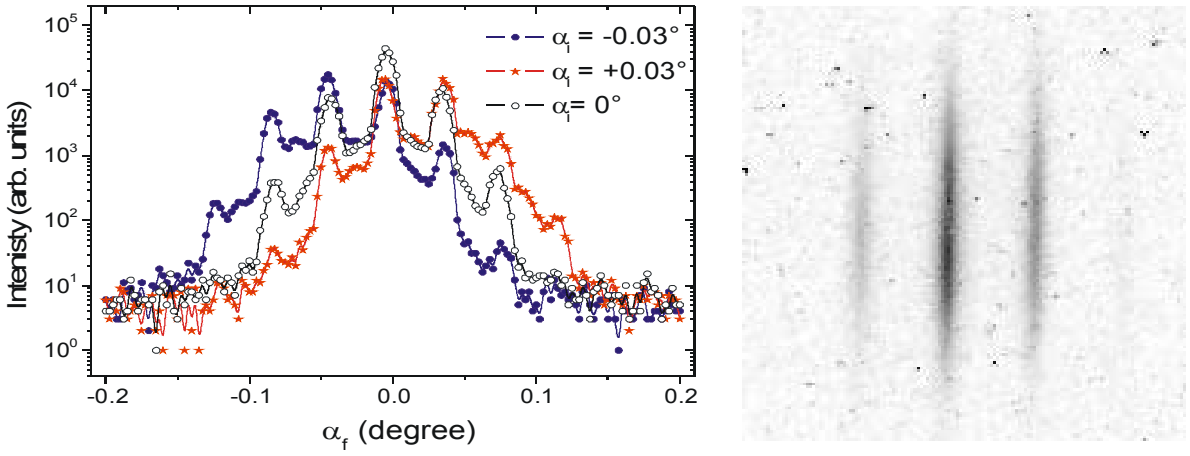


**Fig. 4.**
Changing the incidence angle $\alpha_i$ leads to a change in the center of the envelope of the far field pattern (left). Far-field of a two 2D waveguide lattice as recorded with the CCD (right).

### *Summary*

We have shown that *2D* x-ray waveguides can be characterized without the need of pre-focusing optics and/or undulator beams. A sufficient flux behind the waveguide for device characterization is obtained. The experimental proof that the observed interference pattern indeed stems from the superposition of several waveguide beams (rather than the conventional grating interference) is given by the particular angular ($\alpha_i$) dependence of the pattern, as is shown in Fig. 4. In the future, we hope to use this scheme of fabrication and characterization in order to scale down the geometric parameters to values below 30 nm which is the critical value for the present system to obtain a monomode waveguide in both dimensions.

### *References*


[1] A. Jarre, C. Fuhse, C. Ollinger, J. Seeger, R. Tucoulou, and T. Salditt
Two dimensional hard x-ray beam compression by combined focusing and waveguide optics;
Physical Review Letters **94** (2005) 074801.

[2] C. Fuhse, C. Ollinger and T. Salditt;
Waveguide based off-axis holography with hard x-rays
Physical Review Letters **97** (2006) 254801.

[3] C. Ollinger, C. Fuhse, A. Jarre, and T. Salditt
Two-dimensional X-ray waveguides on a grating
Physica B **357** (2005) 53.

[4] A. Jarre, J. Seeger, C. Ollinger, C. Fuhse, C. David, and T. Salditt
X-ray waveguide nanostructures - design, fabrication and characterization
Journal of Applied Physics (2007, in print)

# 2. Technical Documentation and Statistics

## 2.1. Technical status and developments

### *Overview and optical characteristics*

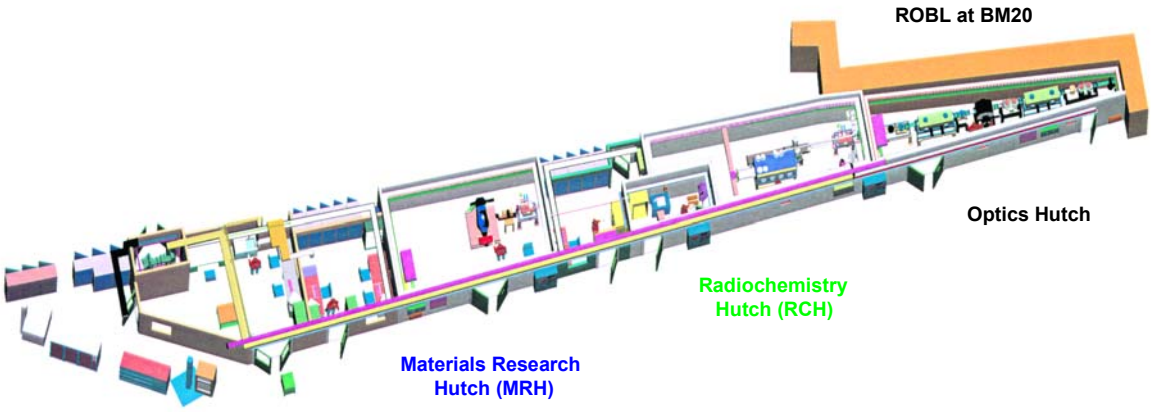


The optics with two mirrors and a double-crystal monochromator in fixed-exit mode provide both a high flux at high angular resolution (for diffraction) and a high flux over a wide energy range with high energy resolution (for EXAFS spectroscopy).

| | |
|---|---|
| **energy range** | **5 – 35 keV** |
| with Si-mirrors | 5 – 12 keV |
| energy resolution Si(111) | 1.5 – 2.5x10$^{-4}$ |
| energy resolution Si(311) | 0.5 – 1.0x10$^{-4}$ |
| **integrated flux** (calc.) | **6·10$^{11}$ phot. / s** @ 20 keV/200 mA |
| standard beam size | 20 × 3 mm$^2$ (w×h) |
| focussed beam size | ≤ 0.5 x 0.5 mm$^2$ |

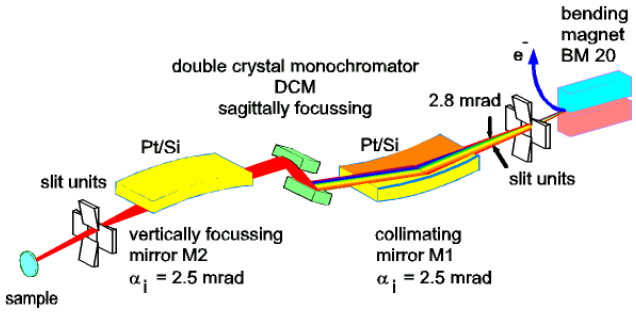


| 1a | 2a | 3b | 4b | 5b | 6b | 7b | 8 | | | 1b | 2b | 3a | 4a | 5a | 6a | 7a | 0 |
|---|---|---|---|---|---|---|---|---|---|---|---|---|---|---|---|---|---|
| H | | | | | | | | | | | | | | | | | He |
| Li | Be | | | | | | | | | | | B | C | N | O | F | Ne |
| Na | Mg | | | | | | | | | | | Al | Si | P | S | Cl | Ar |
| K | Ca | Sc | Ti | V | Cr | Mn | Fe | Co | Ni | Cu | Zn | Ga | Ge | As | Se | Br | Kr |
| Rb | Sr | Y | Zr | Nb | Mo | Tc | Ru | Rh | Pd | Ag | Cd | In | Sn | Sb | Te | I | Xe |
| Cs | Ba | La | Hf | Ta | W | Re | Os | Ir | Pt | Au | Hg | Tl | Pb | Bi | Po | At | Rn |
| Fr | Ra | Ac | Rf | Ha | | | | | | | | | | | | | |

| | | | | | | | | | | | | | | |
|---|---|---|---|---|---|---|---|---|---|---|---|---|---|---|
| Lan | Ce | Pr | Nd | Pm | Sm | Eu | Gd | Tb | Dy | Ho | Er | Tm | Yb | Lu |
| Act | Th | Pa | U | Np | Pu | Am | Cm | Bk | Cf | Es | Fm | Md | No | Lr |

The energy range allows to investigate the elements in yellow by K-edge EXAFS, and those in blue by L-edge EXAFS. Radionuclides presently permitted at the beamline are shown in red.

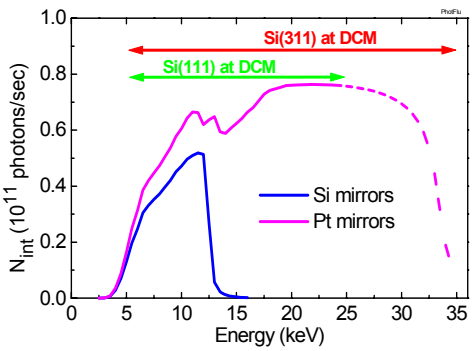


Energy range with different crystals and mirror materials

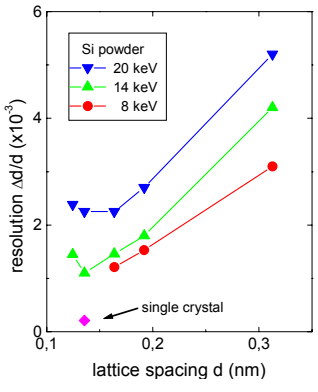


Experimental resolution determined with Si(111) and Si powder

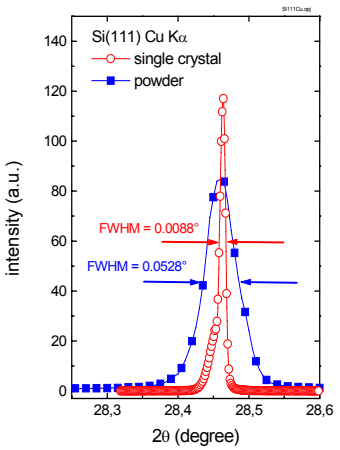


FWHM comparison

### *Technical characteristics of the Radiochemistry station*

The Radiochemistry experimental station is a highly specialized *unique* **radiochemical laboratory** designed for **radioecological research** using x-ray absorption spectroscopy (XAS) in transmission and fluorescence mode. Solid and liquid samples with a total activity of **185 MBq** (5 mCi) and a surface dose rate of **15 μSv/h** can be investigated. A **multi-barrier safety concept** with separate ventilation, constant radiation monitoring and redundancy of all essential components was developed to satisfy legal requirements.

| | | | | | |
|---|---|---|---|---|---|
| **Tc-99** | **Po-208** | **Po-209** | **Ra-226** | **Th-nat** | **Pa-231** |
| 30,000 | 0.008 | 0.3 | 5 | $10^6$ | 106 |
| **U-nat** | **Np-237** | **Pu-238** | **Pu-239** | **Pu-240** | **Pu-241** |
| $10^6$ | 7000 | 0.3 | 80 | 22 | 0.049 |
| **Pu-242** | **Am-241** | **Am-243** | **Cm-244** | **Cm-246** | **Cm-248** |
| 124 | 1.4 | 25 | 0.062 | 17 | 1,156 |

List of permitted **radionuclides** and their maximum amount in mg (shown in blue). Additional radionuclides may be present if accepted by the ESRF safety group.

During the measurement, the **spectroscopic glove box** envelops the samples, which are mounted either on a remote-control 8-fold multistage holder or in a cryostat. The fluorescence and transmission detectors remain outside of the glove box.

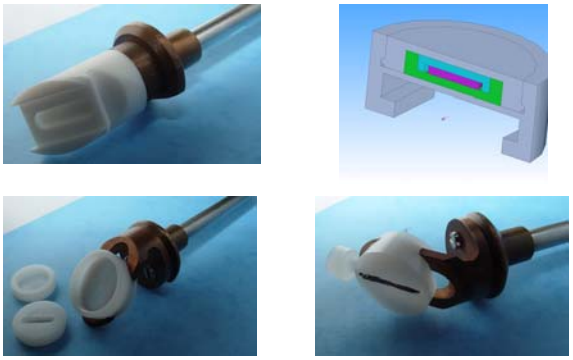

**Sample holders** fulfilling the necessary safety requirements exist in a wide variety to match different sample. Technical drawings and detailed information on filling procedures may be downloaded from our home page.


**13 element LEGe detector** with a high-rate digital multi-channel analysis spectrometer (XIA) and dedicated analysis program integrated into the XAS data collection software XATROS.

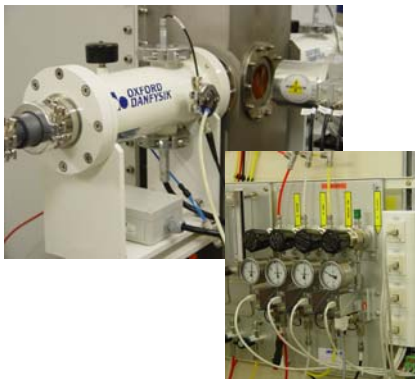


**3-kV ionization chambers** with remote-controlled gas mass-flow controllers.

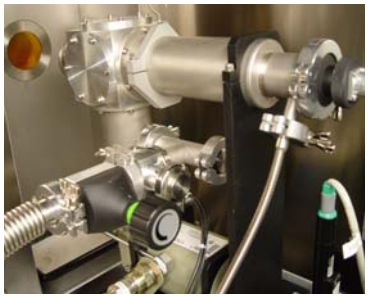

**Closed-cycle He cryostat** with large fluorescence window adapted to the 13-element detector and very low vibration levels cools samples down to 15 K.

## *Technical characteristics of the Materials Research station*

The materials research hutch MRH is designed for the **structural identification and characterisation of modifications of surfaces and interfaces produced by ion beam techniques** (e.g. hard covers, biocompatible materials, or for semiconductor technology) and the study of interfaces in thin films and nanometer multilayers using various x-ray diffraction techniques (XRD, GIXS) and reflectometry (XRR). A specific reference is given in [1] and at http://www.esrf.fr/UsersAndScience/Experiments/ CRG/BM20/.

### Detectors

- **Scintillators** Bede ERD
- **PIN-diodes** AMPTEK XRT-110T
- **2-dim. CCD** Bruker SMART
- **x-ray eye** Photonic Science
- **lin. PSD** Braun
- **analyzer** C, Ge
- **channel-cut** Ge

### Diffractometer HUBER

- **6 circles** 0.001°
- **x/y ; z table** ± 75 / 75 / 12 mm; 10 / 10 / 1 μm
- **15 kg load** at sample position
- **z height** - 200 / + 50 mm

### ML mirror / deflector

- Osmic W / $B_4C$

### Process chambers (suitable for installation into the HUBER goniometer) for

- **annealing** (in neutral / reactive gases, for metals & semiconductors)
- **magnetron sputter deposition** and **ion irradiation**

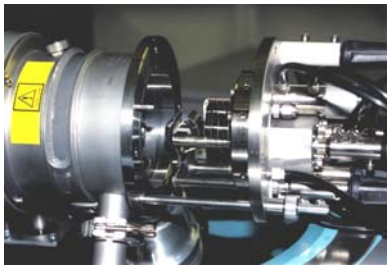

Commercial **high temperature** chamber (Otto) for annealing up to 2000°C in vertical scattering geometry.

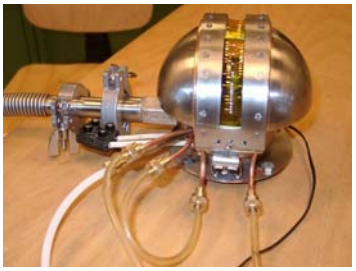

User designed annealing chamber **for reactive gases**.

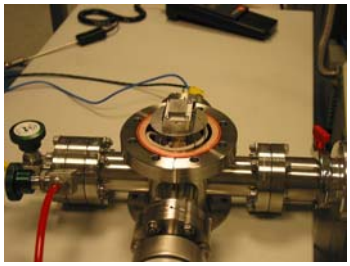

In-house designed chamber with **hemispherical Be-window** (i.e. 2π x-ray access for GIXS) for moderate annealing temperatures (< 900°C).

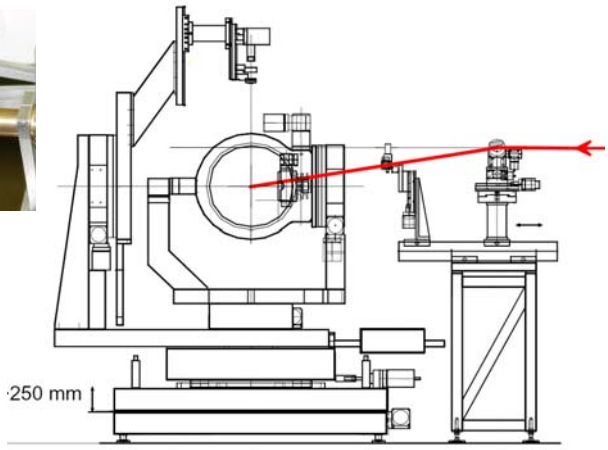


Basic instrument at MRH: **6 circles Huber goniometer**. The possibility of height variation (250 mm) enables x-ray investigations at free liquid surfaces. Upper left: ITME **Ge channel-cut**.

**Two magnetrons sputter deposition chamber** with mounted **ion irradiation gun** (top).

[1] N. Schell, W. Matz, F. Prokert, F. Eichhorn, and F. Berberich, *Synchrotron radiation studies of thin films and implanted layers with the materials research endstation of ROBL.* J. Alloys & Comp., **328** (2001) 105-111.

# Technical developments at ROBL

W. Oehme[1], D. Pröhl[1], S. Dienel[1], J. Claußner[1], U. Strauch[2] , H. Funke[2,3], A.C. Scheinost[2,3]

[1] Department of Research Technology,
[2] The Rossendorf Beamline at ESRF,
[3] Institute of Radiochemistry,
Forschungszentrum Dresden-Rossendorf, P.O.Box 510119, 01314 Dresden, Germany

In the field of technical developments there were the following main directions:

1. Development and/or integration of new technical systems to improve the measurement facilities and the stability of the beam
2. Improving the measurement program XATROS of the Radiochemistry end-station
3. Update of electronics and basic software to enhance the compatibility with the standard equipment used at ESRF beamlines
4. Development of an automated warning system based on SMS to inform the responsible beamline scientist in case of problems during unattended experiments

## New technical systems

### *A new DPT controller and device server*

Due to ongoing problems with the Queensgate DPT-controller (controller-induced beam oscillations), this controller was replaced by a new device from Physik Instrumente (PI) [1]. Integration into the software system was done a newly developed Device Server (PI) [2]. The new controller works now as expected. The controller could also be connected successfully with the digital monochromator stabilizer system (D-Mostab), which operates one of the digital piezo-electric translators using feedback from the first ionization chamber ($I_0$).

### *A new cryostat*

Cooling samples to cryogenic temperatures improves the EXAFS signal because of omitting thermal contributions to the Debye-Waller term. Furthermore, the cooling prevents beam damage of sensitive samples (thermal damage, oxygen radicals), and reduces photo-reduction or photo-oxidation phenomena of redox-sensitive samples. Finally, the use of a He cryostat provides an inert-gas atmosphere excluding $O_2$ and $CO_2$. While these beneficial features were already provided by an Oxford He-closed-cycle cryostat, this piece of equipment had substantial disadvantages. First, the fluorescence exit window was very small, thereby illuminating only the innermost pixels of the 13-element Ge detector, and leaving the outer pixels unused. Second, the coldhead of the cryostat induced large vibrations to the sample, thereby inducing large noise to the EXAFS spectra of samples with significant heterogeneities. Third, the small transmission windows allow the alignment of only one sample at a time, increasing the handling time of radioactive samples, which should always be kept at a minimum. Therefore, a new cryostat had to be designed, which improved these previous restrictions, while maintaining the geometric constraints imposed by the glove box, and providing a similar cooling power (sample temperature of $\geq$ 20 K).

Such a cryostat was custom-made by CryoVac [3] (figure 1). The arrangement of the sample and the size of the fluorescence window (diameter 28 mm) are adjusted to the new 13-element germanium detector. The diameter of the transmission windows was also increased to 15 mm. This makes it possible to cool two samples at the same time and to measure them automatically one after the other. The vibrations of this cryostat are now negligible in relation to the beam size, thereby improving the quality of EXAFS spectra of natural and inhomogeneous samples. The temperature is now measured not only at the cold head, but also directly at the sample. A new control device with an integrated pressure reading is used for purging the sample chamber with helium, providing a reliable operation and a more precise adjustment of the helium pressure during measurements. The cryostat is equipped with the control unit TIC304-MA, offering a computer interface based on the GPIB standard. A GPIB-ENET/100 network controller from National Instruments [4] is used and a dedicated software to integrate the cryostat into the beamline's measurement system. This control unit is less versatile than the previous by Oxford, and for automated temperature scans, an imorved solution has to be found in the future.

### *An universal sample positioning system*

A new universal sample positioning system [5] was developed for improving the measurements performed in the glove box of the radiochemistry end-station and to simplify the handling with different equipments. The scheme of this system is shown in figure 2.

**Fig. 1.**

The new cryostat mounted inside the glove box.

Alternatively the cryostats, the eightfold sample holder, and the electro-chemical cell can be mounted and moved in X- and Y-direction within a range of 50 mm. There are two stepper motors connected to the Pegasus controllers [6]. Further mounting points permit extensions of the positioning system for additional applications. A very important task was the decoupling of vibrations produced by the cryostat from the glove box, which was perfectly achieved. Figure 3 shows the positioning system with a mounted cryostat while figure 4 presents it with the eightfold sample holder.

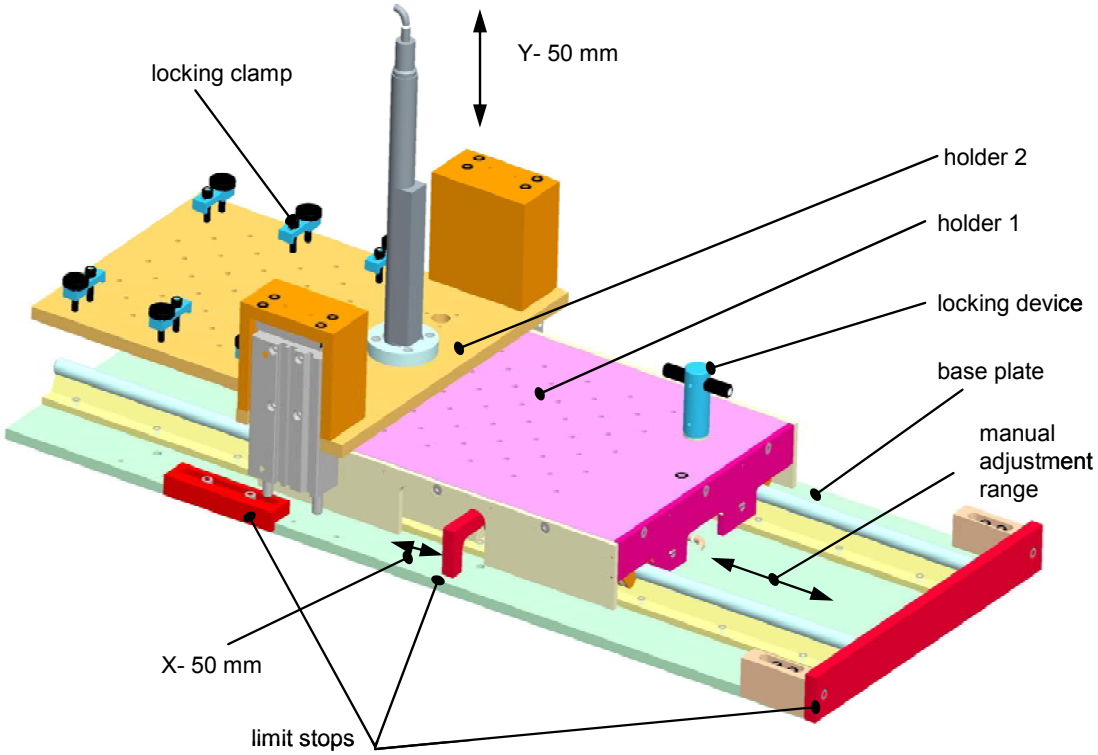


**Fig. 2.**
Universal positioning system

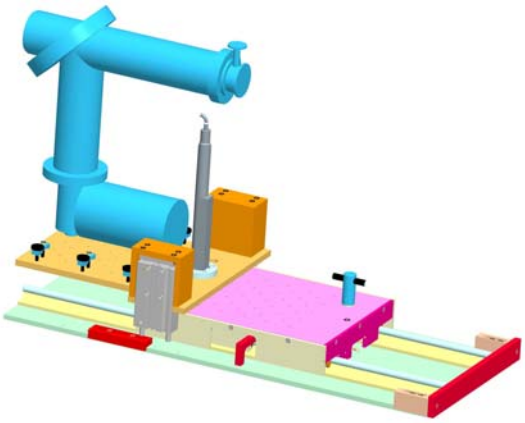

**Fig. 3.**
Positioning system with mounted cryostat

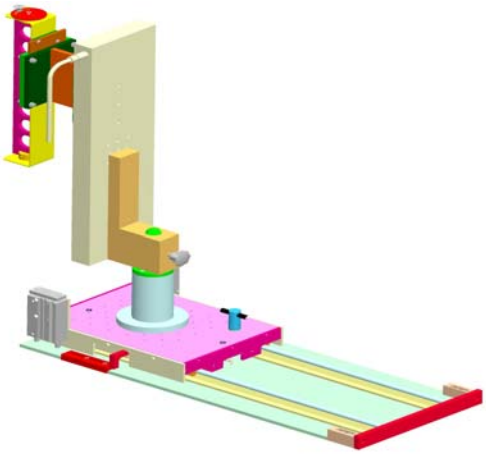

**Fig. 4.**
Positioning system with mounted eightfold sample holder

## Improving the measurement program XATROS

There is a dedicated measurement program XATROS [7] used at ROBL's radiochemistry end-station. The program had been improved in several steps. First, the new devices had to be integrated in the measurement program. A new "count-based" measurement mode is added to the already existing "time-based" measurement mode. This new method can improve the measured spectra under certain conditions, e.g. in the presence of glitches caused by umweganregung in the Si(111) monochromator crystal. Additionally, a reduction of about 20 percent of the time required for EXAFS scans was

achieved. In comparison to the old four element germanium detector and its analogue electronics. the new 13 element germanium detector with its digital electronics considerably increased data collection time. This was mostly due to the greatly increased amount of data (full XRF spectra for each element and each energy step, instead of one integrated value of the ROI) to be transferred between digital electronics and the data collection software XATROS. Data transfer steps and optics adjustment steps are now arranged in a more parallel fashion, e.g. during the time required by the monochromator to adjust the next energy, the thirteen 8K spectra are read out of the electronics. A second measure to improve speed is the so called “difference mode”. In this mode we do not stop and start the digital electronics by software but build the difference between two not cleared measurements. The gate mode ensures that the digital electronics does not count before the next gate is set. The time required for a typical EXAFS scan is now again similar to the old 4-element detector, hence combining the much higher count rate and improved energy resolution of the new 13-element detector with the higher data collection speed of the old system.

## Steps towards the ESRF standard

### *Linux front-end systems*

Up to now three stand-alone VME systems with their own processors were used. Each of the systems was responsible for controlling the optical devices (optics hutch) or one of the two experimental end-stations. The VME system controlling the optical devices was additionally equipped with two auxiliary CPUs dedicated to the support of the four wired X-ray beam position monitors (wxbpms) used at ROBL. All the systems had been controlled by the OS-9 real time operating system and software mainly written by programmers of the ESRF. Some years ago the ESRF started to change the systems to the Linux operating system. Additionally, there was the need to benefit from new hardware developments which in many cases require the PCI bus. For this reason a migration from the old hardware and software to a new basis took place. On the other hand the old investments in hardware (VME modules) should work as long as possible. To be compatible to the new ESRF standards and to benefit from new developments at the ERSF, the electronics and software was changed in the same way. Now, we use two standard industrial PCs running a Linux operating system (SUSE distribution 7.2) and a bus coupler which connects the PCI and the VME bus. With few exceptions all of the drivers and servers are used from the ESRF and adopted to ROBL’s requirements by database configurations. Compared to the past we have replaced three VME systems by two VME systems controlled via Linux and two industrial PCs. One of the reasons is that the radiochemistry end-station has changed a lot of its electronic components and now there is still only one VME module used.

### *Modifications of the wxbpms*

With the new Linux front-end systems there was no support of the old wired X-ray beam position monitors anymore. For this reason the complex electronics and motors were replaced corresponding to one of the ESRF standards. Three of the four wxbpms used at ROBL had been reconstructed with a new gear mechanism, new stepper motors and the amplifiers had been changed from the previously used current mode to count mode. As timer and counter we use the module P201 also developed at the ESRF. The software is based on “spec” [8] and the standard device servers of the ESRF. The fourth wxbpm will be reconstructed in the same way at the beginning of 2007.

***A new double crystal monochromator device server***

In the past we used a DCM device server which wrapped the intelligent motor controllers by a subset of a logical VPAP device server interface. To keep as much as possible of the software unchanged, there was the need to port this DCM device server to the Linux operating system.

***MCA ORTEC926 – a new driver and device server***

This multi channel analyzer is occasionally used in the materials research end-station. Changing from OS-9 to Linux required the development of a driver and a new device server to maintain the experimental possibilities.

## A simple SMS based alarm system - gsmPro

At the radiochemistry end-station there are often experiments which run for a long time and can be left in unattended mode. To avoid the loss of measurement time in case of unexpected events, a SMS based alarm system was developed. The system sends a SMS to a list of pre-defined phone-numbers and informs the scientist in charge about the loss of beam. This way the scientist can react even if not present at the beamline (nights, weekends). It is also possible to interrogate the state of the experiment at any time by sending a SMS from the operator's cellular phone and to receive an answer concerning the state or the remaining measurement time usually within one minute. There is a separate program gsmPro which has been designed to perform the communication part via the GSM terminal and which is able to deal with status information produced by the program XATROS.

The principle of this solution is shown in figure 4.

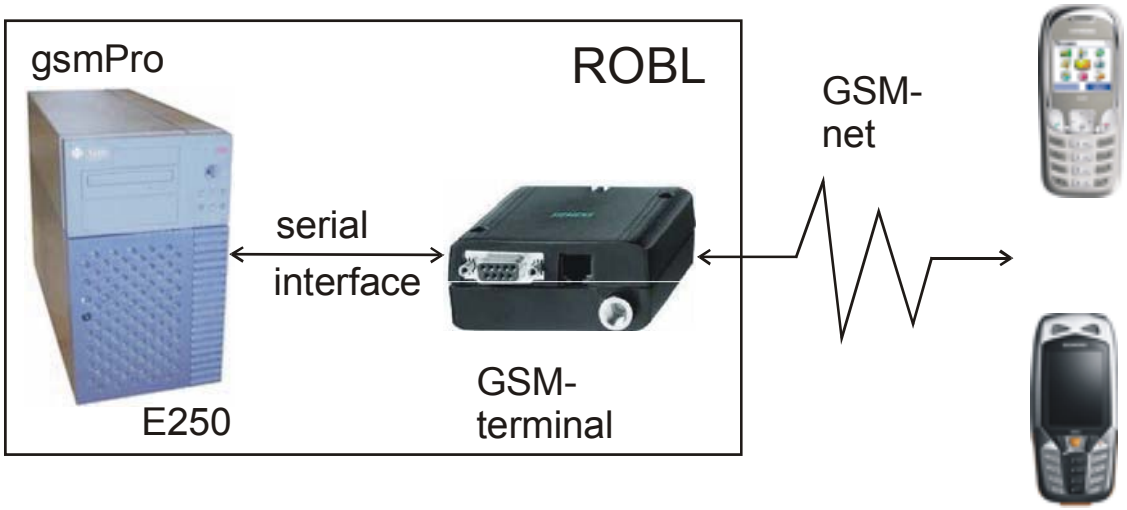


**Fig. 4.**
gsmPro – principle scheme SMS alarm system

## *References*


[1] Technical Documentation: „PZ102E – User Manual“, Product description and operating notes, Physik Instrumente (PI) GmbH & Co.KG, D-76338 Karlsruhe, Germany

[2] W. Oehme: „Description of the PI Device Server“, Internal ROBL documentation, 17.3.2005

[3] CryoVac Gesellschaft für Tieftemperaturphysik mbH & Co KG, Heuserweg 14, 53842 Troisdorf

[4] National Instruments Germany GmbH, Konrad-Celtis-Str. 79, D-81369 München

[5] J. Claußner: Interne Dokumentation, Forschungszentrum Dresden-Rossendorf e.V., PF 51 01 19, 01314 Dresden

[6] Technical Documentation: „SMC pegasus”, Micos GmbH, Freiburger Straße 30, 79427 Eschbach

[7] W. Oehme, T. Reich, Ch. Hennig, A. Scheinost: “Program XATROS – User’s Guide”, Internal ROBL documentation, 24.2.2005

[8] Certified Scientific Software, spec™ X-Ray Diffraction Software, User’s Manual (2001)

# Parabolic capillary optics with less than 50 µm focus and large focal distance for synchrotron radiation scattering

N. Schell[1,2*], F. Eichhorn[1], U. Strauch[2], A. Bjeoumikhov[3]

[1] Institute of Ion Beam Physics and Materials Research, Forschungszentrum Dresden-Rossendorf, P.O. Box 51 01 19, 01314 Dresden, Germany

[2] The Rossendorf Beamline at ESRF, Grenoble, France

[3] Institute for Scientific Instruments, Rudower Chaussee 29/31, 12489 Berlin, Germany

[*] now at GKSS Research Center Geesthacht, Max-Planck-Str. 1, 22502 Geesthacht, Germany

### *Introduction*

The Rossendorf Collaborating Research Group beamline (ROBL-CRG) at bending magnet BM20 at ESRF (European Synchrotron Radiation Facility) has been designed for performing experiments on two different alternatively running experimental stations [1]. One is a radiochemistry hutch which employs x-ray absorption techniques for the chemical speciation of radionuclides, the other is a general-purpose materials research hutch using various x-ray diffraction techniques and reflectivity for the characterization of surfaces and interfaces modified by ion-beam techniques.

During the last years there had been an ever increasing general demand, especially in the synchrotron radiation community, for microbeam scattering experiments, leading to sophisticated instrumentation, dedicated beamlines and a correspondingly rich literature [2]. However, for split beamlines with a common optics, as for ROBL, it is sometimes not possible for technical or budgetary reasons to modify the general optics. In order to preserve the current optical specifications for the two independent experimental stations (flux, resolution, beam size at fixed distances) – and also in view of specific safety considerations for the radiochemical hutch), but on the other hand in order to fulfill a spot reduction <100 µm and a flux gain >100 for planned experiments in the materials research hutch (MRH), we decided to install a low-cost, versatile capillary optics in MRH. One additional requirement was a focal length >200 mm to allow the installation of various sample environments, like furnaces or sputter-deposition chambers. Thus, in co-operation with the Institute for Scientific Instruments in Berlin [3] a unique parabolic capillary optics was developed which satisfies our demands. Making use of third generation synchrotron radiation, channel waveguide structures produce highly coherent and slightly divergent x-rays with a size on the order of a few 10 nm - 100 nm. These waveguide structures are made of a low electron density guiding layer (e.g. a polymer) embedded in a high electron density (e.g. silicon) cladding. Coupling an x-ray beam into these waveguide structure leads to the propagation of only a discrete number of modes, resulting in a coherent and slightly divergent beam in the waveguide far-field. Using these optical elements, objects can be illuminated, magnified and imaged in holographic geometry [2]. In order to characterize these waveguide structures, several experiments had previously been carried out at ROBL.

### *Capillary Instrumentation*

Capillary optics is based on the principle of total external reflection at a smooth glass surface. This kind of optics has been intensively developed during the last ten years. There are two main types of capillary optical elements: poly-capillary lenses and mono-capillaries.

In a poly-capillary lens the focusing is realized by x-radiation transport through a tapered (focusing) arrangement of capillaries with multiple reflections at the capillary walls. A monolithic system consisting of a large number of capillaries which was named poly-

capillary lens has a rather large aperture and can concentrate radiation into a spot of 15 µm in size and better [4, 5]. Unlike poly-capillary lenses the focusing in mono-capillaries is realized by single reflections at the internal capillary surface. In this case the capillary has a defined shape of a paraboloid or an ellipsoid [6-9].

The well known geometrical property of a paraboloid allows focusing a parallel beam into a point or a divergent beam to transform into a parallel one. This property is very important for focusing of synchrotron radiation which is to a high degree parallel. Earlier elliptical capillaries have been used for these purposes because their manufacturing technology is easier than that for a paraboloid. But using ellipsoidal capillaries, usually a "pure" focusing cannot be realized because besides single reflections also double reflections occur which deteriorate the focal spot characteristics. Therefore, for the formation of small focal spot sizes correspondingly short focal distances of about 1 mm were required. However, many experiments need free space around the focal spot, e.g. for positioning a detector or a microscope or a device for modification of the sample environment.

Recently, a new generation of mono-capillaries with correct focusing properties due to a highly precise form of a paraboloid or an ellipsoid has been developed, but these optical elements must be adapted to the concrete geometry of the primary beam. In this case only single reflections occur and a parallel beam is focused into a small spot size which is only determined by the precision of capillary manufacturing and the degree of non-parallelism of the incoming beam. Such optical elements were called "one-bounce capillary optics" [10, 11]. Capillaries of a paraboloidal form allow enlarging the focal distances up to tens of mm.

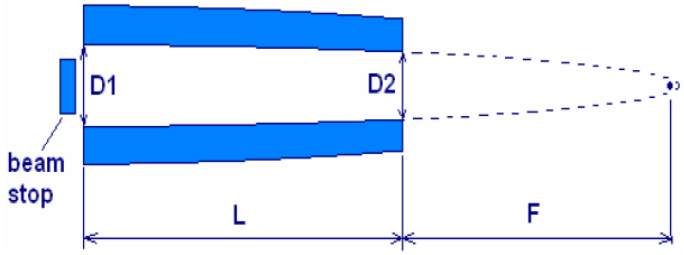


| | |
|---|---|
| P (mm) | 0.004 |
| L (mm) | 346 |
| F (mm) | 230 |
| D1 (mm) | 4.47 |
| D2 (mm) | 2.91 |
| D housing (mm) | 10 |

**Fig. 1.**
Schematic drawing and geometric parameters of the capillary.

In our investigations a capillary with an extreme long focal distance of 230 mm for crystallographic wavelengths were used. Such an optical element was required by the given experimental conditions for closed experimental chambers where the distance between window and sample is unchangeably fixed. The paraboloid has been manufactured by a highly precise re-drawing procedure of a cylindrical capillary. The manufactured capillary, schematically shown in Fig. 1, is a paraboloidal mono-capillary with internal beam-stop (avoiding the transmission of unfocused photons) and the parameter p = 0.004 mm [$r = (2px)^{1/2}$ with the coordinate x in the optical axis].

### *Laboratory Characterization*

At the manufacturing site the focal spot size was measured at a 50 µm micro-focal x-ray tube with Cu-target (MCBM 50 – 0.6 B Cu, Röntgen-Technik Dr. Warrikhoff, Germany) placed at a distance of 3100 mm from the capillary in order to simulate a parallel synchrotron radiation beam. For radiation detection a CCD-Hamamatsu C6086 [12] and an energy dispersive SDD X-Flash [13] together with a 50 µm pinhole were used. Figure 2 shows the intensity distribution in the focal plane at the focal length of 230 mm together with normalized 1-dim. cuts along two perpendicular directions for the energies

used, i.e. with the region-of-interest of the SDD detector set for CuK$_\alpha$ and the Bremsstrahlung, respectively. The quantitative results are given in Table 1. Slight differences in focal spot size, focal distance and gain in comparison to conditions with a parallel beam are expected. Taking a square-root contribution of the pinhole to the measured full width half maximum (FWHM) values of the spot as indicated in Fig. 2 and Table 1 prove a nearly symmetric focal spot of < 50 µm with gains > 1000.

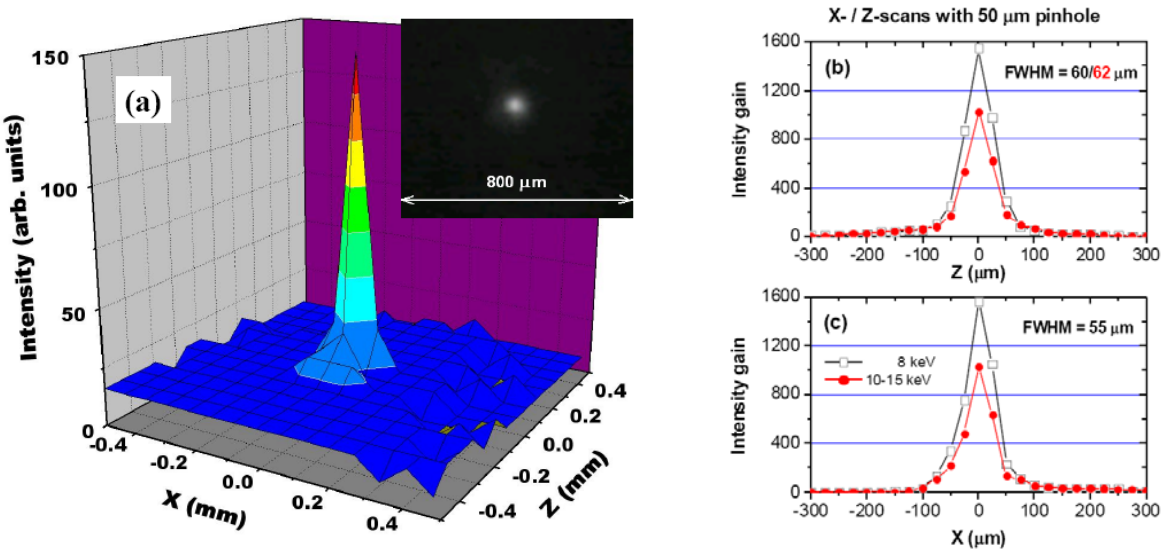


**Fig. 2.**
Intensity distribution of 8 -15 keV x-ray radiation in the focal plane of the capillary measured in the laboratory (a). The background is the noise from the CCD. The right side shows radial intensity cuts along the horizontal x-direction (a) and the vertical z-direction (b) measured with the energy dispersive SDD detector and the pinhole. Note that the measured intensity is normalized to the incoming intensity, i.e. it gives the gain.

**Tab. 1.**
Focal spot size and intensity gain at 230 mm distance of the capillary as measured with the 50 µm pinhole at the laboratory source.

| E (keV) | 8.05 | 10-15 |
|---|---|---|
| Focal spot size horizontal / vertical FWHM (µm) | 55/60 | 55/62 |
| Intensity gain | 1550 | 1027 |

### *Synchrotron Radiation Characterization at ROBL*

After pre-characterisation at the manufacturer's laboratory, the capillary optics was transferred to the later site of operation at ROBL-MRH (Fig. 3). For two energies, 8.05 keV (CuK$\alpha$) and 11.5 keV, it was aligned with a Photonics Science CCD camera (FDI2) with 10 µm pixel size [14] at the nominal focal length of 230 mm, determined at the laboratory source, by horizontal and vertical tilts and lateral glides with motors of 0.1 µm step accuracy [15]. The focus spot was then scanned with a 10 µm Pt pinhole [16] in front of an open BEDE EDRc scintillator [17] at varying distances from the capillary along the optical axis.

Figure 4 illustrates the photon distribution in the xz-plane for different distances around this focal length of 235 mm. The behaviour is similar for the higher energy of 11.5 keV. Pre-focusing with a vertically focussing mirror (M2) in the optics hutch of ROBL – with its standard design of two mirrors with Pt/Si stripes and a double-crystal Si(111)

monochromator in fixed-exit mode in between – gives slightly worse spot characteristics. Table 2 summarises the results for two evaluation procedures. The divergence of the capillary was determined to be 0.11°. It was measured as FWHM of the rocking curve in Si(400) of a single crystal wafer at 11.5 keV with unbent mirror, i.e. without pre-focusing.

**Fig. 3.**
Capillary inside the positioning system (pitch, roll, height, lateral movements) in front of the alignment setup at ROBL-MRH with CCD and calibration needle at center position of the 6-circle Huber goniometer.

Meanwhile, the capillary has been used in ROBL-MRH experiments for stress measurements in copper interconnect structures on micro-devices and the characterization of planar waveguide structures. Details and results of these investigations can be found in the experimental reports 20_02_617 / 627, respectively or corresponding papers [18, 19].

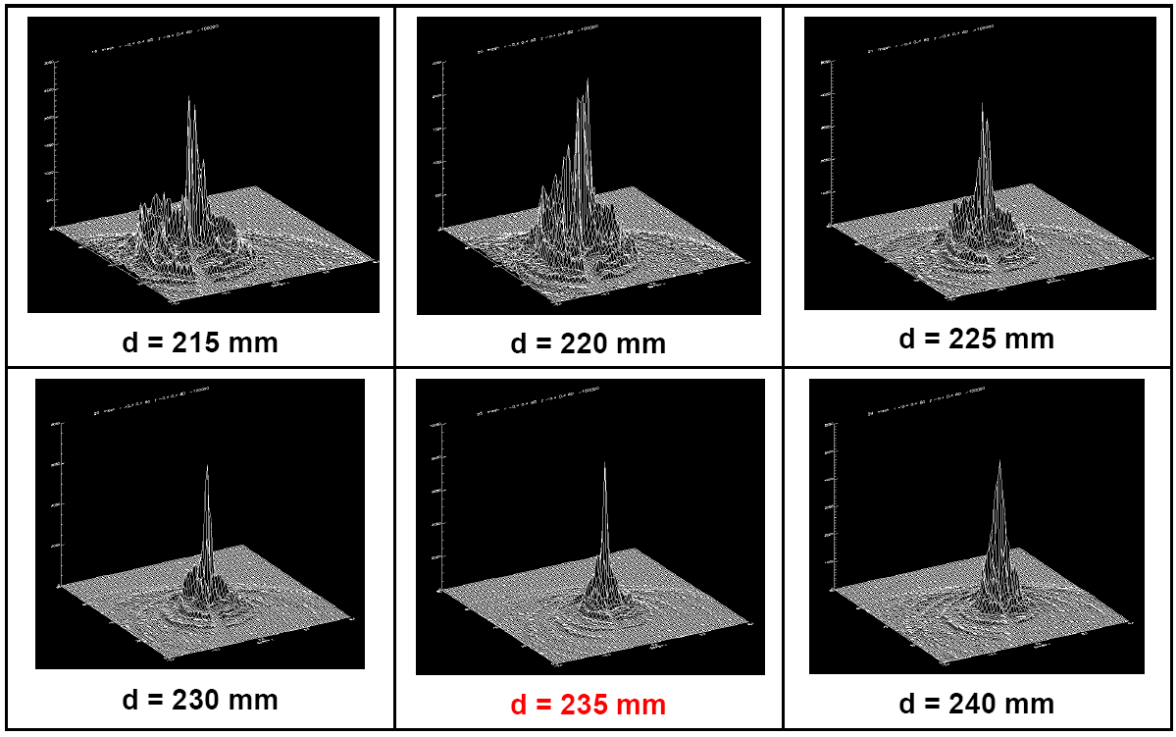


**Fig. 4.**
Series of spot intensity distributions in dependence of its distance *d* from the capillary for CuK$\alpha$ radiation as measured with a scanned 10 µm pinhole. The incoming beam was not pre-focused and limited in size by slits to 4 x 5 mm$^2$. The scintillation detector was shielded by 700 µm Al absorber foils. The peak-intensity at the focal length 235 mm, i.e. optimum intensity distribution, was ≅ 8500 cps, the FWHM of the spot ≅ 30 µm, the peak gain ≅ 1400.

## *Conclusions*

On an existing split bending magnet beamline (BM20 at ESRF) there was the need to increase the flux by a gain > 100 within a spot < 100 µm for planned future experiments without change of the overall optical specifications for the two independent experimental stations. One additional requirement was a focal length > 200 mm to allow the installation of various sample environments. A special parabolic glass capillary optics was thus developed, installed and recently tested. Comparing the averaged peak intensity without pre-focusing (mirror M2 not bent) with the "background", i.e. the intensity in a 10 µm pinhole without capillary, and pre-focusing (M2 bent) which is the reference for an effective gain in comparison to the usual operating mode for ROBL-MRH we reach a net gain of ≈ 200 within a spot of 25 x 40 µm$^2$ for CuK$\alpha$, and a net gain of ≈ 590 within a spot of 19 x 32 µm$^2$ for an x-ray energy of 11.5 keV. The original design specifications have thus been reached with this versatile and relatively low-cost optics.

**Tab. 2.**
Focal spot characteristics of the capillary as measured at ROBL. Accepted horizontal and vertical divergence of the photon beam of the bending magnet are 2.8 mrad and 49 µrad, respectively [1]. Without pre-focusing (mirror M2, at 30.8 m from the source and 20 m from the capillary, bent-off), the beam size was chosen to be 4 x 5 mm$^2$, with pre-focusing (M2 bent to 15.5 km) to be 2 x 5 mm$^2$, respectively, so that the capillary opening was maximal illuminated. With 270 x 80 µm$^2$ (horizontal x vertical) source size, focal length f = 230 mm, and source distance 50.8 m, the theoretical achievable spot size is 1.2 x 0.36 µm$^2$.

| Energy (keV) | Bending of M2 (km) | Focal distance (mm) | Focal spot *via* min/max$^{FWHM}$ (µm) | Focal spot *via* Gaussian x-/z-cuts (µm) | Gain |
|---|---|---|---|---|---|
| 8.05 | off | 235 | 25 / 40 | 28 / 17 | ≈1400 |
| 8.05 | 15.5 | 242 | 27 / 86 | 57 / 23 | ≈240 |
| 11.5 | off | 249 | 19 / 32 | 29 / 19 | ≈1600 |
| 11.5 | 15.5 | 244 | 32 / 34 | 30 / 31 | ≈220 |

## *References*


[1] W. Matz et al., J. Synchrotron Rad. **6**, 1076-1085 (1999).

[2] L. Vincze and C. Riekel, X-Ray Spectrom. **32**, 208-214 (2003).

[3] Institute for Scientific Instruments (IfG), http://www.ifg-adlershof.de

[4] N. Gao and K. Janssens, "Polycapillary x-ray optics", in X-ray spectrometry: recent technological advances, edited by K. Tsuji, J. Injuk, and R. Van Grieken, John Wiley & Sons Ltd., New York, 2004, pp.89-110.

[5] A. Bjeoumikhov et al., Rev. Sci. Instrum. **76**, 063115-1-063115-7 (2005).

[6] D.H. Bilderback, Rev. Sci. Instrum. **66**, 2059-2063 (1995).

[7] Y. Hosokawa et al., X-Ray Spectrom. **26**, 380-387 (1997).

[8] Yu.I. Dudchik et al. Tech. Phys. Lett. **24**, 954-955 (1998).

[9] S.V. Kukhlevsky et al., X-Ray Spectrom. **29**, 354-359 (2000).

[10] R. Huang and D.H. Bilderback, Nucl. Instrum. Meth. A **467**, 978-981 (2001).

[11] R. Huang and D.H. Bilderback, J. Synchrotron Rad. **13**, 74-84 (2006).

[12] Hamamatsu Photonics, http://www.hamamatsu.com

[13] Bruker AXS Microanalysis GmbH, Schwarzschildstr. 12, 12489 Berlin, Germany, http://www.bruker-axs-microanalysis.de

[14] Photonic Science, Millham, Robertsbridge, East Sussex TN32 5LA, http://www.photonic-science.co.uk

[15] CMG, Karlstr. 6, 64521 Gross-Gerau, Germany, http://www.cmg-germany.com

[16] Plano GmbH, Ernst-Befort-Str. 12, 35578 Wetzlar, Germany, http://www.plano-em.de

[17] Bede Scientific Instruments, Belmont Business Park, Durham, DH1 1TW, UK, http://www.bede.co.uk

[18] H. Prinz et al., AMC Conference Proceedings 22, Colorado Springs, 2005, in press.

[19] C. Fuhse et al., Appl. Phys. Lett. **85**, 1907-1909 (2004); A. Jarre et al., Phys. Rev. Lett. **94**, 074801 (2005).

## 2.2. Beamline personnel

| | | |
|---|---|---|
| Head of the beamline / CRG spokesperson: | Andreas Scheinost | (-2462) |
| Responsible for MRH *(until 30.09.2006)*: | Norbert Schell | (-2367) |
| *(from 01.01.2007)*: | Carsten Bähtz | (-2367) |
| Responsible for RCH: | Andreas Scheinost | (-2462) |
| Responsible for Radiochemical Safety: | Christoph Hennig | (-2005) |

| | Name (phone) | Position/Education/Research Interests |
|---|---|---|
| | Manuela Strauch (-2463) | Office administration |
| | Udo Strauch (-2372) | Beamline Technician |
| **Radiochemistry** | Harald Funke (-2339) | Beamline Scientist<br>Ph.D. in Physics (1974), University of Moscow (Russia)<br>application of wavelet analysis to EXAFS |
| | Christoph Hennig (-2005) | Beamline Scientist<br>Ph.D. in Crystallography (1995), Universität Leipzig<br>structure of uranyl complexes by XRD and EXAFS<br>aqueous chemistry and electrochemistry of actinides |
| | Andre Rossberg (-2847) | Postdoc<br>Ph.D. in Chemistry (2002), TU Dresden<br>new methods for EXAFS analysis<br>aqueous chemistry and sorption processes of actinides |
| | Andreas Scheinost (-2462) | Head of Beamline, responsible for RCH<br>Ph.D. in Agricultural Engineering (1994), TU München<br>radionuclide speciation in soils, sediments and aquifers, biogeochemistry of radionuclides focusing on redox processes |
| **Materials Research** | Carsten Baehtz (-2367) | Beamline Scientist, responsible for MRH *(from 01.01.2007)*<br>Ph.D. in Chemistry (2000), TU Darmstadt<br>structural analysis by XRD |
| | Valentina Cantelli (-2849) | Beamline Scientist (*until 01.06.2005)*<br>Masters in Physics (1995), University of Torino (Italy)<br>characterizing of *in-situ* structurally modified thin magnetic materials |
| | Rui Martins (-2872) | Ph.D. student<br>Masters in Materials Engineering (2004), New University of Lisbon (Portugal)<br>characterization of the growth process of sputter deposited thin films (TiAlN hard coatings and NiTi shape memory alloys) |
| | Norbert Schell (-2367) | Beamline Scientist, responsible for MRH *(until 01.10.2006)*<br>Ph.D. in Physics (1994), LMU München<br>XRD *in-situ* film growth characterisation for magnetron sputter deposition |

**Postal address** Rossendorf Beamline
(ROBL-CRG, BM20)
ESRF / sector 21
BP 220
F-38043 Grenoble cedex France

Phone: +33 (476) 88 xxxx
Fax: +33 (476) 88 2505
E-mail: surname@esrf.fr

**FZD personnel involved in the scientific and technical programme**

*Department of Research Technology*

| | | |
|---|---|---|
| Siegfried Dienel | Winfried Oehme | Jürgen Claussner |
| Dieter Proehl | | |

*Institute of Ion Beam Physics and Materials Research*

| | | |
|---|---|---|
| Manfred Beckers | Johannes von Borany | Frank Eichhorn |
| Birgit Gebauer | Joerg Grenzer | Joachim Kreher |
| Sybille Kirch | Andrea Scholz | Natalia Shevchenko |
| Rene Weidauer | | |

*Institute of Radiochemistry*

| | | |
|---|---|---|
| Thuro Arnold | Gerd Bernhard | Heidemarie Friedrich |
| Gerhard Geipel | Alix Guenther | Astrid Koban |
| Mandy Leckelt | Mohamed Merroun | Henry Moll |
| Cordula Nebelung | Anette Rumpel | Kai-Uwe Ulrich |

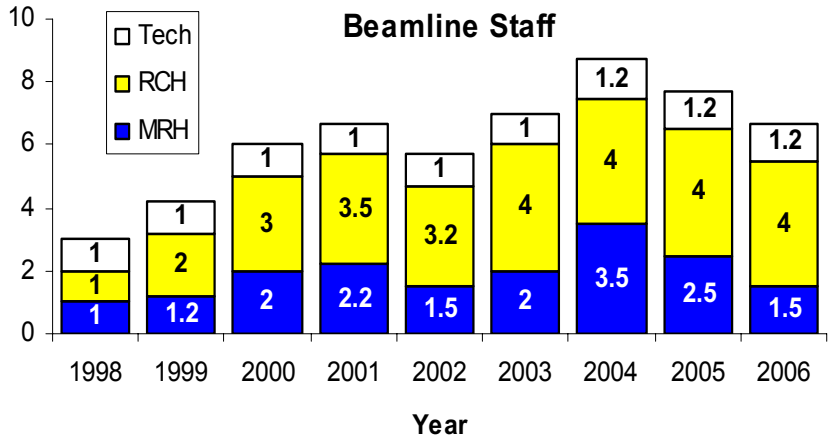


**Fig. 2.2.1.**
Evolution of beamline personnel since 1998.

## 2.3. Beamtime allocation and user groups

In the past two years, a total of 84 experiments have been performed at the beamline (Table 2.3.1). For these experiments, a total of 1178 shifts have been delivered. About 66 % of the beamtime has been used for FZD in-house experiments, and 23 % for ESRF experiments. About 22% of the inhouse shifts of RCH have been provided for Radiochemistry experiments in the framework of ACTINET - EU Network of Excellence (see below). With this, RCH belongs to one of the most heavily used facilities of ACTINET, providing a fundamental contribution to actinide research. In addition to the experimental shifts, 111 shifts have been used for the commissioning of new equipment and the development of new techniques. A total of 169 different users, including users from the FZD but excluding the beamline staff, have worked at the beamline in the past two years.

**Table 2.3.1.** Use of beamtime at the Rossendorf Beamline.

| | Year | FZD shifts | ESRF shifts | Actinet shifts | Technical shifts | Experiments FZD / ESRF / Actinet | Users |
|---|---|---|---|---|---|---|---|
| **RCH** | **2005** | 199 | 54 | 45 | 39 | 14 / 6 / 5 = 25 | 18 / 21 / 15 = 54 |
| **RCH** | **2006** | 172 | 69 | 74 | 9 | 13 / 7 / 7 = 27 | 13 / 18 / 18 = 49 |
| **MRH** | **2005** | 208 | 71 | ./. | 63 | 11 / 4 / ./. = 15 | 19 / 12 / 0= 31 |
| **MRH** | **2006** | 209 | 77 | ./. | ./. | 12 / 5 / ./. = 17 | 20 / 15 / 0= 35 |
| **sum** | | **788** | **271** | **119** | **111** | **50 / 22 / 12 = 84** | **70 / 66 / 33 = 169** |

Figure 2.3.1 shows the development of shift allocation from the last year of the construction period (1998) to December 2006. Since 2000, beamtime usage has reached a plateau with the beamline running at full capacity. A higher fluctuation of in-house beamtime at MRH is counterbalanced by the number of technical shifts used for the development of new techniques and short staff experiments. Both end-stations used about the same amount of shifts, in accordance with the agreement between the Institute of Radiochemistry and the Institute of Ion Beam Physics and Materials Research at the FZD, which are the main supporters of the beamline.

271 shifts have been provided for ESRF experiments and 53 more are provided in the first two months of 2007, i.e. within the ESRF scheduling period 2006/II. Thus, ROBL delivered more than the maximum of 142 shifts per year agreed upon between the ESRF and the CRG beamlines.

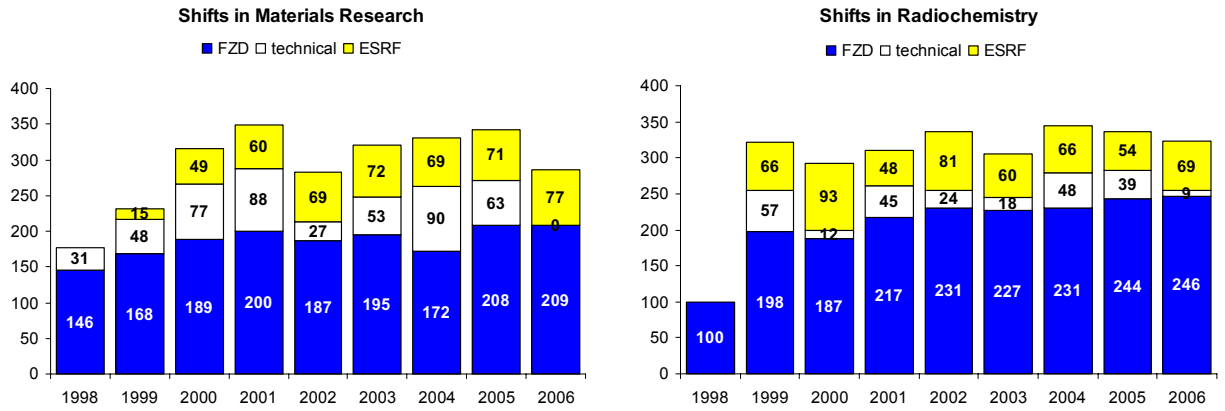


**Fig. 2.3.1.**
Development of shift allocation for Materials Research and Radiochemistry since 1998.

The figure below shows the beamtime delivery of all CRG beamlines in 2005. The Rossendorf Beamline has delivered the greatest number of shifts per independent experimental station of all CRG beamlines. In the past years it has always been among the top three in terms of shift delivery.

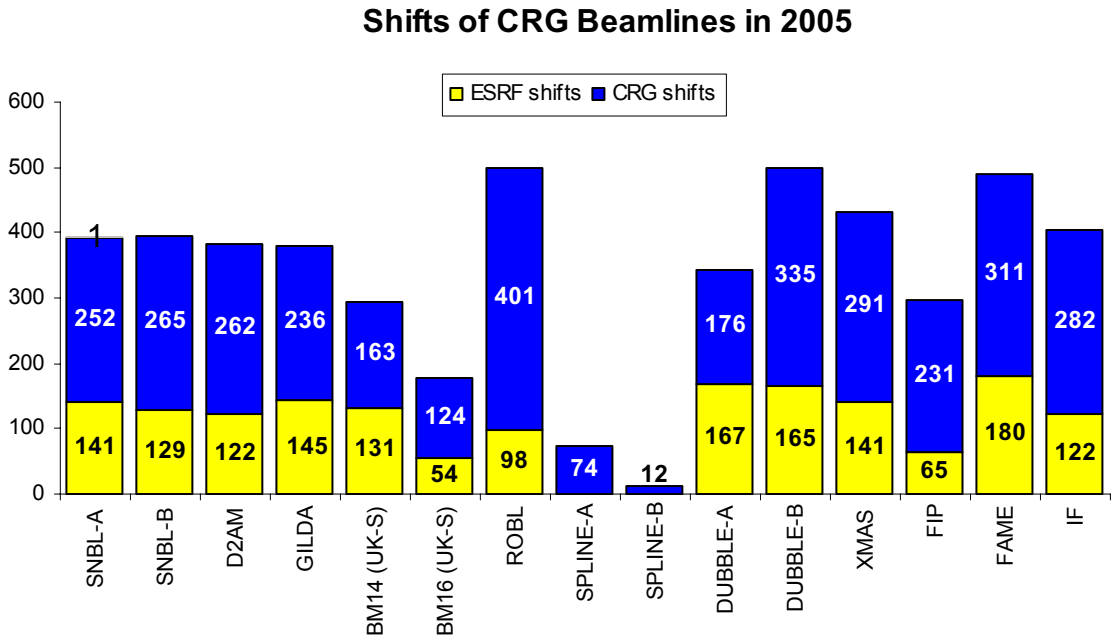


**Fig. 2.3.2.**
Delivery of shifts for in-house (CRG) and ESRF experiments by the CRG beamlines of the ESRF (Courtesy ESRF User Office).

## User Group Institutions

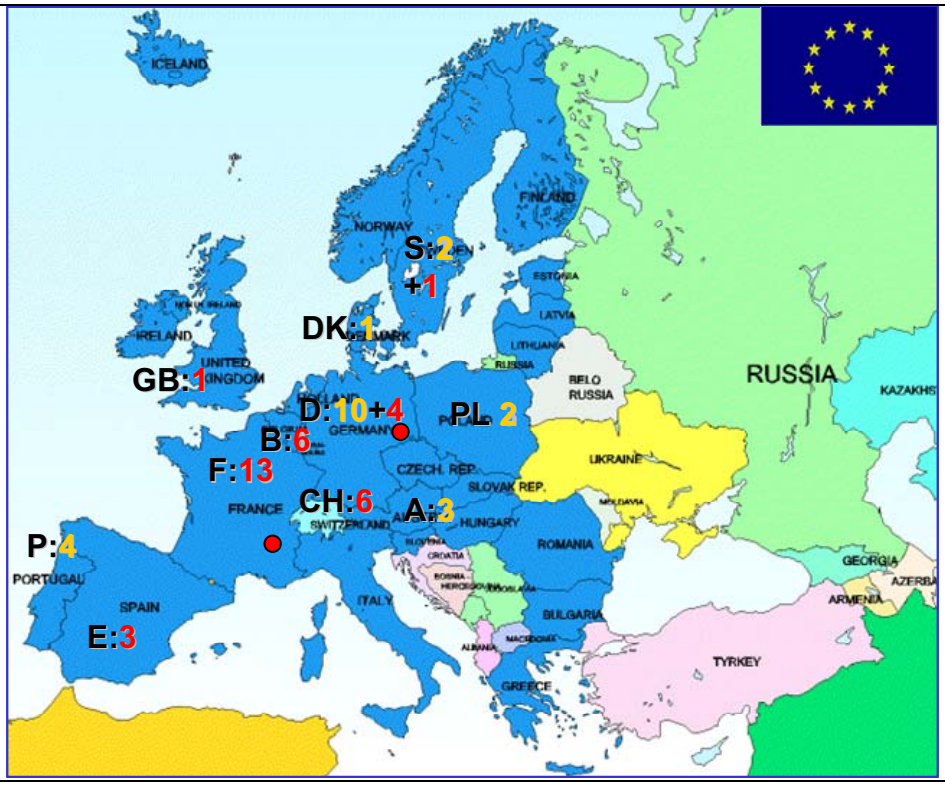


**Fig. 2.3.3.** Country specific dis-tribution of the different experi-ments done at ROBL (in red color for RCH and in yellow for MRH). Only external user groups or FZD collaborations are listed, i.e. no pure FZD in-house experiments.

**Germany**
- Advanced Micro Devices (AMD) Saxony, Dresden
- Geoforschungszentrum Potsdam
- GKSS Geesthacht
- Hochschule Mittweida
- Institut für Ionenstrahlphysik und Materialforschung (FWI), FZD, Dresden
- Institut für Kernchemie, Universität Mainz
- Institut für Materialwissenschaft und Technologie der TU Berlin
- Institut für Optik und Quantenelektronik, Friedrich-Schiller-Universität Jena
- Institut für Radiochemie (FWR), FZD, Dresden
- Institut für Röntgenphysik, Universität Göttingen
- Institut für Transurane (ITU), Eggenstein-Leopoldshafen
- Institute for Scientific Instruments (IFG), Berlin
- Max-Planck Institut für Eisenforschung GmbH (MPIE), Düsseldorf
- Qimonda, Dresden

**Austria**
- Institute for Materials Sciences, University of Leoben
- Institut für Werkstoffkunde der TU Wien

**Belgium**
- Departement Interfasechemie, Katholieke Universiteit Leuven
- Studiecentrum voor Kernenergie (SCK), Brussels

**Denmark**
- Institute of Physics and Astronomy, University of Aarhus

**France**
- CEA Valrhô and Valduc
- Centre National de la Recherche Scientifique (CNRS)
- Institut de Physique Nucléaire, Université Paris XI, Orsay
- IRES Strasbourg
- Laboratoire Subatech, Nantes
- Université Joseph Fourier (UJF), Grenoble

| | |
|---|---|
| **Great Britain** | – Dalton Nuclear Institute, University of Manchester |
| **Poland** | – Institute of Electronic Materials Technology (ITME), Warsaw |
| **Japan** | – Department of Nuclear Engineering & Management, The University of Tokyo |
| **Portugal** | – CENIMAT F.C.T./Universidade Nova de Lisboa, Monte da Caparica |
| **Spain** | – CIEMAT, Madrid<br>– Polytechnical University of Catalonia (UPC), Barcelona |
| **Sweden** | – Royal Institute of Technology , KTH Stockholm<br>– Linköping University, Linköping |
| **Switzerland** | – Department of Environmental Sciences, ETH Zurich<br>– Swiss Federal Institute of Environ. Science & Technology (EAWAG) |


## ACTINET European Network for Actinide Sciences

Since March 2004 the beamline is a member of ACTINET – European Network for Actinide Science, one of the Networks of Excellence within the 6th Framework Programme for Research and Technological Development. ACTINET gathers more than twenty-five European research institutions into a consortium dedicated to actinide sciences. The objective of ACTINET is to take steps in order to bring both research infrastructures and human expertise in Europe to an adequate performance level, thereby contributing to the development of the European Research Area in the fields of physics and chemistry of actinides. The three lines of action are:

- Stimulating the emergence of a European infrastructure policy by pooling the major actinide laboratory facilities
- Promoting excellence by supporting ambitious shared research programmes, taking advantage of the pooled facilities
- Increasing the attractiveness of actinide sciences among European students and young researchers, and allowing the next generation of actinide scientists and engineers to gain hands-on experience as part of their training.

The Rossendorf beamline contributes its radiochemistry end station to the ACTINET Pooled Facilities, providing beamtime for Joint Research Projects granted by ACTINET. In return, ROBL receives annual funds for user support. Within the first 2.5 years, 57 Joint Research Projects have been accepted by ACTINET during 5 calls, 14 of these experiments (≈ 25%) requesting beamtime at ROBL. In 2005/2006, 12 experiments have been performed for ACTINET (see list of experiments 2.5.1.). ROBL has thus provided 25 % of its available inhouse beamtime in agreement with ACTINET. During the 6th and last call, four Joint Research Projects have been submitted requesting beamtime. Together with the projects from previous calls, this will require the provision of beamtime at or even beyond the 25%-limit.

## 2.4. Publications

This section lists publications which are based on experiments at the Rossendorf Beamline, independent of whether they have been performed using in-house or ESRF allocated shifts. Only peer-reviewed journal articles, monographs and reviewed proceedings have been taken into consideration.

Figure 2.4.1 gives an overview on the publication activities since the commissioning of the beamline.

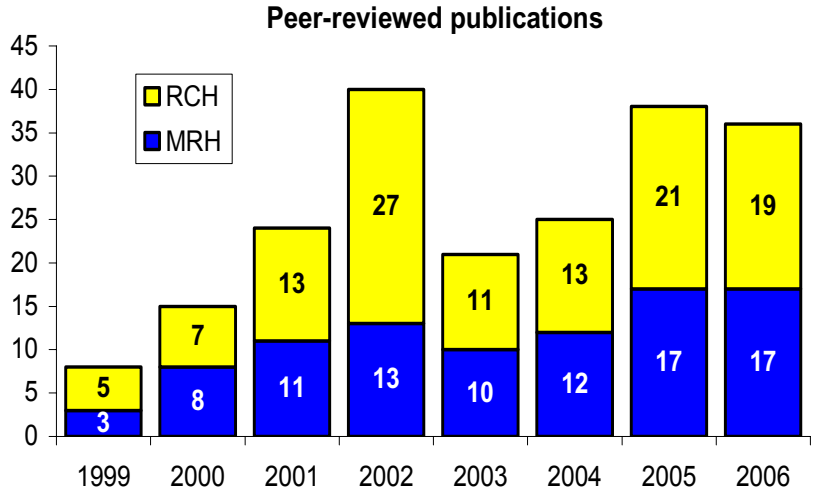


**Fig. 2.4.1.** Peer-reviewed publications in Materials Research (MRH) and Radiochemistry (RCH) since 1999, the first year of operation.

## 2.4.1. Publications in Radiochemistry

### 2005


Den Auwer, C., Llorens, I., Moisy, P., Vidaud, C., Goudard, F., Barbot, C., Solari, P.L., and Funke, H.
*Actinide uptake by transferrin and ferritin metalloproteins*
Radiochimica Acta **93** (2005) 699-703

Denecke, M.A., Rossberg, A., Panak, P.J., Weigl, M., Schimmelpfennig, B., and Geist, A.
*Characterization and comparison of Cm(III) and Eu(III) complexed with 2,6-di(5,6-dipropyl-1,2,4-triazin-3-yl)pyridine using EXAFS, TRFLS, and quantum-chemical methods*
Inorganic Chemistry **44** (2005) 8418-8425

Funke, H., Chukalina, M., and Rossberg, A.
*Wavelet analysis of extended x-ray absorption fine structure data*
Physica Scripta **T115** (2005) 232-234

Funke, H., Scheinost, A.C., and Chukalina, M.
*Wavelet analysis of extended X-ray absorption fine structure data*
Physical Review **B 71** (2005) 094110

Gaillard, C., El Azzi, A., Billard, I., Bolvin, H., and Hennig, C.
*Uranyl complexation in fluorinated acids (HF, HBF4, HPF6, HTf2N): A combined experimental and theoretical study*
Inorganic Chemistry **44** (2005) 852-861

Hennig, C., Reich, T., Kraus, W., Reck, G., Prokert, F., and Schell, N.
*Combining EXAFS and X-ray powder diffraction to solve structures containing heavy atoms*
Physica Scripta **T115** (2005) 352-355

Hennig, C., Tutschku, J., Rossberg, A., Bernhard, G., and Scheinost, A.C.
*Comparative EXAFS investigation of uranium(VI) and -(IV) aquo chloro complexes in solution using a newly developed spectroelectrochemical cell*
Inorganic Chemistry **44** (2005) 6655-6661

Kunicke, M., Kamensky, I.Y., Babanov, Y.A., and Funke, H.
*Efficient determination of optimal regularization parameter for inverse problem in EXAFS spectroscopy*
Physica Scripta **T115** (2005) 237-239

Le Naour, C., Trubert, D., Di Giandomenico, M.V., Fillaux, C., Den Auwer, C., Moisy, P., and Hennig, C.
*First structural characterization of a protactinium(V) single oxo bond in aqueous media*
Inorganic Chemistry **44** (2005) 9542-9546

Llorens, I., Den Auwer, C., Moisy, P., Ansoborlo, E., Vidaud, C., and Funke, H.
*Neptunium uptake by serum transferrin*
Febs Journal **272** (2005) 1739-1744

Merroun, M.L., Raff, J., Rossberg, A., Hennig, C., Reich, T., and Selenska-Pobell, S.
*Complexation of uranium by cells and S-layer sheets of Bacillus sphaericus JG-A12*
Applied and Environmental Microbiology **71** (2005) 5532-5543

Rossberg, A. and Scheinost, A.C.
*Linking Monte-Carlo Simulation and Target Transformation Factor Analysis: A novel tool for the EXAFS analysis of mixtures*
Physica Acta **T115** (2005) 912-914

Rossberg, A. and Scheinost, A.C.
*Three-dimensional modeling of EXAFS spectral mixtures by combining Monte Carlo simulations and target transformation factor analysis*
Analytical and Bioanalytical Chemistry **383** (2005) 56-66

Sachs, S., Schmeide, K., Reich, T., Brendler, V., Heise, K.H., and Bernhard, G.
*EXAFS study on the neptunium(V) complexation by various humic acids under neutral pH conditions*
Radiochimica Acta **93** (2005) 17-25

Scheinost, A.C., Rossberg, A., Marcus, M., Pfister, S., and Kretzschmar, R.
*Quantitative zinc speciation in soil with XAFS spectroscopy: Evaluation of iterative transformation factor analysis*
Physica Scripta **T115** (2005) 1038-1040

Schmeide, K., Reich, T., Sachs, S., Brendler, V., Heise, K.-H., and Bernhard, G.
*Neptunium(IV) complexation by humic substances studied by X-ray absorption fine structure spectroscopy*
Radiochimica Acta **93** (2005) 187-196

Schumacher, M., Christl, I., Scheinost, A., Jacobsen, C., and Kretzschmar, R.
*Heterogeneity of water-dispersible soil colloids investigated by Scanning Transmission X-ray Microscopy and C-1s XANES micro-spectroscopy*
Environmental Science & Technology **39** (2005) 9094-9100

Servaes, K., Hennig, C., Van Deun, R., and Gorller-Walrand, C.
*Structure of UO2Cl4 (2-) in acetonitrile*
Inorganic Chemistry **44** (2005) 7705-7707

Vantelon, D., Lanzirotti, A., Scheinost, A.C., and Kretzschmar, R.
*Spatial distribution and speciation of lead around corroding bullets in a shooting range soil studied by micro-X-ray fluorescence and absorption spectroscopy*
Environmental Science & Technology **39** (2005) 4808-4815

Voegelin, A., Pfister, S., Scheinost, A.C., Marcus, M.A., and Kretzschmar, R.
*Changes in zinc speciation in a field soil after contamination with zinc oxide*
Environmental Science & Technology **39** (2005) 6616-6623

Walter, M., Arnold, T., Geipel, G., Scheinost, A., and Bernhard, G.
*An EXAFS and TRLFS investigation on uranium(VI) sorption to pristine and leached albite surfaces*
Journal of Colloid and Interface Science **282** (2005) 293-305

## 2006

Cachia, J.N., Deschanels, X., Den Auwer, C., Pinet, O., Phalippou, J., Hennig, C., and Scheinost, A.
*Enhancing cerium and plutonium solubility by reduction in borosilicate glass*
Journal of Nuclear Materials **352** (2006) 182-189

Deschanels, X., Picot, V., Glorieux, B., Jorion, F., Peuget, S., Roudil, D., Jegou, C., Broudic, V., Cachia, J.N., Advocat, T., Den Auwer, C., Fillet, C., Coutures, J.P., Hennig, C., and Scheinost, A.
*Plutonium incorporation in phosphate and titanate ceramics for minor actinide containment*
Journal of Nuclear Materials **352** (2006) 233-240

Den Auwer, C., Moisy, P., Guillaumont, D., Vidaud, C., Funke, H., and Hennig, C.
*Structural investigation of neptunium(V) in toxicological processes*
Material Research Society Symposium Proceedings **893** (2006) 315-323

Fahmy, K., Merroun, M., Pollmann, K., Raff, J., Savchuk, O., Hennig, C., and Selenska-Pobell, S.
*Secondary structure and Pd-(II) coordination in S-layer proteins from Bacillus sphaericus studied by infrared and x-ray absorption spectroscopy*
Biophysical Journal **91** (2006) 996-1007

Geissler, A., Scheinost, A.C., and Selenska-Pobell, S.
*Changes of bacterial community structure of a uranium mining waste pile sample induced by addition of U(IV)*
In *Uranium in the Environment: Mining Impact and Consequences* (ed. B. J. Merkel and A. Hasche-Berger), Springer Verlag, (2006) 199-205.

Hennig, C., Tutschku, J., Rossberg, A., Scheinost, A.C., and Bernhard, G.
*In situ speciation of actinides in solution with a newly developed spectro-electrochemical cell*
In *Speciation, Techniques and Facilities for Radioactive Materials at Synchrotron Light Sources (NEA No. 6046)*, OECD (2006) 43-46.

Merroun, M., Nedelkova, M., Rossberg, A., Hennig, C., and Selenska-Pobell, S.
*Interaction mechanisms of bacterial strains isolated from extreme habitats with uranium*
Radiochimica Acta **94** (2006) 723-729

Moll, H., Merroun, M.L., Hennig, C., Rossberg, A., Selenska-Pobell, S., and Bernhard, G.
*The interaction of Desulfovibrio äspöensis DSM 10631T with plutonium*
Radiochimica Acta **94** (2006) 815-824

Montavon, G., Hennig, C., Janvier, P., and Grambow, B.
*Comparison of complexed species of Eu in alumina-bound and free polyacrylic acid: A spectroscopic study*
Journal of Colloid and Interface Science **300** (2006) 482-490

Poineau, F., Fattahi, M., Den Auwer, C., Hennig, C., and Grambow, B.
*Speciation of technetium and rhenium complexes by in situ XAS-electrochemistry*
Radiochimica Acta **94** (2006) 283-289

Pollmann, K., Merroun, M., Raff, J., Hennig, C., and Selenska-Pobell, S.
*Manufacturing and characterization of Pd nanoparticles formed on immobilized bacterial cells*
Letters in Applied Microbiology **43** (2006) 39-45

Scheinost, A.C.
*The Rossendorf Beamline at the ESRF: An XAS experimental station for actinide research*
In *Speciation, Techniques and Facilities for Radioactive Materials at Synchrotron Light Sources (NEA No. 6046)*, OECD (2006) 95-101.

Scheinost, A.C., Hennig, C., Somogyi, A., Martinez-Criado, G., and Knappik, R.
*Uranium speciation in two Freital mine tailing samples: EXAFS, micro-XRD, and micro-XRF results*
In *Uranium in the Environment: Mining Impact and Consequences* (ed. B. J. Merkel and A. Hasche-Berger), Springer Verlag, (2006) 117-126.

Scheinost, A.C., Rossberg, A., Vantelon, D., Xifra, I., Kretzschmar, R., Funke, H., and Johnson, C.A.
*Quantitative antimony speciation in shooting-range soils by EXAFS spectroscopy*
Geochimica et Cosmochimica Acta **70** (2006) 3299-3312

Schmeide, K., Reich, T., Sachs, S., and Bernhard, G.
*Plutonium(III) complexation by humic substances studied by X-ray absorption fine structure spectroscopy*
Inorganica Chimica Acta **359** (2006) 237-242

Stumpf, S., Stumpf, T., Dardenne, K., Hennig, C., Foerstendorf, H., Klenze, R., and Fanghanel, T.
*Sorption of Am(III) onto 6-line- ferrihydrite and its alteration products: Investigations by EXAFS*
Environmental Science & Technology **40** (2006) 3522-3528

Ulrich, K.-U., Rossberg, A., Foerstendorf, H., Zaenker, H., and Scheinost, A.C.
*Molecular characterization of uranium(VI) sorption complexes on iron(III)-rich acid mine water colloids*
Geochimica et Cosmochimica Acta **70** (2006) 5469-5487

Ulrich, K.-U., Rossberg, A., Scheinost, A.C., Foerstendorf, H., Zaenker, H., and Jenk, U.
*Speciation of colloid-born uranium by EXAFS and ATR-FTIR spectroscopy*
In *Uranium in the Environment: Mining Impact and Consequences* (ed. B. J. Merkel and A. Hasche-Berger), Springer Verlag, (2006) 137-148.

Vulpius, D., Geipel, G., Baraniak, L., Rossberg, A., and Bernhard, G.
*Complex formation of uranium(VI) with 4-hydroxy-3-methoxybenzoic acid and related compounds*
Journal of Radioanalytical and Nuclear Chemistry **270** (2006) 661-667

## 2007

Ghabbour, E.A., Scheinost, A.C., and Davies, G.
*XAFS studies of cobalt(II) binding by solid peat and soil-derived humic acids and plant-derived humic acid-like substances*
Chemosphere **67** (2007) 285-291

Hennig, C.
*Evidence for double-electron excitations in the $L_3$-edge x-ray absorption spectra of actinides*
Physica Review **B 74** (2007)

Soldatov, A.V., Lamoen, D., Konstantinovic, M.J., Berghe, S.V.d., Scheinost, A.C., and Verwerft, M.
*Local structure and oxidation state of uranium in some ternary oxides: X-ray absorption analysis*
Journal of Solid State Chemistry **180** (2007) 53-60

## 2.4.2. Publications in Materials Research

### 2005

Abd El-Rahman, A.M., El-Hossary, F.M., Prokert, F., Negm, N.Z., Schell, N., Richter, E., and Möller, W.
*In-situ stability study of nitrocarburized 304 stainless steel during heating*
Surface and Coating Technology **200** (2005) 602-607

Almtoft, K.P., Bøttiger, J., Chevallier, J., Schell, N., and Martins, R.M.S.
*Influence of the substrate bias on the size and thermal stability of grains in magnetron-sputtered nanocrystalline Ag films*
Journal of Materials Research **20** (2005) 1071-1080

Andreasen, K.P., Bøttiger, J., Chevallier, J., and Schell, N.
*Real time in-situ diagnostics of PVD growth using synchrotron radiation*
Surface and Coating Technology **200** (2005) 602-607

Beckers, M., Schell, N., Martins, R.M.S., Mücklich, A., and Möller, W.
*The influence of the growth rate on the preferred orientation of magnetron sputtered Ti-Al-N thin films studied by in situ x-ray diffraction*
Journal of Applied Physics **98** (2005) 044901-1-044901-7 and
ESRF NEWSLETTER **42** (2005) 20-21

Beckers, M., Schell, N., Martins, R.M.S., Mücklich, A., and Möller, W.
*In situ x-ray diffraction studies concerning the influence of Al concentration on the texture development during sputter deposition of Ti-Al-N thin films*
Journal of Vacuum Science and Technology A: Vacuum, Surfaces, and Films **23** (2005) 1384-1391
and Virtual Journal of Nanoscale Science and Technology, August 22, 2005

Cantelli, V., Borany, J.v., Mücklich, A., and Schell, N.
*Investigation of the formation and phase transition of small Ge and Co nanoparticles in a $SiO_2$ matrix*
Nuclear Instruments and Methods in Physics Research B **238** (2005) 268-271

Eichhorn, F., Gaca, J., Heera, V., Schell, N., Turos, A., Weishart, H., and Wojcik, M.
*Structural studies on ion-implanted semiconductors using x-ray synchrotron radiation: Strain evolution and growth of nanocrystals*
Vacuum **78** (2005) 303-309

Krause-Rehberg, R., Bondarenko, V., Thiele, E., Klemm, R., and Schell, N.
*Determination of absolute defect concentrations for saturated positron trapping – deformed polycrystalline Ni as a case study*
Nuclear Instruments and Methods in Physics Research B **240** (2005) 719-725

Martins, R.M.S., Schell, N., Silva, R.J.C., and Braz Fernandes, F.M.
*Structural in situ studies of shape memory alloy (SMA) Ni-Ti thin films*
Nuclear Instruments and Methods in Physics Research B **238** (2005) 319-322

Meduňa, M., Novák, J., Falub, C.V., Chen, G., Bauer, G., Tsujino, S., Grützmacher, D., Müller, E., Campidelli, Y., Kermarrec, O., Bensahel, D., and Schell, N.
*High temperature investigations of Si/SiGe based cascade structures using x-ray scattering methods*
Journal of Physics D: Applied Physics **38** (2005) A121-A125

Paula, A.S., Canejo, J.P.H.G., Schell, N., and Braz Fernandes, F.M.
*Structural evolution on thermal cycling in Ti-rich NiTi SMA*
Nuclear Instruments and Methods in Physics Research B **238** (2005) 111-114

Paula, A.S., Mahesh, K.K., Braz Fernandes, F.M., Martins, R.M.S., Cardoso, A.M.A., and Schell, N.
*In-situ high temperature texture characterisation in NiTi shape memory alloy using synchrotron radiation*
Materials Science Forum **495-497** (2005) 125-130

Rogozin, A., Shevchenko, N., Vinnichenko, M., Prokert, F., Cantelli, V., Kolitsch, A., and Möller, W.
*Real-time evolution of ITO film properties and structure during annealing in vacuum*
ESRF Highlights 2004 (2005) 28-30

Sass, J., Mazur, K., Eichhorn, F., Strupinski, W., Turos, A., and Schell, N.
*Determination of In concentration in InGaAs/GaAs 001 epilayers in the early stage of anisotropic stress relaxation*
Journal of Alloys and Compounds **401** (2005) 249-253

Schell, N., Andreasen, K.P., Bøttiger, J., and Chevallier, J.
*On the dependence on bias voltage of the structural evolution of magnetron-sputtered nanocrystalline Cu films during thermal annealing*
Thin Solid Films **476** (2005) 280-287

Schell, N., Martins, R.M.S., and Braz Fernandes, F.M.
*Real-time and in-situ structural design of functional NiTi SMA thin films*
Applied Physics A: Materials Science & Processing **81** (2005) 1441-1445

Thiele, E., Klemm, R., Hollang , L., Holste, C., Schell, N., Natter, H., and Hempelmann, R.
*An approach to cyclic plasticity and deformation-induced structure changes of electrodeposited nickel*
Materials Science and Engineering A **390** (2005) 42-51

## 2006

Beckers, M., Schell, N., Martins, R.M.S., Mücklich, A., and Möller, W.
*Phase stability of epitaxially grown $Ti_2AlN$ thin films*
Applied Physics Letters **89** (2006) 074101-1-074101-3

Beckers, M., Schell, N., Martins, R.M.S., Mücklich, A., Möller, W., and Hultman, L.
*Microstructure and non-basal plane growth of epitaxial MAX phase $Ti_2AlN$ thin films*
Journal of Applied Physics **99** (2006) 034902-1-034902-8

Braz Fernandes, F.M., Paula, A.S., Canejo, J.P.H.G., Mahesh, K.K., Martins, R.M.S., Cardoso, A.M.A., and Schell, N.
*Texture evolution during annealing of Ni-Ti SMA*
Proc. of Shape Memory and Superelastic Technologies Conference (SMST -2004) (2006) 45-50

Cantelli, V., Borany, J. von, Grenzer, J., Kaltofen, R., Schumann, J., and Fassbender, J.
*Influence of He-ion-irradiation on thin NiMn/NiFe exchange bias films*
Journal of Applied Physics **99** (2006) 8, 08C102

Hahn, T., Cieslak, J., Metzner, H., Eberhardt, J., Reislöhner, U., Gossla, M., Witthuhn, W., and Kräußlich, J.
*Metastability of $CuInS_2$ and its implications on thin film growth*
Applied Physics Letters **88** (2006) 171915-1-171915-3

Martins, R.M.S., Braz Fernandes, F.M., Silva, R.J.C., Beckers, M., and Schell, N.
*In-situ observation of Ni-Ti thin film growth by synchrotron radiation scattering*
Materials Science Forum **514-516** (2006) 1588-1592

Martins, R.M.S., Braz Fernandes, F.M., Silva, R.J.C., Beckers, M., and Schell, N.
*Structural in-situ studies of Ni-Ti thin films*
Proc. of Shape Memory and Superelastic Technologies Conference (SMST- 2004) (2006) 421-426

Martins, R.M.S., Braz Fernandes, F.M., Silva, R.J.C., Pereira, L., Gordo, P.R., Maneira, M.J.P., Beckers, M., Mücklich, A., and Schell, N.
*The influence of a poly-Si intermediate layer on the crystallization behaviour of Ni-Ti SMA magnetron sputtered thin films*
Applied Physics A: Materials Science & Processing **83** (2006) 139-145

Martins, R.M.S., Schell, N., Beckers, M., Mahesh, K.K., Silva, R.J.C., and Braz Fernandes, F.M.
*Growth of sputter-deposited Ni-Ti thin films: effect of a $SiO_2$ buffer layer*
Applied Physics A: Materials Science & Processing **84** (2006) 285-289

Paula, A.S., Canejo, J.H.P.G., Mahesh, K.K., Silva, R.J.C., Braz Fernandes, F.M., Martins, R.M.S., Cardoso, A.M.A., and Schell, N.
*Study of the textural evolution in Ti-rich NiTi using synchrotron radiation*
Nuclear Instruments and Methods in Physics Research B **246** (2006) 206-210

Pełka, J.B., Brust, M., Gierłowski, P., Paszkowicz, W., and Schell, N.
*Structure and conductivity of self-assembled films of gold nanoparticles*
Applied Physics Letters **89** (2006) 063110-1-063110-3

Pereira, L., Martins, R.M.S., Schell, N., Fortunato, E., and Martins, R.
*Nickel assisted metal induced crystallization of silicon: effect of native silicon oxide layer*
Thin Solid Films **511-512** (2006) 275-279

Potzger, K., Zhou, S.Q., Reuther, H., Mücklich, A., Eichhorn, F., Schell, N., Skorupa, W., Helm, M., Fassbender, J., Herrmannsdörfer, T., and Papageorgiou, T.
*Fe doped ZnO – a diluted magnetic semiconductor*
Applied Physics Letters **88** (2006) 052508-1-052508-3

Potzger, K., Zhou, S., Eichhorn, F., Helm, M., Skorupa, W., Mücklich, A., Fassbender, J., Herrmannsdörfer, T., Bianchi, A.
*Ferromagnetic Gd-implanted ZnO single crystals*
Journal of Applied Physics **99** (2006) 063906

Rogozin, A., Shevchenko, N., Vinnichenko, M., Seidel, M., Kolitsch, A., and Möller, W.
*Annealing of indium tin oxide films by electric current: properties and structure evolution*
Applied Physics Letters **89** (2006) 061908

Sass, J., Mazur, K., Surma, B., Eichhorn, F., Litwin, D., Galas, J., and Sitarek, S.
*X-ray studies of ultra-thin Si wafers for mirror application*
Nuclear Instrument in Physics Research B **253** (2006) 236

Talut, G., Reuther, H., Mücklich, A., Eichhorn, F., Potzger, K.
*Nanocluster formation in Fe implanted GaN*
Applied Physícs Letters **89** (2006) 161909

## 2.5. Experiments

The following tables list all experiments which have been performed at the beamline, separated by end-station (Radiochemistry, Materials Research) and by type of experiment (In-house (= CRG), ESRF, Actinet, Technical Shifts). Experiments with more than 18 shifts indicate that these experiments have been performed during several experimental runs and are part of long-term research programs.

## 2.5.1. List of Radiochemistry Experiments

**In-house experiments 2005**

| Number | Title | Proposers | Institution | Experimenters | Shifts |
|---|---|---|---|---|---|
| 20-01-065 | Interaction between Pseudomonas sp. and uranium using EXAFS | M. Merroun, S. Selenska-Pobell, T. Reich | FZD-FWR | M. Merroun, H. Funke, A. Rossberg | 20 |
| 20-01-611 | Interaction of actinides with predominant bacteria isolated at nuclear waste repositories using X-ray absorption spectroscopy | H. Moll, Ch. Hennig, M. Merroun, H. Funke, A. Rossberg | FZD-FWR | H. Moll, H. Friedrich, M. Merroun, Ch. Hennig, H. Funke, A. Rossberg, A. Scheinost | 6 |
| 20-01-618 | Spectroelectrochemical cell for in situ XAS measurements of uranium solution species | Ch. Hennig, J. Tutschku, G. Geipel, A. Rossberg, G. Bernhard | FZD-FWR | Ch. Hennig, A. Rossberg, A. Scheinost, H. Funke, A. Ikeda | 21 |
| 20-01-622 | Chemical speciation of metals in shooting-range soils | A. Scheinost, Ch. Hennig, D. Vantelon, I. Xifra | FZD-FWR, ETHZ, EAWAG, UPC | A. Scheinost, X. Martinez, I. Rojo, A. Rossberg, Ch. Hennig, H. Funke | 12 |
| 20-01-625 | Interaction between microorganisms and metals using EXAFS | M. Merroun, S. Selenska-Pobell, J. Raff, Ch. Hennig | FZD-FWR | M. Merroun, Ch. Hennig, A. Rossberg, A. Scheinost | 12 |
| 20-01-626 | Oxidation state and local structure of uranium in soils and sediments | A. Scheinost | FZD-FWR | H. Funke, A. Scheinost, Ch. Hennig, A. Rossberg | 23 |
| 20-01-632 | Uranium sorption onto natural iron colloids in mine waters | K.-U. Ulrich, A. Scheinost, H. Zaenker | FZD-FWR | A. Rossberg, K.-U. Ulrich, A. Scheinost, Ch. Hennig, H. Funke | 24 |
| 20-01-638 | X-ray absorption spectroscopy on gold nanoparticles formed by bacteria and their surface layer proteins | M. Merroun, S. Selenska-Pobell, A. Scheinost, Ch. Hennig | FZD-FWR | A. Rossberg, M. Merroun, A. Scheinost, Ch. Hennig, H. Funke | 3 |

**In-house experiments 2005 [cont.]**

| Number | Title | Proposers | Institution | Experimenters | Shifts |
|---|---|---|---|---|---|
| 20-01-641 | Uranyl(VI) sorption on gibbsite and quartz | Th. Arnold, N. Baumann, V. Brendler | FZD-FWR | A. Scheinost, Ch. Hennig, A. Rossberg, H. Funke | 9 |
| 20-01-642 | Local structure of U(IV) and U(VI) in natural and synthetic minerals | A. Scheinost, A. Rossberg, Ch. Hennig, H. Funke, Th. Arnold | FZD-FWR | A. Scheinost, A. Rossberg, Ch. Hennig, H. Funke | 33 |
| 20-01-649 | EXAFS investigation of gradual chloride complexation to the uranyl cation in acetonitrile | R. van Deun, K. Servaes | KU Leuven | Ch. Hennig, R. van Deun, A. Rossberg, K. Servaes, L. Fluyt | 9 |
| 20-01-652 | Reduction of Eu and Se by Fe(II) at the clay edge surface | A. Scheinost, Ch. Hennig, L. Charlet, A. Gehin | FZD-FWR, UJF | A. Scheinost, L. Charlet, A. Gehin, H. Funke, Ch. Hennig | 9 |
| 20-01-653 | Uranyl sorption to clay minerals and analogues | A. Scheinost, Ch. Hennig, A. Rossberg, N. Baumann, Th. Arnold, V. Brendler | FZD-FWR | A. Scheinost, Ch. Hennig, H. Funke | 9 |
| 26-01-727 | EXAFS study on the structural and binding behaviour of uranyl oxalate complexes in different solvents | R. van Deun | KU Leuven | R. van Deun, A. Rossberg, A. Scheinost, Ch. Hennig, H. Funke, K. Servaes, A. Lunstroot | 9 |

**ESRF experiments 2005**

| Number | Title | Proposers | Institution | Experimenters | Shifts |
|---|---|---|---|---|---|
| CH-1931 | EXAFS/XANES studies on the speciation of Tc(IV) in mixtures of the low an high molecular weight organics | A. Maes,<br>E. Breynaert,<br>C. Bruggeman | KU Leuven | A. Maes,<br>E. Breynaert,<br>C. Bruggeman,<br>Ch. Hennig,<br>A. Scheinost,<br>H. Funke,<br>A. Rossberg | 12 |
| ME-938 | Local environment of Pu in borosilicate glass | X. Deschanels,<br>C. Den Auwer,<br>J.N. Cachia | CEA Valrhô | X. Deschanels,<br>C. Den Auwer,<br>J.N. Cachia,<br>B. Glorieux,<br>Ch. Hennig,<br>A. Scheinost | 9 |
| ME-939 | XAS study of $PuO_{2+x}$ | M. Ripert,<br>Ph. Martin,<br>S. Grandjean,<br>Ch. Robisson-Thomas,<br>C. Valot,<br>C. Sabathier | CEA Valrhô | M. Ripert,<br>Ph. Martin,<br>A. Pieragnoli,<br>H. Plancher,<br>J. Lechelle,<br>Ch. Hennig,<br>H. Funke,<br>U. Strauch,<br>A. Scheinost | 6 |
| ME-1090 | EXAFS study of neptunium(V) uptake by kaolinite | T. Reich,<br>S. Amayri | Uni Mainz | T. Reich,<br>S. Amayri,<br>A. Jermolajev,<br>Ch. Hennig,<br>A. Rossberg,<br>H. Funke | 9 |
| SI-1174 | Study of the sorption mechanisms of selenium and cesium onto magnetite as steel corrosions product of radioactive waste canisters | T. Missana,<br>N. Granizo-Iñigo,<br>M. Garcia-Gutierrez,<br>U. Alonso | CIEMAT | T. Missana,<br>N. Granizo-Iñi.,<br>M. Garcia-Gutierrez,<br>U. Alonso,<br>A. Scheinost,<br>Ch. Hennig,<br>H. Funke,<br>A. Rossberg | 9 |
| SI-1262 | Study of the interaction between uranium(VI) and hydroxyapatite | F. Seco,<br>M. Grive,<br>X. Martinez | UPC | F. Seco,<br>A. Rey,<br>Ch. Hennig,<br>A. Rossberg,<br>H. Funke,<br>A. Scheinost | 9 |

## Actinet experiments 2005

| Number | Title | Proposers | Institution | Experimenters | Shifts |
|---|---|---|---|---|---|
| 20-01-639 | Investigation of U(VI)/U(V) carbonato complexes in aqueous solution by spectro-electrochemistry | Ch. Hennig, I. Grenthe, G. Palladino, A. Scheinost | FZD-FWR, KTH | Ch. Hennig, G. Palladino | 12 |
| 20-01-643 | Determination of the structure of uranium(IV) chloro-complexes highly coordinated in room temperature ionic liquids by EXAFS and XANES measurements | D. Trubert | IPN | D. Trubert, Ch. Hennig, C. Le Naour, S. Nikitenko | 6 |
| 20-01-644 | Interaction of actinide cations with metalloproteins | C. Den Auwer, Ph. Moisy, C. Vidaud | CEA | C. Den Auwer, D. Trubert, V. DiGiando., C. Fillaux, L. Bonin, Ch. Hennig, A. Rossberg, A. Scheinost, H. Funke | 6 |
| 20-01-645 | Spectroscopic approach of aqueous chemistry of protactinium(V) | D. Trubert, C. Den Auwer, C. Le Naour | IPN, CEA Valrhô | A. Rossberg, D. Trubert, C. Den Auwer, V. DiGiando., C. Fillaux, L. Bonin, Ch. Hennig, A. Scheinost, H. Funke | 9 |
| 20-01-651 | Structural and magnetic properties of ternary uranates | M. Konstantinovic, A. Scheinost | SCK | M. Konstant., A. Scheinost, A. Rossberg, H. Funke, Ch. Hennig | 12 |

## In-house experiments 2006

| Number | Title | Proposers | Institution | Experimenters | Shifts |
|---|---|---|---|---|---|
| 20-01-065 | Interaction between Pseudomonas sp. and uranium using EXAFS | M. Merroun, S. Selenska-Pobell, T. Reich | FZD-FWR | M. Merroun, H. Funke, A. Rossberg | 12 |
| 20-01-618 | Spectroelectrochemical cell for in situ XAS measurements of uranium solution species | Ch. Hennig, J. Tutschku, G. Geipel, A. Rossberg, G. Bernhard | FZD-FWR | Ch. Hennig, A. Rossberg, A. Scheinost, H. Funke, A. Ikeda | 30 |

**In-house experiments 2006 [cont.]**

| Number | Title | Proposers | Institution | Experimenters | Shifts |
|---|---|---|---|---|---|
| 20-01-622 | Chemical speciation of metals in shooting-range soils | A. Scheinost, Ch. Hennig, D. Vantelon, I. Xifra | FZD-FWR, ETHZ, EAWAG, UPC | A. Scheinost, X. Martinez, I. Rojo, A. Rossberg, Ch. Hennig, H. Funke | 26 |
| 20-01-624 | Speciation of Zn in rhizosphere soil | A. Scheinost, Ch. Hennig, A. Rossberg, H. Funke, A. Voegelin, S. Pfister | FZD-FWR, ETHZ | A. Scheinost, A. Rossberg, H. Funke | 6 |
| 20-01-625 | Interaction between microorganisms and metals using EXAFS | M. Merroun, S. Selenska-Pobell, J. Raff, Ch. Hennig | FZD-FWR | M. Merroun, Ch. Hennig, A. Rossberg, A. Scheinost | 6 |
| 20-01-626 | Oxidation state and local structure of uranium in soils and sediments | A. Scheinost | FZD-FWR | H. Funke, A. Scheinost, Ch. Hennig, A. Rossberg, | 27 |
| 20-01-638 | X-ray absorption spectroscopy on gold nanoparticles formed by bacteria and their surface layer proteins | M. Merroun, S. Selenska-Pobell, A. Scheinost, Ch. Hennig | FZD-FWR | A. Rossberg, M. Merroun, A. Scheinost, Ch. Hennig, H. Funke | 12 |
| 20-01-642 | Local structure of U(IV) and U(VI) in natural and synthetic minerals | A. Scheinost, A. Rossberg, Ch. Hennig, H. Funke, Th. Arnold | FZD-FWR | A. Scheinost, A. Rossberg, Ch. Hennig, H. Funke | 3 |
| 20-01-652 | Reduction of Eu and Se by Fe(II) at the clay edge surface | A. Scheinost, Ch. Hennig, L. Charlet, A. Gehin | FZD-FWR, UJF | A. Scheinost, L. Charlet, A. Gehin, A. Fernandez, N. Geoffroy, H. Funke, Ch. Hennig | 15 |
| 20-01-653 | Uranyl sorption to clay minerals and analogues | A. Scheinost, Ch. Hennig, A. Rossberg, N. Baumann, Th. Arnold, V. Brendler | FZD-FWR | A. Scheinost, Ch. Hennig, H. Funke | 15 |
| 20-01-656 | EXAFS investigations of uranium species formed by monocellular and polycellular algae | A. Guenther, A. Rossberg, A. Scheinost | FZD-FWR | A. Rossberg, H. Funke, A. Guenther | 6 |
| 20-01-657 | EXAFS-investigations on U(IV) pseudocolloids | S. Weiss | FZD-FWR | Ch. Hennig, H. Funke, A. Rossberg | 6 |
| 20-01-660 | EXAFS study of U(VI) complexation in acetate solution | T. Reich, A. Rossberg | Uni Mainz | A. Rossberg, E. Adler, H. Funke | 8 |

**ESRF experiments 2006**

| Number | Title | Proposers | Institution | Experimenters | Shifts |
|---|---|---|---|---|---|
| CH-2083 | Structure of the serum transferring metal binding site upon actinide(IV) uptake | Ch. DenAuwer, Ph. Moisy, C. Vidaud | CEA | A. Scheinost, Ch. DenAuwer, Ph. Moisy, C. Vidaud | 12 |
| CH-2086 | Study of the influence of humic acid on the U(VI) sorption onto kaolinite | A. Krepelova | FZD-FWR | H. Funke, Ch. Hennig, A. Rossberg, A. Scheinost | 9 |
| CH-2192 | Local atomic structure in (Zr,Pu,Am)N | M. Walter, J. Somers | ITU | M. Walter, C. Naestren, S. Stohr, D. Bregioux, A. Rossberg, A. Scheinost, Ch. Hennig, H. Funke | 9 |
| CH-2306 | Complexation of uranyl to crown ethers: influence of solvent, concentration ratio and counter-ions | R. VanDeun, K. Servaes | Uni Leuven | Ch. Hennig, R. Van Deun, E. Cartuyvels | 9 |
| EC-23 | EXAFS study of neptunium(V) sorption at alpha-Fe203 | T. Reich, S. Amayri | Uni Mainz | A. Rossberg, Ch. Hennig, H. Funke, T. Reich | 9 |
| ME-1256 | XAS study of chromium in MOX fuel | A. Pieragnoli, J. Lechelle, H. Palancher, P. Martin, M. Ripert, C. Valot | CEA | Ph. Martin, J. Lechelle, A. Pieragnoli, C. Gilles, Ph. Beaugelin, A. Scheinost, H. Funke, Ch. Hennig, A. Rossberg | 12 |
| SI-1347 | Study of the sorption mechanisms of selenium and cesium onto magnetite as steel corrosions product of radioactive waste canisters | T. Missana, N. Granizo-Iñigo, M. Garcia-Gutierrez, U. Alonso | CIEMAT | T. Missana, N. Granizo-Iñigo, U. Alonso, A. Scheinost, Ch. Hennig, H. Funke, A. Rossberg | 9 |

**Actinet experiments 2006**

| Number | Title | Proposers | Institution | Experimenters | Shifts |
|---|---|---|---|---|---|
| 20-01-632 | Uranium sorption onto natural iron colloids in mine waters | K.-U. Ulrich,<br>A. Scheinost,<br>H. Zaenker | FZD-FWR | A. Rossberg,<br>K.-U. Ulrich,<br>A. Scheinost,<br>Ch. Hennig,<br>H. Funke | 15 |
| 20-01-645 | Spectroscopic approach of aqueous chemistry of protactinium(V) | D. Trubert,<br>C. Den Auwer,<br>C. Le Naour | IPN<br>CEA<br>Valrhô | A. Rossberg,<br>D. Trubert,<br>C. Den Auwer,<br>V. DiGiando.<br>C. Fillaux,<br>L. Bonin,<br>Ch. Hennig,<br>A. Scheinost,<br>H. Funke | 9 |
| 20-01-651 | Structural and magnetic properties of ternary uranates | M. Konstantinovic,<br>A. Scheinost | SCK | M. Konstant.,<br>A. Scheinost,<br>A. Rossberg,<br>H. Funke,<br>Ch. Hennig | 8 |
| 20-01-654 | Solvation and complexation of uranium(VI) in room temper-ature ionic liquids(RTILs): Influence of the dissolved salt and of the RTIL composition | C. Gaillard,<br>I. Billard | IRES | Ch. Hennig,<br>C. Gaillard,<br>I. Billard,<br>A. Rossberg,<br>H. Funke,<br>A. Scheinost | 9 |
| 20-01-655 | Uranyl spectroscopy and spectroelectrochemistry in various matrices | I. May,<br>C. Sharrad,<br>J. Charnock,<br>S. Corn | Univ.<br>Man-<br>chester | I. May,<br>C. Sharrad,<br>Ch. Hennig,<br>A. Rossberg,<br>H. Funke,<br>A. Scheinost | 9 |
| 20-01-658 | Studies of the chemical forms of actinides and fission products adsorbed on nanocrystalline magnetite | S. Nikitenko,<br>A. Scheinost | CNRS | S. Nikitenko, A. Scheinost, H. Funke, A. Rossberg, Ch. Hennig | 12 |
| 20-01-659 | Actinide selective recognition by biomimetic molecules | C. Den Auwer,<br>A. Jeanson,<br>S. Coantic,<br>V. Giandomenico | CEA,<br>IPN | C. Den Auwer,<br>A. Jeanson,<br>V. Giandomen.,<br>C. Le Naour,<br>E. Bosse,<br>S. Petit,<br>Ph. Moisy,<br>H. Funke,<br>A. Rossberg | 12 |

## 2.5.2. List of Materials Research Experiments

### In-house experiments 2005

| Number | Title | Proposers | Institution | Experimenters | Shifts |
|---|---|---|---|---|---|
| 20-02-608 | *In-situ* x-ray diffraction during sputter deposition of TiAlN | M. Beckers, N. Schell | FZD-FWI | M. Beckers, N. Schell, R. Martins | 48 |
| 20-02-617 | SR-μ-XRD stress measurements of dual damascene inlaid copper interconnect structures at tempera-tures between RT and 500°C | J. Rinderknecht, H. Prinz | AMD Saxony | J. Rinderknecht, H. Prinz, I. Zienert, N. Schell | 35 |
| 20-02-622 | Structural studies of semiconductor materials for optoelectronic applications | J. Sass, F. Eichhorn, J. Gaca, K. Mazur, M. Wojcik | ITME, FZD-FWI | J. Sass, J. Gaca, K. Mazur, M. Wojcik, F. Eichhorn, N. Schell | 27 |
| 20-02-627 | Two-dimensional x-ray waveguide gratings | T. Salditt | Uni Göttingen | C. Ollinger, C. Fuhse, N. Schell | 15 |
| 20-02-628 | Structural studies of oxygen implanted NiTi surfaces | N. Shevchenko | FZD-FWI | N. Shevchenko, A. Rogozin, R. Martins, N. Schell | 15 |
| 20-02-629 | The nanostructural development of magnetron sputtered Ag-Cu films studied by in-situ XRD | J. Bøttiger, N. Schell | University of Aarhus | J. Bøttiger, K. P. Pakh Almtoft, A. M. Ejsing, Schell, Martins | 18 |
| 20-02-630 | Ion beam induced atomic displacements in periodic multilayers and consequent changes in properties | B. N. Dev, J. Grenzer, N. Schell | FZD-FWI | B. N. Dev, J. Grenzer, N. Schell | 17 |
| 20-02-631 | Surface layer structure in ion implanted Si | F. Eichhorn, R. Koegler | FZD-FWI | N. Schell | 6 |
| 20-02-633 | Polfigure measurement on coarse grained black tourmaline | K. Walther | GFZ Potsdam | K. Walther, N. Schell | 9 |
| 20-02-635 | $L1_0$ ordering in FePt films designed for future magnetic memory materials | J. v. Borany, V. Cantelli | FZD-FWI | J. v. Borany, V. Cantelli, N. Schell, R. Martins | 18 |

## ESRF experiments 2005

| Number | Title | Proposers | Institution | Experimenters | Shifts |
|---|---|---|---|---|---|
| ME-936 | *In-situ* study of the co-sputtering of ternary (Ni-Ti-X, X=Cu, Hf) SMA thin films | F. M. Braz Fernandes, R. J. Cordeiro Silva, M. Silva | CENIMAT | F. M. Braz Fernandes, R. J. C. Silva, K. Mahesh, R. Martins, N. Schell | 18 |
| ME-1087 | *In-situ* study during co-sputtering of NiTi-TiN nanocomposite thin film | F.M. Braz Fernandes, K. Mahesh, R.J. Cordeiro Silva | CENIMAT | F. M. Braz Fernandes, C. R. J. Silva, K. Mahesh, R. Martins, N. Schell | 21 |
| ME-1089 | Oxide growth on novel TiAl-Nb alloys | A. Pyzalla, W. Reimers, H. Clemens, P. Silva | TU Wien, TU Berlin, Montanuni Leoben | A. Pyzalla, P. Silva, C. Juricic, N. Schell | 21 |
| SI-1173 | 2nd run of Cu(In,Ga)$S_2$ thin film characterization using GID | J. Kräußlich, T. Hahn, J. Cieslak | FSU Jena | J. Kräußlich, T. Hahn, J. Cieslak, V. Cantelli | 11 |

## In-house experiments 2006

| Number | Title | Proposers | Institution | Experimenters | Shifts |
|---|---|---|---|---|---|
| 20-02-617 | SR-μ-XRD stress measurements of dual damascene inlaid copper interconnect structures at tempera-tures between RT and 500°C | J. Rinderknecht, H. Prinz | AMD Saxony | J. Rinderknecht H. Prinz, I. Zienert, N. Schell | 17 |
| 20-02-632 | In situ investigations of ITO film crystallization during annealing by electric current | N. Shevchenko, A. Rogozin, M. Vinnichenko | FZD-FWI | N. Shevchenko A. Rogozin, N. Schell | 18 |
| 20-02-634 | Nanophase formation in ZnO implanted with transition or rare earth metal ions | S. Zhou | FZD-FWI | S. Zhou, Zhang, N. Schell, F. Eichhorn, J. v. Borany | 18 |
| 20-02-636 | In-situ x-ray diffraction during sputter deposition of Ti-Al-N MAX phase thin films | M. Beckers, N. Schell, J. Birch | FZD-FWI, Linkoeping University | M. Beckers, N. Schell, R. Martins, C. Höglund | 18 |
| 20-02-637 | In-situ stuty of the preferential orientation of sputtered Ni-Ti thin films as a function of bias and substrate type | R. Martins, N. Schell | FZD-FWI | R. Martins, N. Schell, F. M. Braz Fernandes | 18 |
| 20-02-638 | The influence of He ion irradiation on the texture development of thin films | N. Schell | FZD-FWI | N. Schell, R. Martins, F. M. Braz Fernandes, J. v. Borany | 18 |

## In-house experiments 2006 [cont.]

| Number | Title | Proposers | Institution | Experimenters | Shifts |
|---|---|---|---|---|---|
| 20-02-639 | In situ silicidation of Ni-alloys on strained Si substrates | J. Rinderknecht | AMD Saxony, Hochsch. Mittweida | J. Rinderknecht I. Zienert, T. Fuhrmann, N. Schell | 18 |
| 20-02-640 | *In-situ* x-ray diffraction during sputter deposition of Ti-Al-N MAX phase thin films | M. Beckers, N. Schell | Linkoeping University, FZD-FWI | M. Beckers, N. Schell, C. Höglund | 21 |
| 20-02-641 | *In-situ* investigation of recrystallization of heavily damaged by ion bombardment ZnO thin films during thermal annealing | M. Vinnichenko, N. Shevchenko, A. Rogozin | FZD-FWI | N. Shevchenko A. Rogozin, U. Strauch | 18 |
| 20-02-643 | Materials characterization for DRAM-Trench-Technology | J. v. Borany | FZD-FWI | S. Teichert, F. Eichhorn, J. v. Borany | 9 |
| 20-02-644 | GISAXS Tests at ROBL | J. Grenzer | FZD-FWI | J. Grenzer, F. Eichhorn | 18 |
| 20-02-646 | In-situ structural investigations of the L10 ordering in FePt layers during magnetron sputtering | V. Cantelli, J. v. Borany, U. Strauch | FZD-FWI | V. Cantelli, J. v. Borany, A. Scholz U. Strauch | 18 |

## ESRF experiments 2006

| Number | Title | Proposers | Institution | Experimenters | Shifts |
|---|---|---|---|---|---|
| MA-105 | In-situ study of co-sputtering of Ni-Ti-TiN nanocomposites thin films (cont) | F.M. Braz Fernandes, K. Mahesh, R.J. Cordeiro Silva | CENIMAT, | F. M. Braz Fernandes, R. J. C. Silva, K. Mahesh, R. Martins, N. Schell | 17 |
| MA-106 | Internal strains and stresses in oxide layers formed on advanced high Nb containing $\gamma$-TiAl based alloys | H. Pinto, P. Silva, F. Sket | MPIE | H. Pinto, F. Sket, P. A. S. da Silva, N. Schell | 18 |
| ME-1255 | In-situ study of the co-sputtering of ternary (Ni-Ti-X, X=Cu, Hf) SMA thin films | F.M. Braz Fernandes, R.J. Cordeiro Silva, K. Mahesh | CENIMAT | F. M. Braz Fernandes, R. J. C. Silva, K. Mahesh, R. Martins, N. Schell | 18 |
| SI-1261 | Determination of the chemical composition profile for III-N hetero-structures containing ultra-thin layers | J. Gaca, M. Wojcik | ITME | J. Gaca, M. Wojcik, F. Eichhorn, N. Schell | 15 |
| SI-1346 | In-plane lattice parameter determination of Zn:$LiNbO_3$ thin films epitaxially grown on x-cut LiNbO3 substrates using x-ray grazing-incidence diffraction | J. Kräußlich, C. Dubs, O. Wehrhan | FSU Jena | J. Kräußlich, O. Wehrhan, U. Zastrau, N. Schell | 9 |

## 2.5.3 List of Technical Shifts

### Technical shifts 2005

| Number | Title | Proposers | Institution | Experimenters | Shifts |
|---|---|---|---|---|---|
| IH-MI-349 | Commissioning of new MR experimental equipment | N. Schell | FZD-FWI | N. Schell, V. Cantelli, R. Martins, J. v. Borany | 18 |
| IH-MI-387 | XRD test studies of implanted single crystals, magnetic MLs and sputter-deposited NiTi shape memory alloys [1)] | N. Schell, A. Bjeoumikhov | FZD-FWI, IFG Berlin | N. Schell, R. Martins, A. Bjeoumikh., F. Eichhorn, A. Weiss | 12 |
| IH-MI-388 | Detector commissioning for Ni/C-ML-waveguides | N. Schell | FZD-FWI | U. Strauch, J. Grenzer, R. Martins | 15 |
| IH-HC-777 | Real-time studies of the ITO film structure and resistivity behaviour during annealing | N. Schell | FZD-FWI | R. Martins, N. Schell, N. Shevchenko A. Rogozin | 9 |
| IH-SI-206 | Real-time studies of the ITO film structure and resistivity behaviour during annealing | N. Schell | FZD-FWI | N. Schell, U. Strauch, R. Martins, N. Shevchenko A. Rogozin, V. Cantelli | 9 |
| | Commissioning and Tests | U. Strauch, A. Scheinost | FZD-FWR | U. Strauch, H. Funke, A. Rossberg, Ch. Hennig, A. Scheinost | 39 |

[1)] Part I: Comissioning of a parabolic capillary for XRD at a synchrotron (6 shifts)
Part II: Magnetic nanocrystals in a single crystalline matrix characterization (6 shifts)

### Technical shifts 2006

| Number | Title | Proposers | Institution | Experimenters | Shifts |
|---|---|---|---|---|---|
| | Commissioning and Tests | U. Strauch, A. Scheinost | FZD-FWR | U. Strauch, H. Funke, A. Rossberg, Ch. Hennig, A. Scheinost | 9 |

# 3. Experimental Reports

Below is a compilation of Experimental Reports, as far as they have been provided by the users until January 2007. The responsibility for the communicated results lies with the users. An updated list of experimental reports can also be downloaded from our web-site, which is accessible through the ESRF at http://www.esrf.fr/UsersAndScience/Experiments/CRG/BM20/ or directly at http://www.fzd.de/FWE.

Due to the inevitable delay between the experimental work and the Experimental Report, this compilation lacks some of the most recent experiments.

## 3.1. Experimental Reports Radiochemistry

| ROBL-CRG | **Experiment title:** **Interaction between Pseudomonas sp. and uranium using EXAFS** | **Experiment number:** **20-01-065** |
|---|---|---|
| **Beamline:** BM 20 | **Date of experiment:** 6.3.-8.3.05; 17.7.-19.7.05; 17.9.-20.9.05; 15.4.-18.4.06; 23.7.-24.7.06 | **Date of report:** 12.01.07 |
| **Shifts:** 32 | **Local contact(s):** Dr. Christoph Hennig | *Received at ROBL:* |
| **Names and affiliations of applicants** (* indicates experimentalists): M. Merroun*, M. Nedelkova, A. Rossberg*, A. Scheinost*, C. Hennig*, H. Funke*, S. Selenska-Pobell | | |

**Report:** Three oligotrophic bacterial strains were cultured from the ground water of the deep-well monitoring site S15 of the Siberian radioactive waste depository Tomsk-7, Russia. They were affiliated with *Actinobacteria* from the genus *Microbacterium*. The cells of all three strains accumulated high amounts of uranium, i.e. up to 240 mg U (g dry biomass)$^{-1}$ in the case of *M. oxydans* S15-M2. X-ray absorption spectroscopy (XAS) analysis showed that this strain precipitated U(VI) at pH 4.5 as a meta-autunite-like phase. At pH 2, the uranium formed complexes with organically bound phosphate groups on the cell surface. The results of the XAS studies were consistent with those obtained by transmission electron microscopy (TEM) and energy dispersive X-ray (EDX) analysis [1].

**Experimental***:* Bacterial cells grown to mid-exponential phase were harvested by centrifugation at 8,600 x *g* for 20 min at 4 °C and washed twice with 0.1 M $NaClO_4$. Washed cells were resuspended and shaken for 48 h in 10 ml of uranium solution (119 mg $L^{-1}$) at pH values of 2, 3 and 4.5. We used 0.1 M $NaClO_4$ as a background electrolyte. After contact with the uranium solution, cells were harvested and washed with 0.1 M $NaClO_4$. The pelleted samples were dried in a vacuum incubator at 30 °C for 24 h and powdered.

**Results:** XANES analysis (data not shown) demonstrated that the oxidation state of uranium species bound to the cells was unchanged indicating the bacteria do not reduce U(VI). Information on the local environment of uranium atoms in the uranium treated bacterial samples was provided by analysis of EXAFS data. Uranium $L_{III}$-edge EXAFS spectra of the uranium species formed at pH 2, 3 and 4.5 by the cells of *M. oxydans* S15-M2 and their corresponding Fourier transforms (FT`s) are presented in Fig. 1. Quantitative fit results (data not shown) indicate that the adsorbed U(VI) has the common linear trans-dioxo structure: two axial oxygens at about 1.75 - 1.77 Å, and an equatorial shell of 4 to 5 oxygens at 2.27 - 2.33 Å. The U-$O_{eq1}$ bond distance is within the range of previously reported values for phosphate bound to uranyl [2]. The FT peak, which appears at R+Δ ~ 3 Å (radial distance R = 3.59 - 3.62 Å) is a result of the back-scattering from phosphorus atoms. This distance is typical for a monodentate coordination of U(VI) by phosphate. For the studied *M. oxydans* S15-M2 strain, at pH 3 and 4.5, an FT shell corresponding to a distance of R = 5.19-5.20 Å can be related to a U-U contribution.. At pH 2, however, the U-U peak is absent indicating a lower site symmetry around uranium. All known U(VI) complexes with organic phosphates show a $N_{Oeq} \geq 5$ and are related to a longer U-$O_{eq}$ distance, e.g. 2.32 Å in the case of fructose 6-phosphate (F6P) used as reference in Fig. 1. Interestingly, we have found that EXAFS spectra of the samples at this pH have high similarities to those of organic phosphate ligands complexed with U such as fructose 6-phosphate [3].

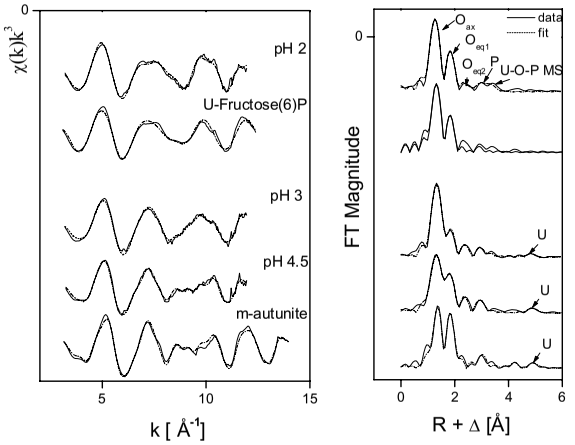


**Fig.1**: Uranium $L_{III}$-edge $k^3$–weighted EXAFS spectra (left) and the corresponding fourier transforms (FT) (right) of the uranium complexes formed by the cells of *M. oxydans* S15-M2 at pH values 2, 3, and 4.5, as well as of the reference compounds (meta-autunite and U-Fructose(6)Phosphate).

**ACKNOWLEDGEMENTS.** This work was supported by grant FIKW-CT-2000-00105 (BORIS) from the European Community.

**REFERENCES**

[1] Nedelkova *et al.* (2007) FEMS Microbiol Ecol (in press)
[2] Merroun *et al.* (2005) *Appl Environ Microbiol* **71,** 5532-5543.
[3] Koban *et al.* (2004) *Radiochim Acta* **92**, 903-908.

| ROBL-CRG | **Experiment title:**<br>**Interaction of actinides with predominant bacteria isolated at nuclear waste repositories using X-ray absorption spectroscopy** | **Experiment number:**<br>**20-01-611** |
|---|---|---|
| **Beamline:**<br>BM 20 | **Date of experiment:**<br>From: 15.06.2005 to: 17.06.2005 | **Date of report:**<br>09.03.2006 |
| **Shifts:**<br>6 | **Local contact(s):**<br>Ch. Hennig | *Received at ROBL:* |
| **Names and affiliations of applicants** (* indicates experimentalists):<br>H. Moll*, Ch. Hennig*, H. Funke*, A. Rossberg*, A. Scheinost*, G. Bernhard, S. Selenska-Pobell | | |

**Report:**

X-ray absorption spectroscopy (XAS) is a powerful tool to characterize the speciation of heavy metals in a broad range of systems. The two parts, XANES and EXAFS, are giving in combination element specific information concerning the oxidation state and local structure of an absorbing metal. In this study, XAS was used for a detailed characterization of the microbial processes taking place in the system Pu – *D. äspöensis*. This strain predominate the indigenous SRB population at the Äspö aquifer system in Sweden.

**Experimental:** The spectrum from the Pu(VI) reference sample (0.05 M in 1 M $HNO_3$) was taken from earlier measurements. The Pu(IV) reference sample (0.08 M in 1 M $HClO_4$) was prepared as described in /1/. 1 mL of the bacterial suspension in 0.9% NaCl was incubated with 5 mL of $^{242}$Pu, 127 mg/L, at pH 5. After shaking the samples for 96 h under $N_2$ atmosphere, the biomass was separated by centrifugation, washed with 0.9% NaCl, and sealed in a polyethylene cuvette. The bacterial sample was measured as wet past.

**Results:** The low intensity of the white line (WL) and the feature near 18080 eV are indicating dominating plutonyl species in the blank, the supernatant and in the Pu(VI) reference (data not shown). This shoulder above the WL, results from multiple scattering processes of the photo electron wave between Pu and the two axial oxygens. The Pu accumulated by *D. äspöensis* occurs in the tetravalent oxidation state. The characteristic changes in the absorption spectra were used to determine the relative concentrations of the Pu species by applying the iterative transformation factor analysis (FA).



The Pu in the blank is surrounded by two close axial oxygens at 1.77 Å and appr. 5 equatorial oxygens at 2.42 Å (see Fig. 1).

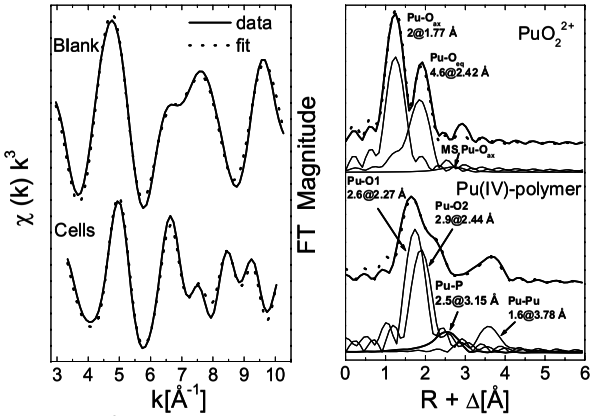


*Fig. 1: Pu $L_{III}$-edge $k^3$-weighted EXAFS spectra (left) and the corresponding Fourier transforms (right) and the theoretical fits (dotted line).*

Unfortunately, we cannot present structural parameter of Pu in the supernatant solution after separating the cells. Changes in the XANES from scan to scan showed that the sample was not stable in the synchrotron beam. The EXAFS oscillation of the cell-bound Pu show close similarities to the spectra of colloidal Pu(IV) species published in /2/. The presence of an additional symmetric EXAFS oscillation giving a FT peak at R+Δ of app. 2.8 Å gives evidence for an interaction of the Pu(IV)-polymers with light atoms of the biomass. The best fit result could be obtained using P which points to an interaction with organic phosphate groups of the cell membrane structure as postulated for Cm(III) in /3/. In conclusion, the XAS investigation of the Pu - *D. äspöensis* system confirmed the results of the solvent extraction experiments /4/. The cell-bound Pu exists as Pu(IV)-polymers which are interacting with the biomass.

**Acknowledgements.** This work is supported by the BMWi (no. 02E9491). We thank Ch. Den Auwer (CEA Marcoule, France) for providing us with the Pu(IV) reference sample.

**Reference**

/1/ Charrin, N. et al. (2000) Radiochim. Acta 88, 25-31.
/2/ Rothe, J. et al. (2004) Inorg. Chem. 43, 4708-4718.
/3/ Moll, H. et al. (2004) Environ. Sci. Technol. 38, 1455-1459.
/4/ Moll, H. et al. (2006) submitted to Radiochimica Acta.

| ROBL-CRG | **Experiment title:** **Spectro-electrochemical cell for in situ XAS measurements of uranium solution species** | **Experiment number:** 20-01-618 |
|---|---|---|
| **Beamline:** BM 20 | **Date of experiment:** between: 04. 05. 2005 and 07. 05. 2005<br>26. 10. 2005 and 30. 10. 2005<br>08. 02. 2006<br>13. 06. 2006 and 17. 06. 2006<br>26. 08. 2006 and 29. 08. 2006<br>17. 12. 2006 | **Date of report:** 15. 12. 2006 |
| **Shifts:** 51 | **Local contact(s):** Christoph Hennig | *Received at ROBL:* 15. 12. 2006 |

**Names and affiliations of applicants** (* indicates experimentalists):

C. Hennig*, K, Schmeide, A. Ikeda,* A. Rossberg*, A. Scheinost*, H. Funke*, A.C. Scheinost*

Forschungszentrum Dresden-Rossendorf e.V., Institute of Radiochemistry, D-01314 Dresden, Germany

**Report:**

In this project we developed and tested a spectro-electrochemical cell, which allows to study the structure and speciation of aqueous actinide complexes *in situ* by x-ray absorption spectroscopy [1,2]. While *in situ* investigations by combining electrochemical cells with XAS are not new, the prevention of gas-release required for safety reasons needed an appropriate counter electrode reaction. We used an Ag metal electrode as counter electrode, where Ag is oxidized during the actinide reduction, $Ag^+$ is released and precipitates with $Cl^-$ from the solution as AgCl. This combination acts as electrode of second kind. The solved $Ag^+$ ions are in equilibrium with solid AgCl and the equilibrium potential of the electrode is given by the solubility constant of the precipitate.

As example we show the EXAFS spectrum of U(IV) sulfate in aqueous solution at pH 1 [2]. The EXAFS spectrum shown here is affected by [2p4f] double-electron excitations, an effect that is more pronounced for actinides in oxidation state III and IV [3]. The shell fit of the U(IV) hydrate shows 9 oxygen atoms at a distance of 2.40 Å. The FT shows two additional peaks 3.08 Å and 3.67 Å indicating approximately two bidentate and two monodentate sulfate groups. We found, that the monodentate coordination generally prevails at low $[SO_4^{2-}]$:[U(IV)] ratios, whereas the bidentate coordination becomes important at higher ones. The analogue solid compound shows only one U-S distance at 3.67±0.02 Å, suggesting a rearrangement of the bonds with predominance of a monodentate linkage between U(IV) and sulfate [2].

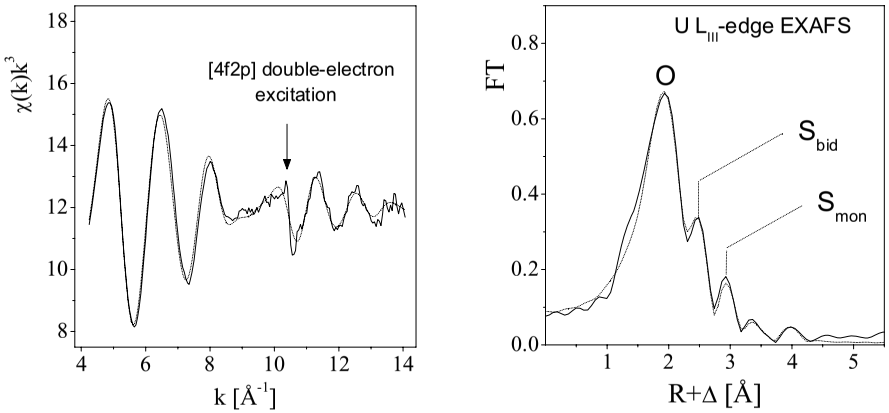


**FIGURE 1.** U $L_3$-edge $k^3$ weighted EXAFS data (left), and the corresponding Fourier transforms (right) of U(IV) sulfato species with 0.05 M $[UO_2^{2+}]$ and 0.4 M $[SO_4^{2-}]$.

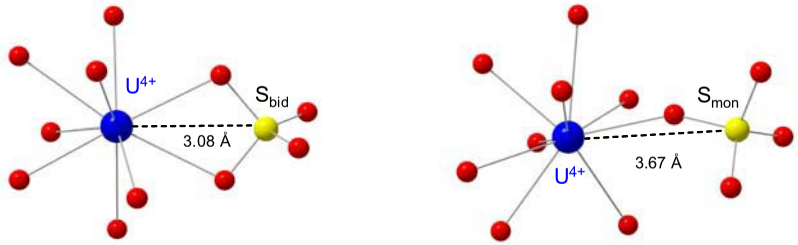


**FIGURE 2.** Structure of $U(SO_4)_{bid}(H_2O)_7^{2+}$ and $U(SO_4)_{mon}(H_2O)_8^{2+}$complexes.

[1] Hennig, C., Tutschku, J., Rossberg, A., Bernhard, G., Scheinost, A.C. Comparative EXAFS investigation of uranium(VI) and –(IV) aquo chloro complexes in solution using a newly developed spectroelectrochemical cell. *Inorganic Chemistry* **44** (2005) 6655

[2] Hennig, C., Schmeide, K., Brendler, V., Moll, H., Tsushima, S., Scheinost, A.C. EXAFS investigation of U(VI), U(IV) and Th(IV) sulfato complexes in aqueous solution. *Inorganic Chemistry*, submitted

[3] Hennig, C. Evidence for double-electron excitations in the $L_3$-edge x-ray absorption spectra of actinides. *Physical Review B* **44** (2007) 035120

| ROBL-CRG | **Experiment title:** **Chemical speciation of metals in shooting-range soils** | **Experiment number:** **20-01-622** |
|---|---|---|
| **Beamline:** BM 20 | **Date of experiment:** 06.07.-10.07.05; 04.04.-08.04.06; 09.09.-12.09.06; 13.09.-15.09.06 | **Date of report:** 11.01.07 |
| **Shifts:** 38 | **Local contact(s):** A. Scheinost, A. Rossberg | *Received at ROBL:* 11.01.07 |

**Names and affiliations of applicants** (* indicates experimentalists):

A. SCHEINOST[1]*, CH. HENNIG[1]*, D. VANTELON[2]*, I. XIFRA[2]*

[1]Institute of Radiochemistry, FZD, Dresden, Germany
[2]Department of Environmental Sciences, ETH Zurich, Switzerland

## Report:

Scheinost, A. C., Rossberg, A., Vantelon, D., Xifra, I., Kretzschmar, R., Funke, H., and Johnson, C. A. (2006). Quantitative antimony speciation in shooting-range soils by EXAFS spectroscopy. *Geochimica et Cosmochimica Acta* **70**, 3299-3312.

**Abstract:** The Sb speciation in soil samples from Swiss shooting ranges was determined using Sb K-edge X-ray Absorption Spectroscopy (XAS) and advanced statistical data analysis methods (Iterative Transformation Factor Analysis, ITFA). The XAS analysis was supported by a spectral data set of 13 Sb minerals and 4 sorption complexes. In spite of a high variability in geology, soil pH (3.1 – 7.5), Sb concentrations (1000 – 17000 mg/kg) and shooting range history, only two Sb species were identified. In the first species, Sb is surrounded solely by other Sb atoms at radial distances of 2.90, 3.35, 4.30 and 4.51 Å, indicative of metallic Sb(0). While part of this Sb(0) may be hosted by unweathered bullet fragments consisting of PbSb alloy, Pb $L_{III}$-edge XAS of the soil with the highest fraction (0.75) of Sb(0) showed no metallic Pb, but only $Pb^{2+}$ bound to soil organic matter. This suggests a preferential oxidation of Pb in the alloy, driven by the higher standard reduction potential of Sb. In the second species, Sb is coordinated to 6 O atoms at a distance of 1.98 Å, indicative of Sb(V). This oxidation state is further supported by an edge energy of 30496-30497 eV for the soil samples with < 10 % Sb(0). Iron atoms at radial distances of 3.10 and 3.56 Å from Sb atoms are in line with edge-sharing and bidentate corner-sharing linkages between $Sb(O,OH)_6$ and $Fe(O,OH)_6$ octahedra. While similar structural units exist in tripuhyite, the absence of Sb neighbors contradicts formation of this Fe antimonate. Hence the second species most likely consists of inner-sphere sorption complexes on Fe oxides, with edge and corner-sharing configuration occurring simultaneously. This pentavalent Sb species was present in all samples, suggesting that it is the prevailing species after weathering of metallic Sb(0) in oxic soils. No indication of Sb(III) was found.

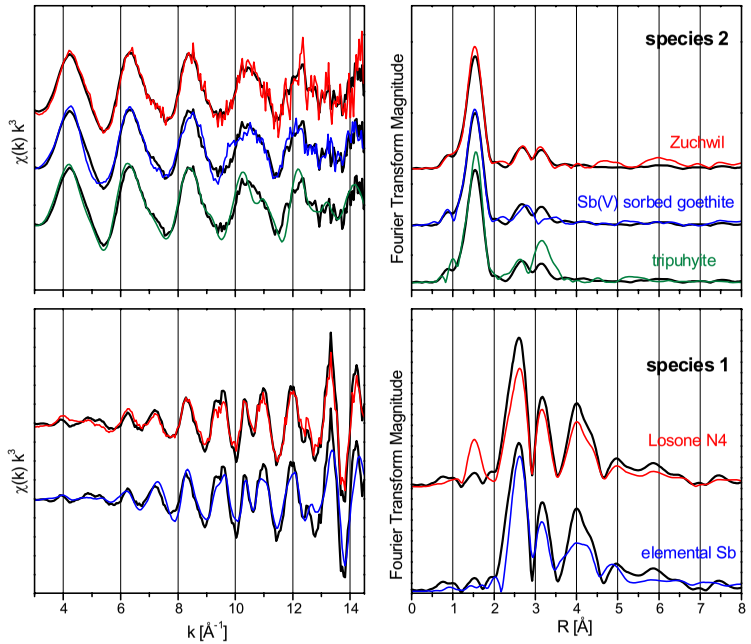


**Fig. 1.** ITFA-derived Sb K-edge EXAFS spectra of the two Sb species in the soil samples (black lines). For comparison are shown the experimental spectra of the soil samples with the largest fraction of the respective species (red), and of selected reference species (blue and .green lines).

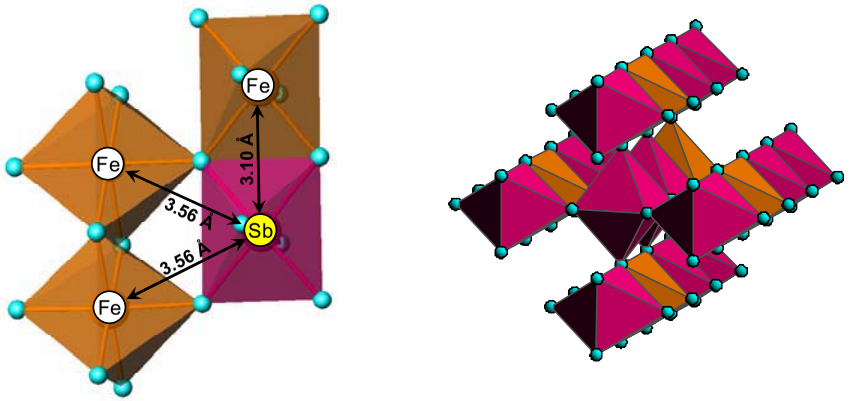


**Fig. 2.** Structural model of species 2 (left) and of tripuhyite, $Fe^{III}Sb^{V}O_4$ (right). Sb octahedra are shown in pink, Fe octahedra in orange.

| ROBL-CRG | **Experiment title:** Speciation of Zn in rhizosphere soil | **Experiment number:** 20-01-624 |
|---|---|---|
| **Beamline:** BM 20 | **Date of experiment:** 13.05.-15.05.06 | **Date of report:** 11.01.07 |
| **Shifts:** 6 | **Local contact(s):** H. Funke | *Received at ROBL:* 11.01.07 |

**Names and affiliations of applicants** (* indicates experimentalists):

A. SCHEINOST[1]*, A. ROSSBERG[1]*, H. FUNKE[1]*, A. VOEGELIN[2]*, S. PFISTER[2]*

[1]Institute of Radiochemistry, FZD, Dresden, Germany
[2]Department of Environmental Sciences, ETH Zurich, Switzerland

## Report:

Layered double hydroxides (LDH) are a group of minerals (hydrotalcites) and synthetic solids. They consist of layers of edge-sharing metal hydroxide octahedra hosting divalent metal cations like, $Ni^{2+}$, $Zn^{2+}$, $Co^{2+}$ and $Cr^{2+}$. In up to 1/3 of the cationic centers, the divalent cations are replaced by $Al^{3+}$ [1,2]. The resulting net positive charge of the hydroxide sheets is counterbalanced by hydrated anions in the aqueous interlayers, responsible for the anion exchange properties.

In comparison with simple metal hydroxides, LDH phases have a significantly lower solubility at relevant geochemical conditions. Therefore, formation of such phases plays an important role in reducing the toxicity of metals and radionuclides in e.g., soils, sediments and nuclear waste repositories [3].

Voegelin et al. examined the solubility of pure Zn and Ni LDHs as well as of mixed Zn-Ni LDH phases in column experiments under acidic conditions [4]. When only Zn was present, 95% of the retained Zn was leached at pH 3. In contrast, only 23% of the retained Ni was leached in experiments with Ni alone. When both Zn and Ni were present, 90% of the retained Zn and 87% of the retained Ni were released. EXAFS analysis performed at room temperature revealed that the LDH phases in the Zn experiment had been completely dissolved, while the LDH phase formed in the Ni experiment was still present. The intention of our study was to investigate whether or not differences in the short-range structure are responsible for these differences in solubility.

**EXPERIMENTAL.** Three samples were prepared: 1) pure $Zn^{2+}$ LDH with 1/3 $Al^{3+}$ inclusion, 2) pure $Ni^{2+}$ LDH with 1/3 $Al^{3+}$ inclusion, 3) mixed LDH with 1/3 $Zn^{2+}$, 1/3 $Ni^{2+}$, 1/3 $Al^{3+}$. The Zn and Ni K-edge spectra were collected in transmission mode at 20 K using a closed-cycle He cryostat.

**RESULTS.** The measured EXAFS spectra had a much lower noise than previously published LDH spectra due to the reduction of the thermal components of the Debye Waller factor (Fig. 2). For the pure ZnAl and NiAl LDH the difference of metal distances is in line with the ionic radii of $Zn^{2+}$ (0.74 Å) and $Ni^{2+}$ (0.69 Å) (Table 1). For the mixed ZnNiAl LDH the coordination distances around Ni and around Zn are again in line with the respective ionic radii. The metal shell distances, however, are intermediate between those of pure NiAl and ZnAl LDH, suggesting an even distribution of Ni and Zn in the hydroxide layers and the absence of a significant clustering of ZnAl hydroxide or NiAl hydroxide regions (Fig. 1). The Al backscattering atoms fitted for the first metal shell are confirmed by the Morlet waverlet method [5]. Using the refined FEFF-Morlet method [6], we could also confirm that Al atoms are present in the third metal shell (≈6.2 Å), but not in the second metal shell (≈5.2 Å), suggesting an even, charge-balanced distribution of $Al^{3+}$ in the mixed-metal hydroxide layers for all investigated LDH phases.

**CONCLUSIONS.** All structures revealed an even distribution of 3d-metals and Al. No significant structural differences were found between the binary Ni-Al and Zn-Al LDH on one hand, and ternary Zn/Ni-Al LDH on the other hand. Hence, the differences in solubility are not caused by structural differences.

## REFERENCES

[1] M. Bellotto et al., *Phys. Chem.*, **100**, 8527 (1996).
[2] J. B. d'Espinose de la Caillerie et al., *Amer. Chem. Soc.*, 117, 11471 (1995).
[3] A. Voegelin, et al. *Env. Sci. Technol.* **36**, 3749 (2002).
[4] A. Voegelin et al., *Env. Sci. Technol.* **39**, 5311 (2005).
[5] H. Funke et al., *Phys. Rev B*, **71**, 094110 (2005).
[6] H. Funke et al., (2005) *Report FZR-443*, p. 63.

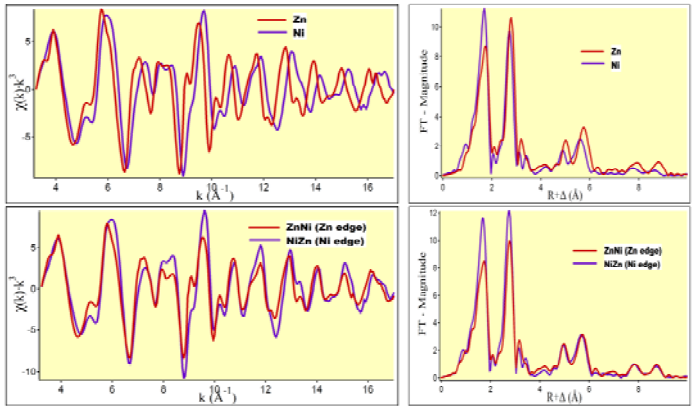


**Fig. 1.** EXAFS spectra and corresponding Fourier transform of the pure Zn-Al and Ni-Al LDH (above) and of the mixed ZnNi-Al LDH (below) measured at Zn-K and Ni-K edges, respectively.

**Table 1. EXAFS fit result of ZnAl LDH, NiAl LDH, and a mixed ZnNiAl LDH phase.**

| Sample | Edge | O | | | 1st metal | | | 1st Al | | | 2nd metal | | | 3rd metal + MS | | |
|---|---|---|---|---|---|---|---|---|---|---|---|---|---|---|---|---|
| | | CN | R | $\sigma^2$ | CN | R | $\sigma^2$ | CN | R | $\sigma^2$ | CN | R | $\sigma^2$ | CN | R | $\sigma^2$ |
| Zn | Zn | 6.0 | 2.08 | 0.0072 | 3.6 | 3.07 | 0.0048 | 2.8 | 3.06 | 0.0036 | 4.6 | 5.32 | 0.0062 | 12.8 | 6.21 | 0.0095 |
| ZnNi | Zn | 5.7 | 2.08 | 0.0070 | 3.1 | 3.05 | 0.0050 | 1.9 | 3.03 | 0.0023 | 4.9 | 5.30 | 0.0063 | 11.5 | 6.18 | 0.0093 |
| ZnNi | Ni | 5.7 | 2.05 | 0.0042 | 5.4 | 3.07 | 0.0040 | 3.9 | 3.11 | 0.0028 | 2.2 | 5.29 | 0.0027 | 9.4 | 6.15 | 0.0083 |
| Ni | Ni | 5.6 | 2.05 | 0.0045 | 1.6 | 3.04 | 0.0027 | 1.0 | 2.91 | 0.0020 | 1.9 | 5.23 | 0.0036 | 8.4 | 6.10 | 0.0092 |

| ROBL-CRG | **Experiment title:** **Interaction between microorganisms and metals using bacteria** | **Experiment number:** 20-01-625 |
|---|---|---|
| **Beamline:** BM 20 | **Date of experiment:** 04.03.-05.03.05; 03.12.-06.12.05; 24.07.-26.07.06 | **Date of report:** 12.01.07 |
| **Shifts:** 18 | **Local contact(s):** Dr. Andreas Scheinost | *Received at ROBL:* |
| **Names and affiliations of applicants** (* indicates experimentalists): M. Merroun*, K. Pollmann, J. Raff, A. Scheinost*, A. Rossberg*, C. Hennig*, H. Funke*, S. Selenska-Pobell | | |

**Report**: The S-layer of *Bacillus sphaericus* strain JG-A12, isolated from a uranium-mining site, exhibits a high metal-binding capacity, indicating that it may provide a protective function by preventing the cellular uptake of heavy metals and radionuclides. This property has allowed the use of this and other S-layers as self-assembling organic templates for the synthesis of nano-sized heavy metal cluster arrays /1, 2/. However, little is known about the molecular basis of the metal protein interactions and their impact on secondary structure. In this work, X-ray absorption spectroscopy was used to determine the structural parameters of the Pd complexes formed by this S-layer protein.

**Experimental***:* For sorption of Pd(II), the protein was dialysed against $H_2O$ and 10 mg of it were incubated in 100 ml of a solution of 2 mM $Na_2PdCl_4$ (pH = 3.1), which was prepared 24 h before the use and kept in dark. After 3 hours of incubation at room temperature under shaking in the darkness the sample was centrifuged and the pellet was resuspended in $H_2O$. Residual salts were removed by dialysis of the metallised proteins against $H_2O$. For XAS analysis, the protein samples were dried in a vacuum oven (48 h, 80°C) and pulverised.

**Results:** Figure 1 shows the XANES regions of the XAS spectrum obtained with the Pd(II)-bound S-layer from strain JG-A12 and for reference compounds containing two oxidation states of palladium: Pd(II) (PdO, $[Pd(NH_3)_4]Cl_2$, $PdCl_2$, $Na_2PdCl_4$) and metallic Pd (0.025 mm thick palladium foil). Comparison of the experimental spectrum to the reference spectra clearly shows that Pd is present as $Pd^{(II)}$ in the Pd-loaded S-layer protein sample because the two absorption maxima (ca. 24360 and ca. 24380 eV) characteristics of metallic Pd (feature a, Fig. 1) are absent. The fine structure of XANES of the Pd-loaded S-layer resembles that of $[Pd(NH_3)_4]Cl_2$ and PdO, indicating that Pd-O and Pd-N bonds contribute to the metal protein binding.

The Pd K-edge EXAFS spectrum of the palladium species formed on S-layer protein from *B. sphaericus* strain JG-A12 and its corresponding FT are shown in Fig. 2. The data exhibit an excellent signal-to-noise ratio allowing the analysis up to 15 $Å^{-1}$. Four peaks are found at bond distances of 2.01, 2.49, 3.02 and 3.41 Å corresponding to Pd-O, Pd-O, Pd-Pd and Pd-Pd bonds, respectively. The distances were identified using Pd-O and Pd-Pd backscattering phase and amplitude functions obtained from atomic coordinates of PdO using the FEFF 8 programme. The first shell can be fitted to about 3-4 oxygen atoms at a distance of 2.01 Å. EXAFS analysis indicated the presence of an additional shell at distance of 2.49 Å which was not found in the PdO (used as model for the EXAFS fit). This shell may be due to a side-lobe peak, originating from a truncation effect due to the limited reciprocal space integrated in the Fourier transform (model a) or may have a structural origin (model b). Therefore, the origin of the peak at 2.49 Å cannot be clarified. However, the data interpretation is not impeded by this ambiguity, because there are also no significant differences between the structural parameters of the S-layer bound Pd complexes determined with either model.

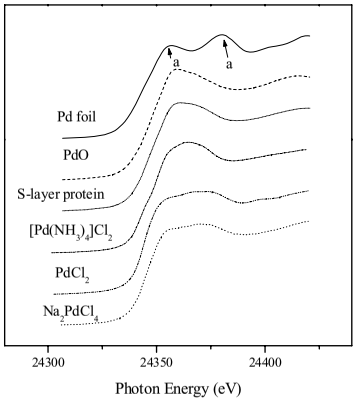


**Fig. 1**: Pd K-edge XANES region of EXAFS spectra of Pd-loaded S-layer protein of *B. sphaericus* JG-A12 and reference compounds.

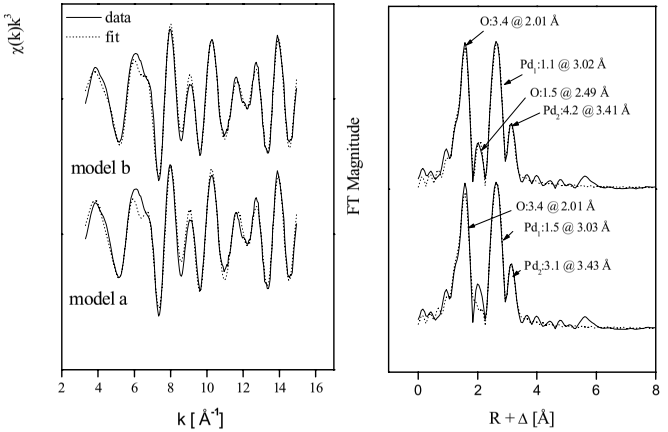


**Fig. 2**: Pd K-edge $k^3$–weighted EXAFS spectra (left) and the corresponding FT (right) of the Pd complexes formed by S-layer of *B. sphaericus* JG-A12.

**ACKNOWLEDGEMENTS**. This study was supported by the Deutsche Forschungsgemeinschaft (DFG, Bonn, Germany) grant SE 671/7-2, by the Ministry of Saxonia (Dresden, Germany) grant 7531.50-03.0370-01, and by the European Community (EC, Bruxelles, Belgium) grand GRD1-413 2001-40424.

**REFERENCES**

[1] Pollmann *et al.* (2006) *Lett. Appl. Microbiol.* **43**, 39-45.
[2] Fahmy *et al*. (2006) *Biophys. J.* **91**, 996-1007.

| ROBL-CRG | **Experiment title:** **Oxidation state and local structure of uranium in soils and sediments** | **Experiment number:** 20-01-626 |
|---|---|---|
| **Beamline:** BM 20 | **Date of experiment:** 12.03.-15.03.05; 10.07.-12.07.05; 05.11.-07.11.05; 25.11.-26.11.05 15.09.-19.09.06; 17.06.-19.06.06 19.07.-20.07.06 | **Date of report:** 11.01.07 |
| **Shifts:** 50 | **Local contact(s):** **A. Scheinost, H. Funke** | *Received at ROBL:* 11.01.07 |

**Names and affiliations of applicants** (* indicates experimentalists):

A. SCHEINOST*

Institute of Radiochemistry, FZD, Dresden, Germany

## Report:

Scheinost, A. C., Hennig, C., Somogyi, A., Martinez-Criado, G., and Knappik, R. (2006). Uranium speciation in two Freital mine tailing samples: EXAFS, micro-XRD, and micro-XRF results. *In* "Uranium in the Environment: Mining Impact and Consequences" (B. J. Merkel and A. Hasche-Berger, eds.), pp. 117-126. Springer Verlag, Berlin.

## Abstract

Risk assessments of actinide-contaminated soils and sediments require detailed knowledge of actinide speciation and its long-term kinetics. Former Saxonian mine tailings, which have been covered but else left undisturbed, are ideally suited to study changes in uranium speciation over timescales of decades. We investigated the major uranium species in two samples from buried mine tailings using a combination of Synchrotron-based microfocus-techniques (μ-XRF, μ-XRD with micrometer resolution), bulk EXAFS spectroscopy, and chemical extractions.

In sample F1 (5 m depth, oxic, pH 8, U=440 mg/kg, high Ca, S, Pb, Cu, Zn concentrations), uranium is diffusely distributed among aggregates of layer silicates (muscovite, illite and kaolinite). The chemical extractions and EXAFS results confirm that uranium is sorbed to these minerals, but is not incorporated into their crystal structure. Sorption is also in line with the high pH and low carbonate concentrations in pore water. In sample F3 (12 m depth, oxic, pH 4, U=430 mg/kg), the combination of μ-XRF and μ-XRD enabled us to identify several U(IV) and U(VI) containing minerals like coffinite, uraninite, uranyl hydroxide, and vanuralite. Only a minor part of U is sorbed to layer silicates as confirmed by chemical extractions and EXAFS spectroscopy.

At smaller depth (F1, 5 m), sulfuric acid from the ore extraction procedure was completely neutralized by the construction waste used as cover material, resulting in precipitation of jarosite and gypsum.

Even 30 years after the ore extraction, uranium remains highly soluble. At greater depth (F3, 12 m), the low pH from ore extraction was conserved. The presence of U(IV) minerals suggest either precipitation of secondary (IV) minerals due to microbial redox activity, or incomplete dissolution of primary (IV) minerals due to ore processing inefficiency of these older sediments. The U(IV) minerals were recalcitrant during chemical extractions, suggesting low uranium solubility even at oxic redox conditions. The results demonstrate a very high variability of uranium speciation and hence potential mobility, which seems to depend on geochemical parameters and site history, but shows little influence of time.

Another task addressed during the most recent runs was to determine the redox situation along a depth profile of the tailings. For this, the oxidation states of U was compared with that of associated elements, i.e. Fe and As, by Iterative Transformation Factor Analysis (ITFA) of XANES spectra (Fig. 1). These results were further complimented by S oxidation mapping using the STXM at ID-21 (CH-1779). All investigated redox-sensitive elements suggest a maximum of reducing conditions at 7 m depth, while both the shallower and the deeper samples are more oxic (Fig. 2). The first 3 samples suggest a closer association of U with S than with Fe and As.

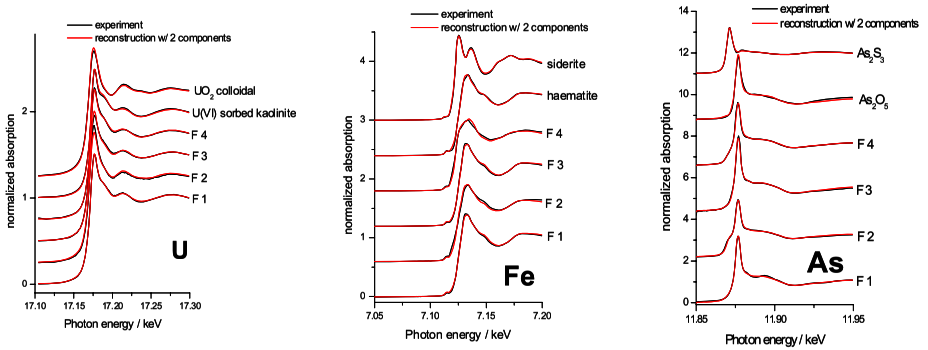


**Fig. 1.** U-$L_3$, Fe-K and As-K edge XANES spectra along the tailings depth profile (F1 to F4) (black lines). The reconstruction by 2 principal components of the tailings samples and of selected references is shown in red.

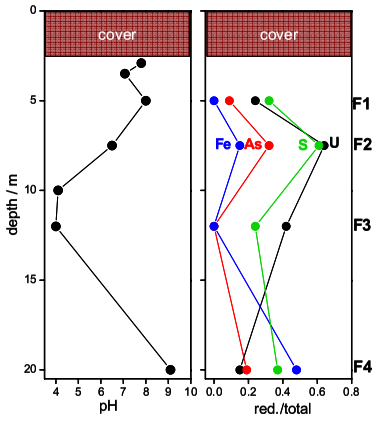


**Fig. 2.** pH and redox profile of the Freital uranium tailings. The ratios of U(IV)/U(VI), Fe(II)/Fe(III), and As(III)/As(V) have been derived from the sets of spectra (Fig. 1) by ITT using the ITFA program package {Rossberg, 2003 #4}. The ratio of Se(-II)/S(VI) has been determined by experiment CH 1779 (see there).

| ROBL-CRG | **Experiment title:**<br>**Uranium sorption onto natural iron colloids in mine waters** | **Experiment number:**<br>**20-01-632** |
|---|---|---|
| **Beamline:**<br>BM 20 | **Date of experiment:**<br>28.04.2005<br>from: 03.11.2005 to: 05.11.2005 | **Date of report:**<br>08.03.2006 |
| **Shifts:**<br>12 | **Local contact(s):**<br>A. Rossberg | *Received at ROBL:* |


**Names and affiliations of applicants** (* indicates experimentalists):

Dr. Kai-Uwe Ulrich[1]*
Dr. André Rossberg[1,2]*
Dr. Andreas Scheinost[1,2]*
Dr. Harald Zänker[1]

[1] Forschungszentrum Dresden - Rossendorf e.V., Institute of Radiochemistry, B.P. 510119, D-01314 Dresden, Germany
[2] ROBL-CRG at the ESRF, B.P. 220, F-38043 Grenoble Cedex, France


## Report:

We applied Fe K-edge EXAFS spectroscopy to elucidate the molecular structure of ferrihydrite contributing by ~65% to colloids of an abandoned uranium mine (# M2) [1]. Ferrihydrite reference samples were prepared in a $N_2$ flushed glove box ($p_{CO2}$ <0.2 Pa) both in the absence (# $FhN_2$) and in the presence of 50 µM $UO_2(NO_3)_2$ (# $FhUN_2$) by rising the pH of a 1 mM $Fe(NO_3)_3 \cdot 9H_2O$ solution with NaOH up to 5.5. EXAFS spectra of the frozen pastes were collected in transmission mode using a He cryostat (30 K).

## Results.

The first peak of the Fourier transform (FT) corresponds to five or six oxygen atoms coordinated to the absorbing Fe atom by two different atomic distances ($R$) (Fig. 1a). Up to three O-atoms were found to be coordinated with $R_{Fe\text{-}O1}$ ~1.94 Å and $R_{Fe\text{-}O2}$ ~2.06 Å, respectively. The second FT peak fits to three Fe-Fe shells with $R_{Fe\text{-}Fe1}$ = 2.89-2.96 Å, $R_{Fe\text{-}Fe2}$ ~3.07 Å, and $R_{Fe\text{-}Fe3}$ = 3.37-3.45 Å. Including a forth Fe shell with $R_{Fe\text{-}Fe4}$ = 3.92-4.00 Å improved the fit of oscillations at higher k values and explained the third FT peak. Neither the EXAFS of sample $FhUN_2$ nor the calculated difference with spectrum $FhN_2$ give evidence on the adsorbed U(VI).

## Discussion.

The splitting of the O-shell into two subshells is due to Fe-O and Fe-OH bonds, confirming the formation of octahedral clusters by deprotonation [2]. Although the Fe-Fe distance of 2.89 Å suggests face sharing octahedra in M2, the structural data do not support hematite, but instead a highly polymerized intermediate stage on the transition from ferrihydrite to hematite [3]. The Fe-$Fe_1$ distance of ~2.95 Å cannot be unequivocally attributed to either face sharing or edge sharing linkage. Therefore, the calculated distances of 3.00±0.07 Å and ~3.45 Å are explained by edge sharing and double-corner sharing linkage, respectively [4]. Two Fe octahedra sharing a single corner exhibit an Fe-Fe distance of 3.92-4.00 Å [5]. The type and number of linkages were combined to a representative basic unit (indicated by dashed circle in Fig. 1b) which consists of six $Fe(O,OH)_6$ octahedra in planar arrangement; four of them are coordinated by edges, and two octahedra are linked to this tetrameric unit by sharing double-corners. Each basic unit representing a section of the homogenous network is linked to two other units of the same type by sharing a single corner (modified from [4]).

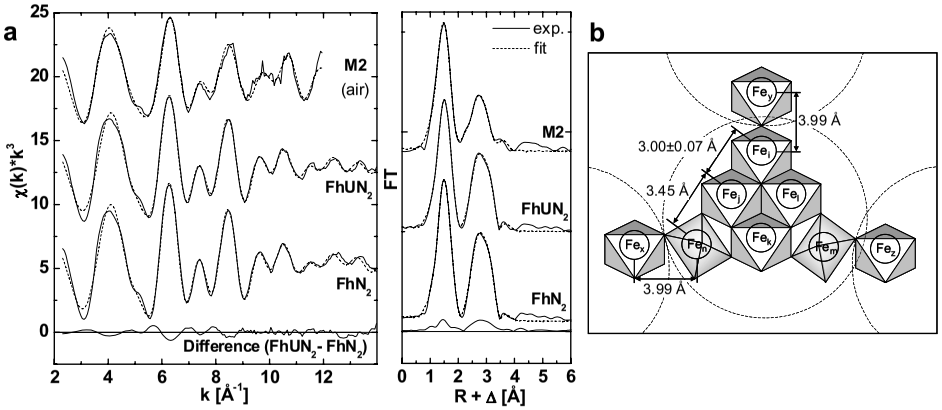


**Fig. 1a.** Fe K-edge EXAFS spectra and FTs of ferrihydrite (M2: mine water colloid sample; $FhUN_2$ and $FhN_2$: samples prepared with and without U(VI) at $p_{CO2}$ < 0.2 Pa). **b.** Molecular topology of ferrihydrite fundamental unit fitting these EXAFS data.

## References


[1] Ulrich K.-U., Rossberg A., Scheinost A.C., Foerstendorf H., Zänker H., Jenk U. (2006) Speciation of colloid-borne uranium by EXAFS and ATR-IR spectroscopy. In: *Uranium in the Environment, Mining Impact and Consequences* (eds. B.J. Merkel and A. Hasche-Berger). Springer Berlin, pp. 137-147.
[2] Combes J.M., Manceau A., Calas G., Bottero J.Y. (1989) *Geochim. Cosmochim. Acta* **53**, 583-594.
[3] Combes J.M., Manceau A., Calas G. (1990) *Geochim. Cosmochim. Acta* **54**, 1083-1091.
[4] Rose J., Manceau A., Masion A., Bottero J.-Y. (1997) *Langmuir* **13**, 3240-3246.
[5] Manceau A., Drits V.A. (1993) *Clay Minerals* **28**, 165-184.

| ROBL-CRG | **Experiment title:** **Uranium sorption onto natural iron colloids in mine waters** | **Experiment number:** **20-01-632** |
|---|---|---|
| **Beamline:** BM 20 | **Date of experiment:** from: 05.02.05 to 07.02.05 and 10.02.2005 | **Date of report:** 08.03.2006 |
| **Shifts:** 12 | **Local contact(s):** A. Rossberg | *Received at ROBL:* |

**Names and affiliations of applicants** (* indicates experimentalists):

Dr. Kai-Uwe Ulrich[1]*
Dr. André Rossberg[1,2]*
Dr. Andreas Scheinost[1,2]*
Dr. Harald Zänker[1]

[1] Forschungszentrum Rossendorf e.V., Institute of Radiochemistry, B.P. 510119, D-01314 Dresden, Germany
[2] ROBL-CRG at the ESRF, B.P. 220, F-38043 Grenoble Cedex, France

## Report:

Previous EXAFS work has shown that U(VI) adsorbs to the surfaces of Fe (hydr)oxides by forming a bidentate, edge sharing complex [1-5]. However, a spectral contribution at 2.4 Å in the Fourier transform (FT) was not explained by this binary complex. Depending on the preparation (ambient air [1,2,5], $CO_2$-free atmosphere [3,4], 0.1 M NaCl [4]) the FT peak is controversially discussed as contribution from C, O or Cl atoms, hence involving a ternary complex structure. We employ Monte Carlo Target Transformation Factor Analysis (MCTFA) [6] to find a fitting 3-D structural model.
Ferrihydrite samples were prepared at ambient atmosphere (#A) and by using $CO_2$-free reagents in a $N_2$-flushed glovebox (#B) to prevent any interaction with carbon. Using NaOH we titrated solutions of 1 mM $Fe(NO_3)_3 \cdot 9H_2O$ and 12 µM $UO_2(NO_3)_2 \cdot 6H_2O$ to pH 5.5 to initiate aggregation of ferrihydrite (96 mg/L) and adsorption/ coprecipitation of $UO_2^{2+}$. The concentrated wet pastes were frozenin liquid $N_2$ before recording fluorescence U $L_{III}$-edge EXAFS spectra with a 13-element germanium detector at 30 K.

## Results:

The difference spectrum between the EXAFS of sample A and B shows no significant spectral contributions (Fig. 1a). Hence inorganic carbon has no influence on the local atomic environment of U(VI) at pH 5.5. Shell fitting identified two axial O-atoms ($O_{ax}$) at ~1.80 Å (FT peak 1), three equatorial O-atoms ($O_{eq}$) at ~2.40 Å and two $O_{eq}$ at 2.30 Å (peak 2), one Fe-atom at 3.39 Å (peak 4). According to the experimental conditions, a contribution of bidentately coordinated carbonate ligands to the peak at 2.4 Å can be excluded in spectrum B. Hence the only possible alternative is an O-atom at a radial distance of 2.86 Å, which improves the fit significantly. Using spectrum B, the Debye-Waller factors from the shell fit, and an Fe octahedron of hematite, we performed MCTFA in order to derive a 3-D model accounting for all shells. The MCTFA fit reproduces the spectrum B up to 4.7 Å (Fig. 1b). It is evident from Fig. 1c that the tilted orientation of the pentagonal bipyramid relative to the edge-shared octahedron is in line with a radial distance of 2.84 Å between the U-atom and the near apical O-atom ($O_{ap1}$), explaining the FT peak at 2.4 Å, and coincides with a radial distance of 4.30 Å to the remote apical O-atom ($O_{ap2}$) and with a U-O distance of 4.70 Å to the two remaining O-atoms of the octahedron. Doubts arise about the very short distance of 1.77 Å between $O_{ax1}$ and $O_{ap1}$, requiring repulsion or other interaction. For instance, distortion of the U(VI) polyhedron would enable a longer distances between $O_{ax1}$ and $O_{ap1}$ and thus the formation of a H-bond. This is subject to further research.

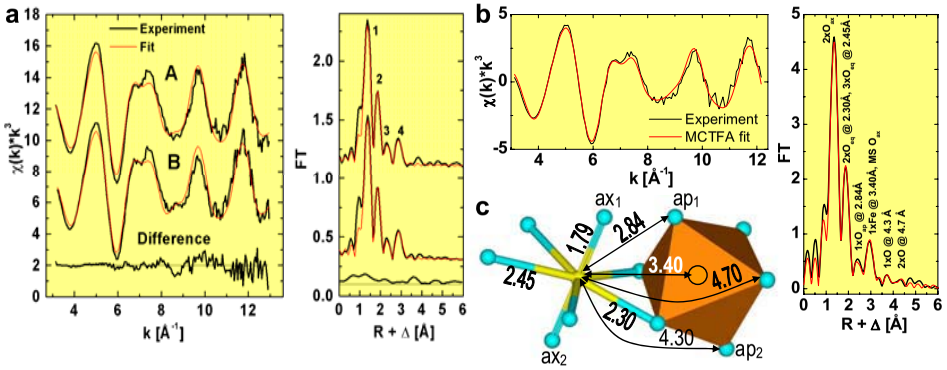


**Fig. 1a.** EXAFS spectra of samples A and B, their difference spectrum (A-B) and FT's. **b.** EXAFS spectrum and FT of sample B, fitted by MCTFA (MS: multiple scattering). **c.** Structure of the U(VI)-$FeO_6$ sorption complex found by MCTFA. Numbers give radial distances in Å, balls in yellow, blue and orange represent atoms of U, O and Fe, respectively.

## References

[1] Waite, T.D. *et al.* (1994) *Geochim. Cosmochim. Acta* **58**, 5465-5478.
[2] Reich, T. *et al.* (1998) *J. Electron Spectrosc. Relat. Phenom.* **96**, 237-243.
[3] Walter, M. *et al.* (2003) *Environ. Sci. Technol.* **37**, 2898-2904.
[4] Redden, G. *et al.* (2001) *J. Coll. and Interface Sci.* **244**, 211-219.
[5] Bargar, J.R. *et al.* (2000) *Geochim. Cosmochim. Acta* **64**, 2737-2749.
[6] Rossberg, A. *et al.* (2005) *Anal. and Bioanal. Chem.* **383**, 56-66.

| ROBL-CRG | **Experiment title:** **Uranium sorption onto natural iron colloids in mine waters** | **Experiment number:** **20-01-632** |
|---|---|---|
| **Beamline:** **BM 20** | **Date of experiment:** from: 06.02.06 to: 08.02.06 and 03.05.06 to: 06.05.06 | **Date of report:** 08.03.2006 |
| **Shifts:** 15 | **Local contact(s):** A. Rossberg | *Received at ROBL:* |


**Names and affiliations of applicants** (* indicates experimentalists):

Dr. André Rossberg[1,2]*
Dr. Andreas Scheinost[1,2]*
Dr. Kai-Uwe Ulrich[3]*

[1] Forschungszentrum Rossendorf e.V., Institute of Radiochemistry, B.P. 510119, D-01314 Dresden, Germany
[2] ROBL-CRG at the ESRF, B.P. 220, F-38043 Grenoble Cedex, France
[3] Department of Environmental Engineering, Washington University, St. Louis, MO 63130-4899, USA


**Report:**

We applied U $L_{III}$-edge EXAFS spectroscopy to elucidate the molecular structure of the aqueous U(VI)-carbonato complexes $UO_2CO_{3aq}$, $UO_2(CO_3)_2^{2-}$ and $(UO_2)_2(CO_3)(OH)_3^-$. The solutions were prepared using aqueous solutions of $UO_2ClO_4$ and $NaHCO_3$ and the pH was adjusted by $HClO_4$ or NaOH. The samples were prepared that most of the attended species is present according speciation calculations. Sample 1 (pH=4.78, $[U]=1\cdot10^{-3}$ M, $[CO_3^{2-}]= 3.4\cdot10^{-2}$ M) contains 73% of $UO_2CO_3$, sample 2 (pH=5.66, $[U]=1\cdot10^{-3}$ M, $[CO_3^{2-}]= 4.3\cdot10^{-2}$ M) contains 51% of $UO_2(CO_3)_2^{2-}$ and sample 3 (pH=7.69, $[U]=5\cdot10^{-3}$ M, $[CO_3^{2-}]= 3.4\cdot10^{-2}$ M) contains 97% of $(UO_2)_2(CO_3)(OH)_3^-$. The U $L_{III}$-edge fluorescent EXAFS spectra of the solutions were collected at room temperature with a 13-element germanium detector.

**Results.** Table 1 contains the structural parameter determined by shell fitting and Figure 1 the corresponding theoretical fits to the experimental spectra.

Table 3: EXAFS structural parameters for sample 1-3.

| Spectrum | Shell | *CN* | *R* [Å] | $\sigma^2$ [Å$^2$] |
|---|---|---|---|---|
| 1 | U=O | 2* | 1.76 | 0.0013 |
| | U-$O_{eq}$ | 4.8 | 2.47 | 0.0065 |
| | U-C | 1.6 | 2.93 | 0.004* |
| | U-$O_{dis}$ | /1.6 | 4.16 | 0.004* |
| | U-U | 1.6 | 3.98 | 0.004* |
| | U-U | 1.1 | 4.32 | 0.004* |
| | U-U | 1.2 | 4.92 | 0.004* |
| 2 | U=O | 2* | 1.78 | 0.0015 |
| | U-$O_{eq}$ | 5.2 | 2.43 | 0.0089 |
| | U-C | 2.1 | 2.91 | 0.003* |
| | U-$O_{dis}$ | /2.1 | 4.17 | 0.0088 |
| 3 | U=O | 2* | 1.78 | 0.0026 |
| | U-$O_{eq1}$ | 3* | 2.21 | 0.0097 |
| | U-$O_{eq1}$ | 3* | 2.41 | 0.0108 |
| | U-U | 1.2 | 3.84 | 0.006* |

CN - Coordination number, R - atomic distance, σ - Debye-Waller factor, $\Delta E_0$ energy shift parameter linked for all paths, * - fixed parameter, / - linked parameter.

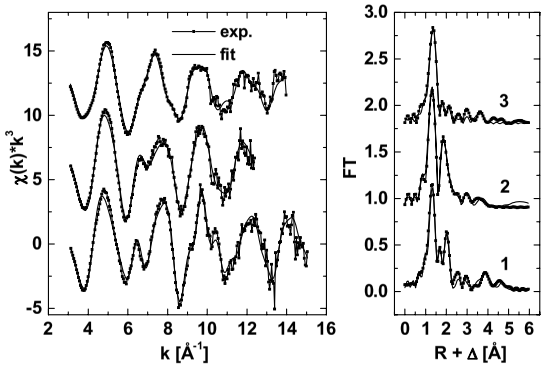


**Figure 1:** U $L_{III}$-edge EXAFS of sample 1-3 and theoretical fit.

In the case of the $UO_2(CO_3)_2^{2-}$ complex (sample 2) we observe two bidentate coordinated $CO_3^{2-}$ groups. The measured U-U interactions for samples 1 (3.98 Å, 4.32 Å) and 3 (3.84 Å) are due to the presence of colloidal rutherfordine and m-schoepite. The spectra helps in the interpretation of U(VI) sorption on ferrihydrite in the presence of $CO_2$.


**Acknowledgement.** This study was done in the framework of the ACTINET Network of Excellence.

| ROBL-CRG | **Experiment title:** **X-ray absorption spectroscopy studies on gold nanoparticles fromed by bacteria and their surface layer proteins** | **Experiment number**: **20-01-638** |
|---|---|---|
| **Beamline**: BM 20 | **Date of experiment**: 05.03.-06.03.05; 29.09.-03.10.06 | **Date of report**: 12.01.07 |
| **Shifts:** 15 | **Local contact(s)**: Dr. André Rossberg | *Received at ROBL:* |
| **Names and affiliations of applicants** (* indicates experimentalists): M. Merroun*, K. Pollmann, A. Rossberg*, A. Scheinost*, C. Hennig*, H. Funke*, S. Selenska-Pobell | | |

**Report**: The fabrication of patterned arrays of nanoparticles whose electronic, optical and magnetic properties will find technological applications, such as ultra-high-density memories, is currently one of the most important objectives of inorganic material research. In this study, the size of the Pt nanoparticles formed on the S-layer proteins of *B. sphaericus* JG-A12 was estimated using a combination of X-ray absorption spectroscopy (XAS) and Iterative Target Test Factor Analysis [1].

**Experimental:** *B. sphaericus* JG-A12 was routinely grown in NB medium. The preparation of S-layer protein was performed as described in [2]. For sorption of Pt(II), 10 mg of dialyzed protein was incubated in 100 ml of a solution of 2 mM $K_2PtCl_4$ overnight at room temperature in the darkness. Pt(II) was reduced by the addition of a few drops of 100 mM DMAB to produce Pt(0)-nanoparticles. The metallized protein samples were centrifuged (20 min, 10000 × g) and dried in a vacuum oven (48 h, 30°C).

**Results**: Figure 1 shows the XANES regions of the EXAFS spectra obtained with Pt-treated S-layer after addition of DMAB and for reference compounds containing three oxidation states of platinum: Pt(II) (solution of 2 mM $K_2PtCl_4$), Pt(IV) and metallic Pt (platinum foil). Comparison of the experimental spectra to the reference spectra clearly shows that Pt is present as metallic Pt and Pt(II) in the Pt-treated S-layer. To determine the relative amounts of Pt(0) and Pt(II) present in the biological sample, we applied Iterative Transformation Factor Analysis. The calculation revealed a mixture of 52% metallic Pt and 48% Pt(II) for the S-layer sample. Pt $L_{III}$-edge EXAFS spectrum of the Pt/S-layers of *B. sphaericus* JG-A12 in presence of DMAB is shown together with Pt foil in Fig. 2. In this sample, Pt is present mainly as metallic phase where the interatomic distances found are comparable with the one of metallic foil. The coordination number (N) is different from the bulk ones, showing the presence of small metal particles. The reduction of the coordination number of the first shell is used to estimate the average particle [3]. The coordination number value of the Pt-Pt found in this work (5.5 ± 0.4) is not the real coordination number of the Pt per nanoparticle. This value corresponds to the coordination number of Pt-Pt per sample. The coordination number of latter bond per nanoparticle is weighted by the atomic percentage of Pt atoms in the metallic phase [3]. It was found that the nanoparticles deposited on the S-layer protein have a mean diameter of about 2.5-3.5 nm. These results are in agreement with those found using synchrotron-based X-ray diffraction studies (v. Borany, personal communication).

Fig. 1.

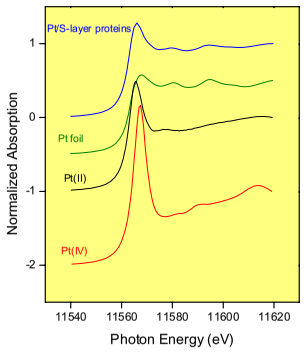


Fig. 2.

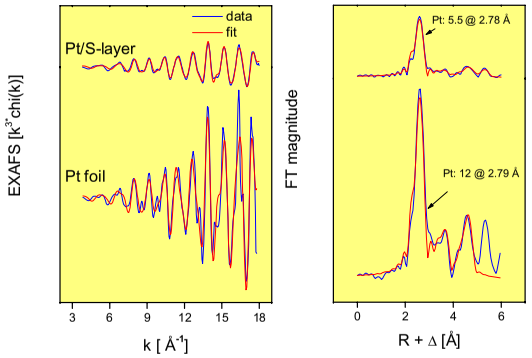


**Fig.1**: XANES region of EXAFS spectra of the Pt $L_{III}$-edge in reference compounds and for Pt-loaded S-layer of *B. sphaericus* JG-A12.

**Fig.2**: Pt $L_{III}$-edge EXAFS spectra and their corresponding fourier transforms of Pt-treated S-layer of *B. sphaericus* JG-A12 and Pt foil.

**ACKNOWLEDGEMENTS.** This work is supported by the EU grant GRD1-2001-00750.

**REFERENCES**

[1] Rossberg, A. *et al.* (2003) *Anal. Bioanal. Chem.* ***376***, 631-638.
[2] Raff, J. (2002) Ph. D. Thesis, FZR-358.
[3] Sun et al. (2006) *Langmuir* **22**, 807-816.

| ROBL-CRG | **Experiment title:** **Investigation of U(VI)/U(V) carbonato complexes in aqueous solution by spectro-electrochemistry** | **Experiment number:** **20-01-639** |
|---|---|---|
| **Beamline:** BM 20 | **Date of experiment:** between: 09.03.2005 and 12.03.2005 10.09.2005 | **Date of report:** 15.12.2006 |
| **Shifts:** 12 | **Local contact(s):** Christoph Hennig | *Received at ROBL:* 15.12.2006 |

**Names and affiliations of applicants** (* indicates experimentalists):
C. Hennig[1]*, A. Ikeda[1]*, G. Palladino[2]*, I. Grenthe[2]

[1]Forschungszentrum Dresden-Rossendorf e.V., Institute of Radiochemistry, D-01314 Dresden, Germany
[2]Royal Institute of Technology, Department of Chemistry, Stockholm, Sweden

**Report:**

U $L_I$- and $L_{III}$-edge XANES spectra for uranyl(VI)- and uranyl(V) tricarbonato complexes are shown in Figures 1 and 2. The fine structure of the absorption edge comprises structures from electron transitions into atom-like orbitals and multiple-scattering features. The $L_{III}$-edge shows a strong resonance (P1) that originates mainly from a dipole-allowed transition of the $2p_{3/2}$ electron to final 6d states. Additional transitions into 8s states are of minor importance. In contrast, the $L_I$-edge reveals a weak resonance related with the $2s \rightarrow 7p$ transition. The difference of the formal charge originates a shift of the absorption edge position.
Several procedures are in use to determine the energy of the absorption edge threshold, $E_0$ [1]. A common reference is the first maximum of the first derivative of the raising edge. It reveals here a chemical shift of -2.2 eV and -0.6 eV between U(VI) and U(V) at the $L_{III}$ and $L_I$ edges, respectively. However, this approximation is not unambiguous, because the edge position is in superposition with discrete resonances.
The multiple scattering (MS) paths in the XANES region of U(VI) were assigned from polarization-dependent measurements. The similarity of the U(V) and the U(VI) spectra allows to indicate the MS paths in analogy to these references. The peak P1 at the $L_I$-edge and the peak P2 at the $L_{III}$-edge arise from multiple scattering with the axial uranyl atoms, the peak P2 at the $L_I$-edge and P3 at the $L_{III}$-edge arise from multiple scattering with the equatorial oxygen or more distant atoms [2]. In general, the MS peaks of the U(V) spectra occur at lower energies than the MS peaks of U(VI). The energy position of the MS peaks are related with the bond lengths R according $\Delta E \sim 1/R^2$, where $\Delta E$ is the difference between the MS resonance and the average potential of the interstitial region $V_0$. It is interesting to note, that due to this energy shift, the MS U-$O_{ax}$ feature in the $L_{III}$-edge spectrum of U(V) is covered by the $2p_{3/2} \rightarrow 6d$ resonance.

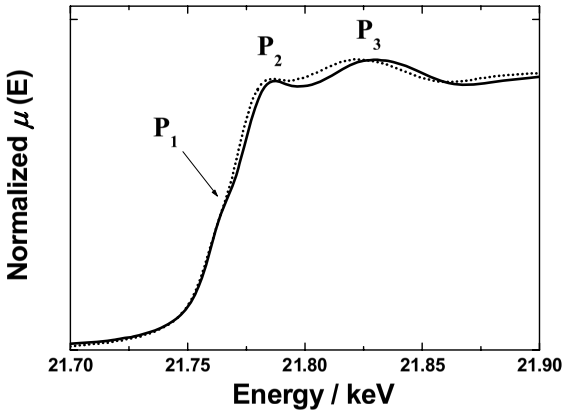


**Figure. 1**
U $L_I$-edge XANES spectra of uranyl(VI)- and uranyl(V) tricarbonato complexes: solid line; uranyl(VI) complex, dotted line; uranyl(V) complex.

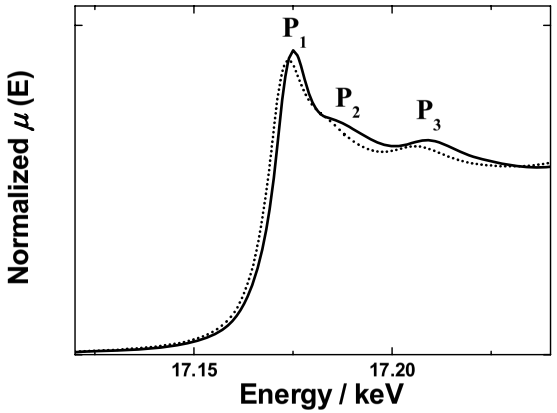


**Figure. 2**
U $L_{III}$-edge XANES spectra of uranyl(VI)- and uranyl(V) tricarbonato complexes: solid line; uranyl(VI) complex, dotted line; uranyl(V) complex.

[1] C. Hennig, Evidence for double-electron excitations in the $L_3$-edge x-ray absorption spectra of actinides, *Phys. Rev. B*, in press.
[2] A. Ikeda, C. Hennig, S. Tsushima, K. Takao, Y. Ikeda, A. C. Scheinost, G. Bernhard, A comparative investigation of U(VI) and U(V) carbonato complexes in aqueous solution, *Inorg. Chem.* submitted.

| ROBL-CRG | **Experiment title:** **Local structure of U(IV) and U(VI) in natural and synthetic minerals** | **Experiment number:** **20-01-642** |
|---|---|---|
| **Beamline:** BM 20 | **Date of experiment:** 11.02.-15.02.05; 29.04.-30.04.05; 20.06.-21.06.05; 28.09.-03.10.05 15.05.-16.05.06 | **Date of report:** 11.01.07 |
| **Shifts:** 36 | **Local contact(s):** H. Funke | *Received at ROBL:* 11.01.07 |

**Names and affiliations of applicants** (* indicates experimentalists):

A. Scheinost*, A. Rossberg*, Ch. Hennig*, H. Funke*, Th. Arnold

Institute of Radiochemistry, FZD, Dresden, Germany

## Report:

Uranium is very immobile in the environment in its tetravalent oxidation state. However, processes like mining and possibly also oxidation of depleted uranium ammunition cause the release of hexavalent uranium (uranyl), which is forming a vast range of aqueous, soluble complexes, and hence regarded as highly mobile. In addition, there is also a large range of relatively poorly soluble minerals containing uranyl, which may also reduce the mobility of uranium in the environment. A recent investigation (Catalano and Brown, 2004; Catalano et al., 2004) demonstrated that these uranyl minerals are difficult to distinguish by EXAFS spectroscopy, since they commonly form layered structures (silicates, vanadates, carbonates, hydroxides, phosphates, etc.). However, this study was based on a relatively limited number of mineral samples, was performed at room temperature and preferential orientation (texture effects) cannot be completely excluded. Hence, we followed up this study using a large range of mineral samples, which Prof. Vochten from Antwerp University and Dr. Massanek from the Mineral Collection of the technical University Freiberg have provided. These samples comprise both synthetic and natural samples. We have used this collection to build a spectral data base for EXAFS speciation of U in environmental samples. Up to now, we have measured 40 samples to measure the samples at both room temperature and 20 K, and to avoid texture effects by using the magic angle geometry. Examples are shown in Figs. 1 and 2. We have also collected XRD, FTIR and TRLFS data of these samples to verify their identity and provide additional chemical and structural information.

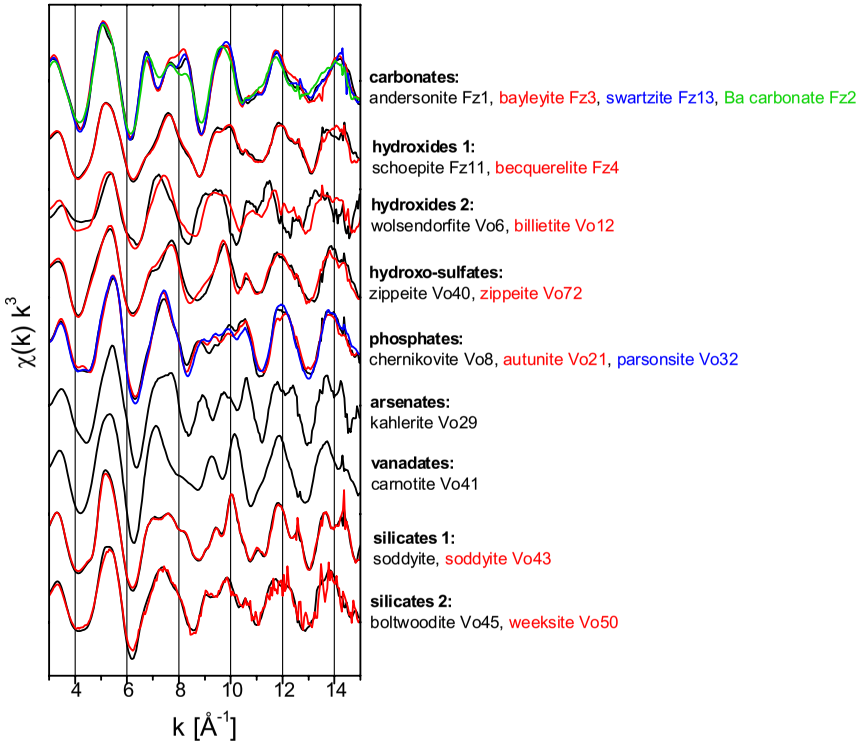


**Fig. 1.**
Comparison of U-$L_3$ EXAFS spectra of different uranyl minerals. The spectra have been measured at room temperature and at the magic angle to avoid orientation effects.

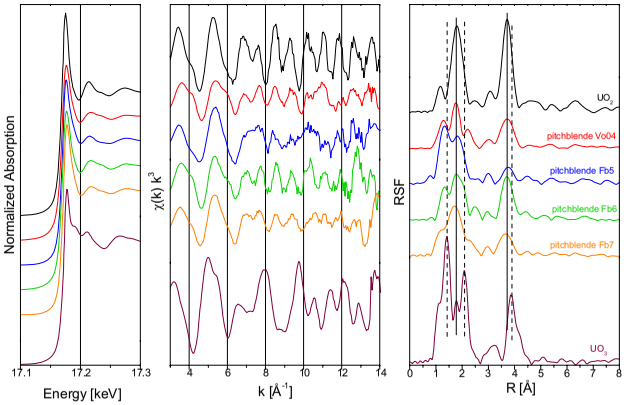


**Fig. 2.**
Comparison of U-$L_3$ EXAFS spectra of natural pitchblende samples in comparison to a freshly precipitated $UO_2$ and to $UO_3$. The spectra have been measured at room temperature and at the magic angle to avoid orientation effects.

| | Experiment title: Determination of the structure of uranium(IV) chloro-complexes highly coordinated in room temperature ionic liquids by EXAFS and XANES measurements | Experiment number: 20-01-643 |
|---|---|---|
| **Beamline:** BM 20 | **Date of experiment:** from: 11.09.2005 to: 13.09.2005 | **Date of report:** |
| **Shifts:6** | **Local contact(s):** Ch. Hennig | *Received at ESRF:* |


**Names and affiliations of applicants** (* indicates experimentalists):

Claire Le Naour*, Didier Trubert*, Celine Cannes,

CNRS/IN2P3/UPS Institut de Physique Nucléaire91406 Orsay Cedex, France

Serguei Nikitenko*, Mikhail Grigor iev

Phsical chemistry Institute, Moscow, (Russia)

Christoph Hennig*

ESRF, ROBL - Forschungszentrum Dresden-Rossendorf, 38000 Grenoble, France

Philippe Moisy

CEA/Valrhô, DEN/DRCP/SCPS, 30207 Bagnols sur Ceze Cedex, France


## Report:

The ionic liquid chosen was: 1-butyl-3-methyl-imidazolium bis(trifluoromethylsulfonyl)imide (there after called [Bumim][$Tf_2N$]). Uranium(IV) hexa-chloro-complexes are introduced under [Bumim]$_2$[$UCl_6$] form. Addition of Chloride is achieved by [Bumim][Cl].
Three liquid samples containing 20mM Uranium in [Bumim][$Tf_2N$] and two solid samples used as reference compound were analysed.

| | |
|---|---|
| **IL_01** | $UCl_6(Bumim)_2$ (pellet in boron nitride ) |
| **IL_02** | $UCl_6(Cs)_2$ (pellet in boron nitride) |
| **IL_03** | $UCl_6(Bumim)_2$ in $BumimTf_2N$ |
| **IL_04** | $UCl_6(Bumim)_2$ in $BumimTf_2N$ + 0.05M Bumin Cl |
| **IL-05** | $UCl_6(Bumim)_2$ in $BumimTf_2N$ + 1M Bumin Cl |

Uranium $L_{III}$-edge EXAFS spectra were collected at the Rossendorf Beamline[1] at the ESRF (6.0 GeV, 200 mA). The measurements were carried out in transmission mode using argon-filled ionization chambers at ambient temperature and pressure. The measurements were performed using a double crystal Si (111) monochromator. Data were collected in equidistant $k$-steps of 0.05 Å$^{-1}$ across the EXAFS region. 6 to 10 scans were recorded for each sample and then averaged. A Y metal foil (first inflection point at 17038 eV) was used for energy calibration. The U $L_{III}$ threshold energy, $E_{k=0}$, was defined as 17185 eV. EXAFS data were extracted from the raw absorption spectra by standard methods including a spline approximation for the atomic background using the program EXAFSPAK [2]. Theoretical phase and amplitude functions were calculated with FEFF 8.2 [3]. The scattering path and amplitude functions were calculated using the crystal structure of $UCl_6(bumim)_2$ described here. The amplitude reduction factor, $S_0^2$, was defined as 1.0 in the FEFF calculation and fixed to that value in the data fits.

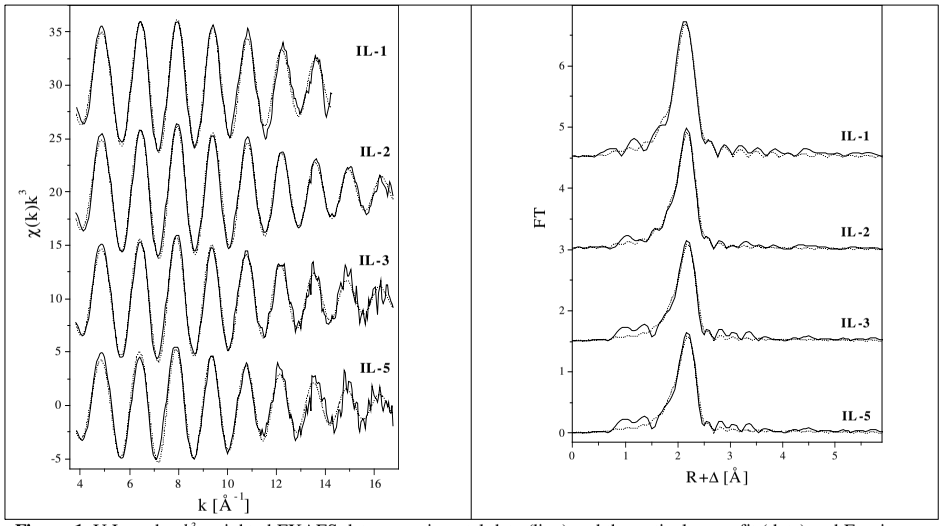


**Figure 1.** U $L_{III}$-edge $k^3$ weighted EXAFS data, experimental data (line) and theoretical curve fit (dots) and Fourier transforms, experimental data (line) and theoretical curve fit (dots).

| sample | $\Delta k$ [Å$^{-1}$] | $N$ | $R$ [Å] | $\sigma^2$ [Å$^2$] | $\Delta E$ [eV] | fit error |
|---|---|---|---|---|---|---|
| IL-1 | 3.8-14.3 | 6.5 | 2.619(2) | 0.0045 | -1.1 | 0.35 |
| IL-2 | 3.8-16.8 | 6.1 | 2.620(1) | 0.0040 | -1.2 | 0.17 |
| IL-3 | 3.8-16.8 | 6.1 | 2.632(2) | 0.0044 | -0.3 | 0.28 |
| IL-5 | 3.8-16.8 | 5.6 | 2.634(2) | 0.0044 | -0.9 | 0.46 |

**Table 1.** Structure parameters obtained from EXAFS shell fit. Errors in distances $R$ are ± 0.01 Å standard deviations for $R$ as estimated by EXAFSPAK are given in brackets, errors in coordination numbers $N$ are ± 15 %, $\sigma$ - Debye-Waller factor.

The bond distances are perfectly identical in all samples, the deviation in coordination numbers are in the typical range of 10-15%. U-Cl distances of both liquids are slightly longer than that of the solids, but the effect is in the error limit and therefore not significant.
Determination of the bond length of $UCl_6$ were achieved for the first time in ionic liquid. However no evidence of highly coordinated complex ($UCl_7$ or $UCl_8$) in concentrated chloride media was demonstrated in the analyzed samples. This could be related to a low concentration of these species in the samples, far out of the range that could be investigated with EXAFS measurements.

Results will be submitted for publication in a near future.


1) Matz, W.; Schell, N.; Bernhard, G.; Prokert, F.; Reich, T.; Claußner, J.; Oehme, W.; Schlenk, R.; Dienel, S.; Funke, H.; Eichhorn, F.; Betzl, M.; Pröhl, D.; Strauch, U.; Hüttig, G.; Krug, H.; Neumann, W.; Brendler, V.; Reichel, P.; Denecke, M.A.; Nitsche, H. *J. Synchrotron Rad.* **1999**, *6*, 1076-1085.
2) George, G. N.; Pickering, I. J. *EXAFSPAK, a suite of computer programs for analysis of X-ray absorption spectra*; Stanford Synchrotron Radiation Laboratory, Stanford, 2000.
3) Ankudinov, A.L.; Ravel, B.; Rehr, J.J.; Conradson, S.D. *Phys. Rev.* **1998**, *B58*, 7565-7576.

| ROBL-CRG | **Experiment title:** **Interaction of actinide cations with metalloprotein** | **Experiment number:** **20-01-644** |
|---|---|---|
| **Beamline:** BM 20 | **Date of experiment:** from: 12.06.2005 to: 14.06.2005 | **Date of report:** 20.02.2006 |
| **Shifts:** 6 | **Local contact(s):** A. Rossberg | *Received at ROBL:* |

**Names and affiliations of applicants** (* indicates experimentalists):

*C. Den Auwer, CEA Marcoule DEN/DRCP/SCPS, 30207 Bagnols sur Cèze

Ph. Moisy, CEA Marcoule DEN/DRCP/SCPS

C. Vidaud, CEA Maroucle DSV/SBTN

## Report:

When tightly bound to protein ligands, metal ions are critical to the function, structure, and stability of proteins, by only allowing specific interactions to take place and/or selective chemistry to occur. Metallobiomolecules are thus considered as elaborated inorganic complexes with well-designed metal active site structures. Although the various interaction processes between the metallic cation and the protein are widely studied in all the fields of biochemistry, focus on the specific actinide family is more seldom [1]. In particular, the knowledge of transportation, fixation and interaction mechanisms of these cations in the biologically active sites are only poorly understood. Plutonium and neptunium have been generated by the industrial nuclear activity. Oxidation state (IV) has been of particular concern for its relative stability in physiological conditions and reactivity similarities with Fe(III). For instance Pu(IV) as well as most of the transition metal cations have been reported to be complexed by transferrin [2-3].
In order to avoid actinide hydrolysis at physiological pH, the Th(IV), Np(IV) and Pu(IV) aquo species were complexed by NTA (nitrilotriacetic acid). Note that U(IV) is unstable under atmospheric conditions and is not included in the series. NTA is an interesting protecting and synergistic anion towards transferrin uptake that has been used in the complex of known crystal structure TfFe(III)NTA [4].

In a first step, the 1:2 complexes of An:NTA (An = Th, Np, Pu at oxidation state IV) have been investigated combining spectrophotometry and EXAFS data. These results are currently being correlated to quantum chemical calculations (manuscript in preparation including the spectrophotometric data). In all cases, the NTA ligand is tetradentate with 3 coordinating carboxylate functions and one nitrogen atom. The overall coordination number is 8. An additional water molecule may enter the first coordination sphere (most probably for the larger actinide cation, i.e. Th(IV)) but no definite conclusion can be drawn from the EXAFS data. Figure 1 summarizes the interatomic distances obtained from the EXAFS data fitting and compared to preliminary quantum chemical calculations (ADF-Zora).

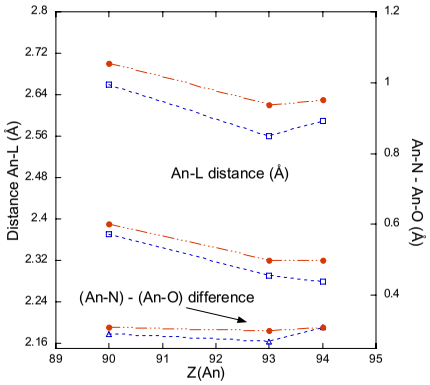


Figure 1 : An-N (top graph) and An-O (middle graph) distances obtained from EXAFS data (λ-λ-λ-λ) and quantum chemical calculations (□-□-□-). The difference between these two distances is reported in the bottom graph from EXAFS data (λ-λ-λ-λ) and quantum chemical calculations (△-△-△-).

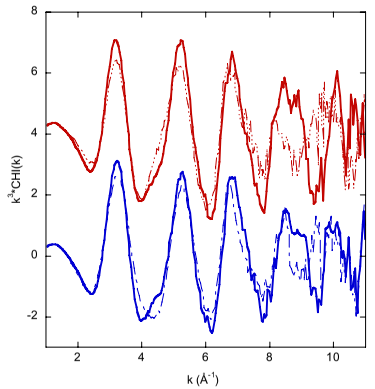


Figure 2 : EXAFS LIII edge of 1:2 An:NTA (____) and 2:1 An:NTA:Tf (-------). An = Np(IV) (top set) and Pu(IV) (bottom set)

Although the calculation is always c.a. 0.03 Å shorter than the EXAFS data, both methods agree well on the distance difference between oxygen and nitrogen ligation.
In a second step, the Np(IV) and Pu(IV) transferrin complexes have been investigated with NTA as a protecting/synergistic ligand. A former XAS investigation of the 1/2 Tf:Np(IV) complex lead to a putative coordination pattern including the NTA anion in the iron binding site [5-6]. Such model must be refined by combining the EXAFS data with models obtained from molecular mechanics. Figure 2 compares the EXAFS data at the Np and Pu $L_{III}$ edge of 1:2 An:NTA and 2:1 An:NTA:Tf (An = Np(IV), Pu(IV)).
From a qualitative point of view there is a clear structural modification of the actinide coordination sphere upon uptake by transferrin. Furthermore, this modification is similar for Np and Pu. Simulations are currently undertaken in order to refine the putative Fe site as the preferred actinide binding site.

[1] : Gorden, A. E. V., Xu, J., Raymond, K. N., Durbin P. W.: *Chem. Rev.* **103**, 4207 (2003).
[2] : Harris, W. R.: *Structure and Bonding* (Springer Verlag, Heidelberg) **92**, 121 (1998).
[3] : Taylor, D. M.: *J. Alloys Comp.* **271**, 10 (1998).
[4] : K. Mizutani, H. Yamashita, H. Kurokawa, B. Mikami, M. Hirose : *J. Biol. Chem.* **274**, 10190 (1999).
[5] : I. Llorens, C. Den Auwer, P. Moisy, E. Ansoborlo, C. Vidaud, H. Funke : *FEBS J.* **272**, 1739 (2005).
[6] : C. Den Auwer, I. Llorens, Ph. Moisy, C. Vidaud, F. Goudard, C. Barbot, P. L. Solari, H. Funke : *Radiochim. Acta*, **93**, 699 (2005).

| | Experiment title: Spectroscopic approach of aqueous chemistry of Protactinium(V) | Experiment number: 20-01-645 |
|---|---|---|
| **Beamline:** BM 20 | **Date of experiment:** from: 08.06.2005 to: 12.06.2005 | **Date of report:** |
| **Shifts: 9** | **Local contact(s):** Ch. Hennig | *Received at ESRF:* |


**Names and affiliations of applicants** (* indicates experimentalists):

Claire Le Naour*, Didier Trubert*, Maria Vita Di Giandomenico*

CNRS/IN2P3/UPS Institut de Physique Nucléaire91406 Orsay Cedex, France

Clara Fillaux*, Christophe Den Auwer*, Philippe Moisy

CEA/Valrhô, DEN/DRCP/SCPS, 30207 Bagnols sur Ceze Cedex, France

Christoph Hennig*

ESRF, ROBL - Forschungszentrum Dresden - Rossendorf, 38000 Grenoble, France


## Report:

Protactinium measurements were carried out on the ROBL beam line at ESRF (6.0 GeV at 200 mA) in fluorescence mode, at room temperature with a (111) water cooled monochromator in a channel cut mode and all data were acquired at the Pa $L_{III}$ edge (16733 eV).

XAS measurements were performed on samples **I** and **II** in specific 600 µL cells for radioactive samples : Sample **I** 10 mM Pa(V) in $H_2SO_4$ 13M and sample **II** 10 mM Pa(V) in HF 0.5 M.

Data fitting was carried out in R space without any prior data filtering with Artemis code. Phases and amplitudes were calculated by Feff8.2 code from crystallographic structures of $Na_{10}[(UO_2)(SO_4)_4](SO_4)_2.3H_2O$ (with Z=92 replaced by Z=91 in the Feff input file).

Figure 1 presents the EXAFS $L_{III}$ edge of samples **I** and **II** (both raw EXAFS spectra and corresponding Fourier transform, FT). FT of sample **I** exhibits a single peak, H, suggesting that only one scatter contributes to the signal. According to the literature[1,2], seven fluoride ligands have been assumed to be in the first coordination sphere. Best fit parameters give the fluoride ligands at 2.16 Å ($\sigma^2$ = 0.0050 Å$^2$) with R factor = 2.6%. The distances obtained by EXAFS agree well with the Pa-F distances in solid state $Na_3PaF_8$ (2.22 Å)[3] and $RbPaF_6$ (2.18 Å)[4]. In the FT spectrum of sample **II**, peak D is clearly attributed to a short Pa-ligand bond. Combining this result with the XANES data and simulation of Figure 1 shows unambiguously that sample **II** exhibits a single short P-O bond in a monooxo form. Peak E contains second sphere O ligands and peak F originates from third sphere S ligands. Adjustment of the raw EXAFS spectrum was carried out according to the general formula $PaO(SO_4)^{bid}_n(SO_4)^{mon}_p$ from n = 0 to 3, p = 0 to 7. Because the coordination number in the equatorial plane of actinyls falls between 4 and 6, the coordination number of Pa-O is estimated between 6 and 7 (2n+p = 6, 7). Fits with only bidentate sulfates or only monodentate sulfates did not reproduce the experimental spectrum. Fits with n = 1, p = 4 or n = 3, p = 1 lead to a bad agreement and the optimum number for n was found to be 2. Within the uncertainty associated to amplitude estimation in EXAFS (and in the absence of experimental model compounds) the fit is more sensitive to number n than to number p because n contributes for 2 oxygen atoms and one sulfur atom. The value of p has then been fixed to 3 but the uncertainty is about ± 1. Best fit structural parameters were obtained with one Pa-O bond at 1.72 Å ($\sigma^2$ = 0.0033 Å$^2$), two bidentate sulfate ligands at 2.41 Å ($\sigma^2$ = 0.0038 Å$^2$) and corresponding S atoms at 3.09 Å ($\sigma^2$ = 0.0012 Å$^2$) and 3 monodentate sulfate ligands at 2.33 Å ($\sigma^2$ = 0.0098 Å$^2$) and corresponding S atoms at 3.73 Å ($\sigma^2$ = 0.0050 Å$^2$). The R factor is equal to 9.0%. Note that peak F is poorly reproduced in the fit (Figure 2b). This is attributed to an amplitude discrepancy between the fit and the experiment since the imaginary parts of the FT are in better agreement. In this scheme, peak G corresponds to multiple scattering contributions from the monodentate sulfate ligands.

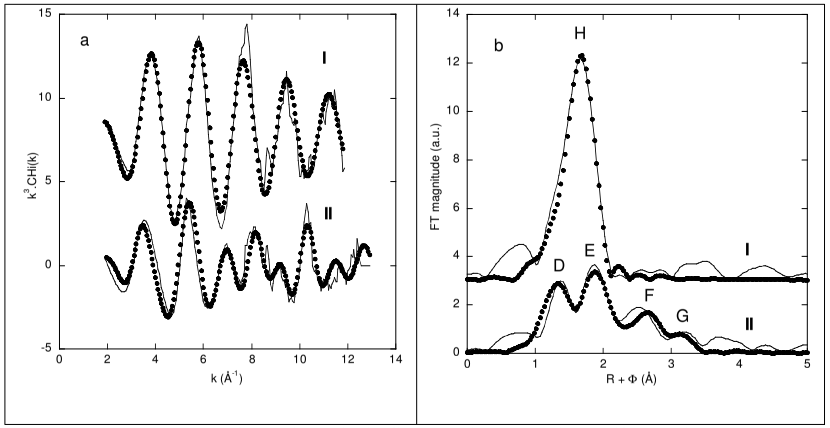


*Fig 1 :$L_{III}$ edge EXAFS spectra of samples I (hydrofluoric solution) and II (sulfuric solution). a) raw EXAFS spectra ——— and fitted curve •••••••• ; b) corresponding Fourier transform (not phase-shift corrected) and fitted curve ••••••••.*

These results indicate unambiguously the presence of an oxo bound in $H_2SO_4$ 13 M medium, as postulated for more dilute media where the species $PaOSO_4^+$ and $PaO(SO_4)_2^{2-}$ have been proposed.[2] Furthermore, the number of mono- and bi-dentate sulfate ligands deduced from EXAFS agrees with one of the formulations of the oxo-trisulfato- protactinate (V) proposed by Bagnall *et al.*.[5]
These results report the first structural characterization in aqueous solution of a Pa-O oxo bond in a Pa(V) sulphato adduct. In contrast, no oxo bond has been found in the Pa(V) fluoro adduct.

Results were submitted and accepted for publication in Inorg. Chem.


These researches are supported by the ACTINET program (work package JRP 02-19), a European network for actinide sciences.



1) R. Guillaumont, G. Bouissières, and R. Muxart, *Actinides Rev.*, 1968, **1**, 135
2) R. Muxart, and R. Guillaumont, Compléments au Nouveau Traité de Chimie Minérale-2-Protactinium, Masson ed, Paris, 1974
3) Brown, D. ; Easey, J.; Rickard, C. E. *J. Chem. Soc. A* **1969**, 1161-1164.
4) Burns, J. H. ; Levy, H. A. ; Keller, O. L. *Acta Cryst.* **1968**, *B24*, 1675-1680.
5) Bagnall, K. W.; Brown, D.; Jones, P. J. *J. Chem. Soc.* **1965**, 27, 176-181.

| | Experiment title: Spectroscopic approach of aqueous chemistry of Protactinium (V) | Experiment number: 20-01-645 |
|---|---|---|
| **Beamline**: BM20 | **Date of experiment**: from: 19.03.06 to: 22.03.06 | **Date of report**: 31.08.2006 |
| **Shifts:** 9 | **Local contact(s)**: A. Rossberg | *Received at ESRF:* |

**Names and affiliations of applicants** (* indicates experimentalists):

**C. Le Naour*, D. Trubert*, M.V. Di Giandomenico*, Institut de Physique Nucléaire Orsay**

**C. Hennig*, ESRF-ROBL, Forschungszentrum Dresden-Rossendorf**

**C. Den Auwer*, C. Fillaux*, A. Jeanson*, P. Moisy, CEA Valrhô**

**Report:**

XAS measurements on Pa samples were carried out on the Rossendorf Beam Line (BM20) at ESRF under dedicated ring conditions (6.0GeV at 200mA). Data were collected in the fluorescence mode with a Si (111) water cooled monochromator used in channel-cut mode. For all Pa samples, data were acquired at the Pa $L_{III}$ edge (16733 eV).

Unlike the other actinides U, Np, Pu that exhibit a linear trans dioxo bond in their higher oxidation states, Pa (V) species in aqueous solution, has been proved to possess one single oxo bond (in concentrated $H_2SO_4$) or no oxo bond in HF 0,5 M (User Report 32757). This experiment was performed with the aim of getting further information about the structure and the coordination of protactinium (V).

Samples prepared in phosphoric and perchloric acids could not be measured because of Pa precipitation. Polymerization of Pa(V) is known to occur with erratic induction time, especially in perchloric media. However the characterization of an aquo species of Pa(V) would assist in future analysis of protactinium complexes with various ligands. Despite these experimental difficulties, we would like to perform new XAS measurements with “fresh” samples by minimizing time between preparation and experiment on ROBL. This time can be reduced to about 10 hours (instead of more than 10 days) by informing in advance the local contact, the EHO and the Radiation Protection Group of ESRF and IPN Orsay.

In dilute HF media ($<10^{-3}$M), mono-oxo-fluorocomplexe(s) is (are) described in the literature, unfortunately at tracer scale ($C_{Pa} < 10^{-10}$M). Only one oxo bond is therefore expected. The XANES spectrum registered during this experiment on the sample of following composition: $10^{-2}$M HF and 6.8 $10^{-3}$ Pa(V), does not exhibit the feature of a linear trans-dioxo bond. However, from our previous results (Pa-O @ 1.72 Å in $H_2SO_4$ and Pa-F @ 2.16 Å in HF 0.5 M), the difference between Pa-oxo and Pa-F distances is expected to be small, leading to an ambiguity with regards to the presence or not of a single oxo bond in these species.

Figure below presents the experimental and fitted Pa $L_{III}$ edge EXAFS spectra of samples in HF $10^{-2}$ (red) and 0.5 M (blue). In HF 0.5 M, best fit parameters have been obtained with 7 fluoride ligands at 2.16(2) Å; this pure fluoride ligation agrees with quantum chemistry calculations, leading to $PaF_7^{2-}$ at 2.18 Å. On the other hand, in dilute HF medium, results of the fit tend to indicate the presence of one oxo bond at 1.71 Å and 7 F(or O) atoms at 2.13(2) Å. However, these results remain ambiguous, due to the too small difference between both distances. New measurements on Pa samples in diluted fluoride media at higher k values than recorded in this experiment could remove this ambiguity.

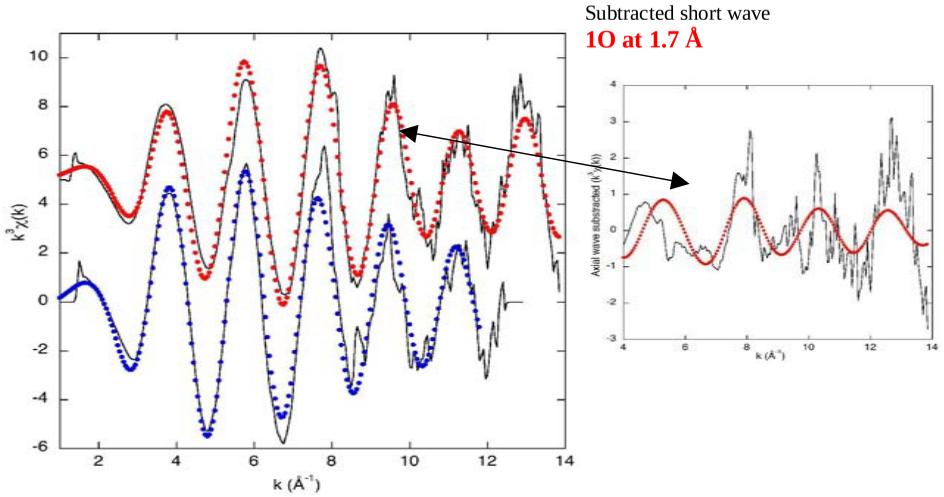

| ROBL-CRG | **Experiment title:**<br>**EXAFS investigation of gradual chloride complexation to the uranyl cation in acetonitrile** | **Experiment number:**<br>**20-01-649** |
|---|---|---|
| **Beamline:**<br>BM 20 | **Date of experiment:**<br>from: 26.11.2005 to: 29.11.2005 | **Date of report:**<br>28.02.2006 |
| **Shifts:**<br>9 | **Local contact(s):**<br>Dr. Christoph Hennig | *Received at ROBL:* |


**Names and affiliations of applicants** (* indicates experimentalists):

Dr. Rik Van Deun — K.U.Leuven
Dr. Linda Fluyt — Chemistry Department
Drs. Kelly Servaes — Molecular Design and Synthesis Division
Coordination Chemistry Group
Celestijnenlaan 200F
3001 Heverlee
Belgium


## Report:

In the course of this experiment, several uranyl samples have been investigated, among which a concentration series of chloride-to-uranyl-complexes. These data are still being interpreted at the moment. Another complex that has been studied is the trinitrato-uranyl-complex. The analysis of the EXAFS-spectrum of this complex has been compared with the UV-vis results that had been obtained in our lab earlier and the total study will be submitted shortly to *Journal of the American Chemical Society*.

## Abstract:


*The complex formation of the uranyl ion $UO_2^{2+}$ with nitrate ions has been studied by UV-Vis and U $L_{III}$ EXAFS spectroscopy both in acetonitrile and in aqueous solution. The investigations point unambiguously to the existence of a $[UO_2(NO_3)_3]^-$ species with $D_{3h}$ coordination symmetry in acetonitrile. The distances in the U(VI) coordination sphere are U-$O_{ax}$ = 1.77 ± 0.01 Å and U-$O_{eq}$ = 2.49 ± 0.01 Å. The U-N distance of 2.94 ± 0.01 Å indicates a bidentate coordination of the $NO_3^-$ group. A structural comparison is made between the uranyl trinitrato complex $[UO_2(NO_3)_3]^-$ and the uranyl tricarbonato complex $[UO_2(CO_3)_3]^{4-}$. No evidence is found for the presence of uranyl nitrato complexes in aqueous solution under moderate conditions (50 mM $UO_2(NO_3)_2 \cdot 6H_2O$, pH 2.4). The UV-Vis spectrum as well as the EXAFS measurements resemble the corresponding spectra of the hydrated free uranyl ion. There are two $O_{ax}$ atoms at 1.77 ± 0.01 Å and five $O_{eq}$ atoms at 2.41 ± 0.01 Å. These values agree well with structural parameters obtained for the $UO_2^{2+}$ aquo ion.*




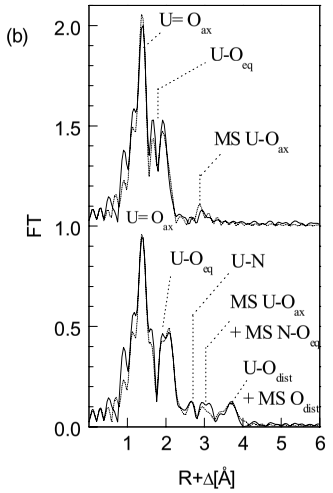


***Figure 1:*** *Fourier transforms of the U $L_{III}$-edge $k^3$-weighted EXAFS data of uranyl nitrate in aqueous solution (top) and $[UO_2(NO_3)_3]^-$ in acetonitrile (bottom); experimental data as line and theoretical curve fit as dots.*

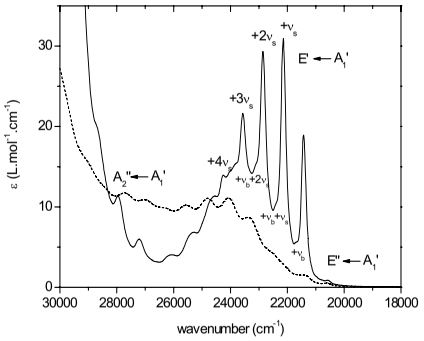


***Figure 2:*** *UV-Vis spectrum of $UO_2(ClO_4)_2 \cdot xH_2O$ (dashed line) and $[UO_2(NO_3)_3]^-$ (solid line) in acetonitrile at room temperature.*

| ROBL-CRG | **Experiment title:** **Structural and magnetic properties of ternary uranates at low temperatures** | **Experiment number:** **20-01-651** |
|---|---|---|
| **Beamline:** BM 20 | **Date of experiment:** from: 03.10.05 to: 07.10.05 | **Date of report:** 18.01.2007 |
| **Shifts:** 12 | **Local contact(s):** A. Scheinost | *Received at ROBL:* 18.01.2007 |

**Names and affiliations of applicants** (* indicates experimentalists):
MILAN J. KONSTANTINOVIC* and SVEN VAN DEN BERGHE
SCK.CEN, Boeretang 200, 2400 Mol, Belgium

## Report:

Soldatov, A.V., Lamoen, D., Konstantinovic, M.J., Berghe, S.V.d., Scheinost, A.C., and Verwerft, M. *Local structure and oxidation state of uranium in some ternary oxides: X-ray absorption analysis* Journal of Solid State Chemistry **180** (2007) 53-60

We investigated the local atomic and electronic structures of two related systematic sets of ternary uranium oxides, $NaUO_3$ - $KUO_3$ - $RbUO_3$ and $BaUO_3$ - $Ba_2U_2O_7$ - $BaUO_4$, by measuring the X-ray absorption near edge structure (XANES). The results are compared with calculations based on self-consistent real space full multiple scattering analysis. We found a very good agreement between measured and calculated spectra, which indicates that the uranium ions are in pure $U^{5+}$ oxidation state in these compounds. The low energy shoulder observed in the U $L_3$ edge XANES is an intrinsic feature of the uranium unoccupied 3d electronic state of the $U^{5+}$ ions. Specific double shoulder features in the higher energy range of the U $L_3$ edge XANES can be interpreted as indicative of the pure cubic perovskite structure.

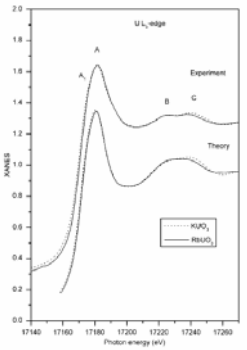


Fig. 1. Comparison of the experimental U $L_3$ edge XANES in $KUO_3$ and $RbUO_3$ with the theoretical spectra.

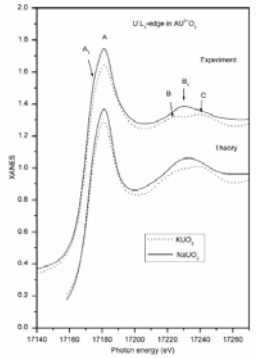


Fig. 2. Comparison of the experimental U $L_3$ edge XANES in $KUO_3$ and $NaUO_3$ with the theoretical spectra.

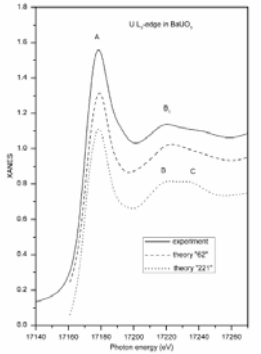


Fig. 3. Comparison of the experimental U $L_3$ edge XANES in $BaUO_3$ with the theoretical spectra. Calculated for two possible structural models (see text).

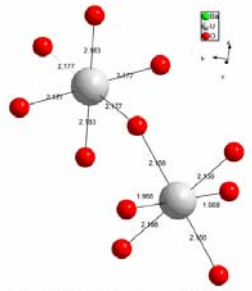

Fig. 4. Local structure around two nonequivalent uranium sites in $Ba_2U_2O_7$.

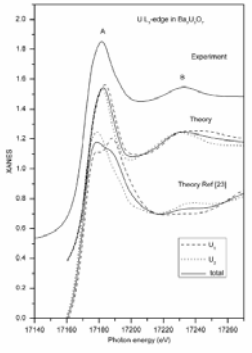


Fig. 5. Comparison of the experimental U $L_3$ edge XANES in $Ba_2U_2O_7$ with the theoretical spectra.

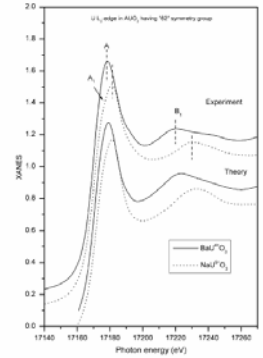


Fig. 6. Comparison of the experimental U $L_3$ edge XANES in $BaUO_3$ and $NaUO_3$ with the theoretical spectra.

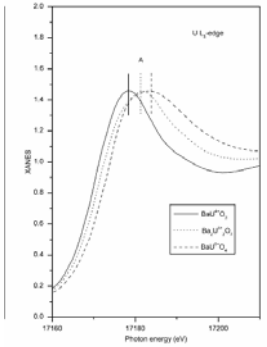


Fig. 7. Comparison of the renormalized (see text) experimental U $L_3$ edge XANES in $BaUO_3$, $Ba_2U_2O_7$ and $BaUO_4$.

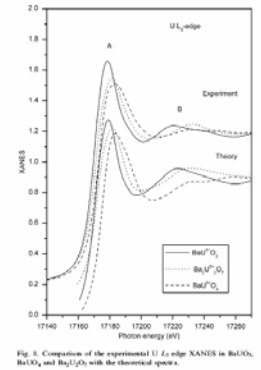


Fig. 8. Comparison of the experimental U $L_3$ edge XANES in $BaUO_3$, $BaUO_4$ and $Ba_2U_2O_7$ with the theoretical spectra.

| ROBL-CRG | **Experiment title:**<br>**Structural and magnetic properties of ternary uranates at low temperatures. Mixed valence effects in $NaV_2O_5$ single crystals.** | **Experiment number**:<br>20-01-651 |
|---|---|---|
| **Beamline**:<br>BM 20 | **Date of experiment**:<br>from: 10.05.2006 to: 13.05.2006 | **Date of report**:<br>09.11.2006 |
| **Shifts:**<br>8 | **Local contact(s)**:<br>Andreas Scheinost | *Received at ROBL:* |
| **Names and affiliations of applicants (* indicates experimentalists):**<br>Milan J. Konstantinovic and Sven Van den Berghe<br>SCK.CEN, Boeretang 200, 2400 Mol, Belgium | | |

**Report:**

We investigated the charge fluctuations and mixed valence effects in $NaV_2O_5$ single crystals. The measurements of the XANES and EXAFS spectra of $NaV_2O_5$ and $N_{0.95}V_2O_5$ are performed at the room temperature and at 15 K. The results are compared with calculations based on self-consistent real space full multiple scattering analysis. A comparison between experimental and theoretical V K edge XANES of NaV2O5 crystals is presented in Figure 1. The lowest energy structure is the peak A with a low energy shoulder A1 is found to be a characteristic feature for all mixed V4.5 +. In the higher energy region of the XANES, we observed the shoulders B and C, which are h are s indicators for the perfect perovskite structure. The D and E doublet appears as a consequence of V-O layered structure along the c-axis.

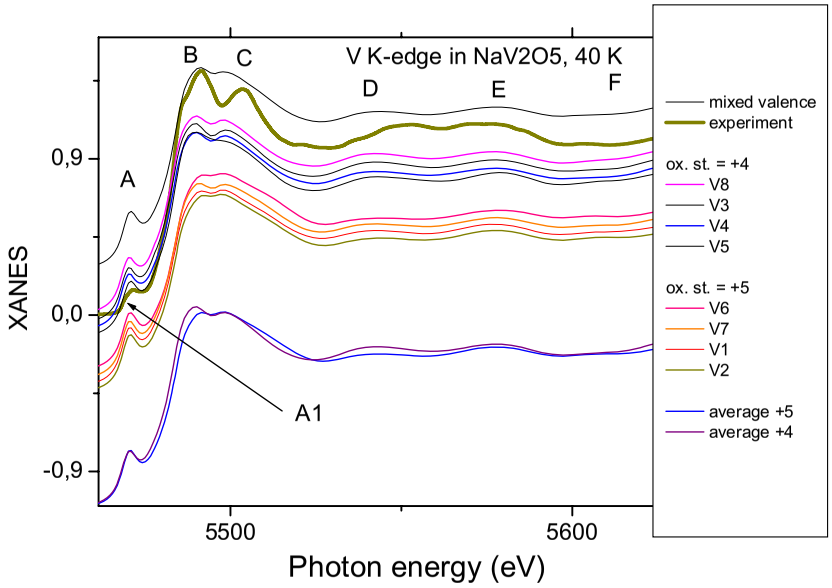


**Figure 1.** Comparison of the experimental V K edge XANES in $NaV_2O_5$ single crystals with the theoretical spectra.

The calculated spectra exhibit an oversmoothed white line feature as compared to experimental spectra and the lack of A1 feature. This seems to be a common fault of calculations in Hedin Lundquist potentials, and indicates that interaction which describes the electron correlations within V-O-V rungs needs to be included in the model.

| ROBL-CRG | **Experiment title:** **Reduction of Eu and Se by Fe(II) at the clay edge surface** | **Experiment number:** **20-01-652** |
|---|---|---|
| **Beamline:** BM 20 | **Date of experiment:** 30.11.-03.12.05; 08.04.-11.04.06; 27.09.-29.09.06 | **Date of report:** 11.01.07 |
| **Shifts:** 24 | **Local contact(s):** A. Scheinost, A. Rossberg | *Received at ROBL:* 11.01.07 |

**Names and affiliations of applicants** (* indicates experimentalists):

A. SCHEINOST[1]*, L. CHARLET[2]*, A. GEHIN[2]*, CH. HENNIG[1]*

[1]Institute of Radiochemistry, FZD, Dresden, Germany
[2]Geochemistry Group, LGIT-OSUG, Université Joseph-Fourier, Grenoble, France

## Report:

Charlet, L., Scheinost, A. C., Tournassat, C., Greneche, J. M., Géhin, A., Fernández-Martínez, A., Coudert, S., Tisserand, D., and Brendle, J. (2007). Electron transfer at the mineral/water interface: Selenium reduction by ferrous iron sorbed on clay. *Geochimica et Cosmochimica Acta*, in review.

## Abstract:

The mobility and availability of the toxic metalloid selenium in the environment is largely controlled by sorption and redox reactions, which may proceed at temporal scales similar to that of subsurface water movement at saturated or unsaturated conditions. Since such waters are often anaerobic and rich in $Fe^{2+}$, we investigated the long-term (≤ 1 month) kinetics of selenite ($Se(IV)O_3^-$) sorption to montmorillonite in the presence of $Fe^{2+}$ at anoxic condition. A synthetic montmorillonite was used to eliminate the influence of structural Fe. In the absence of aqueous $Fe^{2+}$, selenite was sorbed as outer-sphere sorption complex, covering only part of the positive edge sites, as verified by a structure-based MUSIC model and Se K-edge X-ray absorption spectroscopy. When selenite was added to montmorillonite previously equilibrated with $Fe^{2+}$ solution, however, slow reduction of Se and formation of a solid phase was observed with Se K-edge XANES (x-ray absorption near-edge spectroscopy) and EXAFS (extended x-ray absorption fine-structure) spectroscopy. Iterative transformation factor analysis of XANES and EXAFS spectra suggested that only one Se reaction product formed, which was identified as nano-particulate Se(0). Even after one month, only 75 % of the initially sorbed Se(IV) was reduced to this solid species. Mössbauer spectrometry revealed that before and after addition and reduction of Se, 5 % of total sorbed Fe occurred as Fe(III) species on edge sites of montmorillonite (≈ 2 mmol $kg^{-1}$). The only change observed after addition of Se was the formation of a new Fe(II) species (15 %) attributed to the formation of an outer-sphere Fe(II)-Se sorption complex. The combined Mössbauer and XAS results hence clearly suggest that the Se and Fe redox reactions are not directly coupled. Based on the results of a companion paper, we hypothesize that the electrons produced in the absence of Se by oxidation of sorbed Fe(II) are stored, e.g. by formation of surface $H_2$ species, and are then available for the later Se(IV) reduction. The slow reaction rate indicates a diffusion controlled process. Homogeneous precipitation of an iron selenite was thermodynamically predicted and experimentally observed only in the absence of clay. Interestingly, half of Fe was oxidized in this precipitate (Mössbauer). Since DFT calculations predicted the oxidation of Fe at the water-FeSe solid interface only and not in the bulk phase, the average particle size of this precipitate does not exceed 2 nm. A comparison with the Mössbauer and XAS spectra of the clay samples demonstrates that such homogenous precipitation can be excluded as mechanism for the observed slow Se reduction, emphasizing the role of abiotic, heterogeneous precipitation and reduction for the removal of Se from subsurface waters.

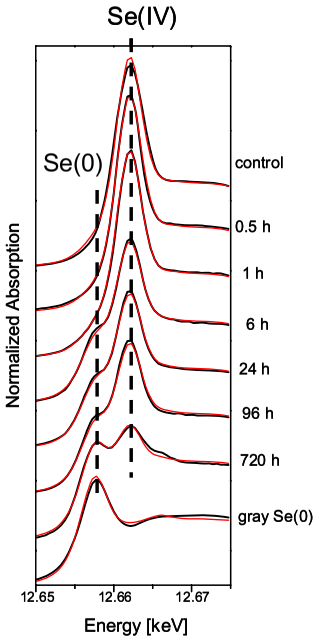


**Fig. 1.**
Time-resolved Se-K edge XANES spectra of the Se(IV)-$Fe^{2+}$-montmorillonite system (black lines) and spectral reconstruction with two components (ITFA). As references, the spectra of a control without $Fe^{2+}$ and of gray Se(0) are shown.

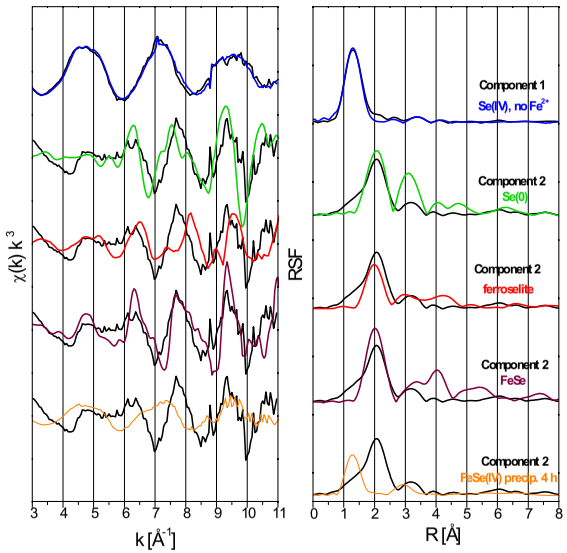


**Fig. 2.**
Se-K edge EXAFS spectra of ITFA-derived spectral components of component/species 1 and 2 (black lines) in comparison to selected references (colored lines).

| ROBL-CRG | **Experiment title:**<br>**Uranyl sorption to clay minerals and analogues** | **Experiment number:**<br>**20-01-653**<br>**(20-01-641)** |
|---|---|---|
| **Beamline:**<br>BM 20 | **Date of experiment:**<br>07.09.-10.09.05; 30.10.-03.11.05;<br>06.05.-09.05.06; 26.11.-28.11.06 | **Date of report:**<br>11.01.07 |
| **Shifts:**<br>33 | **Local contact(s):**<br>A. Scheinost | *Received at ROBL:*<br>11.01.07 |

**Names and affiliations of applicants** (* indicates experimentalists):

A. SCHEINOST*, CH. HENNIG*, A. ROSSBERG*, N. BAUMANN, TH. ARNOLD, V. BRENDLER

Institute of Radiochemistry, FZD, Dresden, Germany

## Report:

After more than one decade of studying uranyl sorption complexes onto surfaces of environmental relevance like clay minerals, Fe or Mn oxyhydroxides, the structure of the surface complexes is often yet not resolved. Open questions include the existence and structure of ternary surface complexes (i.e. with carbonate or silicate monomers), the possible formation of hydrogen bonds between the double-bond oxygen atom of the uranyl moiety and ligand oxygens, and the transition from sorbed uranyl monomers to sorbed uranyl polymers to uranyl surface precipitates. Here we present first results of uranyl sorption to gibbsite, the surface groups representative for a wide range of Al-containing natural minerals relevant for limiting U migration. Experiments were conducted in the pH-range 5 – 8.5, at an ionic strength of 0.01 M $NaClO_4$, $[UO_2^{2+}] = 5\times10^{-6}$ M, a solid to solution ratio of 0.5 g/40 mL, and a contact time of 2 days in the overhead shaker in equilibrium with the athmosphere (speciation as shown in Fig. 2). Two samples at the highest pH of 7.5 and 8.5 were additionally prepared in a carbonate-free inert gas glovebox.

With the exception of the spectrum at pH 8.5 in equilibrium with open atmosphere, all spectra were statistically identical as shown by PCA (example shown in Fig. 1). The Fourier transform peak at 3.1 Å (not corrected for phase shift) was largely (but not completely) fitted by the 4-legged multiple scattering path U-Oax1-U-Oax2, using the constraints as suggested by (*1*) (CN 2, distance 2x U-Oax, Debye-Waller 2xU-Oax). For all samples except of U6-27, inclusion of an U-Al path slightly improved the total fit result. The distance of this U-Al path varied between 3.33 and 3.34 Å. Note that the contribution of this path to the total fit was always small (3-6 %), and especially coordination numbers, but probably even distances may be subject to substantial error. The distance is in line with a bidentate inner-sphere sorption complex to $Al(O,OH)_6$ octahedra, e.g. that on imogolite with 3.3 to 3.35 Å (*2*), but slightly shorter than the 3.40 to 3.44 Å found for montmorillonite (*3*).

Furthermore, for all but sample U6-27, inclusion of a U-U backscattering shell greatly improved the fit. Coordination numbers varied between 0.8 and 1.1, and distances between 4.21 and 4.22 Å. The coordination numbers of approximately one suggest formation of dimeric sorption species. Such oligomeric sorption complexes have been suggested earlier by (*4*), (*5, 6*). However, the distance of 4.22 Å does not agree with 3.9 Å for multimeric uranyl carbonato complexes on hematite at pH > 6.5 (*5*), with 4.01 Å for polynuclear sorption complex on alumina at pH 6.5 (*4*), with quantum-chemical distances of 3.94 to 4.09 Å for uranyl dimers (*7*), with 3.78 to 3.86 Å for polymeric uranyl hydrolysis complexes (*8, 9*). The fitted distance does also not agree with that of schoepite and meta-schoepite (nearest U-U 3.8-3.9 Å) and other precipitates, which may have formed in this system due to local supersaturation (average conditions exclude supersaturation with respect to known likely solids). It agrees well, however, with several uranyl hydroxide structures like beta-hydroxide (4.22 Å) and gamma hydroxide (4.23 Å) and the peroxide mineral studtite (4.21 Å) (*10*).

The possible structure of such uranyl dimers may be derived from simplified geometric considerations, assuming only one distance of Oeq as justified by the comparatively small Debye-Waller factor of 0.006 to 0.008 $Å^2$, and assuming an equal distribution of Oeq in the equatorial plane of the uranyl unit. It follows, that an edge-sharing complex of two pentagonal uranyl units (coordination number of Oeq ≈ 5) with the fitted U-Oeq distance of 2.4 Å would result in a maximum U-U distance of 3.88 Å.

The fitted coordination numbers of Oeq=6 suggest, however, hexagonal uranyl units. In this case, the maximum U-U distance for an edge-sharing arrangement is 4.16 Å, hence only slightly smaller than the experimental value of 4.2 Å. Therefore, formation of edge-sharing, hexagonal uranyl dimers is the most likely arrangement. The small size mismatch of 0.04 Å is at the limit of the EXAFS precision for such a distance. Furthermore, small variations of the Oeq-U-Oeq angels from the average value of 60° can easily account for the observed mismatch, as for instance in studtite (*10*).

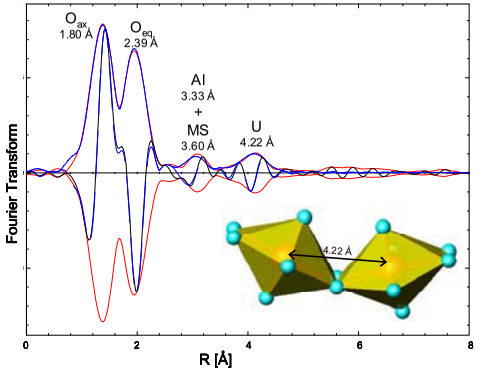


**Fig. 1.**
Fit of uranyl-gibbsite spectra of sample U6-24. Experimental Fourier magnitude (red) and imaginary part (black) along with fit (blue). The peak at about 3 Å (uncorrected for phase shift) is dominated by multiple scattering (MS) from the axial oxygen atoms (15 % of the total area), while the Al path contributes only 5 %. Inset: Proposed dimer structure consisting of two edge-sharing hexagonal uranyl units.

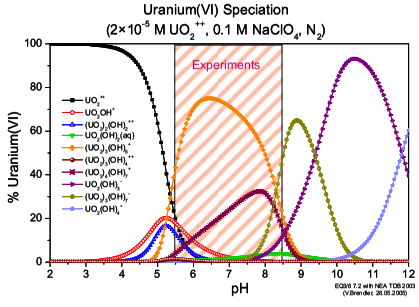


**Fig. 2.**
Aqueous uranyl speciation in equilibrium with CO2-free N2-atmosphere calculated for the experimental conditions. In the relevant pH-range from 5.5 to 8.5, the trimeric 3-5 hydroxo complex is predicted t o prevail.

1. P. G. Allen, J. J. Bucher, D. K. Shuh, N. M. Edelstein, T. Reich, *Inorganic Chemistry* 36, 4676-4683 (Oct 8, 1997).
2. Y. Arai, M. McBeath, J. R. Bargar, J. Joye, J. A. Davis, *Geochimica Et Cosmochimica Acta* 70, 2492-2509 (May 15, 2006).
3. C. Hennig, T. Reich, R. Dahn, A. M. Scheidegger, *Radiochimica Acta* 90, 653-657 (2002).
4. E. R. Sylwester, E. A. Hudson, P. G. Allen, *Geochimica Et Cosmochimica Acta* 64, 2431-2438 (Jul, 2000).
5. J. R. Bargar, R. Reitmeyer, J. J. Lenhart, J. A. Davis, *Geochimica Et Cosmochimica Acta* 64, 2737-2749 (Aug, 2000).
6. A. Kowal-Fouchard, R. Drot, E. Simoni, J. J. Ehrhardt, *Environmental Science & Technology* 38, 1399-1407 (Mar 1, 2004).
7. S. Tsushima, T. Reich, *Chemical Physics Letters* 347, 127-132 (Oct 19, 2001).
8. M. Aberg, *Acta Chemica Scandinavica* 24, 2901-& (1970).
9. M. Aberg, *Acta Chemica Scandinavica* 25, 368-& (1971).
10. P. C. Burns, K. A. Hughes, *American Mineralogist* 88, 1165-1168 (Jul, 2003).

| ROBL-CRG | **Experiment title:** **Solvation and complexation of uranium(VI) in room temperature ionic liquids** | **Experiment number:** **20-01-654** |
|---|---|---|
| **Beamline:** BM 20 | **Date of experiment:** from: 22.02.2006 to: 25.02.2006 | **Date of report:** 24.11.2006 |
| **Shifts:** 9 | **Local contact(s):** C. Hennig | *Received at ROBL:* |

**Names and affiliations of applicants** (* indicates experimentalists):

C. Gaillard*, I. Billard, A. Ouadi*, J. Champion*
Institut Pluridisciplinaire Hubert Curien, Chimie Nucléaire, Strasbourg, France.

## Report:

The aim of this work is to gain insights on the coordination properties of uranyl in room temperature ionic liquids (ILs), as a function of the nature of the uranyl counterions, and of the ionic liquid. Using UV-visible spectroscopy and EXAFS, we investigate the coordination sphere of uranyl after dissolution of various uranyl salts ($UO_2X_2$ with $X^- = NO_3^-$, triflate $TfO^-$, $ClO_4^-$) in four different ionic liquids. Three of them ($C_4mimPF_6$, $C_4mimTf_2N$ and $C_4mimBF_4$) are based on the imidazolium cation ($C_4mim$ = 1-methyl-3-butyl-imidazolium) and differ by their anionic components ($PF_6^-$, $(CF_3SO_2)_2N^-$ hereafter noted $Tf_2N^-$ and $BF_4^-$, respectively) while the $Me_3NBuTf_2N$ liquid is based on a quaternary ammonium $Me_3NBu^+$ cation, allowing us to assess the role of anionic and cationic components of the liquid. We also investigate the reactivity of the uranyl towards chloride ions introduced in solutions.
EXAFS experiments were carried out at ROBL-ESRF beamline, at the U $L_{III}$ edge, in transmission mode using argon-filled ionisation chambers at ambient temperature. Fits of the Fourier transform (FT) $k^3$-weighted EXAFS data to the EXAFS equation were performed in R-space between 1 and 4 Å. The k-range used was 3.5-16 $Å^{-1}$.

The dissolution of uranyl salts, in absence of chlorides, could be achieved only in $C_4mimTf_2N$ and $Me_3BuNTf_2N$. EXAFS experiments, coupled with UV-visible measurements, show that the counter-anions triflate, perchlorate and nitrate remain, at least partially, in the uranium first coordination sphere. Thus, dissolution of the salts does not impy the uranyl solvation by $Tf_2N^-$ anions of the solvent. No influence of the IL cationic part was observed. Introduction of chlorides in solution was shown to improve the solubility of uranyl salts, in particular in $C_4mimPF_6$ and $C_4mimBF_4$. The ratio [Cl]/[U] in solutions was equal to 4. EXAFS clearly show that the tetra-chloro complex of uranyl $UO_2Cl_4^{2-}$ is formed in all samples, excepting in $C_4mimBF_4$ (see figure 1). In the latter, the complexation is not total ($N_{Cl}$ ~1), probably because of the presence of fluoride ions likely formed by the decomposition of $BF_4^-$ anions.

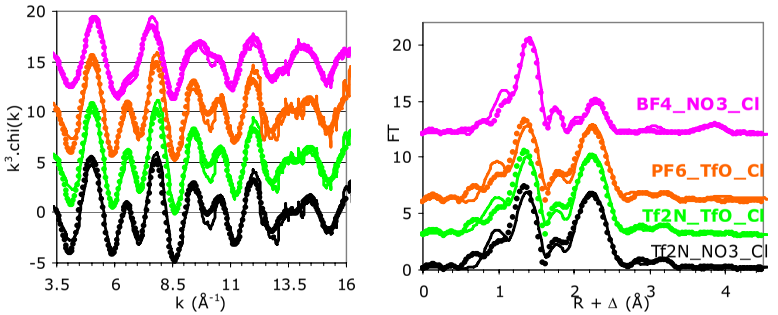


**Fig. 1:** Influence of the uranyl salt and of IL on the complexation of uranium(VI) with chlorides: EXAFS spectra and their corresponding Fourier Transform. For sake of clarity, EXAFS and FT were shifted along the y-axis.

| ROBL-CRG | **Experiment title:**<br>**EXAFS investigations of uranium species formed by monocellular and polycellular algae** | **Experiment number:**<br>**20-01-656** |
|---|---|---|
| **Beamline:**<br>BM 20 | **Date of experiment:**<br>from: 21.07.06 to: 23.07.06 | **Date of report:**<br>10.12.06 |
| **Shifts:**<br>6 | **Local contact(s):**<br>A. Rossberg | *Received at ROBL:* |

**Names and affiliations of applicants** (* indicates experimentalists):

A. Günther[1], A. Rossberg*[2], A. Scheinost*[2], C. Hennig*[2], H. Funke*[2]

[1]Forschungszentrum Dresden-Rossendorf e.V., Institute for Radiochemistry, P.O. Box 510119, 01314 Dresden, Germany

[2]ESRF-ROBL/CRG, Avenue des Matryrs, B.P. 220, 38043 Grenoble Cedex, France

## Report

***Experimental:*** The aim of this study is to determine the structural parameters of the formed uranyl complex species in monocellular Chlorella vulgaris cells at pH 3, 5 and 6 and low temperature. The stored algal biomass was re-suspended in 0.9% $NaClO_4$ solution and contacted 72 h with $UO_2(ClO_4)_2$. In each reaction solution the concentration of the algal biomass was 0.75 g dry mass /L. The uranium concentration was $1 \cdot 10^{-4}$ M. The pH values of the solutions were adjusted with $HClO_4$ or NaOH. After separation of the washed algae biomass by centrifugation the fresh samples were put into polyethylene sample holder surrounded with Kapton tape. The U $L_{III}$-edge spectra were measured in fluorescence mode at 30K using a closed-cycle He-cryostat. The EXAFS spectra were analyzed using the suite of program EXAFSPAK /1/. The theoretical scattering phases and amplitudes were calculated by using x-ray structural data of meta-autunite with the scattering code FEFF8 /2/.

***Results and discussion:*** Figure 1 shows the raw U $L_{III}$-edge $k^3$-weighted EXAFS spectra and their corresponding Fourier transforms (FT) of uranium containing algal cells (samples A-C) at 30 K. The corresponding structural parameters are summarized in Table 1. At pH 3 the U-$O_{ax}$ and U-$O_{eq}$ radial distances are similar to those obtained for uranyl hydrate. The spectrum is well reproduced by taking only backscattering on O atoms into account (Fig. 1). At pH 5 and 6 short U-$O_{eq}$ bond distances of 2.28 Å and 2.29 Å and a U-P interaction were found (Tab. 1). The radial U-P distance of 3.57 Å indicates a monodentate binding of uranium on phosphate groups. In addition both samples show a U-U interaction (Fig. 1, Tab. 1). The structural parameters of the samples at pH 5 and 6 are similar to those of meta-autunite (Vo21, Fig. 1, Tab. 1).



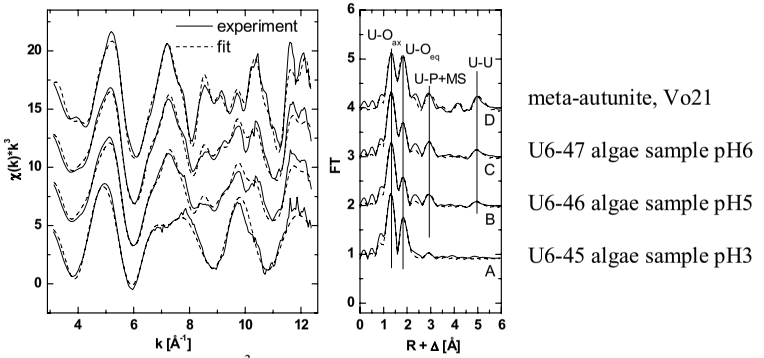


**Fig. 1**. Raw U $L_{III}$-edge $k^3$-weighted EXAFS spectra (left) and corresponding Fourier transform (right) of the algae samples and meta-autunite at 30 K.

**Tab. 1.** EXAFS structural parameters of the uranyl complex species in different algae sample and of a reference sample at 30K

| Sample | U-$O_{ax}$ | | U-$O_{eq}$ | | | U-P + MS | | | U-U | | |
|---|---|---|---|---|---|---|---|---|---|---|---|
| | R [Å] | $\sigma^2 \cdot 10^3$ [Å$^2$] | N | R [Å] | $\sigma^2 \cdot 10^3$ [Å$^2$] | N | R [Å] | $\sigma^2 \cdot 10^3$ [Å$^2$] | N | R [Å] | $\sigma^2 \cdot 10^3$ [Å$^2$] |
| Vo21 | 1.77 | 3.9 | 3.8 | 2.29 | 2.0 | 3.8 | 3.59 | 3.0 | 4 | 5.27 | 3.0 |
| U6-47 | 1.77 | 2.2 | 4* | 2.28 | 5.6 | 4* | 3.57 | 3.8 | 4* | 5.22 | 7.0 |
| U6-46 | 1.77 | 2.3 | 4* | 2.29 | 7.9 | 4* | 3.57 | 5.7 | 4* | 5.22 | 9.0 |
| U6-45 | 1.77 | 1.8 | 4.7 | 2.39 | 7.7 | - | - | - | - | - | - |

N - coordination number with an uncertainty of 25%, N $O_{ax}$ was held constant at N=2, R - radial distance with an uncertainty of ±0.02Å, $\sigma^2$ - Debye-Waller factor, * fixed during the shell fitting

***Acknowledgements***

The authors thank Prof. R. Vochten for providing the meta-autunite sample.

***References***

/1/ George, G. N., Pickering, I. J.: EXAFSPAK A Suite of Computer Programs for Analysis of X-Ray Absorption Spectra. Stanford Synchrotron Radiation Laboratory, Stanford, CA. USA. (1995)

/2/ Ankudinov et al.: Real-space multiple scattering calculation and interpretation of x-ray absorption near-edge structure, Phys. Rev. B 58 (1998), 7565-7576

| ROBL-CRG | **Experiment title:** **Studies of the chemical forms of actinides and fission products adsorbed on nanocrystalline magnetite** | **Experiment number:** **20-01-658** |
|---|---|---|
| **Beamline:** BM 20 | **Date of experiment:** from: 22.10. to: 26.10.2006 | **Date of report:** 26.01.07 |
| **Shifts:** 12 | **Local contact(s):** A. Scheinost | *Received at ROBL:* |

**Names and affiliations of applicants** (* indicates experimentalists):
Dr. NIKITENKO Serguei*, C.N.R.S. - UMR 5084, CENBG, Domaine du Haut Vigneau, B.P.120, F-33175 Gradignan Cedex, France
Dr. SCHEINOST Andreas, ROBL

**Speciation of selenium and uranium adsorbed at superparamagnetic magnetite by XAFS**

Magnetite nanocrystals were obtained by co-precipitation of Fe(II) and Fe(III) in basic solutions in the presence of argon under the effect of power ultrasound (f= 20 kHz, I= 30 W/cm$^2$, $P_{ac}$= 0.75 W/mL, T=30-32°C). Transmission electron microscopy (Philips SM 120) reveal that the average particles size is equal to 4-6 nm (Fig.1a). Mössbauer spectroscopy (MS, $^{57}$Co as a γ-source, with respect to metallic iron) show the superparamagnetic behaviour (Fig. 1b).

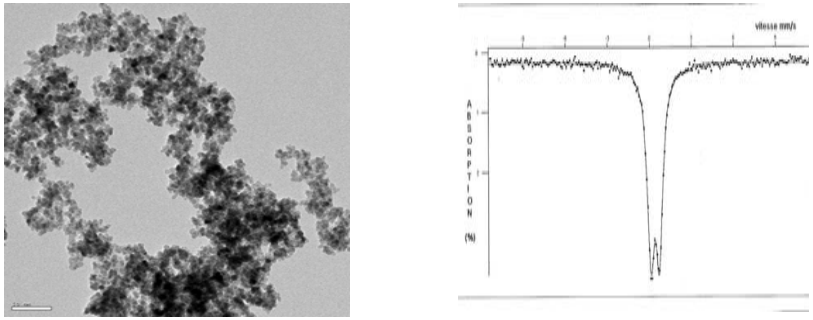

Fig. 1. TEM (left) and Mössbauer spectra of nanocrystalline magnetite.

Table 1.

| Experiment | Adsorbent | Initial chemical form | pH | Time of contact to reach an equilibrium, min |
|---|---|---|---|---|
| 1 | $Fe_3O_4$ (4-6 nm) | Se(IV) ($HSeO_3^-$, $SeO_3^{2-}$) | 7.9 | 15 |
| 2 | $Fe_3O_4$ (4-6 nm) | Se(VI) ($SeO_4^{2-}$) | 7.9 | 15 |
| 3 | $Fe_3O_4$ (4-6 nm) | U(VI) | 6.5 | 60 |
| 4 | $Fe_2O_3$ (5-30 nm) | Se(IV) ($HSeO_3^-$, $SeO_3^{2-}$) | 5.5 | 15 |
| 5 | $Fe_2O_3$ (5-30 nm) | U(VI) | 4.0 | 60 |
| 6 | Fe (≅ 5 μm) | U(VI) | 5.4 | 12 hours |

Sorption was performed in an inert atmosphere from 0.1M NaCl solutions at room temperature. The phase ratio solution (L)/solids (S) was equal to L/S= 200. Concentration of adsorbed species was typically about 1000 ppm. XAFS of the slurries of adsorbents were measured in fluorescence mode at 15 K at the Se K-edge and at room temperature at the U-$L_{III}$ edge. The studied systems are summarised in Table 1.

XAFS of the systems 1,2, clearly show the absence of Se(IV) and Se(VI) reduction at the surface of nanomagnetite at the studied experimental conditions (Fig. 2). From the thermodynamic point of view Fe(II) of magnetite is able to reduce selenium. It can be assumed that reduction is very slow in basic solutions. The experiment will therefore be repeated at pH≅ 5. Metallic iron reduces U(VI) to U(IV) hydroxo-species immobilised at its surface (experiment 6, Fig. 3). By contrast, U(VI) adsorption at the magnetite occurs without chemical reduction (Fig. 3, left). Appearance of XANES band typical for U(IV) after several scans (experiment 3) most probably is related to U(VI) photoredution rather than reduction with magnetite. XAFS studies of this system at 15 K is necessary to minimise the photoreduction effect.

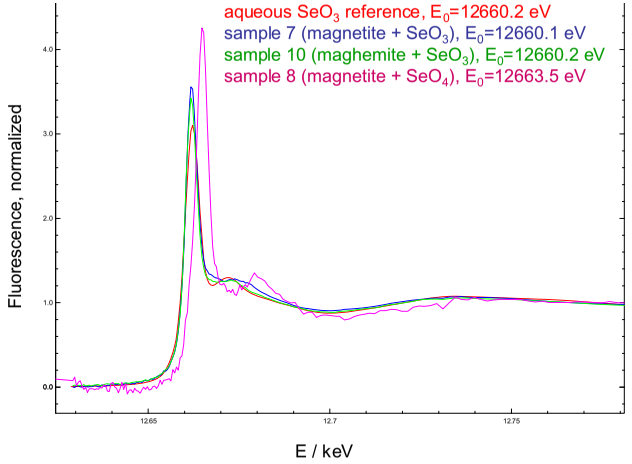


Fig. 2. Se K-edge XANES at 15 K

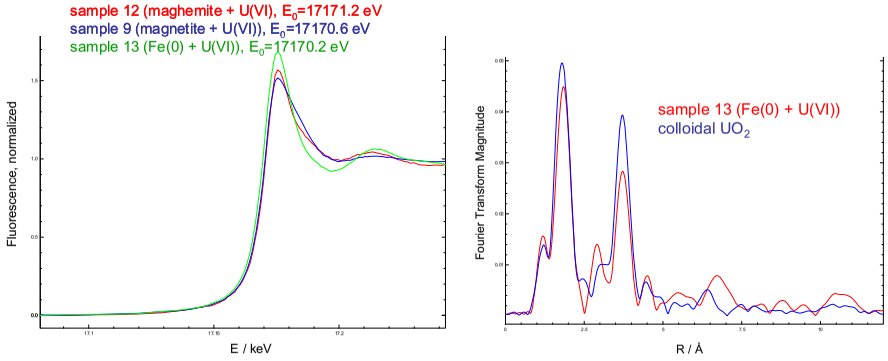


Fig. 3. U $L_{III}$-edge XANES (left) and EXAFS (right) measured at RT.

| ROBL-CRG | **Experiment title:**<br>**EXAFS study on the structural and binding behaviour of uranyl oxalate complexes in different solvents** | **Experiment number:**<br>26-01-727 |
|---|---|---|
| **Beamline:**<br>BM 20 | **Date of experiment:**<br>from: 30.04.2005 to: 03.05.2005 | **Date of report:**<br>28.02.2006 |
| **Shifts:**<br>9 | **Local contact(s):**<br>Ch. Hennig | *Received at ROBL:* |


**Names and affiliations of applicants** (* indicates experimentalists):

Dr. Rik Van Deun — K.U.Leuven
Drs. Kelly Servaes — Chemistry Department
Drs. Kyra Lunstroot — Molecular Design and Synthesis Division
Coordination Chemistry Group
Celestijnenlaan 200F
3001 Heverlee
Belgium


## Report:

During this experiment, several uranyl samples were measured, among which also the tetrachloro complex. The analysis of the EXAFS-spectrum of this complex has been compared with the UV-vis results that had been obtained in our lab earlier and the total study has been published in *Inorganic Chemistry*.

## Abstract:


*The complex formation of uranyl $UO_2^{2+}$ with chloride ions in acetonitrile was studied by UV-Vis and U $L_{III}$ EXAFS spectroscopy. The investigations unambiguously point to the existence of a $[UO_2Cl_4^{2-}]$ species in solution with $D_{4h}$ symmetry. The distances in the U(VI) coordination sphere are U-$O_{ax}$ = 1.77±0.01 Å and U-Cl = 2.68±0.01 Å.*



Full reference:
Structure of $[UO_2Cl_4]^{2-}$ in acetonitrile
K. Servaes, C. Hennig, R. Van Deun and C. Görller-Walrand, *Inorg. Chem.*, **44** (2005) 7705-7707.




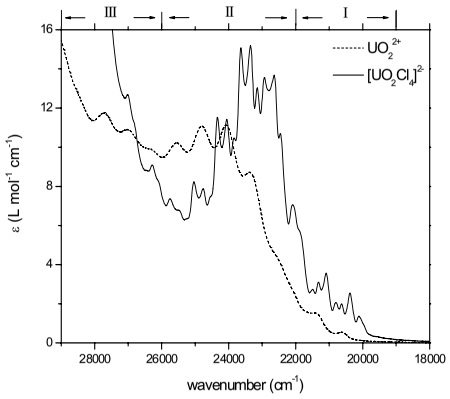


***Figure 1:*** *UV-vis absorption spectrum of free $UO_2^{2+}$ (dashed line) and $[UO_2Cl_4]^{2-}$ (solid line) in acetonitrile at room temperature. Concentrations are $[UO_2^{2+}]$ = 50mM and [Cl] = 0.25M.*

We have investigated the complexation of the uranyl ion $UO_2^{2+}$ with chloride ions in acetonitrile by UV-Vis spectroscopy and EXAFS. With a metal-to-ligand ratio higher than 1:4, the main features in the spectrum remain constant, which indicates that the uranyl complex reached the maximal coordination of $Cl^-$ ions in the equatorial plane (see Figure 1). Based on the similarity between single crystals of the type $M_2UO_2Cl_4$, which have been thoroughly studied by Denning et al., and solution, we can conclude that a $[UO_2Cl_4]^{2-}$ complex with $D_{4h}$ coordination symmetry is present in solution.

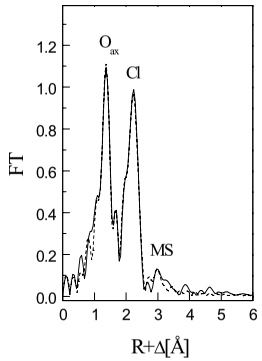


***Figure 2:*** *Fourier transforms of the U $L_{III}$-edge $k^3$ weighted EXAFS data taken over k = 3.2-16.6 $Å^{-1}$; experimental data as line and theoretical curve fit as dots.*

| ESRF | **Experiment title:** EXAFS/XANES studies on the speciation of Tc(IV) in mixtures of low and high molecular weight organics | **Experiment number:** CH 1931 |
|---|---|---|
| **Beamline:** BM20 | **Date of experiment:** from: 13/07/05 to: 16/07/05 | **Date of report:** 01/03/06 |
| **Shifts:** 12 | **Local contact(s):** Dr. Christophe HENNIG | *Received at ESRF:* |

**Names and affiliations of applicants** (* indicates experimentalists):

**Prof.Dr. André MAES**
**Ir. Eric BREYNAERT**
**Ir. Christophe BRUGGEMAN**

Laboratory for Colloïd Chemistry – K.U.Leuven
Kasteelpark Arenberg 23
B-3001 Leuven - BELGIUM

Introduction

The redox-sensitive fission product technetium-99 (Tc) is of great interest in nuclear waste disposal studies because of its potential for contaminating the geosphere due to its very long half-life ($2.13\times10^5$ year) and high mobility under oxidising conditions, where technetium forms pertechnetate ($TcO_4^-$) [1]. Under suitable reducing conditions, e.g. in the presence of an iron(II) containing solid phase which can act as an electrondonor, the solubility can be limited by the reduction of pertechnetate followed by the formation of a surface precipitate [2]. However, upon association with mobile humic substances (HS), the solubility of reduced Tc species may be drastically enhanced [3].

Previous EXAFS/XANES campaigns (CH-1050, SI-790, CH-1454, CH-1671) performed at ESRF have demonstrated that pertechnetate is reduced to Tc(IV) in reducing natural systems containing humic matter [4, 5]. A large fraction of this Tc(IV) was observed to be in a colloidal form and associated with the organic matter through a "hydrophobic" interaction mechanism. The results from the last campaigns however also proved (unpublished) that in the presence of small organic molecules, different spectra were obtained for Tc(IV), i.e. Tc(IV) was not in the colloidal form. Some spectra could already be fully modelled, e.g. with pyrogallol as natural organic matter precursor. It was found that Tc(IV) can make chelating complexes with pyrogallol at neutral to high pH by means of a ligand exchange between the hydrolysed Tc(IV) molecules and –OH functional groups present on the organics. EXAFS modelling was thereby supported by Density Functional Theory calculations (ub3lyp/lanl2dz [6]).

Experimental setup

The main objective of experiment CH-1931 was two-fold :

1) to obtain spectra for Tc(IV) reference compounds whose atomic model is known from literature in order to verify the pursued analysis methodology.
Experimentally $TcO_4^-$ was chemically reduced to Tc(IV) and different "Tc(IV) reference compounds":$TcCl_6^{2-}$ [10], Tc(IV)-acetyl acetonate [7]) were prepared.

2) to study the contribution of both above described mechanisms in the association of Tc(IV) with mixed systems of small organic molecules and humic substances.
Experimentally, mixed systems of Tc(IV) complexes with small organic molecules and colloidal Tc(IV) interacting with large humic substance molecules were prepared. Chemically reduced Tc(IV) was therefore contacted with 1) pyrogallol (containing phenol ligands), 2) citric acid (containing carboxyl ligands) and 3) humic substances (colloidal interaction) at a fixed pH and with mixtures of two of these compounds.

All samples were preconcentrated and transferred into heat-sealed poly-ethylene microtubes as a slurry.

Results

1) The technique used for the preparation of the samples produced relatively pure samples with technetium concentrations high enough for XAS-measurements in fluorescence mode and in some cases also transmission mode. The complete XAS campaign resulted in spectra for 17 samples. The installation of a new monochromator crystal in the beamline optics (BM20) solved a problem with glitches in the raw spectra as compaired to the 4th campaign.

2) XANES analysis of the reference spectra and the pure samples revealed that the relation between the edge shift and the formal oxidation state is not straightforward and highly depends on the ligands and structure of the species under investigation. This observation corresponds to previous literature data [8].

| Compound | formal oxidation state | K edge shift (eV) |
|---|---|---|
| $TcO_4^-$ | VII | 0 |
| $Tc(acac)_3$ | III | -8.34 |
| $TcCl_6^{2-}$ | IV | -9.16 |

3) In the pH range from 2 to 11, using pure pyrogallol as complexing agent a competition mechanism was observed between Tc(IV) dimer/polymer formation (dominant pH 2; see fig.) and the formation of monomeric and dimeric pyrogallol complexes (dominant pH 5 – 11). Next to the formation of monomeric and dimeric complexes, a pH dependant change in complex structure was also observed, yielding 5-coordinated complexes at the lower pH range (pH 5) and 6-coordinated complexes at high pH (pH 11; see fig).

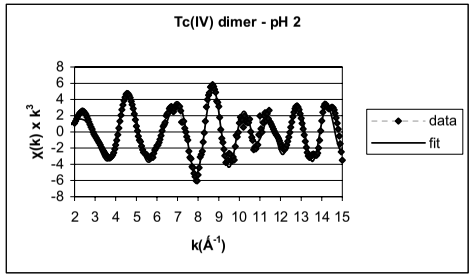


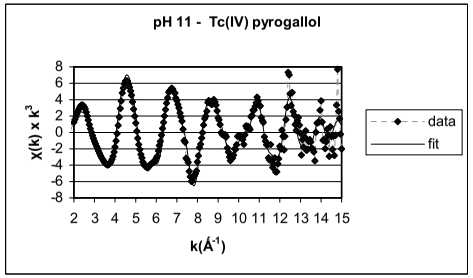


References

1. Lieser, K.H. and C. Bauscher, *Technetium in the Hydrosphere and in the Geosphere .1. Chemistry of Technetium and Iron in Natural-Waters and Influence of the Redox Potential on the Sorption of Technetium.* Radiochimica Acta, 1987. **42**(4): p. 205-213.
2. Cui, D.Q. and T.E. Eriksen, *Reduction of pertechnetate in solution by heterogeneous electron transfer from Fe(II)-containing geological material.* Environmental Science & Technology, 1996. **30**(7): p. 2263-2269.
3. Sekine, T., et al., *Complexation of Technetium with Humic-Acid.* Radiochimica Acta, 1993. **63**: p. 87-90.
4. Geraedts, K., et al., *Evidence for the existence of Tc(IV) - humic substance species by X-ray absorption near-edge spectroscopy.* Radiochimica Acta, 2002. **90**(12): p. 879-884.
5. Maes, A., et al., *Evidence for the Formation of Technetium Colloids in Humic Substances by X-Ray Absorption Spectroscopy.* Environmental Science & Technology, 2004. **38**(7): p. 2044-2051.
6. Gancheff, J., et al., *Density functional study of technetium and rhenium compounds.* Journal of Molecular Structure-Theochem, 2002. **580**: p. 107-116.
7. Schwochau, K., *Technetium : chemistry and radiopharmaceutical applications*. 2000, Weinheim ; Chichester: Wiley-VCH. xii, 446.
8. Almahamid, I., et al., *Electronic and Structural Investigations of Technetium Compounds by X-Ray-Absorption Spectroscopy.* Inorganic Chemistry, 1995. **34**(1): p. 193-198.

| ESRF | **Experiment title:**<br>**Structure of the serum transferrin metal binding site upon actinide(IV) uptake.** | **Experiment number:**<br>**CH-2083** |
|---|---|---|
| **Beamline:**<br>BM 20 | **Date of experiment:**<br>from: 15.03.2006 to: 19.03.2006 | **Date of report:**<br>27.11.2006 |
| **Shifts:**<br>12 | **Local contact(s):**<br>A. Scheinost | *Received at ROBL:* |

**Names and affiliations of applicants** (* indicates experimentalists):
Dr. Christophe DEN AUWER* DEN/DRCP/SCPS
Dr Philippe MOISY DEN/DRCP/SCPS
Dr Claude VIDAUD* DSV/DIEP/SBTN

CEA Marcoule
30207 Bagnols sur Cèze, France

**Report:**

In the field of human toxicology, internal contamination with actinides can induce both radiological and chemical toxicity. Whatever the way of contamination (inhalation, ingestion or wound), the radionuclide is absorbed into, and then transported by blood, before being deposited in its target organs in which it is stored and then slowly eliminated through urines and faeces. Although there is a tremendous volume of data available on the interaction of plutonium with living organisms as plants, nearly all the studies are limited to macroscopic or physiological measurements with no specific information at the molecular level. Molecular approaches have been more seldom due to the combined intricacy of metallo biochemistry and actinide chemistry. Transferrin (Tf), a well known metalloprotein devoted to iron transport in the human serum, has been targeted in the past as one potential carrier of actinide(IV) (An(IV)) in the human body [1]. Since 2005, our project aims to better understand the interaction between An(IV) and Tf at the molecular level [2].

Spectra of the complexes Th(IV)/Tf, U(VI)/Tf, Np(IV)/Tf and Pu(IV)/Tf with synergistic NTA have been recorded since the beginning of this project, at the ROBL beam line (*cf* report 20-01-644) and interpretation is still in progress for both An(IV)/NTA and An(IV)/NTA/Tf series. Those interpretations are complicated by the complexity of the chelation site of transferrin and the large type of coordination polyhedra of the actinide elements.

In the mean time, a reliable model to fit the experimental spectrum of holotransferrin (Fe(III)/Tf) has been developed. A screening of transferrin structures published in the Protein Data Bank (PDB) was carried out. All structures are in agreement with the iron site, *i.e.* two tyrosine residues, one aspartate, one histidine and one synergistic bidentate carbonate anion. However these structures vary from each other. These variations must be due to the experimental methods used to obtain transferrin crystals as for 1GVC, obtained with an excess of NTA. Some structures are also incompletely resolved, like the 1A8E. Moreover our spectra were recorded in solution whereas PDB structures describe transferrin in the solid state. The EXAFS spectrum of each adequate PDB structure was calculated with the feff8 code, and compared to the experimental spectrum of holotransferrin. From this comparison the 1LCT structure was chosen as an acceptable model for the fit. Note that the distinction between the coordination sites of each lobes of transferrin is impossible with EXAFS technique because of their structural similarity. Both iron ions were thus considered equivalent. The multiple scattering approach was necessary to obtain a satisfactory adjustment of the experimental spectrum (R factor = 0.03). The first contribution was fitted with a shell of 6 oxygen atoms at 2.02 Å ($\sigma$ = 0.019 Å$^2$). In order to obtain a good adjustment of the second shell, two types of carbon were taken into account: 5 carbon atoms at 3.09 Å ($\sigma$ = 0.017 Å$^2$) and 1 at 2.51 Å ($\sigma$ = 0.001 Å$^2$) as well as the corresponding 3-leg scattering paths. It is thus in good agreement with the pseudo-octahedral coordination polyhedron of Fe(III) in holotransferrin.

Parallely, studying the interaction of An(IV) with each amino-acid present in the iron site of transferrin (aspartate, tyrosine and histidine) should help us to better understand the structure of the An-Tf chelation site. Consequently, peptides mimicking parts of the iron site have been synthesized and their interaction with An(IV) investigated by spectrophotometry, and EXAFS. The three AcAsp-Asp-Pro-Asp-AspNH$_2$, AcHis-Tyr-Pro-His-TyrNH$_2$ and AcTyr-Tyr-Pro-Tyr-TyrNH$_2$ pentapeptides, have been investigated. In order to avoid hydrolysis of the actinide cation above the pentapeptide pKas, complexation has been carried out in HEPES buffer. Spectrophotometric measurements have shown the complexation of Np(IV) by the AcAsp-Asp-Pro-Asp-AspNH$_2$ peptide and not by the AcTyr-Tyr-Pro-Tyr-TyrNH$_2$ pentapeptide (due to the higher pKa of the phenolate group compared to the carboxylate group). Comparison with the acetate ligand has also been undertaken. To our knowledge, the interaction of actinide(IV) with acetic acid has only been described in the case of Th(IV) [3]. The EXAFS data at the neptunium $L_{III}$ edge have also been recorded at the ROBL beam line. To our surprise, oxidation of Np(IV) into Np(V)$O_2^+$ has occurred during sample transportation from CEA to ESRF for the Np/acetate complex while the Np/AcAsp-Asp-Pro-Asp-AspNH$_2$ complex did not show any evolution. Another synthetic route has been employed since then and the Np(IV)/acetate complex has been stabilized. Corresponding Fe(III) complexes have also been prepared and EXAFS data at the Fe K edge have recently been recorded at the FAME beam line of ESRF. The first fitting results on the Np/AcAsp-Asp-Pro-Asp-AspNH$_2$ complex tend to show the participation of water molecules and bidentate carboxylate groups to the Np(IV) coordination sphere at 2.21 and 2.41 Å respectively (compared to 2.37 and 2.52 Å for the Th(IV)/acetate complex [3]). Surprisingly, the EXAFS spectrum shows an additional contribution at higher distances that has been characterized as a Np-Np contribution at 3.8 Å. To our knowledge this is the first time a polynuclear complex of Np(IV) is observed with such type of ligands. We are presently working on the elaboration of a molecular model to account for these EXAFS data. Parallely, the EXAFS data of the An(IV)/NTA/Tf systems are being investigated.

**References**

[1] : A. E. Gorden, J. Xu, K. N. Raymond, P. Durbin, *Chem. Rev.* (2003), **103**, 4207.
[2] : A. Jeanson, C. Den Auwer, P. Moisy, C. Vidaud, Proc. Of the NEA/XAS-actinide conferences (2006), Karlsruhe, Germany.
[3] : L. Rao, Z. Zhang, P. L. Zanonato, P. Di Bernardo, A. Bismondo, S. B. Clark, *Dalton Trans.* (2004), 2867.

| ESRF | **Experiment title:** Study of the influence of humic acid on the U(VI) sorption onto kaolinite | **Experiment number:** CH-2086 |
|---|---|---|
| **Beamline:** BM 20 | **Date of experiment:** from: 25.02.2006 to: 28.02.2006 | **Date of report:** 08.11.2006 |
| **Shifts:** 9 | **Local contact(s):** Harald Funke | *Received at ROBL:* |

**Names and affiliations of applicants** (* indicates experimentalists):
A. Křepelová, S. Sachs, T. Reich[1], A. Rossberg*, H. Funke*, H. Hennig*, A. Scheinost*, G. Bernhard

Forschungszentrum Dresden-Rossendorf e.V., Institute of Radiochemistry, D-01314 Dresden
[1]Johannes Gutenberg-Universität Mainz, Institute of Nuclear Chemistry, 55128 Mainz

**Report:**

In the present study we investigated the influence of humic acid (HA) on the near-neighbor surrounding of U(VI) in kaolinite surface complexes. Results of the EXAFS measurements in the ternary system U(VI)-HA-kaolinite were interpreted and compared with those from literature. U(VI) was adsorbed onto kaolinite under the following conditions: [U(VI)]: $1 \cdot 10^{-5}$M, [HA]: 10 mg/L, S/L ratio: 4 g kaolinite/L, pH 3–8.5, $p(CO_2)$: $10^{-3.5}$ atm, I: 0.1 M $NaClO_4$. The sorption procedure is described elsewhere [1]. Uranium $L_{III}$-edge absorption spectra were recorded in fluorescence mode at room temperature.

Fig. 1 shows U $L_{III}$-edge $k^3$-weighted EXAFS oscillations and their corresponding Fourier transforms (FTs, not corrected for phase shift) of the samples prepared at pH ~ 7 with and without HA. Both samples exhibit comparable EXAFS oscillations and FTs without any significant differences. The structural model for fitting the EXAFS oscillations was derived from the EXAFS investigations of the binary system U(VI)-kaolinite KGa-1b [2]. The obtained structural parameters are summarized in Tab.1.

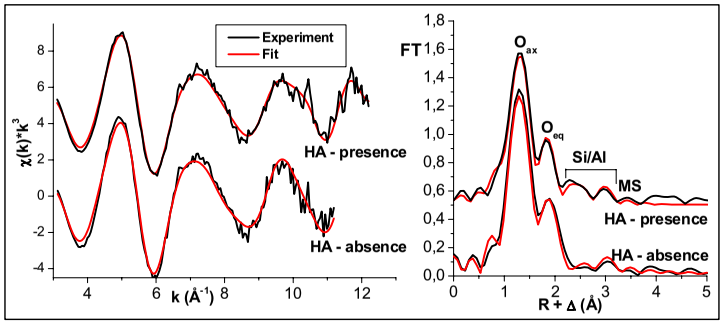


**Fig.1:** Uranium $L_{III}$-edge $k^3$-weighted EXAFS spectra (left) and corresponding FTs (right) of uranyl-kaolinite sample at pH ~ 7 with and without HA.

**Tab.1:** Structural parameters of the uranyl-kaolinite samples with and without HA.

| pH ~ 7 | 2 x $O_{ax}$ | | 5 x $O_{eq}$ | | 1 x $Si_1/Al_1$ | | 1x $Si_2/Al_2$ | | | |
|---|---|---|---|---|---|---|---|---|---|---|
| | R (Å) | $\sigma^2$ (Å$^2$) | R (Å) | $\sigma^2$ (Å$^2$) | R (Å) | $\sigma^2$ (Å$^2$) | R (Å) | $\sigma^2$ (Å$^2$) | ΔE (eV) | Red. error |
| HA-presence | **1.77** | 0.0041 | **2.33** | 0.0145 | **3.08** | 0.0030 | **3.29** | 0.0032 | -13.0 | 0.113 |
| HA-absence | **1.77** | 0.0030 | **2.34** | 0.0123 | **3.06** | 0.0040 | **3.26** | 0.0042 | -12.6 | 0.155 |

ΔR: ± 0.02 Å, $\Delta\sigma^2$: ± 0.001 Å,
R: interatomic distance, $\sigma^2$: Debye-Waller factor, ax: axial, eq: equatorial

The obtained EXAFS data are comparable for both samples, only the U-Si/Al distance is slightly reduced in the presence of HA. The values of the structural parameters obtained for the ternary system U(VI)-HA-kaolinite studied in this work are similar to those of the binary system [2]. Furthermore, they are comparable to values obtained for other systems, e.g., $UO_2$-silica [3], $UO_2$-kaolinite KGa-2 [4] and $UO_2SiO_4H_2$ [5]. Therefore, it could be concluded that HA has no effect on the EXAFS structural parameters in the system U(VI)-HA-kaolinite. Moreover, it seems that in spite of the presence of HA, U(VI) prefers to adsorb rather directly onto kaolinite than via HA, otherwise no U-Si/Al interactions could be detected.

*Acknowledgement:* This work was supported by BMWi (no. 02E9673)

*References:*

[1] Křepelová, A. et al.: Radiochim. Acta, in press.
[2] Reich, Ta.Ye. et al.: AIP Proceedings of XAFS 13, in press.
[3] Reich, T. et al.: J. El. Spectr. Rel. Phenom. **96**, 237 (1998).
[4] Thompson, H.A. et al.: In: Adsorption of Metals by Geomedia. Academic Press, 349 (1998).
[5] Wheaton, V. et al.: Chem. Phys. Letters **371**, 349 (2003).

| ESRF | **Experiment title:** Complexation of uranyl to crown ethers: influence of solvent, concentration ratio and counter-ions | **Experiment number:** CH-2306 |
|---|---|---|
| **Beamline:** BM 20 | **Date of experiment:** from: 06.09.2006 to: 09.09.2006 | **Date of report:** 06.12.2006 |
| **Shifts:** 9 | **Local contact(s):** Dr. Christoph Hennig | *Received at ROBL:* |


**Names and affiliations of applicants** (* indicates experimentalists):

Drs. Kelly Servaes
Drs. Els Cartuyvels

K.U. Leuven
Chemistry Department
Molecular Design and Synthesis Division
Coordination Chemistry Group
Celestijnenlaan 200F
3001 Heverlee
Belgium


## Report:

The uranyl ion $UO_2^{2+}$ can easily form complexes with various types of ligands: small inorganic ligands (e.g.$NO_3^-$, $Cl^-$, $SO_4^{2-}$), small organic ligands (e.g. $CH_3COO^-$, $C_2O_4^{2-}$) or macrocyclic ligands (e.g. Schiff bases, crown ethers). Different types of crown ethers (dibenzo-18-crown-6, dibenzo-24-crown-6, dicyclohexano-18-crown-6,...) are used in solvent extraction processes to separate mixtures of actinides and rare earths.[1] Polymeric sorbents containing crown ethers in their chains are being used for the isolation of metals from natural waters and uranium from seawater.[1] Hitherto, the crystal structures of several uranyl crown ether complexes have been described in the literature, whilst studies in solution are scarce.[2-8] In the solid state, the inclusion of the uranyl ion in a crown ether (or azacrown) of appropriate size was already demonstrated by single crystal structure determinations.[3,4] But in solution, the uranyl inclusion is in competition with the solvation of the ligand cavity, as well as with the solvation of uranyl itself. The inclusion of a metal into the ring strongly depends on the used solvent.

In the past, we already studied the complexation of the uranyl ion with crown ethers in acetonitrile and propylene carbonate by UV-Vis absorption spectroscopy and magnetic circular dichroism (MCD).[9,10] These preliminary results about the coordination environment of the uranyl ion in crown ether complexes can be complemented by the structural data obtained by EXAFS.

The diameter of the oxacrown ether 18-crown-6 (2.6 - 3.2 Å) matches perfectly with the ion diameter of uranium(VI), e.g. 2.8 Å. Indeed, the vibrational fine structure in the UV-Vis absorption spectrum as well as the high luminescence intensity and the changes in the luminescence peak maxima point to the formation of an inclusion complex with $D_3$ coordination symmetry (Figure 1).[9,10]



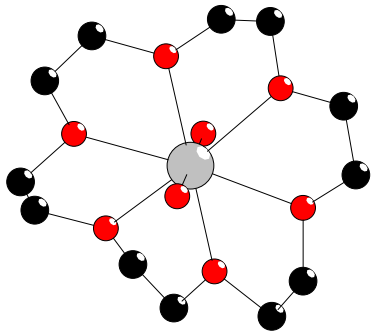

*Figure 1: The $[UO_2(18\text{-crown-}6)]^{2+}$ cation.*[11]

But when we replace the oxygen atoms in this 'ideal' ring by nitrogen, one finds a totally different story: very stable azacrown complexes are formed, where the ligands are externally coordinated, which is reflected by the structureless bands in the UV-Vis absorption spectra (Figure 2).[10]

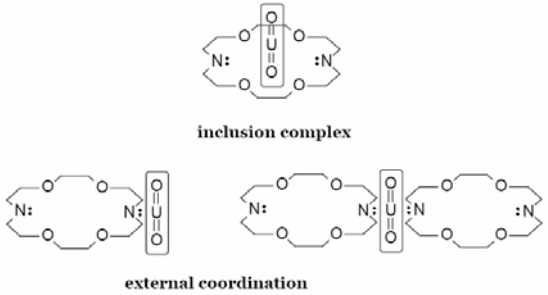


*Figure 2: Common structures of uranyl azacrown complexes.*

As already mentioned, the inclusion of a metal into the ring depends strongly on the used solvent. Indeed, uranyl inclusion complexes are not formed in aqueous solution.[8] Due to a high water content of 18-crown-6 (hygroscopic) we did not get the expected EXAFS spectrum for a $[UO_2(18\text{-crown-}6)]^{2+}$ inclusion complex. These problems can be avoided by using extra dry acetonitrile and 18-crown-6 and by working in a glove box.

**References**


1 Zolotov, Y.A. *Macrocyclic Compounds in Analytical Chemistry*, John Wiley & Sons, New York, **1997**.
2 Rogers, R.D.; Zhang, J.; Campbell, D.T. *J. Alloys Compd.* **1998**, *271*, 133.
3 Nierlich, M.; Sabattie, J.-M.; Keller, N.; Lance, M.; Vigner, J.-D. *Acta Cryst.* **1992**, *C50*, 52.
4 Deshayes, L.; Keller, N.; Lance, M.; Nierlich, M.; Vigner, D. *Acta Cryst.* **1993**, *C49*, 16.
5 Rogers, R.D.; Benning, M.M.; Etzenhouser, R.D.; Rollins, A.N. *J. Coord. Chem.* **1992**, *26*, 299.
6 Rogers, R.D.; Benning, M.M. *J. Incl. Phenom. Recognit. Chem.* **1991**, *11*, 121.
7 Rogers, R.D.; Bond, A.H.; Hipple, W.G.; Rollins, A.N.; Henry, R.F. *Inorg. Chem.* **1991**, *30*, 2671.
8 (a) Lagrange, J.; Metabanzoulou, J.P.; Fux, P.; Lagrange, P. *Polyhedron* **1989**, *8*, 2551. (b) Brighli, M.; Fux, P.; Lagrange, J.; Lagrange, P. *Inorg. Chem.* **1985**, *24*, 80. (c) Fux, P.; Lagrange, J.; Lagrange, P. *J. Am. Chem. Soc.* **1985**, *107*, 5927.
9 De Houwer, S.; Servaes, K.; Görller-Walrand, C. *Phys. Chem. Chem. Phys.* **2003**, *5*, 1164.
10 Servaes, K.; De Houwer, S.; Görller-Walrand, C.; Binnemans, K. *Phys. Chem. Chem. Phys.* **2004**, *6*, 2946.
11 Deshayes, L.; Keller, N.; Lance, M.; Navaza, A.; Nierlich, M.; Vigner, J. *Polyhedron* **1994**, *13*, 1725-1733.

| ESRF | **Experiment title:** EXAFS study of neptunium(V) sorption at $\alpha$-$Fe_2O_3$ | **Experiment number:** EC-23 |
|---|---|---|
| **Beamline:** BM 20 | **Date of experiment:** from: 28.06.06 to: 01.07.06 | **Date of report:** 06.12.2006 |
| **Shifts:** 9 | **Local contact(s):** André ROSSBERG | *Received at ROBL:* |

**Names and affiliations of applicants** (* indicates experimentalists):
S. AMAYRI*, M. BRECKHEIMER*, P. PAPAPETROU*§, T. REICH*
* Institute of Nuclear Chemistry, Johannes Gutenberg-Universität Mainz, Fritz-Strassmann-Weg 2, 55128 Mainz, Germany, § University of Western Ontario, Canada

## Report:

In rock systems, iron oxides are expected to play an important role in regulating the migration of radionuclides because of their widespread existence, high surface area, high sorptive capacity, and common occurrence as grain coatings. The aim of this study is to understand the sorption mechanism of neptunium(V) on $\alpha$-$Fe_2O_3$ (hematite) at a molecular level and to obtain spectroscopic evidence using EXAFS for the postulated ternary carbonate complexes (e.g. $\equiv FeONpO_2(O_2COH)_2^{2-}$) by Kohler et al. [1]. The sorption of Np(V) on synthetic $\alpha$-$Fe_2O_3$ (synthesis according to Schwertmann and Cornell [2]) has been investigated as a function of pH in the absence and presence of ambient $CO_2$. A detailed description of the sorption expereminets can be found elsewere [3].

Five EXAFS samples with different amounts of Np(V) sorbed were prepared from a 4.6 mM Np(V) stock solution of $^{237}Np$. The stock solution had been purified from traces of $^{239}Pu$ and $^{233}Pa$. The total Np(V) concentration in each sample was 8 µM. The neptunium loading of the samples was between 422-474 ppm. Three EXAFS samples labeled A, B, and C were prepared in the presence of ambient $CO_2$ at pH 7.0, 9.0, and 10.0, respectively. Samples D and E were prepared in a glove box under Ar atmosphere at pH 8.5 and 9.0, respectively. These samples can be compared with samples which were prepared in equilibrium with air. For EXAFS investigations at room temperature, centrifuged wet $\alpha$-$Fe_2O_3$ pastes were loaded into standard Perspex sample holders with Kapton windows for EXAFS analysis. For measurements at 13 K, the solid residues were dried and loaded into a polyethylene sample holder. The EXAFS spectra were collected at the Np $L_{III}$-edge (17610 eV) at room/low temperature (see Tab. 1, Fig. 1) using a Canberra 13-element Ge detector. Chromium foils were used to reject Fe $K_\alpha$ fluorescence from the samples. The raw Np $L_{III}$-edge data were analyzed using the EXAFSPAK software [4]. Backscattering phase and amplitude functions required for fitting the spectra were obtained from FEFF 8.20 calculations [5] using the crystal structure of iron(III) uranium oxide [6], where U was replaced by Np to model a possible Np-Fe interaction with the hematite surface. The EXAFS spectra of all samples show similar oscillations, indicating similar neptunium near-neighbor surroundings. According to the fit results (Tab.1), the structural model of possible Np(V) surface species on hematite is shown in Fig 2. One possible bidentate inner-sphere structural model implying an edge sharing between the Np(V) and Fe octahedra was developed on the basis of structural parameters determined by EXAFS. Figure 2 (left) shows the coordination of Np(V) sorbed on hematite if the angel (Np, Fe, $O_{(FeO6)}$) is ~ 60°. In this study the distances of the coordination shells Np-$O_{ax}$, Np-$O_{eq}$, and Np-Fe measured by EXAFS suggest that Np(V) was bonded in an inner-sphere fashion. This is based on the presence of a Np-Fe interaction near 3.46 Å. This distance is in accord with an edge-sharing, bidentate surface complex. In the presence/absence of atmospheric $CO_2$, the average Np-$O_{eq}$ distances are the same in all samples and much shorter than in $NpO_2(CO_3)_3^{5-}$. There is no evidence of the formation of Np(V) carbonato species at the hematite surface, that means there is no finding regarding the ternary carbonate complexes (e.g. $\equiv FeONpO_2(O_2COH)_2^{2-}$) postulated by Kohler et al. [1]. There was no evidence for Np neighbors in the EXAFS spectra, suggesting that the sorbed Np(V) complexes were predominantly monomeric.

**Figure 1.** Np $L_{III}$-edge $k^3$-weighted EXAFS spectra (left) and the corresponding Fourier transforms (right) for Np(V) sorbed on hematite.

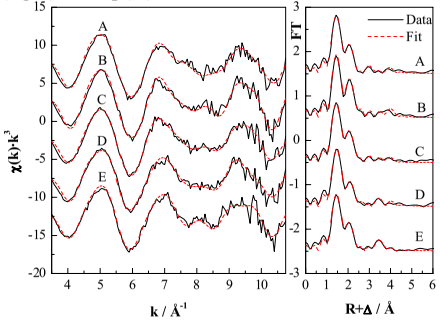


**Figure 2.** Schematic diagram illustrating a possible Np(V) coordination environment on the hematite surface (left) and the arrangement of the $FeO_6$ octahedra in the hematite structure (right).

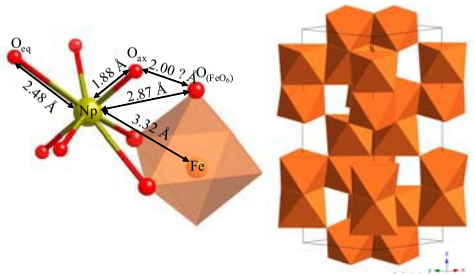


**Table 1.** EXAFS fit results ($\Delta R = \pm 0.02$ Å, $\Delta\sigma^2 = 0.001$ Å$^2$, RT-Room temperature).

| Sample | Description | 2x(Np-$O_{ax}$) | | 4x(Np-$O_{eq}$) | | 2x(Np-O) | | 0.5x(Np-Fe) | | $\Delta E_0$/ eV |
|---|---|---|---|---|---|---|---|---|---|---|
| | | R/Å | $\sigma^2$/Å$^2$ | R/Å | $\sigma^2$/Å$^2$ | R/Å | $\sigma^2$/Å$^2$ | R/Å | $\sigma^2$/Å$^2$ | |
| **A** | pH 7.0, air, RT | 1.87 | 0.003 | 2.48 | 0.010 | 2.86 | 0.016 | 3.43 | 0.006 | 5.7 |
| **B** | pH 9.0, air, 13 K | 1.88 | 0.002 | 2.48 | 0.006 | 2.84 | 0.010 | 3.44 | 0.011 | 7.0 |
| **C** | pH 10.0, air, RT | 1.87 | 0.003 | 2.46 | 0.009 | 2.86 | 0.013 | 3.46 | 0.014 | 4.2 |
| **D** | pH 8.5, argon, RT | 1.88 | 0.003 | 2.49 | 0.013 | 2.87 | 0.010 | 3.74 | 0.003 | 7.2 |
| **E** | pH 9.0, argon, 13 K | 1.87 | 0.003 | 2.46 | 0.010 | 2.84 | 0.015 | 3.73 | 0.002 | 5.1 |
| **[7]** | $NpO_2(H_2O)_4^+$ | 1.82 | 0.002 | 2.49 | 0.006 | - | - | - | - | - |
| **[8]** | $NpO_2(CO_3)_3^{5-}$ | 1.86 | 0.001 | 2.53 | 0.013 | - | - | - | - | - |

**Acknowledgement**
This work was supported by Bundesministerium für Wirtschaft und Technologie (BMWi) under contract No. 02E9653. We acknowledge the ESRF for provision of synchrotron beam time and thank A. Rossberg, C. Hennig, H. Funke, and A. Scheinost from Forschungszentrum Dresden-Rossendorf for assistance in using beamline BM20.

**References**

[1] M. Kohler, B.D. Honeyman et al., Radiochim. Acta **85**, 33-48 (1999).
[2] U. Schwertmann and R.M. Cornell, Iron Oxides in the Laboratory, Wiley-VCH, Weinheim (2000).
[3] S. Amayri, M. Breckheimer et al., Proc. of Actinide-XAS-2006 Workshop, NEA-OECD (in press).
[4] G.N. George and I.J. Pickering, EXAFSPAK: A suite of computer programs for analysis of X-ray absorption spectra; Stanford Synchrotron Radiation Laboratory, Stanford, CA, USA (1995).
[5] A.L. Ankudinov, C.E. Bouldin et al., Phys. Rev. B **65** (10), 104107/1-11 (2002).
[6] M. Bacmann and E.F. Bertaut, Bull. Soc. Franc. Mineral. Crist. B **90**, 257-258 (1967).
[7] T. Reich, G. Bernhard et al., Radiochim. Acta **88**, 633-637 (2000).
[8] D.L. Clark, S.D. Conradson et al., J. Am. Chem. Soc. **118**, 2089-2090 (1996).

| ESRF | **Experiment title:** Local environment of Pu in borosilicate glass | **Experiment number:** ME-938 |
|---|---|---|
| **Beamline:** BM 20 | **Date of experiment:** from: 02.02.2005 to: 05.02.2005 | **Date of report:** |
| **Shifts: 6** | **Local contact(s): A. Hennig** | *Received at ROBL:* |

**Names and affiliations of applicants** (* indicates experimentalists):

Deschanels Xavier[(*a)], Den Auwer Christophe[(*a)], Cachia Jean-Nicolas[(*a)], Glorieux Benoît[(*b)], Picot Valérie[(*c)]

[(a)] CEA Valrhô/Marcoule, [(b)]CNRS/PROMES Perpignan, [(c)] CNRS/CERI Orléans

## Context :

A possible plutonium management solution consists in conditioning it in a borosilicate glass. In this framework, the effect of the temperature and redox conditions on the solubility of plutonium and surrogates during glass processing were studied. Previous works have shown that the trivalent elements (Nd, La, Gd..) exhibit higher solubility than the tetravalent elements (Hf, Th, Pu) in this matrix [1]. The greatest increase in solubility was observed for cerium: the higher solubility limit was attributable not only to the higher temperature processing but also to the reduction of this element at the trivalent state. These results show that oxidation state and processing temperature are two correlated parameters. In order to determine which one is the most important parameter for the Ce solubility increase, a glass was melted under reductive conditions at 1100°C with silicon nitride addition. In these conditions, the cerium solubility was multiplied by 20 and XANES characterization of this glass indicated a complete reduction of the cerium in this sample. Pu as Ce can tune its oxidation state from (IV) to (III) in the glass. In the continuity of the study undertaken for Ce, we have fabricated glasses doped with Pu under reductive conditions.

A first goal of our analysis is to check the reduction of Pu in the glasses fabricated under reductive conditions. A second one is to have a better understanding of structural role of trivalent plutonium in the glass network. For that, XAFS and NMR investigation were undertaken. The structural data obtained by XAFS analysis (bond length and coordination) for actinides and surrogates were used to calculate the field strenght parameter $Z/d^2$ defined by Dietzel. According to this model, all these elements are characterized by intermediate field strengtht i.e. that they have an intermediate role in the glass network [2]. However there is a significant difference between the trivalent and tetravalent elements: the former resemble the network-modifying elements by their field strength, while the latter are closer to the network-forming elements. A correlation was established between the field strength and the solubility limits of the elements: the greater the field strength, the lower the solubility of the relevant element.



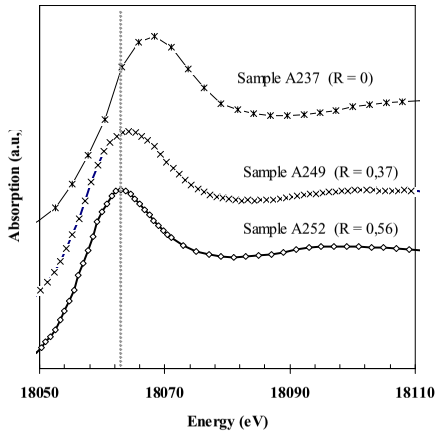


***Figure 1**. Comparison Pu $L_{III}$-edge XANES spectra in glass produced under oxidizing conditions (A237) and reducing conditions (A249 and A252). R corresponds to the $(m_{Si_3N_4})/(m_{PuO_2})$ mass ratio.*

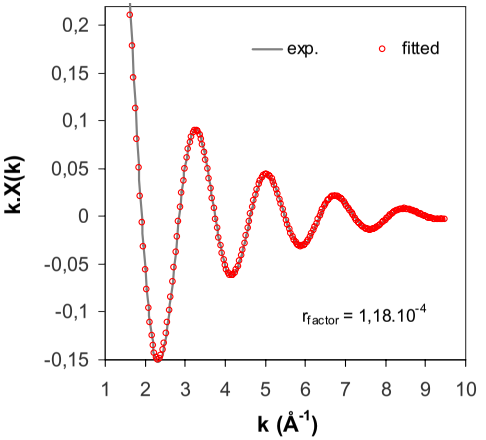


***Figure 2**. Comparison between experimental Pu(III) XAFS spectra in a borosilicate glass and fitted spectra with $PuO_2$ reference compound.*

## Results :

The fabrication at 1400°C of plutonium-doped glasses under reductive conditions increased the solubility of this element up to 4 wt% $PuO_2$ without reaching the solubility limit. At the same temperature, the solubility limit of plutonium-doped glasses under oxidizing conditions is 2 wt% $PuO_2$ [3]. XANES analysis showed plutonium reduction in the glass produced under reducing conditions (Figure 1).

The best fit of the experimental spectra for Pu(III) in borosilicate glass was obtained using $PuO_2$ reference compound (Figure 2). The first-neighbour shell consists of 8±2 oxygen atoms at a distance of 2.33±0.02Å. These results confirm the network-modifying role of the trivalent plutonium in the glass network and they also confirm the correlation between the field strength as defined by Dietzel and the solubility limit of the elements (Figure 3).

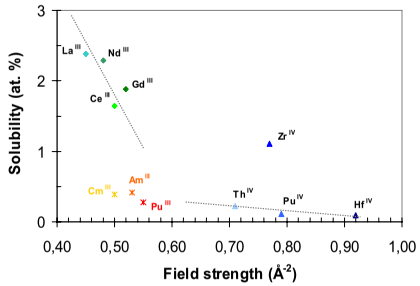


***Figure 3**. Correlation between the field strenght and the solubilty limit of different elements.*

1. J-N. Cachia (2005), PhD thesis, University of Montpellier.
2. A. Dietzel, *Z. Electrochemie* 48 (1942).
3. J-N Cachia, X. Deschanels, C. Den Auwer, O. Pinet, J. Phalippou, C. Hennig, A. Scheinost, accepted for publication in *J. Nucl. Mater, Numa 42055.*

| ESRF | **Experiment title:** Xas study of uranium and plutonium local environment in $Cr_2O_3$-doped $(U_{1-y},Pu_y)O_2$ (y=0,11 et 0,275) mixed oxide | **Experiment number:** ME-939 |
|---|---|---|
| **Beamline:** BM 20 | **Date of experiment:** from: 02 March 2005 to: 04 March 2005 | **Date of report:** 31/08/2005 |
| **Shifts:** 6 | **Local contact(s):** Dr. HENNIG C., Dr. FUNKE H. | *Received at ESRF:* |

**Names and affiliations of applicants** (* indicates experimentalists):

* PIERAGNOLI A., * Dr. MARTIN P., * Dr. RIPERT M., * Dr. PALANCHER H., * LECHELLE. J.
Centre du CEA de Cadarache DEN/DEC, F-13108 Saint Paul Lez Durance Cedex

## Report:

The next generations of nuclear power plant (LWR, HTR, GFR) will use, gradually, on mixed uranium and plutonium oxide as the ceramic fuel, namely MOX (Mixed OXide) of generic formula $(U_{1-y},Pu_y)O_2$. Currently, some nuclear reactors already use this kind of fuel which usually contains 4 to 9 Pu wt%. In $UO_2$ fuel, the fissile isotope is $U^{235}$ which is dispersed homogeneously in the ceramic lattice. In the case of MOX fuel, Pu isotopes are the fissile atoms. To take advantage of the $UO_2$ fuel acquired experience, Pu should be dispersed as homogeneously as possible in a $(U,Pu)O_2$ solid solution. Fuel designers and manufacturers are focused on Pu-rich oxide fuel with a fraction of Pu higher than 10 Pu wt% and the improvement of the Pu distribution.

An optimization of the process conditions could allow us to reach this objective. On the whole, the manufacture of MOX fuel consists in $UO_2$ and $PuO_2$ powders co-crushing, milling, pelletizing and sintering. With this method, a fluorite-type solid solution $(U,Pu)O_2$ might be obtained. The formation of the solid solution, with a Pu ratio between 0 and 100%, is thermodynamically allowed but kinetically slow due to the powder process of milling and to the thermal treatment of sintering.Industrualy, to keep the compacting ability of a pure $UO_2$ powder, a powder co-crushing of $UO_2$-$PuO_2$ with high $PuO_2$ content is softly mixed with pure $UO_2$. Thus, pellets made with this raw materials are constituted of $UO_2$ and $PuO_2$ closely mixed aggregates diluted in a majority phase of $UO_2$. In order to improve compatibility between fuel, clad and coolant, the MOX is usually made with an O/(U+Pu) ratio of 2.00. To get this stoichiometry, it is necessary to maintain a reducing atmosphere in the sintering furnace with a mixture of Ar-$H_2$-$H_2O$ ($\Delta GO_2$ between –350 and –500 kJ/mol at 1700-1750°C). At this oxygen potential, the diffusion coefficients of U and Pu in the $(U,Pu)O_2$ ceramic are still small. In these conditions, a density close to 95% of the theoretical one can be reached with a grain size sightly smaller than 10 $\mu$m and the phenomenon of homogenisation are limited, two phases with high and low Pu concentration still remaining.

Although encouraging results were reported for coarse-grained and homogeneous MOX in the case of an oxidizing sintering, this approach has been avoided due to an incompatibility with the current technology of the industrial furnaces. Positive results were obtained for coarse-grained $UO_2$ by the addition of $Nb_2O_5$, MgO, $Al_2O_3$, $V_2O_5$, $TiO_2$ or $Cr_2O_3$ and for coarse-grained and homogeneous MOX by the addition of $TiO_2$, $Cr_2O_3$ or UOS. **The aim of this study is therefore to examine the impact on the Pu distribution of one of these dopants, i.e. $Cr_2O_3$ when it is introduced up to 2000 ppm as a powder during the $UO_2$-$PuO_2$ milling.** Under the temperature and atmosphere conditions used during sintering, $Cr_2O_3$ is particularly interesting because of its property to give rise to a liquid phase (eutectic $Cr_s$+$Cr_3O_{4s}$ →$CrO_l$) which usually helps grain growth. Moreover, the possible presence of $Cr^{3+}$ in the fluorine lattice of $(U,Pu)O_2$ could increase the default concentration and enhance the Pu distribution. A PhD thesis is ongoing to determine the mechanisms of the solid solution formation in presence of chromium.

However we had to verify the formation of a $(U,Pu)O_2$ solid solution in the presence of $Cr^{3+}$ dopant (introduced under chromium sesquioxide, $Cr_2O_3$, form). EXAFS turned out to be a key technique to probe Pu and U environnements and to evaluate the structural order [1].

During our experiment, we analysed samples obtained by the usual powder process the plutonium content of which was equal to 11 wt% (two samples, *a* and *b1*) and 27.5 wt% (one sample, *b2*). For the 11 wt% sample, two ways of synthesis, co-crushing (*b1*) and micronization of a master blend (*a*), have been investigated to determine, during sintering, the impact of mixing on the $(U,Pu)O_2$ microstructure. As it has been shown for the face centred cubic structure $(U,Pu)O_2$, the cell parameter of the solid solution obeys a Vegard's law: $a_{(U1-y,Puy)O2-x}$ = 5,470 - 0,074y + 0,32x (Å)

| % Pu | a (Vegard's law) (Å) | First shell Metal-O (Å) | Second shell Metal-Metal (Å) | Third shell Metal-O (Å) |
|---|---|---|---|---|
| 0 | 5,4700 | 2.369 | 3.868 | 4.535 |
| 11 | 5.4619 | 2.365 | 3.862 | 4.529 |
| 27.5 | 5.4497 | 2.360 | 3.854 | 4.519 |
| 100 | 5.3960 | 2.337 | 3.817 | 4.475 |

For each sample, fluorescence and transmission signals were collected at the uranium (17.126 keV) and plutonium (18.056 keV) $L_{III}$ edges. Energy calibration of XANES data was achieved using the Y foil (17.052 keV) and Zr foil (17.998 keV) references positioned behind the second ionisation chamber. As observed on these XANES spectra, the positions of the white lines are those of the $UO_2$ at the uranium edge, and those of $PuO_2$ at the plutonium edge. Thus, whatever the plutonium content is, the oxidation state of uranium and plutonium remains equal to +IV. At the uranium $L_{III}$ edge, EXAFS spectra were collected up to 15 $Å^{-1}$ but only up to 10.5 $Å^{-1}$at the plutonium $L_{III}$ edge. This limitation is due to the presence in the samples of small amount of americium induced by the used plutonium isotopy (americium $L_{III}$ edge: 18.514 keV).

The evolution of the Fourrier transforms are summarised on the figures 1 and 2.

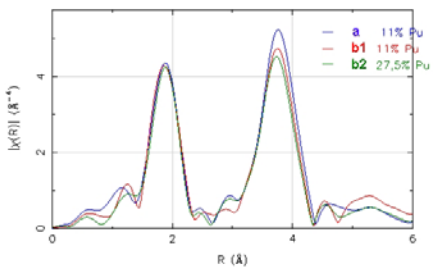


*Figure 1 : Fourier transforms of the uranium $L_{III}$ edge EXAFS (k-range: 3 – 12.6 $Å^{-1}$).*

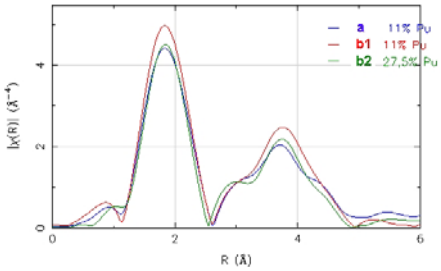


*Figure 2 : Fourier transforms of the plutonium $L_{III}$ edge EXAFS (k-range: 2 – 10.5 $Å^{-1}$).*

At uranium and plutonium $L_{III}$ edges, best fits were obtained, in each case, after the introduction of an additionnal asymmetry term (third cumulant) to describe the first Metal-O shell. For the first three shells, refined distances are in good agreement with those derived from Vegard's law (see table above). This is the signature of the presence of an $(U,Pu)O_2$ solid solution. Whatever the process and the plutonium content (11% or 27.5%) are, the addition of $Cr^{3+}$ dopant during the synthesis is favourable. In comparison with the spectra obtained on wet route solid solution (co-precipitated, without any dopant and at low temperature) [1], the addition of $Cr^{3+}$ and the different ways of synthesis show that the structure is better ordered. For the first shell (Metal–O) Debye-Waller factors remain low (0.007 $Å^2$) and far below those measured on wet $(U,Pu)O_2$ prepared without additive [1].

At the end of the allocated beam time, a test at chromiun (5.989 keV) K edge was performed. However, a fluorescence signal of too low intensity was collected. Together with the beamline staff, we are already working on instrumental optimization in order to perform successful measurements at low energies. Indeed, a better knowledge of Cr behaviour (quantity of residual Cr and its chemical environnement) in the fuel would allow us to understand the responsible mechanism for the solide solution development. Beamtime has already been allocated for this project [2].

[1] : P.Martin, M.Ripert, G.Carlot, S.Grandjean, T.Petit, P.Blanc (2002) *experimental report* ME-312.
[2] : A.Pieragnoli, J.Lechelle, P.Martin, H.Palancher, M.Ripert, C.Valot (2005) *proposal* ME-1256.

| ESRF | **Experiment title:** EXAFS study of neptunium(V) uptake by kaolinite | **Experiment number:** ME - 1090 |
|---|---|---|
| **Beamline:** BM20 | **Date of experiment:** from: 17/06/2005 to: 20/06/2005 | **Date of report:** 27/02/2006 |
| **Shifts:** 9 | **Local contact(s):** Harald FUNKE | *Received at ESRF:* |


**Names and affiliations of applicants** (* indicates experimentalists):

Samer AMAYRI*, Aleksandr JERMOLAJEV*, James R. KASBOHM*§, Tatiana REICH*, Tobias REICH*

*Institute of Nuclear Chemistry, Johannes Gutenberg-Universität Mainz, Fritz-Strassmann-Weg 2, 55128 Mainz, Germany, § University of Arkansas at Fayetteville, USA


## Report:

The sorption of Np(V) on kaolinite has been investigated as a function of pH in the absence and presence of ambient $CO_2$. Seven samples with different amounts of Np(V) sorbed were prepared from a 1.1 mM Np(V) stock solution of $^{237}$Np. The stock solution had been purified from traces of $^{239}$Pu and $^{233}$Pa. 200 mg kaolinite KGa-1b (Source Clays Repository) were suspended in 50 mL deionized water. The ionic strength was 0.1 M $NaClO_4$. The pH was adjusted using NaOH and $HClO_4$. Samples A, B, and C were prepared in the presence of ambient $CO_2$ at pH 8.0, 9.0, and 10.0, respectively. Samples D, E, F, and G were prepared in a glove box with Ar atmosphere at pH 8.0, 9.0, 10.0, and 10.5, respectively. These samples can be compared with samples A - C prepared in equilibrium with air. After shaking the kaolinite suspensions for 72 hours, aliquots of the Np(V) stock solution were added with immediate readjustment of the pH. The total neptunium concentration in each sample was $8 \cdot 10^{-6}$ mol/L. After a contact time of 72 hours, the solid and liquid phases were separated by centrifugation at 4025 g for seven minutes. The neptunium uptake was determined by measuring the neptunium concentration in solution by liquid scintillation counting. The solid residues were loaded without drying into EXAFS sample holders. Table 1 summarizes the preparation conditions of samples A – G and the amount of neptunium sorbed in each sample.

**Table 1.** Summary of the wet-paste samples prepared at $8 \cdot 10^{-6}$ M Np(V) and 0.1 M $NaClO_4$ for EXAFS measurements.

| Sample | $CO_2$/Ar | pH | Np loading / ppm | T/K | No. of sweeps |
|---|---|---|---|---|---|
| A | Air | 8.0 | 240 | 293 | 8 |
| B | Air | 9.0 | 330 | 25 | 12 |
| C | Air | 10.0 | 190 | 293 | 6 |
| D | $CO_2$-free | 8.0 | 70 | 293 | 2 |
| E | $CO_2$-free | 9.0 | 215 | 293 | 7 |
| F | $CO_2$-free | 10.0 | 380 | 293 | 3 |
| G | $CO_2$-free | 10.5 | 430 | 293 | 7 |

Since kaolinite KGa-1b contains traces of zirconium, the EXAFS spectra were collected at the Np $L_2$-edge (21.6 keV) and not at the $L_3$-edge. The energy of the single-channel analyzers (SCA) of the 13-element Ge solid-state detector was set to 17.8 keV for recording the Np $L\beta_1$ fluorescence radiation. Except for sample B, which was measured at 25 K, all samples were studied at room temperature. The SCA signals were corrected for detector dead time using the measured total incoming count rates. EXAFS analysis was performed with the software packages EXAFSPAK [1] and FEFF8.20 [2]. The scattering phases and amplitudes were calculated using the crystal structures of $NaNpO_2(CO_3)$ [3] and $(UO_2)_2SiO_4 \cdot 2H_2O$ [4], where U was replaced by Np to model a possible Np-Si/Al interaction with the kaolinite surface.

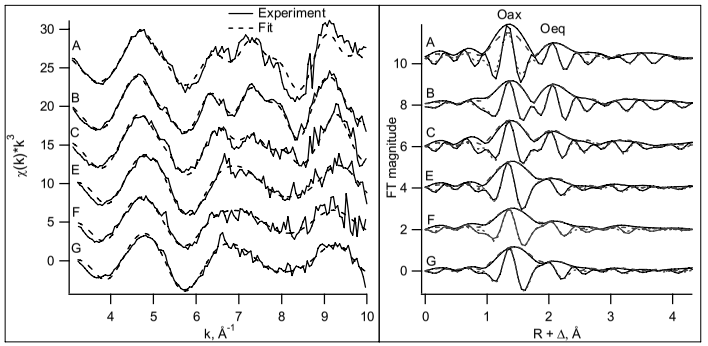


**Figure 1.** Np $L_2$-edge $k^3$-weighted EXAFS spectra (left) and the corresponding Fourier transform magnitudes and real parts (right) of samples A-C and E-G.

Figure 1 shows the raw Np $L_2$-edge $k^3$-weighted EXAFS data, the best theoretical model, and the corresponding Fourier transforms. The spectrum of sample D has not been included in Fig. 1 due to the low-signal-to-noise ratio. As can be seen from Fig. 1, samples A – C prepared in the presence of $CO_2$ show a different EXAFS pattern compared to samples E – G. Table 2 summarizes the metrical parameters derived from the EXAFS fits. The neptunium coordination shells and bond distances of samples A, B, and C are consistent with the formation of a Np(V) carbonato species at the kaolinite surface due to precipitation (see also the previous feasibility study 20-01-637). Due to a poor signal-to-noise ratio in the spectra E – G, only axial and equatorial oxygen coordination shells of Np, $O_{ax}$ and $O_{eq}$, respectively, could be analyzed. The average Np-$O_{eq}$ bond distance of samples E and G is somewhat shorter than in the Np(V) aquo ion (see Tab. 2). This could indicate the existence of a Np(V) hydrolysis species at pH ≥ 9.0 at the kaolinite surface. Unfortunately, the data quality does not allow concluding on inner-sphere versus outer-sphere Np(V) sorption to kaolnite in the $CO_2$-free system.

**Table 2.** EXAFS metrical parameters for sorption samples A - C and E - G. Multiple-scattering paths are not listed. Coordination numbers were held constant during the final fit according to the results of previous fits. Distances R are given in Å and Debye-Waller factors $\sigma^2$ in Å$^2$. Comparison with literature: a) ref. 5, b) ref 6.

| Sample | 2 $O_{ax}$ | | 4 $O_{eq}$ | | 2 C | | 2 $O_{dis}$ | | 1 Np | | $\Delta E_0$/eV | Error |
|---|---|---|---|---|---|---|---|---|---|---|---|---|
| | R | $\sigma^2$ | R | $\sigma^2$ | R | $\sigma^2$ | R | $\sigma^2$ | R | $\sigma^2$ | | |
| A | 1.84 | 0.0028 | 2.56 | 0.0077 | 3.00 | 0.0036 | 4.25 | 0.0058 | 4.90 | 0.0028 | 0.7 | 1.13 |
| B | 1.85 | 0.0037 | 2.57 | 0.0037 | 2.97 | 0.0012 | 4.28 | 0.0033 | 4.88 | 0.0030 | 0.3 | 0.184 |
| C | 1.86 | 0.0025 | 2.52 | 0.0062 | 2.90 | 0.0033 | 4.23 | 0.0102 | 4.88 | 0.0031 | 0.8 | 0.558 |
| E | 1.85 | 0.0025 | 2.45 | 0.0125 | - | - | - | - | - | - | 0.4 | 0.403 |
| F | 1.86 | 0.0051 | 2.50 | 0.0172 | - | - | - | - | - | - | 0.4 | 0.595 |
| G | 1.87 | 0.0033 | 2.47 | 0.0126 | - | - | - | - | - | - | 1.1 | 0.285 |
| [a] $NpO_2(H_2O)_4^+$ | 1.82 | 0.0023 | 2.49 | 0.006 | - | - | - | - | - | - | - | - |
| [b] $NpO_2(CO_3)_3^{5-}$ | 1.86 | 0.001 | 2.53 | 0.013 | 2.98 | 0.0004 | 4.22 | Na | - | - | - | - |


**Acknowledgement**

This work was supported by the German Bundesministerium für Wirtschaft (Project 02 E 9653). We acknowledge the ESRF for provision of synchrotron beam time and thank H. Funke, C. Hennig, A. Roßberg, and A. Scheinost from Forschungszentrum Rossendorf for assistance in using beamline BM20.


**References**


[1] G. N. George, I.J. Pickering, EXAFSPAK – A suite of computer programs for analysis of X-ray absorption spectra, SSRL (2000).
[2] A. L. Ankudinov et al., Phys. Rev. B 65 (2002) 104107.
[3] Yu. F. Volkov et. al., Radiokhimiya 21 (1979) 668.
[4] F. Demartin et al., Acta Cryst. C 48 (1992) 1.
[5] T. Reich et al., Radiochim. Acta 88 (2000) 633.
[6] D. L. Clark et al., J. Am. Chem. Soc. 118 (1996) 2089.

| ESRF | **Experiment title:** XAS study of chromium in MOX fuel | **Experiment number:** ME-1256 |
|---|---|---|
| **Beamline:** BM 20 | **Date of experiment:** from: 06.12.06 to: 10.12.06 | **Date of report:** 22.01.2007 |
| **Shifts:** 12 | **Local contact(s):** A. Scheinost. | *Received at ESRF:* |

**Names and affiliations of applicants** (* indicates experimentalists):
* PIERAGNOLI A., * Dr. LECHELLE. J., * CECILILA G., * BEAUGELIN P., * Dr. MARTIN P.
Centre du CEA de Cadarache DEN/DEC, F-13108 Saint Paul Lez Durance Cedex

## Report:

High local Pu concentrations and fission gas release in the mixed uranium oxide-plutonium oxide (MOX) fuels irradiated to high burn-ups significantly affect the fuel performances. On the whole, the manufacture of MOX fuel consists in $UO_2$ and $PuO_2$ powders co-crushing, milling, pelletizing and sintering. An evolution of the manufacture route giving rise to a microstructure optimization of nuclear fuel pellets could allow us to improve the fuel performance.

Pu should be dispersed as homogeneously as possible in a $(U,Pu)O_2$ solid solution by an enhanced powder process. In this aim, several doping agents have been studied. Encouraging results were reported for coarse-grained $UO_2$ by the addition at low concentration of $Nb_2O_5$, MgO, $Al_2O_3$, $V_2O_5$, $TiO_2$ or $Cr_2O_3$. In the case of $Cr_2O_3$, the first results for MOX show an increase on grain size and, above all, an increase of the Pu spreading. Pu distribution and grain size are both key parameters to reach high burn-ups.

Under the temperature and atmosphere conditions used during sintering, $Cr_2O_3$ is particularly interesting because of its property to give rise to a liquid phase (eutectic $Cr_s+Cr_3O_{4s} \rightarrow CrO_l$) which usually helps grain growth. Moreover, the possible presence of $Cr^{3+}$ in the fluorine lattice of $(U,Pu)O_2$ could increase point defect concentration and enhance Pu diffusion. A specificity of the Cr-doping in presence of plutonium is the formation of a line compound the composition of which is $PuCrO_3$. It is the main difference between the U-O-Cr system and the Pu-O-Cr one at the temperature and atmosphere used during sintering. A PhD thesis is ongoing to determine the mechanisms allowing the microstructure enhancement of a Cr-doped MOX pellet.

**The aim of this study is therefore to examine $Cr_2O_3$ impact on Pu distribution when the dopant is introduced up to 2000 ppm as a powder during the $UO_2$-$PuO_2$ milling and to determine the sintering temperature dependence.** We had to verify the formation of a $(U,Pu)O_2$ solid solution in the presence of a doping agent (introduced under chromium sesquioxide form) and determine the oxidation states of U and Pu. **Moreover, we want to improve our knowledge of the crystallographic structure of $PuCrO_3$ and obtain data on oxidation states of Pu and Cr in this compound.** EXAFS turned out to be a key technique to probe Pu and U environments or oxidation states and to evaluate the structural order.

During our experiment, we analyzed three samples with 2000 ppm of $Cr_2O_3$, *Mic55, Mic67 and Mic7540*, obtained by the usual MOX powder process (*MIMAS, micronization of a master blend*) for a sintering temperature of respectively 1530°C, 1630°C and 1700°C. The Pu/(U+Pu) ratio of the samples was equal to 11 wt%.

A $PuCrO_3$ sample was analyzed. $PuCrO_3$ had been obtained by sintering a $PuO_2$-$Cr_2O_3$ powder mixture heated at 1700°C under argon. A small amount (less than 3 wt%) of $PuO_2$ and amorphous chromium oxide still remained after the thermal treatment. Prior to the experiment, $PuCrO_3$ crystal structure was investigated by XRD. The first results are summarized in this table :

| | | | |
|---|---|---|---|
| Pbnm | a = 5.439 Å | b = 5.498 Å | c = 7.720 Å |
| | Cr-O = 1.97 Å | Pu-O = 2.34 - 2.66 Å | Pu-Cr = 3.19 Å |

For each sample, fluorescence and transmission signals were collected at the uranium (17.126 keV) $L_{III}$ edges, plutonium (18.056 keV) $L_{III}$ and (22.266 keV) $L_{II}$ edges and chromium (5.989 keV) K edge. Energy calibration of XANES data was achieved using the Cr foil (5.989 keV), Y foil (17.052 keV), Zr foil (17.998 keV) and Rh foil (23.220 keV) references located behind the second ionization chamber. As observed on these XANES spectra, the white line positions are those of the $UO_2$ at the uranium edge, and those of $PuO_2$ at the plutonium edge.

At the uranium $L_{III}$ edge, EXAFS spectra were collected up to 15 $Å^{-1}$ but only up to 10.5 $Å^{-1}$ at the plutonium $L_{III}$ edge and 13.5 $Å^{-1}$ at the plutonium $L_{II}$ edge. The plutonium $L_{III}$ edge limitation is due to the presence of a small amount of americium ($L_{III}$ edge at 18.514 keV) in the samples (induced by the used plutonium isotopy). At the chromium K edge, EXAFS spectra were collected up to 12.5 $Å^{-1}$ and show a non-linear decrease after the edge. **In MOX, whatever the sintering temperature is, the oxidation state of uranium and plutonium remains equal to +IV, the oxidation state of chromium is +III.**

**In $PuCrO_3$, plutonium and chromium are both at the oxidation state +III.** These results are summarized on in figure 1 for the four samples. $Cr_2O_3$ XANES are added as references for $Cr^{3+}$.No combination of the $Cr_2O_3$ and the $PuCrO_3$ XANES allow us to reproduce correctly the XANES of the chromium in the MOX. Considering the absence of the two peaks observed in $Cr_2O_3$ white line and the differences with $PuCrO_3$ in each chromium XANES, the main chromium amount in the MOX microstructure is certainly dissolved in the fluorine lattice of $(U,Pu)O_2$ (after sintering between 1530°C and 1700°C). **In a Cr-doped MOX, the local environment of chromium changes gradually with the increase of the sintering temperature.**

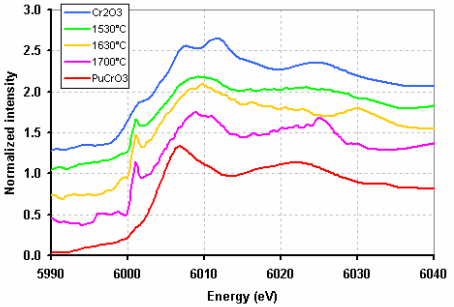


*Figure 1 : XANES spectra at the chromium (5.989 kev) K edge.*

Fourier transforms of EXAFS spectra collected at uranium $L_{III}$ edges and plutonium $L_{II}$ edges are given in figure 2 and 3. For both edges, the first peak which corresponds to the Metal-Oxygen shell, is similar for each of the MOX samples and is characteristic of a stoichiometric oxide with an O to M ratio equal to 2. The second peak which corresponds to the Metal-Metal shell, shows differences between uranium and plutonium. Indeed, in the uranium case, all samples give rise to a second peak which is close to that obtained for $UO_2$ powder, indicating that the uranium environment in $UO_2$ and $U_{0.89}Pu_{0.11}O_2$ is equivalent due to an $UO_2$ matrix effect. In the plutonium case , the large range of plutonium concentration due to the synthesis process (a high plutonium concentrated powder mixture diluted in $UO_2$), results in a broadening of the peak [1], [2]. The temperature moderates this phenomenon by a more even plutonium spreading in presence of the doping agent. **This accounts for an increase with the temperature of the $(U,Pu)O_2$ solid solution homogeneity in presence of a small amount, 2000 ppm, of $Cr_2O_3$.**

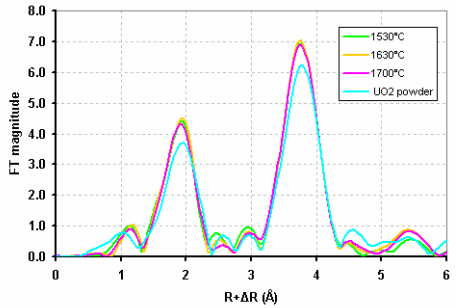


*Figure 2 : Fourier transforms of the uranium $L_{III}$ edge EXAFS (k-range: 3 – 12.6 $Å^{-1}$).*

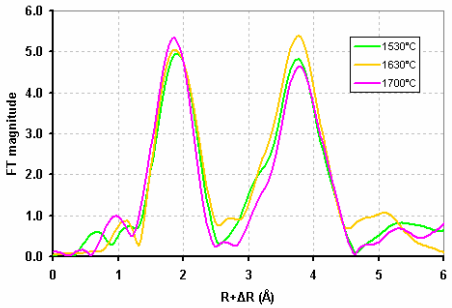


*Figure 3 : Fourier transforms of the plutonium $L_{II}$ edge EXAFS (k-range: 3 – 11.9 $Å^{-1}$).*

During this experiment, we have been able to determine plutonium, uranium and chromium oxidation states and local environments in enhanced MOX fuel. The homogeneity of the Cr-doped $(U,Pu)O_2$ solid solution with temperature was followed through by EXAFS. Finally, it appears that the environment of chromium added in the MOX powder evolves with the sintering temperature.

[1] : A.Pieragnoli, P.Martin, M.Ripert, H.Palancher, J.Lechelle (2005) *experimental report* ME-939.
[2] : P.Martin, S.Grandjean, C.Valot, G.Carlot, M.Ripert, P.Blanc, C.Hennig (2007) *XAS study of $(U_{1-y}Pu_y)O_2$ solid solutions* accepted and to be published in Journal of Alloys and Compounds.

| ESRF | **Experiment title:** **Study of the sorption mechanisms of selenium and cesium onto magnetite as steel corrosion product of radioactive waste canisters.** | **Experiment number:** **SI-1174** |
|---|---|---|
| **Beamline:** BM 20 | **Date of experiment:** from: 07.05.2005 to: 10.05.2005 | **Date of report:** March 2006 |
| **Shifts:** 9 | **Local contact(s):** **A. Scheinost** | *Received at ROBL:* |
| **Names and affiliations of applicants**: U. Alonso, N. Granizo, T. Missana (CIEMAT). | | |

## Report:

### INTRODUCTION

Magnetite is one of the main stable end member of oxides transformations in moderate to strong reducing environments and neutral-alkaline conditions (CORNELL and SCHWERTMANN, 1996). Therefore, it is considered to be one of the most important corrosion products of radioactive waste canisters in a repository. The study of the interactions of critical radionuclides with magnetite has to be evaluated to predict their migration within these systems. The aim of this experiment is to study the sorption mechanisms of cesium and selenium onto magnetite. A limited amount of literature about cesium sorption onto magnetite is available and the results are often contradictory. In the case of selenium, the presence of Fe(II) ions in the magnetite surface can contribute to reduce the selenium to a lower oxidation state and/or to produce (surface) precipitation that can affect sorption and the overall mobility of the element in the repository.

### EXPERIMENTAL and PRELIMINAR RESULTS

Detailed batch sorption experiments varying pH (3-12), ionic strength ($I=1\cdot10^{-3}$ - 0.1 M in $NaClO_4$), radionuclide concentration ($1\cdot10^{-9}$ – $1\cdot10^{-3}$ M) and contact time (from hours to months) were carried out with Cs and Se as first step for elucidating their retention mechanisms onto magnetite.

Cesium sorption was shown to be non negligible only at pH higher than 8.5 and to increase when the ionic strength of the solution decrease. In addition, desorption experiments showed that part of the Cs becomes irreversibly sorbed. Even the sorption behavior of cesium could be fit with a simple surface complexation model, the mechanisms of retention were not completely clear. 6 magnetite samples with Cs were prepared for EXAFS analysis with pH between 8 and 11 and Cs concentration from 0.01 to 0.1 M.

Selenite sorption onto magnetite, as a function of pH, presented a different behavior to that previously observed for the sorption of the same element in goethite. This behavior could be an indication that reduction of selenium at the magnetite surface occurs (even in oxic conditions) and, for this reason, apart from establishing the possible binding mechanisms at the magnetite surface, it was considered of importance to determine if the Se oxidation state is stable or not in the medium. For EXAFS/XANES analysis, 8 magnetite samples with Se(IV) adsorbed in aerobic conditions were prepared (pH ranged between 2.5 and 7.5 and Se(IV) concentration from $5\cdot10^{-2}$ and $5\cdot10^{-3}$). 2 additional samples (pH 5 and 7, $[Se(IV)] = 5\cdot10^{-2}$ M) in which the selenium was adsorbed onto magnetite in anoxic conditions ($N_2$ atmosphere) were prepared for comparison.

***Measurements at ROBL***

All the spectra were collected in fluorescence mode at room temperature and a preliminary analysis of data obtained was performed with the WINXAS 3.1 software package and using the FEFF8 and ATOMS codes (ZABINSKI ET AL., 1995) for ab-initio calculations.

The measurements performed on the magnetite samples with cesium were not successful since the concentration of the tracer was not enough to obtain spectra with acceptable resolution.

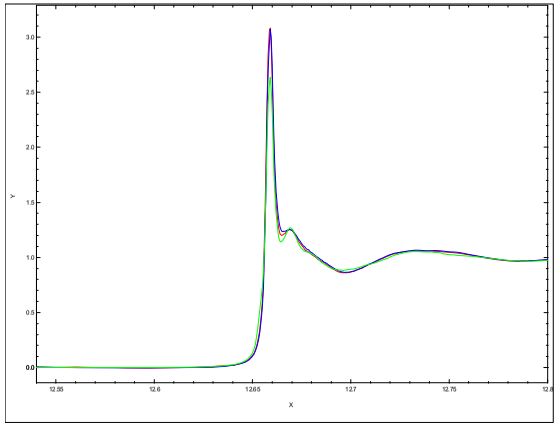

*Figure 1: Comparison of the XANES spectra of selenium adsorbed in magnetite at different pH (green 2.89, red 4.45 and blue 7.46)*

Figure 1 shows the comparison of the XANES spectra of Se(IV) adsorbed onto magnetite at different pH, prepared in oxic conditions. Apart from the sample prepared at very low pH, which shows a small desplacement of the edge, the edges are always very similar in all the spectra, this suggesting that the oxidation state of selenium does not change with pH as a consequence of interaction with Fe(II) of the magnetite. The behavior observed in the samples prepared in anoxic conditions was similar even if the resolution of the spectra was worst due to the lower selenium concentration. The information on possible variation on the se oxidation state in contact with the oxide surface in anoxic is still unclear.

By the other hand, the preliminary analysis of the EXAFS region seems indicating that the coordination of Se is different at different pH. More detailed multicomponent analysis is needed to draw further conclusions. Apart from the measurements of new samples prepared in anoxic conditions, it is necessary to measure some reference samples (Se(IV), Se(VI) salts and the mineral mandarinoite) for the reliable the interpretation of all the data obtained.

### REFERENCES


Cornell R. M. and Schwertmann U. (1996) *The Iron Oxides*. VCH.

Zabinski, S.I., Rehr, J.J., Ankudinov, A., Albers, R.C. and Eller, M.J., 1995. Multiple scattering calculations of X-ray absorption spectra. *Phys. Rev. B* 52**,** p. 2995.

| ESRF | **Experiment title:** Study of the interaction between Uranium(VI) and Hydroxyapatite | **Experiment number:** SI-1262 |
|---|---|---|
| **Beamline:** BM 20 | **Date of experiment:** from: 14.09.05 to: 17.09.05 | **Date of report:** October , 2005 |
| **Shifts:** 9 | **Local contact(s):** Christoph Hennig | *Received at ROBL:* |
| **Names and affiliations of applicants** (* indicates experimentalists): Ferran Seco*, Alexandra Rey*, Ernesto Gonzalez-Robles*, Joan de Pablo, Jordi Bruno | | |

**Introduction:** The role of different phosphate minerals intended to be used in a High Level Nuclear Waste repository in retarding the migration of radionuclides is a matter of concern for the performance assessment (PA) of the repository system. Interest in the use of hydroxyapatite as a possible barrier in the nuclear waste storage process has developed on the basis of its high sorption capacity for actinides and heavy metals, low water solubility of metal phosphates that form by interaction with phosphate released from hydroxyapatite and its high stability under reducing and oxidizing conditions. Although the mechanism of the interaction of U(VI) with hydroxyapatite is not completely understood, different processes have to be taken into account: precipitation of secondary phosphate phases as autunite, $Ca(UO_2)_2(PO_4)_2$, or chernikovite, $H_2(UO_2)_2(PO_4)_2$; ion exchange and surface sorption processes.

**Experimental:** Different sorption experiments have been performed as a function of total dissolved carbonate concentration. A weighed amount of synthetic hydroxyapatite has been equilibrated with a $10^{-5}$ mol.dm$^{-3}$ uranyl nitrate solution under different experimental conditions. Samples HAPUC2 and HAPUC3 were prepared with $10^{-2}$ and $10^{-3}$ mol.dm$^{-3}$ $NaHCO_3$, respectively, while samples HAPU5 and HAPU8 were prepared in a glove box under $N_{2(g)}$ atmosphere at different pH, 4.4 and 7.8, respectively.

**Results:** Preliminary data analysis was performed using the EXAFSPAK software. Theoretical scattering amplitudes and phases for each absorber and backscattered pair were calculated with the program FEFF8. Figure 1 shows the uranium $L_{III}$-edge EXAFS spectra and the corresponding Fourier Transforms for HAPUC2, HAPUC3 and HAPU5 samples. The first peak of the FT corresponds to the axial oxygen atoms and the second to the equatorial oxygen shell. The third peak is due to the contribution of carbon atoms in the case of samples HAPUC2 and HAPUC3 while the fourth peak corresponds to a phosphorous backscatterer. In sample HAPU5, the third peak at R+Δ~2.7Å is atributted to a phosphorous contribution instead of a U-C interaction. These results indicate that carbonate has an important influence in the sorption process of uranium onto hydroxyapatite. A different sorption mechanism is expected to take place as a function of carbonate concentration and therefore, either the formation of secondary solid phases such as autunite or calcium uranyl carbonate and surface complexation processes have to be considered.

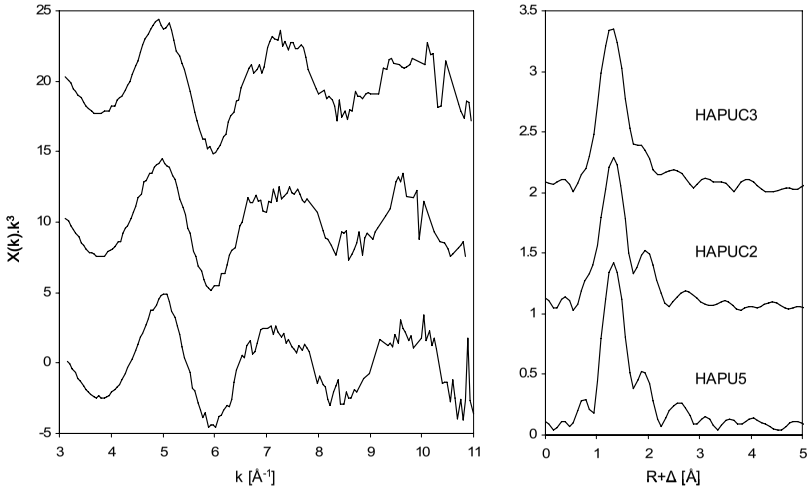

## 3.2. Experimental Reports Materials Research

To avoid repetition, experimental reports have been excluded from the following compilation of Materials Research Experiments if the main results are presented in an extended version (as Scientific or Technical Highlight) in this Annual Report.

This concerns:

IH-MI-349 Commissioning of new MR experimental equipment – polycapillary large large semi-lens
N. Schell (23.-28.02.2005)

IH-MI-387 Part I: Commissioning of a parabolic capillary for XRD at a synchrotron
N. Schell, F. Eichhorn, A. Bjeoumikhov, A. Weiss (23.-27.08.2005)
(see Report, page 43)

SI-1173 $Cu(In,Ga)S_2$ thin film characterization using grazing incidence diffraction
J. Kraeusslich, T. Hahn, J. Cieslak (11.-15.05.2005)
(see Report, page 27)

The experimental reports are requested within six months after performing the experiments. Due to the inevitable delay between the experimental work and the report, this printed compilation lacks some of the most recent results from late autumn 2006.

| ROBL-CRG | **Experiment title:** ***In-situ* x-ray diffraction during sputter deposition of $Ti_{1-x}Al_xN$ – Part III: MAX Phases** | **Experiment number:** **20_02_608** |
|---|---|---|
| **Beamline:** BM 20 | **Date of experiment:** from: 25.01.2005 to: 01.02.2005 | **Date of report:** 22.04.2005 |
| **Shifts:** 21 | **Local contact(s):** Dr. Norbert Schell | *Received at ROBL:* *22.04.05* |

**Names and affiliations of applicants** (* indicates experimentalists):

*M. Beckers, Forschungszentrum Rossendorf, Germany

*N. Schell, *R.M.S. Martins, ROBL-CRG, France

## Report:

The heteroepitaxial growth of ***MAX phase $Ti_2AlN$*** ($M_{n+1}AX_n$ with M = Ti, A = Al, X = N and n = 1) ***on*** single crystal substrates ***MgO(001) and MgO(111)***, deposited by reactive magnetron co-sputtering from Ti and Al targets in an $Ar/N_2$ atmosphere at a temperature of ***690 °C***, has been studied *in situ*. Using real-time specular x-ray reflectivity, ***layer-by-layer growth*** first of an approximately 10 nm thick epitaxial fcc $Ti_{0.63}Al_{0.37}N$ seed layer, then, after changing the deposition parameters, of the MAX phase itself was observed, with an increased surface-roughening on MgO(001) substrate. Using off-plane Bragg-Brentano x-ray scattering, the pseudomorphic growth of $Ti_2AlN$ to the underlying seed-layer as well as MgO was established with lattice parameters of $c = 1.3463$ nm and $a = 0.2976$ nm. From *ex-situ* pole figures at a laboratory source the epitaxial relationship between film and substrate lattice was determined to be ***MgO {111}<110> // $Ti_2AlN$ {10$\bar{1}$2}<$\bar{1}$2$\bar{1}$0>***, regardless of choice of substrate orientation during deposition. They furthermore reveal "pseudo-twinning" of the $Ti_2AlN$ thin films along MgO<110>, leading to a threefold grain orientation as also seen in cross-sectional transmission electron microscopy.

## EXPERIMENTAL

A constant bias voltage of -30 V was applied for all depositions. The base pressure at the deposition temperature of 690 °C was ~8 x $10^{-5}$ Pa. For the fcc $Ti_{1-x}Al_xN$ seed layer an $Ar/N_2$ flux of 13.8/6.9 sccm was chosen leading to a working pressure of 0.35 Pa. The Ti and Al magnetron powers were 60 W and 20 W, respectively, leading to a composition of $Ti_{0.63}Al_{0.37}N$ as near as possible to the nominal corresponding MAX ratio. In order to achieve stable growth conditions for the $Ti_2AlN$ MAX phase layer the deposition pressure was increased to 0.8 Pa at an $Ar/N_2$ flux of 39.7/2.4 sccm. The Ti and Al magnetron powers were 80 W and 26 W, respectively, leading to the Ti/Al ratio of 2/1 as required and calculated from preceding work.

The energy of the incident x-rays was monochromatized to 12.917 keV ($\lambda = 0.961$ Å).

Two different scattering geometries were employed: (1) low angle specular reflectivity either at a fixed incidence angle to determine the growth mode or scanned for the determination of the thickness; (2) large angle x-ray diffraction (XRD) in Bragg-Brentano geometry in order to determine the off-plane lattice parameter. (Pole figures were measured at a laboratory source with $CuK_\alpha$ radiation. The final film composition was derived from Rutherford back-scattering (RBS). Cross sectional transmission electron microscopy (TEM) measurements were carried out using a CM300 microscope at 300 keV.)

## RESULTS

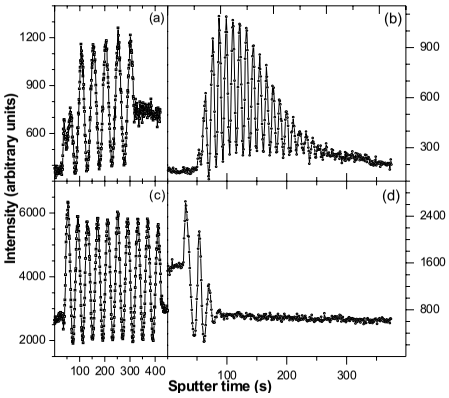


**FIG. 1:** Time dependent *in-situ* **XRR** of fcc $Ti_{0.63}Al_{0.37}N$ seed layers (a, c) and MAX phases $Ti_2AlN$ (b, d) on the substrates MgO(111) (a, b) and MgO(001) (c, d) under fixed incidence & scattering angles. The oscillatory behaviour for the deposited seed layers as well as the films on top are a fingerprint of *layer-by-layer* growth. The decreasing amplitudes of the oscillations reveal increasing roughness or island growth which is more pronounced for the film on MgO(001).

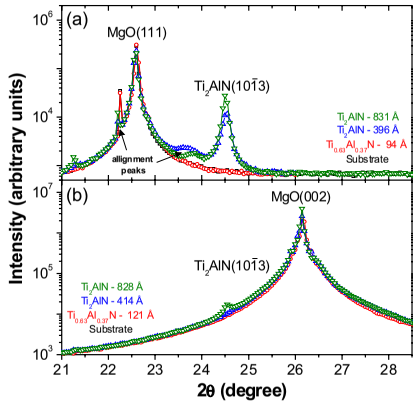


**FIG. 2:** *In-situ* **x-ray diffractograms** recorded in vertical Bragg-Brentano geometry on the substrates MgO(111) (a) and MgO(001) (b) after deposition of the seed layer and two MAX film layers of approximately 40 nm each.

**FIG. 3: Cross sectional TEM** micrograph of $Ti_2AlN$ grown on MgO(111) along the [112] zone axis. (a) shows an overview over the film morphology consisting of large crystal regions, (b) a high resolution micrograph at the interface with the typical MAX phase layered structure of (000l) planes as confirmed from d-spacing calculation by FFT (c).

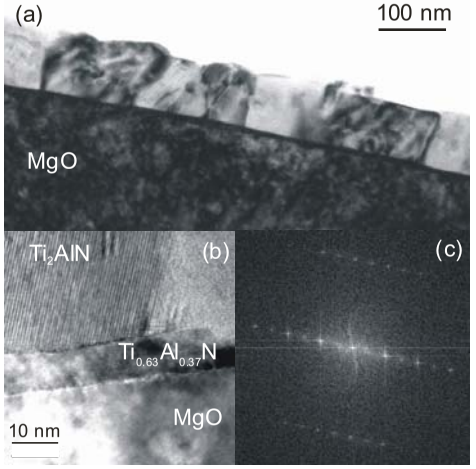


**FIG. 4: Pole figure** of MAX phase $Ti_2AlN$ grown on MgO(111) substrate, measured in the Bragg peak $Ti_2AlN(10\bar{1}3)$ (left) with theoretical poles, including $Ti_2AlN\{10\bar{1}3\}$, $\{10\bar{1}2\}$, {0006} and MgO{111}, {110}, $(1\bar{2}1)$, calculated from a stereographic projection (right).

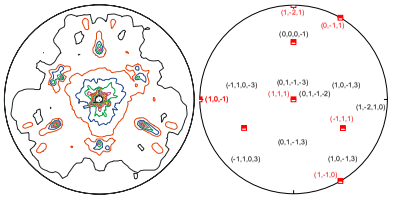

Beckers, M., Schell, N. Martins, R., Mücklich, A., and Möller, W., *The growth and microstructure of epitaxial MAX phase $Ti_2AlN$ thin films characterized by in-situ x-ray diffraction. submitted* to JAP.

| ROBL-CRG | **Experiment title:**<br>***In-situ* x-ray diffraction during deposition of $Ti_{1-x}Al_xN$ – Part IV: Single crystal substrates** | **Experiment number:**<br>**20_02_608** |
|---|---|---|
| **Beamline:**<br>BM 20 | **Date of experiment:**<br>from: 29.06.2005 to: 05.07.2005 | **Date of report:**<br>19.11.2005 |
| **Shifts:**<br>18 | **Local contact(s):**<br>Dr. Norbert Schell | *Received at ROBL:*<br>*20.11.2005* |

**Names and affiliations of applicants** (* indicates experimentalists):

M. Beckers*, N. Schell*,+, R.M.S. Martins*,+

Forschungszentrum Rossendorf (FZR), Institute of Ion Beam Physics & Materials Research, Dresden
+ FZR and ROBL-CRG, Grenoble, France

## Report

### AIM:

The meta-stable nitride $Ti_{1-x}Al_xN$ finds widespread use as wear-protective hard coating in metal forming industries. Previous studies comprised the influence of growth rate, temperature and Al content on the development of $Ti_{1-x}Al_xN$ preferred orientation for deposition on amorphous substrates [1,2], which crucially effects the coating's performance. Also the heteroepitaxial $M_{n+1}AX_n$ phase $Ti_2AlN$ growth on a $Ti_{0.63}Al_{0.37}N$ seed layer on MgO single crystal substrates at substrate temperatures of ~700°C was reported [3]. The epitaxial $Ti_2AlN$ growth mode and hence its microstructure was found to depend on the substrate temperature. To conclude for the role of the seed layer, during the present experiment we investigated the growth mode of $Ti_{1-x}Al_xN$ on MgO, varying its orientation varying as wells as the Al content x, and substrate temperature.

### EXPERIMENTAL:

A total of ***six $Ti_{1-x}Al_xN$ samples*** were deposited onto single crystal MgO(111) and MgO(100) substrates by reactive magnetron **co-*sputtering from Ti and Al targets*** in an $Ar/N_2$ atmosphere at substrate temperatures of 300 and 700°C. Prior to deposition, all substrates were degassed and reconstructed by holding 700°C for one hour. All samples were deposited at a working pressure of 0.35 Pa with Ar and $N_2$ fluxes of 2.76 and 1.38 sccm, respectively. To keep the deposition rate constant at ~0.5 Å/s, the total output of the Ti plus Al magnetrons were kept at 85 W, with the Ti/Al power ratios changed from 80/5 W to 60/25 W, in order to change the Al concentration from x = 0.05 to 0.37. The total film thickness of up to 400 nm was achieved in four to five deposition steps of approximately 100 nm. Each sequential deposition step was characterized in two different scattering geometries: (1) low angle specular reflectivity (XRR), either time-resolved at a fixed angle to monitor each layer's growth mode by the corresponding x-ray intensity oscillations, or angle-resolved for thickness and roughness determination. (2) Large angle x-ray diffraction (XRD) to determine phase formation and off-plane lattice parameters. The energy of the incident x-rays was monochromatized to $\lambda = 0.961$ Å.

### THEORY:

The x-ray intensity oscillations observed during growth are associated with diffraction from alternating monolayer coverages $\theta_n$, running from 0 to 1, with $\theta_{n+1} < \theta_n$. The intensity for an ideal layer-by-layer growth of $n$ monolayers, disregarding absorption, roughening, and substrate, can be written as $I = (F \cdot \sum_n \theta_n e^{-iqdn})^2$, with $F$ being the structure amplitude, $q$ the momentum transfer during measurement, and $d$ the layer spacing. Roughness can be included by interlayer diffusion rates or Gaussian height distributions. Lu *et al.* [4] demonstrated that in case of roughening the intensity curve can be parameterized by a combination of oscillatory and exponential decay terms.

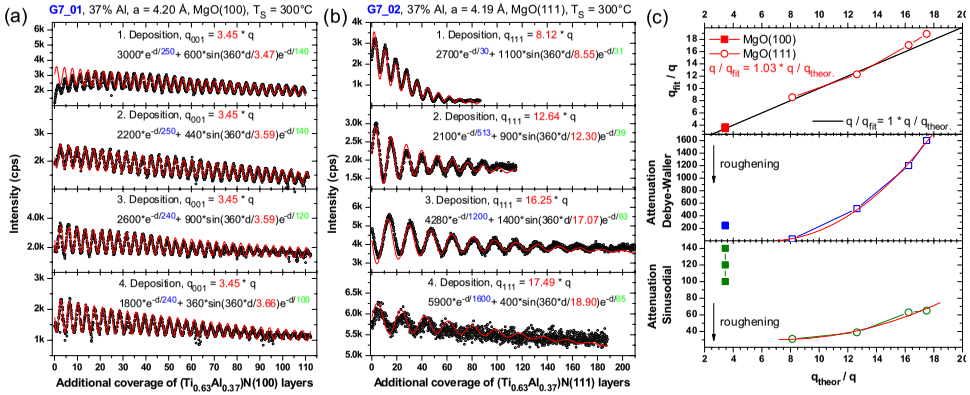


**Fig. 1**: *In situ* growth oscillation results and fittings for $(Ti_{0.63}Al_{0.37})N$ deposited onto (a) MgO(100) and (b) MgO(111).(c) shows the individual fit paramters plotted over the ratio of theoretical and measured q values.

### RESULTS:

Figure 1 shows exemplary results and fittings to *in situ* data with the above parameterization, as displayed in the legends of Figs. 1(a) and 1(b), with the individual fitting parameters highlighted. The data were obtained during the growth of $Ti_{0.63}Al_{0.37}N$ films, deposited at 300°C onto (a) MgO(100) and (b) MgO(111), respectively. The measured data are plotted over the nominal additional $Ti_{0.63}Al_{0.37}N(100)$ and $Ti_{0.63}Al_{0.37}N(111)$ monolayers, calculated from XRR thicknesses and XRD lattice constants obtained after each of the four sequential deposition steps.

In general, oscillation measurements are carried out at the anti-Bragg ½*$q_d$ position, with d being the film lattice spacing along the hkl direction of the measured crystal truncation rod. This means every intensity oscillation represents the completion of another monolayer. However when substantial surface roughening is involved only very few oscillations can usually be observed under these conditions. Therefore, all data here were taken at a $q_{exp}$ value off the anti-Bragg position, at corresponding incidence angles where the initial intensity is high enough to detect several oscillations during growth. Hence, at a constant growth rate the number of oscillations per completed monolayer changes for each measurement, as can be seen in Fig. 1(b). Yet, the ratio between fitted and measured $q$ value $q_{fit}/q$ plotted over the ratio between theoretical and measured $q$ value $q_{theor}/q$ yield a straight line, as illustrated in the top layer of Fig. 1(c). Therefore, also measurements at different $q_{exp}$ values can still be fitted with the same single layer-by-layer growth model.

Furthermore, the decay of the oscillation amplitudes in Figs. 1(a) and 1(b) clearly indicate surface roughening, which are accounted for by exponential attenuation of the sinusoidal oscillation and the overall intensity, whose factors are shown in the middle and bottom layers of Fig. 1(c). Following Lu *et al.*,[4] also these can be deduced back to any q value position, with a $q^2$ dependence as illustrated by the fitted curves. Comparing the different attenuation factors, the $Ti_{0.63}Al_{0.37}N$ surface roughening is by far more pronounced for the MgO(111) than for the MgO(100). Data for low Al content $Ti_{0.92}Al_{0.08}N$ not shown here reveals an even more pronounced difference in roughening. This can be understood by the difference in Ti adatom binding energies on the TiN surface being 10.09 eV for (111) and 3.3 eV for (100), respectively. The difference in adatom mobilities is attenuated at a deposition temperature of 700°C. Hence the exponential decay for (111) and (100) orientation is of the same low order, as has been shown also in previous experiments.[3]

### REFERENCES:

[1] M. Beckers, N. Schell, *et al.*, Journal of Vacuum Science and Technology **23-5**, 1384 (2005).
[2] M. Beckers, N. Schell, *et al.*, Journal of Applied Physics **98**, 44901 (2005).
[3] M. Beckers, N. Schell, *et al.*, Journal of Applied Physics **99**, 34902 (2006).
[4] T.-M. Lu, G.-C. Wang and Y.-P. Zhao, Surface Review and Letters **5**, 899 (1998).

| ROBL-CRG | **Experiment title:** ***In-situ* x-ray diffraction during sputter deposition of $Ti_{1-x}Al_xN$ – Part IV: A new sputter chamber for MAX phase deposition** | **Experiment number:** **20_02_608** |
|---|---|---|
| **Beamline:** BM 20 | **Date of experiment:** from: 31.08.2005 to: 03.09.2005 | **Date of report:** 14.10.2005 |
| **Shifts:** 9 | **Local contact(s):** Dr. Norbert Schell | *Received at ROBL:* *14.10.05* |

**Names and affiliations of applicants** (* indicates experimentalists):

*M. Beckers, Forschungszentrum Rossendorf, Germany

*N. Schell, *R.M.S. Martins, ROBL-CRG, France

## Report:

The heteroepitaxial growth of ***MAX phase $Ti_2AlN$*** ($M_{n+1}AX_n$ with M = Ti, A = Al, X = N and n = 1) ***on*** single crystal substrates ***MgO(111) and $Al_2O_3$(0001)***, deposited by reactive magnetron co-sputtering from Ti and Al targets in an $Ar/N_2$ atmosphere at a temperature of ***>850°C***, has been studied *in situ*. Using real-time specular x-ray reflectivity, ***layer-by-layer growth*** first of an approximately 10 nm thick epitaxial fcc $Ti_{0.63}Al_{0.37}N$ seed layer, then, after changing the deposition parameters, of the MAX phase itself was observed. Using off-plane Bragg-Brentano x-ray scattering, ***basal plane growth*** on both substrates can be deduced. ***Annealing up to 1200***°C gives a first indication of the ***phase stability of thin film MAX phase $Ti_2AlN$***.

### EXPERIMENTAL

In order to improve the ***base pressure down into the range of 10E-7 mbar*** (thereby minimizing any involuntary oxidation of the growing films) and in order to enlarge the accessible x-ray scattering range (in-plane and off-plane), a new magnetron sputter depositon chamber with ***larger Be-window openings*** was commissioned at the material research station of ROBL (Fig. 1).

→

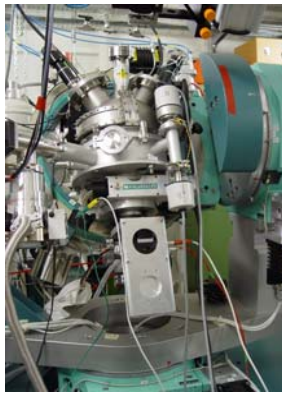

**FIG. 1:** Improved sputter depositon chamber with larger window openings made of Beryllium installed into the 6-circle ROBL diffractometer.

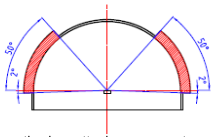

vertical scattering geometry

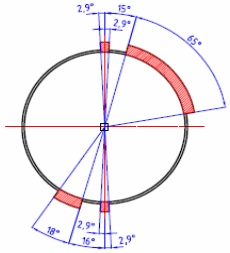

horizontal scattering geometry

A constant bias voltage of -30 V was applied for all depositions. The base pressure at the deposition temperature of ~850°C was ~2 x $10^{-6}$ Pa. For the fcc $Ti_{1-x}Al_xN$ seed layer an $Ar/N_2$ flux of 13.8/6.9 sccm was chosen leading to a working pressure of 0.35 Pa. The Ti and Al magnetron powers were 60 W and 20 W, respectively, leading to a composition of $Ti_{0.63}Al_{0.37}N$ as near as possible to the nominal corresponding MAX ratio. In order to achieve stable growth conditions for the $Ti_2AlN$ MAX phase layer the deposition pressure was increased to 0.8 Pa at an $Ar/N_2$ flux of 39.7/2.4 sccm. The Ti and Al magnetron powers were 80 W and 26 W, respectively, leading to the Ti/Al ratio of 2/1 as required and calculated from preceding work.

The energy of the incident x-rays was monochromatized to 12.917 keV (λ = 0.961 Å).

Two different scattering geometries were employed: (1) low angle specular reflectivity either at a fixed incidence angle to determine the growth mode or scanned for the determination of the thickness; (2) large angle x-ray diffraction (XRD) in Bragg-Brentano geometry at stepwise increased temperatures up 1050°C in order to determine the off-plane lattice parameter and the phase stability, respectively.

### RESULTS

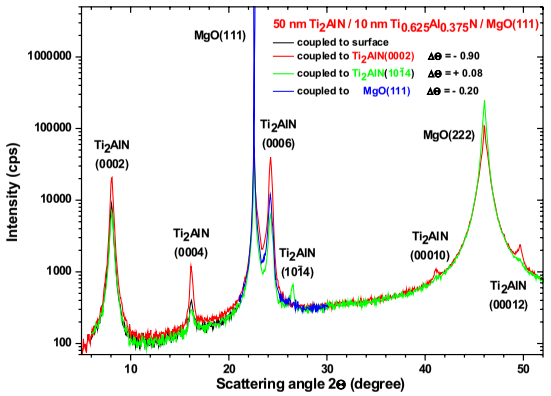


**FIG. 2:** *In-situ* XRD of the 10 nm thick fcc $Ti_{0.63}Al_{0.37}N$ seed layer and 50 nm thick MAX phase $Ti_2AlN$ on the substrate MgO(111). At the higher deposition temperature of 850°C the multiplicity peaks (000x) are clearly seen over the now much larger angular range of more than 50° revealing ***basal plane growth*** in contrast to the *non*-basal plane growth at a deposition at 650°C (M. Beckers *et al.*, *Micro-structure and non-basal plane growth of epitaxial MAX Phase Ti2AlN thin films*, JAP (2005) *in press*, compare also Experimental Report 20_02_608 Part III).

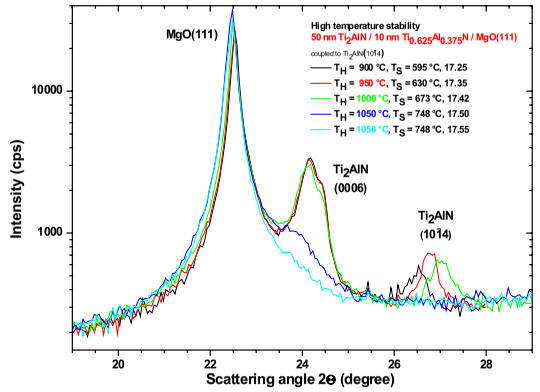


**FIG. 3:** ***Phase stability*** of a 60 nm thick MAX phase $Ti_2AlN$ (on top of a 10 nm thick fcc $Ti_{0.63}Al_{0.37}N$ seed layer) on MgO(111) substrate : ***Above 1000°C the MAX phase disappears*** (probably by forming a spinell) indicating the tight phase diagram for the growth of perfect MAX phase thin films with their basal planes parallel to the substrate (as is necessary for future application).

On $Al_2O_3$ substrate the $Ti_2AlN$ MAX phase is not prone to a spinell formation. However, it does not grow as well as on MgO (data not shown).

| ROBL-CRG | **Experiment title:** **SR-µ-XRD stress measurements of dual damascene inlaid copper interconnect structures at high temperatures** | **Experiment number:** **20_02_617** |
|---|---|---|
| **Beamline:** BM 20 | **Date of experiment:** from: 16.03.2005 to: 21.03.2005 | **Date of report:** 20.12.2005 |
| **Shifts:** 17 | **Local contact(s):** Dr. Norbert Schell | *Received at ESRF:* *20.12.05* |
| **Names and affiliations of applicants (* indicates experimentalists):** Dr. Jochen Rinderknecht, Dr. Hartmut Prinz, Inka Zienert AMD Saxony LLC. & Co. KG | | |

## Report:

### Introduction

The ***stress state*** of dual damascene ***copper interconnect structures*** in low-k materials was measured by XRD at ***temperatures between RT and 400°C***. Stress in the interconnect structure on micro-devices is a very important issue for long term reliability. With smaller dimensions and implementation of many materials with different mechanical and thermo-mechanical properties, interpolation and simulation of the final stress state is becoming more unreliable and experimental characterisation is desperately needed.

### Experimental

A small heating stage (DHS900, Anton Paar) fixed to the BM20 diffractometer allowed a wide range in Chi (±50) and Phi (±60) to be measured. Exact sample positioning, which is necessary for very small structured samples, was enabled with a video camera system. The beam energy was fixed to copper-$K_{\alpha 1}$ (***$\lambda = 1.541$ Å***) and the ***beam size reduced down to 300 x 300 µm²***.

It is of high importance for stress measurements to choose a high angle reflection. The difference in the angle caused by the elastic deformation of the lattice is higher for larger angles and the precision of the measurement is much better. In our experiment the ***Cu(311) reflection at 2theta = 89.943°*** was chosen. The use of an ***area detector*** (SMART1000, Bruker AXS) enabled a simultaneous measurement in a 10°-Chi range and further reduces time and increases accuracy. The large Chi range is of special importance for copper structures. These samples show a ***pronounced texture***, together with the low divergence of the synchrotron beam diffracted intensity is only observed at certain Chi and Phi angles. As the texture may slightly change from sample to sample, measurements with point detectors will often miss the signal and get very complicated and time consuming.

After alignment, the sample was measured at room temperature and subsequently heated up to 400°C in 50°C steps. At each temperature, ***12 frames with 4 different Chi angles and 3 different Phi angles were taken***. Finally the ***stress tensor*** was calculated by fitting the deformation of the diffraction cone for different directions with the fundamental stress equation.

### Results

Samples with two arrays of parallel ***copper lines*** in low-k dielectrics ***with 130 nm and 4 µm line widths*** and a supplementary ***massive copper pad*** were manufactured in a standard production line. For this special study, the ***barrier layer*** (pure Tantalum *vs*. TaN/Ta bilayer) and the ***cap layer*** (very thin $SiN_x$ *vs*. an additional thick $SiO_2$ layer) were ***varied***. The barrier layer (Ta or TaN/Ta) had only a low impact on the temperature-stress relation. However an additional thick $SiO_2$ capping layer lowered the room temperature stress state significantly. The effect of this thick capping layer on the stress-temperature relation is even more dramatically. Uncapped samples show the intersection from in-plane tensile stress to compressive stress between 150°C and 250°C (top Figure), while thick $SiO_2$ capped samples reach this point at higher temperatures or in some cases may even stay tensile up to 400°C (bottom Figure). This shift depends also on the copper line width: 130 nm lines are strongly influenced and the intersection is shifted for more than 150°C. The effect is much lower for 4 µm lines, where a 50°C shift is measured. A special feature that emerges in 4 µm wide, thick $SiO_2$ capped lines is that the out-of-plane stress becomes more tensile with rising temperature (S33 in bottom Figure). This means a reversed temperature stress curve compared to the uncapped sample.

The prolongation of the tensile stress state up to temperatures of 400°C together with the dependence of the stress on the structure geometry is supposed to cause ***stress migration problems*** in chip designs with combined low-k and $SiO_2$ ILD layers.

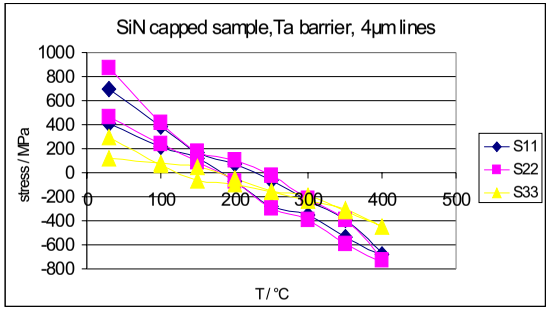


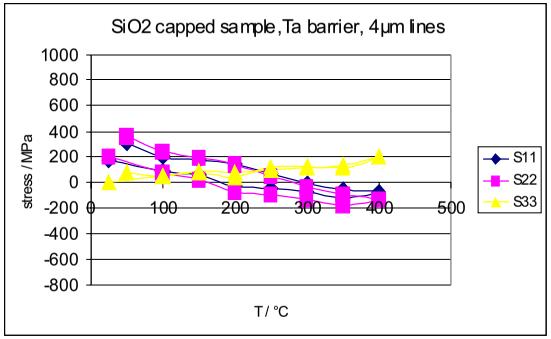


S11 represents the stress along, S22 across the line, and S33 stands for out-of-plane stress.

| ROBL-CRG | **Experiment title:** **Structural studies of semiconductor materials for optoelectronic applications** **Part I: Investigation of the shape of the chemical composition profile in InGaAs/GaAs heterostructures** | **Experiment number:** **20_02_622** |
|---|---|---|
| **Beamline:** BM 20 | **Date of experiment:** from: 20.04.2005 to: 26.04.2005 | **Date of report:** 12.12.2005 |
| **Shifts:** 18 | **Local contact(s):** Dr. Norbert Schell | *Received at ROBL:* *12.12.05* |

**Names and affiliations of applicants** (* indicates experimentalists):

J. Gaca*, M. Wójcik*, J. Sass*, K. Mazur*, Institute of Electronic Materials Technology, Wolczynska 133, 01 919 Warsaw, Poland

N. Schell*, F. Eichhorn*, FZR, FWI, P.O. Box 510119, 01314 Dresden, Germany

## Report:

The aim of the experiment was two-fold. First, to ***investigate the dependence of the growth rate on the deposition time for the highly strained $In_{0.73}Ga_{0.27}As$ epitaxial layer in the early stage of epitaxial growth*** and to ***determine the chemical composition profile of the $In_{0.53}Ga_{0.47}As/In_{0.73}Ga_{0.27}As/In_{0.53}Ga_{0.47}As$ quantum well as a function of interruption time***. Second, to ***investigate the full RCE photodiode heterostructure*** presented in Fig 4(a), for which the above mentioned heteroepitaxial system is the most essential part.

In order to establish the dependence between growth rate and deposition time, investigations were carried out with series of samples containing $In_{0.73}Ga_{0.27}As$ layers on different stages of epitaxial growth. The deposition time for the layer varied from 5 to 30 sec. For each sample its chemical composition profile was determined employing numerical analysis by finding the best fit between experimental and calculated x-ray diffraction profiles. An example is presented in Fig. 1. It was shown that ***the growth rate of the $In_{0.73}Ga_{0.27}As$ layer in the early stage of epitaxial growth is not constant*** but varies with the deposition time. It is seen that the ***greatest value of the growth rate is observed for the shortest deposition time***. As the deposition time increases, the value of the growth rate gradually decreases and finally gets constant for times greater than 20 sec. This dependence is presented in Fig. 2.

The same method of investigation was used to determine the chemical composition profile of the $In_{0.53}Ga_{0.47}As/In_{0.73}Ga_{0.27}As/In_{0.53}Ga_{0.47}As$ quantum well. The investigations were carried out with a series of quantum wells. Different values of the interruption time were applied to each sample during the MOCVD epitaxy. The chemical composition profile of the quantum wells are presented in Figs 3(a), (b), and (c). It was found that ***there is an optimum interruption time for the interface to be the least diffused one***.

These results allow to optimize the values of the deposition and interruption times during the growth of each element of the full RCE photodiode heterostructure. The x-ray diffraction profile for such a heterostructure is presented in Fig. 4(d). The calculated profile presented in the same figure was obtained assuming for the simulation the values of parameters describing the heterostructure resulting from TEM dark field images Figs 4(b) and (c).

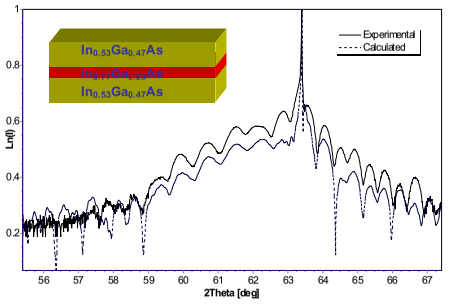


**Fig. 1:** Experimental and calculated diffraction profiles for a very thin InGaAs layer on a 001 GaAs substrate.

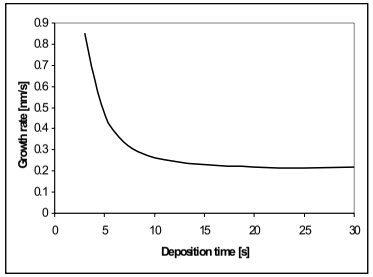


**Fig. 2:** The growth rate *versus* deposition time.

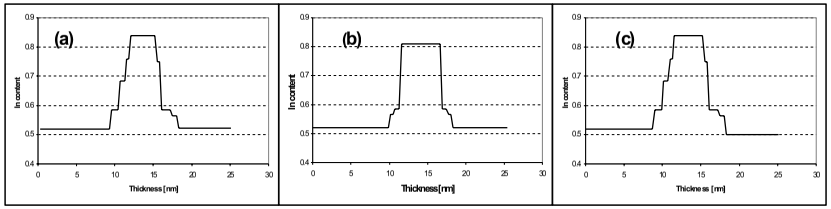


**Fig. 3:** The chemical composition profile for the 001 growth direction for $In_{0.53}Ga_{0.47}As/In_{0.83}Ga_{0.17}As/In_{0.53}Ga_{0.47}As$ quantum well with interruption times: (a) 0.5s, (b) 3s, and (c) 7s.

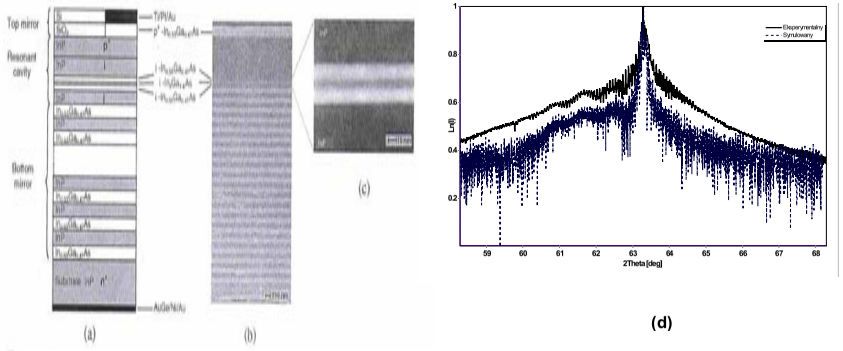


**Fig. 4:** Schematic structure of the designed RCE photodiode (a), cross-sectional SEM image of a fabricated RCE photodiode heterostructure (b), cross-sectional TEM image of the QW region formed by $InP/In_{0.53}Ga_{0.47}As/In_{0.73}Ga_{0.27}As/In_{0.53}Ga_{0.47}As/InP$ layers (c), and experimental and calculated diffraction profiles for RCE photodiode heterostructure (d).

| ROBL-CRG | **Experiment title:**<br>**Structural studies of semiconductor materials for optoelectronic applications**<br>**Part II: Determination of the coherency range between epilayer and substrate in highly strained $In_{0.13}Ga_{0.87}As/GaAs$ heterostructures** | **Experiment number:**<br>**20_02_622** |
|---|---|---|
| **Beamline:**<br>BM 20 | **Date of experiment:**<br>from: 27.08.2005 to: 30.08.2005 | **Date of report:**<br>16.12.2005 |
| **Shifts:**<br>9 | **Local contact(s):**<br>Dr. Norbert Schell | *Received at ROBL:*<br>*16.12.05* |

**Names and affiliations of applicants** (* indicates experimentalists):

J. Gaca*, M. Wójcik*, J. Sass*, K. Mazur*, Institute of Electronic Materials Technology, Wolczynska 133, 01 919 Warsaw, Poland

N. Schell*, F. Eichhorn*, FZR, FWI, P.O. Box 510119, 01314 Dresden, Germany

## Report:

The aim of the experiment was to ***determine the coherency range between epilayer and substrate above the critical thickness in highly strained $In_{0.13}Ga_{0.87}As/GaAs$ heterostructures***. The chemical composition as well as the lattice strain were evaluated from reciprocal space maps (RSMs) obtained from asymmetric reflections.

RSMs for 80 nm thick epilayers executed in the vicinity of $\bar{2}\bar{2}4$ and $\bar{2}24$ reciprocal lattice points (RLPs) applying the $\phi_+$ geometry in the two perpendicular [110] azimuths are shown in Figs 1(a) and 1(b). Due to the different relaxation states the position of the maximum intensity of the layer peak on the relaxation line is different in Fig. 1(b) compared to Fig. 1(a). Also the width of the intensity distribution increases due to inhomogeneous relaxation.

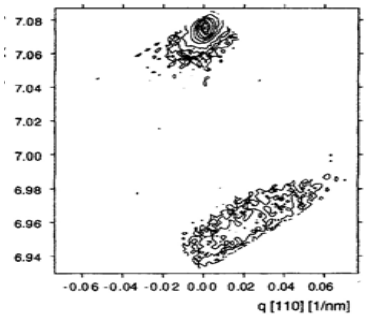


**Fig. 1(a):** $\bar{2}\bar{2}4$ reciprocal space map of the $In_{0.13}Ga_{0.87}As/GaAs$ heterostructure with thickness equal 80 nm.

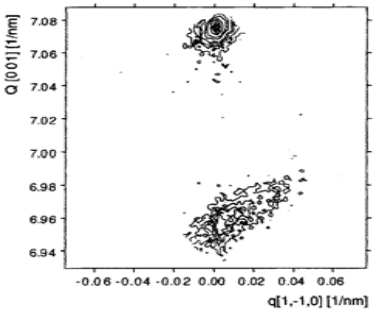


**Fig. 1(b):** $\bar{2}24$ reciprocal space map of the $In_{0.13}Ga_{0.87}As/GaAs$ heterostructure with thickness equal 80 nm.

Fig. 2 shows 004 transverse scans across the layer RLP for the same sample as in Figs 1(a) and (b). As can be seen in the latter case, the diffuse intensity is dominating. Since only dislocations perpendicular to the incidence plane contribute to the diffuse scattering, its intensity is proportional to their density. The different shifts of the layer RLP in the $110$ and $\bar{1}10$ directions visible in Fig. 1 indicate orthorhombic layer distortion.

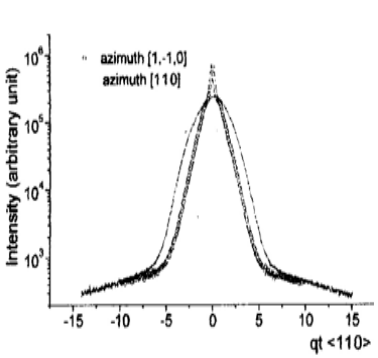


**Fig. 2:** Transverse scans in the two [110] azimuths of the 004 reflection of the $In_{0.13}Ga_{0.87}As/GaAs$ heterostructure with thickness equal 80 nm.

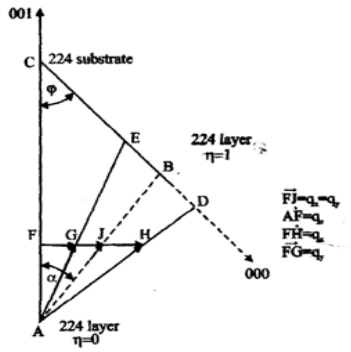


**Fig. 3:** Relaxation triangle: ABC – tetragonal distortion, ADC – orthorhombic distortion ($\rho_x + \rho_y$ = const., $q_x$,$q_y$ $q_z$ – shift components).

The ***mechanism of orthorhombic stress relaxation*** is presented in Fig. 3. The relaxation triangles ADC and AEC correspond to two different [110] azimuth directions. One can notice that the isotropic stress relaxation – tetragonal layer distortion – takes place when the misfit dislocation density $\rho_x = \rho_y$.

Analyzing the experimental results and assuming that the relaxation mechanism is due to the slipping of 60° misfit dislocations on the tilted (111) glide planes, it was found that the relaxation of the $In_{0.13}Ga_{0.87}As/GaAs$ (001) epitaxial system with lattice misfit $\Delta a/a = 0.0093$ and the critical thickness 15 nm starts with the layer thickness $\approx$ 70 nm, i.e. 4.5 times the critical thickness. This means that measurement of the layer composition for this lattice misfit with an accuracy of 1% is feasible well above the critical thickness.

| ROBL-CRG | **Experiment title:** Two-dimensional x-ray waveguide gratings | **Experiment number:** 20_02_627 |
|---|---|---|
| **Beamline:** BM 20 | **Date of experiment:** from: 23.03.2005 to: 27.03.2005 and 03.09.2005 to: 06.09.2005 | **Date of report:** 02.12.2005 |
| **Shifts:** 6 + 9 | **Local contact(s):** Dr. Norbert Schell | *Received at ROBL:* *02.12.05* |

**Names and affiliations of applicants** (* indicates experimentalists):

*C. Ollinger, *C. Fuhse, *T. Salditt

Institut für Röntgenphysik, Friedrich-Hund-Platz 1, 37077 Göttingen, Germany

**Report:**

We have carried out ***measurements of the far-field pattern of two-dimensional x-ray waveguides arranged on a lattice***. These waveguide structures are prepared by spin-coating an e-beam resist (e.g. Polymethylmethacrylate, PMMA) on cleaned Silicon wafers. The resist is then structured in an e-beam lithography system (Lion LV1, Leica, Germany). After development of the structures a cladding material (here Silicon) is evaporated on top. As described in [1] these ***devices were recently used to produce a coherent and slightly divergent beam with a size of 25 nm * 47 nm at the exit of the waveguide***.

Measurements of single two-dimensional waveguides with a bending magnet beam are possible (see Figure 1, each peak corresponds to the illumination of a single two dimensional waveguide), but a detailed analysis of their properties is limited due to the flux density at the entrance of such a waveguide. The photon energy was set to E = 12 keV with an ***integral flux of 5*10E5 photons/sec/mm$^2$***.

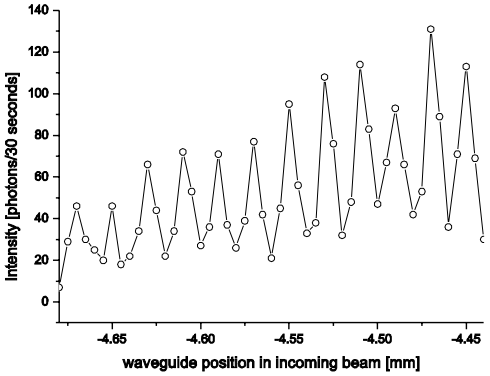


**Fig. 1:** Translational scan of two-dimensional waveguides through the incoming beam. Each peak correspond to transmission through a single two dimensional waveguide.

To overcome the demand of a high flux density at the entrance of such a two-dimensional waveguide these structures can be arranged on a lattice with period $d_L$. As described in [2] the field distribution behind such a structure is enveloped by the far field pattern of a single two-dimensional waveguide (averaged over the lattice) and peaked at angles $\alpha_p = \arcsin(n\,\lambda/d_L)$. By changing the incidence angle the center of the envelope of the far field pattern is shifted by $\alpha_{PC} = \alpha_I$ as is shown in Figure 2:

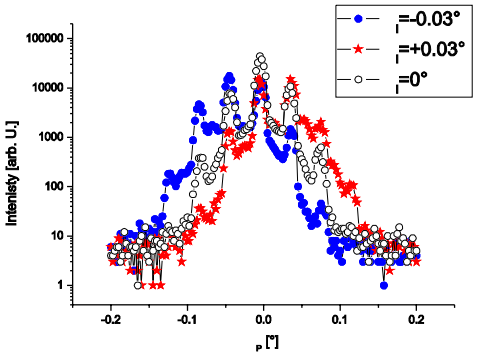


**Fig. 2:** Changing the incidence angle $\alpha_I$ leads to a change in the center of the envelope $\alpha_{PC}$ of the far field pattern with $\alpha_{PC} = \alpha_I$ .

A series of ***two-dimensional CCD images*** of these waveguide lattice far fields were recorded. A typical pattern is shown in Figure 3. From these far field patterns it should be possible to reconstruct the E-field distribution at the exit of a single two-dimensional waveguide and thus obtain information about efficiency of the optics. This *work is currently in progress*.

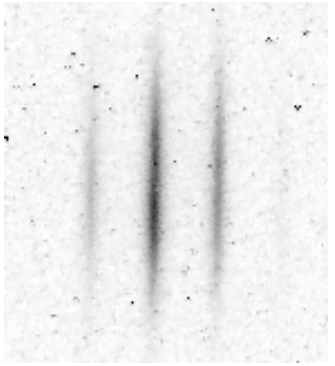

**Fig. 3:** Far field of a two-dimensional waveguide lattice as recored with the CCD.

**References:**

[1] A. Jarre *et al.*, Physical Review Letters, **94** (2005) 074801.

[2] C. Ollinger *et al.*, Physica B, **357** (2005) 53-56.

| ROBL-CRG | **Experiment title:**<br><br>**Structural studies of oxygen implanted NiTi surfaces** | **Experiment number:**<br><br>**20_02_628** |
|---|---|---|
| **Beamline:**<br>BM 20 | **Date of experiment:**<br>from: 24.09.2005 to: 27.09.2005 | **Date of report:**<br>05.06.2006 |
| **Shifts:**<br>9 | **Local contact(s):**<br>Rui Martins | *Received at ROBL:*<br>*09.06.06* |
| **Names and affiliations of applicants** (* indicates experimentalists):<br><br>R. Martins*, FZ Rossendorf, IIM, Dresden, Germany<br>N. Shevchenko*, FZ Rossendorf, IIM, Dresden, Germany<br>A. Rogozin*, FZ Rossendorf, IIM, Dresden, Germany | | |

**Report:**

The shape memory and superelastic NiTi alloy has a high nickel concentration of 50 at% which may result in nickel ion release in biological solutions. Recently, it was demonstrated that the nickel surface concentration may be reduced significantly using plasma immersion ion implantation (PIII) [1, 2]. Formation of nickel depleted $TiO_2$ surfaces by oxygen implantation was established. The titanium oxide surface prevents corrosion and out-diffusion of Ni ions.

So far, the ion implantation processes for NiTi surface modification have only been studied using polycrystalline NiTi substrates. It is well known that a nanostructure formation in the NiTi alloy leads to enhancement of the mechanical properties. The aim of our work was to investigate surface modifications of nanostructured NiTi alloy by means of PIII. To study the thermal stability of the nanostructured (or ultrafine-grained) NiTi *in-situ* XRD analysis of the NiTi structure-evolution during annealing in vacuum was performed. These data are also required for the optimization of the implantation temperature of the PIII process.

To create the ultrafine- and nanograined structure an equal-channel angular pressing and a subsequent cold rolling were used (Prof. E.F. Dudarev, Siberian Physical and Technical Institute, Tomsk, Russia). Three types of NiTi samples were annealed: NiTi sample after the equal-channel angular pressing (ECAP), ECAP + cold rolling by 40 %, ECAP + cold rolling by 80 % (where 40 and 80 % are rolling strains). Figure 1 shows typical XRD patterns of the ECAP and cold rolled by 40 % NiTi sample during *in situ* annealing.

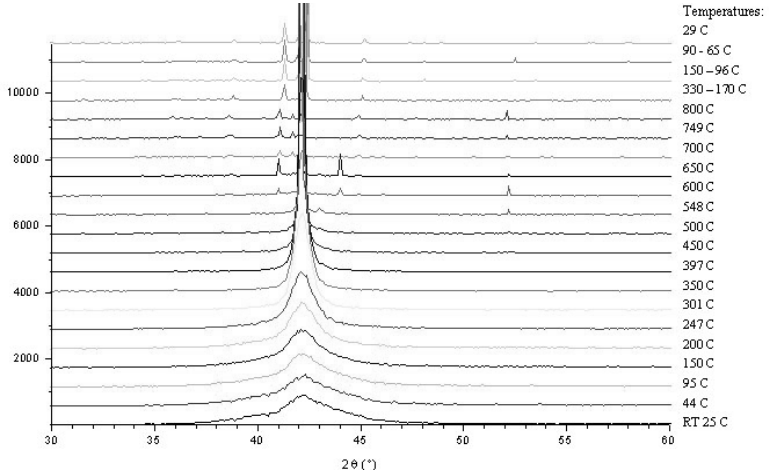


**Fig. 1:** Evolution of the (110) peak of NiTi B2 phase during annealing in vacuum.

At room temperature the XRD pattern reveals only a broad peak around 42.5°, indicating the presence of ultrafine-grain sturucture or nanostructure. The absence of any structural changes below 200°C is clearly observed. The intensity of the (110) B2 phase strongly increases and the FWHM decreases within the temperature range of 350-600°C, pointing to significant structure changes and a grain growth in the NiTi alloy. The structural evolution of NiTi alloy and processes during annealing are required for future analysis.

To suppress any structural changes of the NiTi substrate due to thermal heating at the ion implantation, the PIII treatment will be performed at low temperatures (< 250°C).

**References:**

1. Shevchenko N., Pham M.-T., Maitz M.F., Applied Surf. Sci. **235** (2004) 126.
2. Poon RWY, Ho JPY, Liu XY, *et al.*, Material Sci. & Eng. A **390** (2005) 444.

| ROBL-CRG | **Experiment title:** The nanostructural development of magnetron sputtered Ag-Cu films studied by *in-situ* XRD | **Experiment number:** 20_02_629 |
|---|---|---|
| **Beamline:** BM 20 | **Date of experiment:** from: 22.06.2005 to: 28.06.2005 | **Date of report:** 09.12.2005 |
| **Shifts:** 18 | **Local contact(s):** Dr. Norbert Schell | *Received at ROBL:* *10.12.05* |

**Names and affiliations of applicants** (* indicates experimentalists):

J. Bøttiger*, K.P. Almtoft*, A.M. Ejsing*, University of Aarhus, Denmark

N. Schell*, R. Martins*, Forschungszentrum Rossendorf, ROBL-CRG, Germany

## Report:

Cu-Ag alloy films were prepared by magnetron cosputtering. A ***two-phase nanocrystalline (nc) structure of Cu grains supersaturated with Ag and Ag grains saturated with Cu*** was always observed. When alloying Ag with Cu or Cu with Ag, the ***grain sizes decreased dramatically and the supersaturation increased with the amount of alloying element***. During ***annealing*** of the Cu-Ag films, the grain sizes increased and the solubilities decreased.

### EXPERIMENTAL

The nc Cu-Ag thin films were deposited *in situ* at ROBL as well as *ex situ* in Aarhus. The relevant parameters had been: base pressure ≈$6\times10^{-5}$ Pa; Ar (purity 99.9996%) was used as sputter gas at a pressure of 0.5 Pa; the substrates, mounted on a resistive heater, were Si(001) wafers (15×15 $mm^2$) with a 100 nm amorphous $SiO_2$ layer on top. The films were deposited at RT (and slightly above) at a bias voltage of -50 V with the Cu target (purity 99.999%) and the Ag target (purity 99.99%) running between 20-50 W, respectively, for deposition times of 5-6 mins (leading to alloy films of ≈1700-2300 Å thickness). They were annealed at various temperatures up to 305°C. The x-ray wavelength at ROBL had been $\lambda = 0.960$ Å (12.915 keV) and Cu-$K_\alpha$ in Aarhus.

During *in-situ* film deposition and subsequent annealing, Bragg-Brentano θ-2θ scans were carried out repeatedly. The exact peak positions yield information about the out-of-plane lattice distance and – assuming ***Vegard's law*** - the ***solubility of Ag in Cu or Cu in Ag***. The grain sizes were obtained from the FWHM of the Bragg peaks by use of the Scherrer equation $L = \lambda/\Delta(2\theta)\cos(\theta)$. They were in agreement with later TEM observations.

### RESULTS

Figs 1 and 2 show raw data for the film deposition (allowing to determine its composition) as well as the annealing behaviour (change of integrated intensity, peak shifts), while Fig. 3 shows the result of a quantitative analysis of the x-ray data of Fig. 1. The Cu grain size decreased a factor of six with increasing Ag content, while the Ag grain size decreased a factor of three with increasing Cu content.

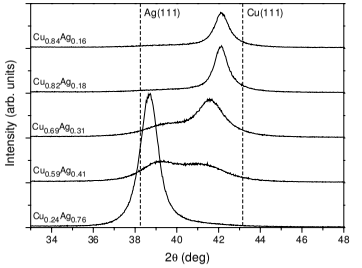


**Fig. 1:** Series of Bragg-Brentano *ex-situ* diffractograms for ~1750 Å Cu-Ag alloy films as-deposited at RT with ***various composition***.

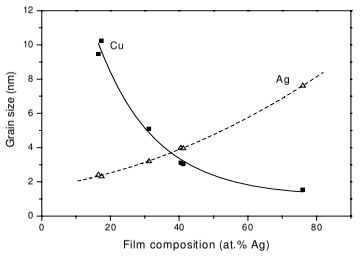


**Fig. 3:** ***Grain size*** of Cu (filled squares) and Ag (open triangles) grains ***as a function of the Ag content*** of the films of Fig. 1.

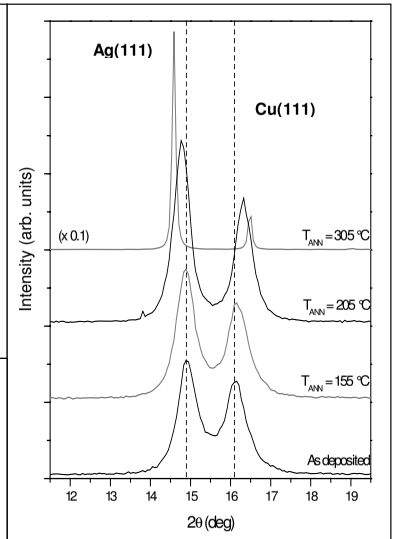


**Fig. 2:** Bragg-Brentano *in-situ* scans from a 2300 Å ***$Cu_{65}Ag_{35}$ film*** deposited at 75°C as-deposited (open circles) and after ***annealing*** at 155°C (filled squares) followed by annealing at 205°C (line) and 305°C (dashed line).

It is tempting to suggest this large decrease in grain size with alloying being evidence of segregation of a surface-covering layer stopping the grain growth. However, the solubility of Ag in the Cu grains and Cu in the Ag grains (*data not shown*) as a function of the composition of the films suggest a different growth mode.For example, the solubility of Ag in the Cu grains of the film with 16 at.% Ag was about 30 at. % Ag, i.e. larger than the percent Ag in the film. This indicates the presence of an amorphous phase, which we did not observe neither with XRD or TEM. We suggest that ***the film initially was deposited as an amorphous structure, which quickly partially crystallized into two crystalline phases during further growth***.

The ***diffusional processes*** were so fast that we were not able to observe a possible amorphous structure or *accurately* observe the nanostructure before the deposition was stopped after 6 min. However, we were able to observe, that ***the two-peak structure was formed within a minute after the growth started***. After deposition, we followed the development in time of the Cu and Ag grain sizes and the supersaturation of Ag in the Cu grains and Cu in the Ag grains, both processes being controlled by diffusional processes. The increasing grain sizes arose from ***normal grain growth***, where the lower free energy is a result of a smaller total grain-boundary area, while the decreasing supersaturation corresponded to a lower free energy because of the positive heat of mixing of Cu and Ag. We exclude that the two-phase structure originated from spinodal decomposition, since, in this case, coherent interfaces, which we did not observe, should have formed.

| ROBL-CRG | **Experiment title:** **Ion beam induced atomic displacements in periodic multilayers and consequent changes in properties** | **Experiment number:** **20_02_630** |
|---|---|---|
| **Beamline:** BM 20 | **Date of experiment:** from: 16.11.2005 to: 21.11.2005 | **Date of report:** 06.11.2006 |
| **Shifts:** 17 | **Local contact(s):** Dr. Norbert Schell | *Received at ROBL:* *13.11.2006* |

**Names and affiliations of applicants** (* indicates experimentalists):

**Bhupendra N. Dev*[1], J. Grenzer*, N. Schell***
Forschungszentrum Rossendorf, Institute of Ion Beam Physics and Materials Research, P.O.B. 510119, D-01314 Dresden, Germany
[1] Marie Curie Incoming Fellowship from Institute of Physics, Bhubaneswar, India

## Report

Ion irradiation causes many interesting changes in properties of multilayered systems. In multilayers showing giant magnetoresistance and antiferromagnetic coupling, e.g. Co/Cu multilayers, ion irradiation causes significant suppression of antiferromagnetic coupling [1]. Ion irradiation induced magnetization reorientation occurs in Co/Pt multilayers [2]. Even ferro-magnetic behavior can be obtained by ion irradiation of nonmagnetic multilayers like Pt/C with Fe impurities [3]. Ion beam induced atomic displacement is responsible for these changes in properties. We have developed an analytical method combining X-ray standing wave (XSW) and X-ray reflectivity (XRR) techniques [4] and successfully used the method to study ion-beam induced microstructural changes in multilayers [5].

This combined XSW-XRR method was used to study ion-beam-induced structural changes in Ni/C multilayer systems and Si/Ni/Si double layers during the beamtime.Laterally graded Ni/C multilayers (Ni-layer thickness fixed whereas C-layer thickness varied laterally) were fabricated on float glass substrates, by ion beam sputtering. The Ni/C multilayer samples used in this study were prepared at Nagoya University. The sample specifications are: N = 15 (the number of layer-pairs in the multilayer stack), d = 3.3 nm to 4.1 nm (multilayer period, i.e. the thickness of a Ni/C layer-pair). Different parts of a large sample (30 x 70) $mm^2$ were cut into strips with dimensions (30 X 5) $mm^2$. Then the virgin samples were irradiated with 2 MeV $Cu^{2+}$ ions by rastering the ion beam on the five samples at fluences (ions/cm2) [1A (virgin, not implanted), 2B($1x10^{14}$), 3C($3x10^{14}$), 4D($5x10^{1}$), 5E($7x10^{1}$)] at Institute of Physics, Bhubaneswar, India. For comparison only 1 half of the sample surface was irradiated. The range of 2 MeV Cu ions in such Ni/C multilayers sample is about three times larger than multilayer film thickness. Thus the implanted Cu ions are buried deep into the glass substrate passing through the multilayer stack, which is about 55 to 60 nm thick.

One virgin and all irradiated strips were analyzed with combined X-ray standing wave and X-ray reflectivity experiments at the ROBOL beam-line using 9.0 keV monochromatized X-rays. We have measured ion beam induced expansion in the multilayer period as a function of ion fluence. Up to a certain dose we have observed mixing between Ni and C atoms across the interfaces. At higher doses demixing effect has been pronounced. This mixing-demixing phenomenon can be explained in terms of two competitive processes including ballistic and chemically guided atomic movements.

The pristine sample exhibits an enhanced diffuse signal caused by an almost perfect roughness correlation of the layer interfaces demonstrating an almost perfect superlattice. Figure 1 shows the reciprocal space map and the specular scattering of that sample. An enhancement of the diffusely scattered intensity can be observed at the position of the second satellite if the incidence or exit angle equals the value of the first one. The change of the reflectivity signal due to ion beam implantation can be seen in figure2; thickness oscillations are suppressed; the multilayer period increases, accordingly changed the X-ray standing wave signal.

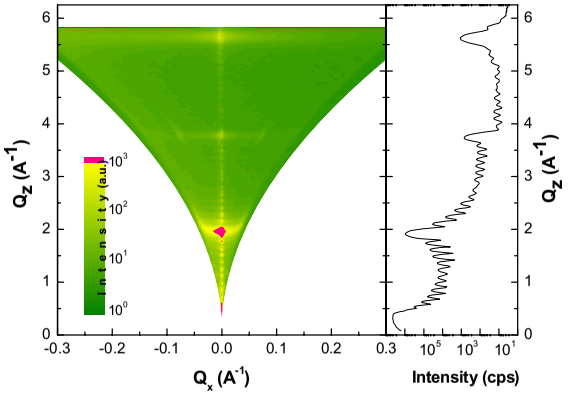


**Figure 1:** RSM and specular scattering of the not implanted sample

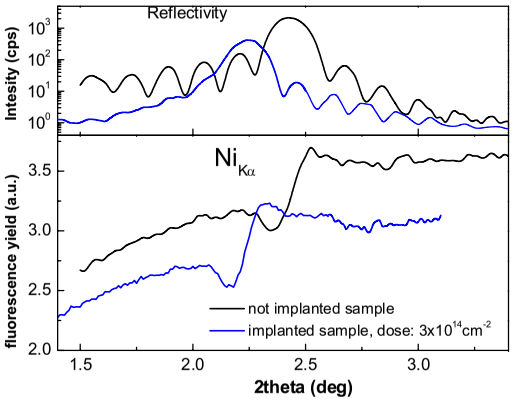


**Figure2:** XRR and XSW signal around the first Bragg peak

## References

[1] M. Cai et al., J. Appl. Phys. **95** (2004) 2006.
[2] D. Weller et al. J. Appl. Phys. **87** (2000) 5768.
[3] B.N. Dev et al., *Nonmagnetic to magnetic nanostructures via ion irradiation* (Invited talk in the 31st International Conference on Micro- and Nano-Engineering, Vienna, Austria, 19-22 September, 2005).
[4] S. K. Ghose and B. N. Dev, Phys. Rev. B **63** (2001) 245409.
[5] S.K. Ghose et al, Appl. Phys. Lett. **79** (2001) 467

| ROBL-CRG | **Experiment title:** **Surface layer structure in ion implanded silicon – *Pr compound formation in Si by ion beam synthesis*** | **Experiment number:** **20_02_631** |
|---|---|---|
| **Beamline:** BM 20 | **Date of experiment:** from: 17.12.2005 to: 19.12.2005 | **Date of report:** 26.04.2006 |
| **Shifts:** 6 | **Local contact(s):** Dr. Norbert Schell | *Received at ROBL:* *26.04.06* |

**Names and affiliations of applicants** (* indicates experimentalists):

F. Eichhorn, R. Kögler, N. Schell*, Forschungszentrum Rossendorf, Institute of Ion Beam Physics and Materials Research, P.O. Box 510119, 01314 Dresden, Germany

**Report:**

Downscaling of nanoelectronic devices requires the replacement of the common $SiO_2$ gate oxide by high-K dielectrics. Among other materials $Pr_2O_3$ is one potential candidate of a new gate dielectric material because of its higher dielectric constant, thermal stability and structural fitting with crystalline Si. $Pr_2O_3$ is almost always deposited on Si(111) or Si(100) surfaces by chemical vapor deposition (CVD) [1] or by molecular beam epitaxy (MBE) [2]. Recent investigations show that beside $Pr_2O_3$ also other compounds are formed like Pr silicide and Pr silicate [2]. Pr silicate seems to be a useful buffer layer to Si, it offers higher k-values as well [3].

The present study is focused on the general issue of which compounds are formed in the ternary system of Pr-Si-O. The compounds are formed inside the solid (not at the surface) by application of ion beam synthesis. Room temperature Pr implantation was performed with an ion energy of 800 keV to fluences of $3x10^{16}$ and $2x10^{17}$ $cm^{-2}$ into n-type Cz-Si(100) substrates (1 … 5 Ωcm). The Si substrate contained an intrinsic O concentration of ≈ $1x10^{18}$ $cm^{-3}$. Few samples were additionally implanted by 140 keV O ions to $4.5x10^{16}$ $cm^{-2}$. The implantation parameters of O were chosen in order to fit with the Pr depth profile. The sub-stoichiometric implants of Pr and O result in maximum concentrations for Pr of 3.5 and 12 at% and for O of 4.5 at%.

As an example for the results the figure below shows the x-ray diffractogram of a Si(100) wafer implanted with $3.5x10^{16}$ $cm^{-2}$ $Pr^+$ (with an energy of 800 keV) and annealed at 1100°C for 1h in an Ar atmosphere. Finally, $4.5x10^{16}$ $cm^{-2}$ $O^+$ (with an energy of 140 keV) were implanted. The measurements were carried out with synchrotron x-rays with a wavelength of 0.154 nm (CuKα radiation). The beam had a size of 0.4 mm x 2.5 mm and hit the sample surface under an angle of 2 °.

The most intense lines are the Si diffraction lines (111), (220), (311) and (400) at the positions 2θ = 28.5°, 47.4°, 56.2° and 69.3° (PDF 27-1402), respectively. Furthermore, there are a lot of lower intensity lines which may be identified as $PrSi_2$ (PDF 11-256) and $Pr_{9.33}Si_6O_{26}$ (PDF 23-1389). They are indicated by filled and open triangels, respectively. Diffraction lines of Pr oxides were not observed. The material consists of crystals without a preferential orientation (similar to the crystal orientation in a powder).

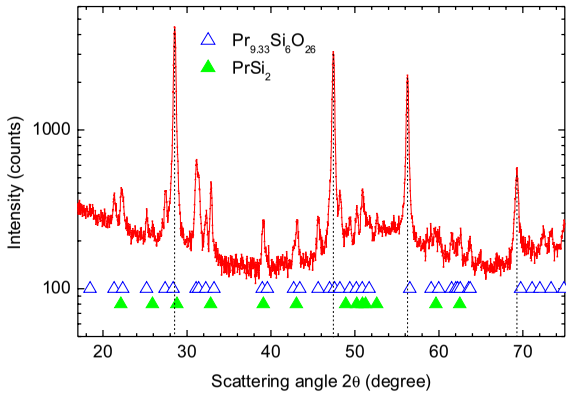


The Pr implantation creates an amorphous surface layer in Si of about 350 nm thickness. During annealing the amorphous layer recrystallizes leaving multi-crystalline Si. In summary, the obtained results can be understood by the simple consideration that the energy necessary for realigment of the material by formation of compounds inside the solid should be minimized [4].

**References**

[1] R.L. Nigro, V. Raineri, C. Bongiorno, R. Toro, G. Malandrino, and I.L. Fragila, Appl. Phys. Lett. **83**, 129 (2003)
[2] D. Schmeißer, H.-J. Müssig, and J. Dabrowski, Appl. Phys. Lett. **85**, 88 (2004)
[3] R.L. Nigro, R.G. Toro, G. Malandrino, G.G. Condorelli, V. Raineri, and I.L. Fragila, Advanced Functional Materials **15**, 838 (2005)
[4] R. Kögler, A. Mücklich, F. Eichhorn, and J. Christensen, J. Appl. Phys. (*in preparation*)

| ROBL-CRG | **Experiment title:** ***In situ* investigations of ITO film crystallization during electric current annealing** | **Experiment number:** **20-02-632** |
|---|---|---|
| **Beamline:** BM 20 | **Date of experiment:** from: 17.05.2006 to: 23.05.2006 | **Date of report:** 03.11.2006 |
| **Shifts:** 18 | **Local contact(s):** Dr. Norbert SCHELL | *Received at ROBL:* *04.11.2006* |

**Names and affiliations of applicants** (* indicates experimentalists):

**A. Rogozin, N. Shevchenko, N. Schell, and M. Vinnichenko**

Forschungszentrum Rossendorf, Institute of Ion Beam Physics and Materials Research, PO Box 51 01 19, D-01314 Dresden, Germany

## Report:

The present study is an extension of the experiment IH-HC-777 with the aim to investigate ITO thin film annealing by electric current in vacuum and compare to the isothermal annealing [1, 2]. In order to identify the crystallization mechanism during electric current annealing, an effect of film thickness on the crystallization starts and transformation rate at the thermal and electric current annealing has been experimentally studied.

The amorphous ITO films with thicknesses in the range of 50 – 400 nm were deposited by reactive middle frequency pulsed magnetron sputtering at the base pressure of $8.6\times10^{-4}$ Pa. The 4 groups of ITO samples were studied with following thicknesses: ~50, 170 - 180, 315 - 325, and 370 - 385 nm. Cross-sectional TEM of as-deposited films shows a thickness-dependent film morphology. A thin homogeneous layer (~ 30 - 40 nm) at the film-substrate interface turns into a pronounced columnar structure with sharp intercolumnar boundaries through the film, which is typical of reactive magnetron deposition. So, only the 50 nm films have almost homogeneous morphology without the colomnar structure.

The films are investigated by real-time synchrotron XRD analysis (λ = ... Å, Bragg-Brentano geometry, use of multi-channel position sensitive detector) simultaneously with four-point resistivity measurements during isothermal or electric current annealing. All experiments are performed at constant substrate temperature of 310 °C.

The time dependences of normalized integral intensity for different film thicknesses have a typical S-like shape and are shown in Fig. 1, 2. At present the evaluation of the measurements is not yet completed. However, first results show that a variation of the film thickness within the range 170 - 320 nm practically does not influence on the crystallisation outset time (fig. 1, 2). Within the experimental error no difference between isothermal and electrical annealing has been obtained.

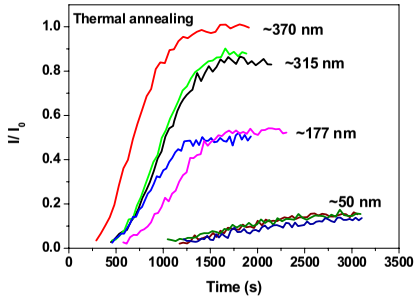


**Fig. 1:** Evolution of the normalized XRD (222) peak integral intensity at different film thicknesses during isothermal annealing.

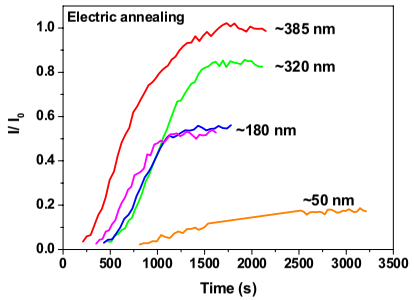


**Fig. 2:** Evolution of the normalized XRD (222) peak integral intensity at different film thicknesses during annealing by electric current.

The ITO films with higher thickness (370 – 385 nm) show a slight decrease of the crystallization outset time. However, the XRD data and resistivity measurements demonstrate a significant effect for the 50 nm films. In this case the crystallization outset time enhances by factor of ~ 2 at thermal annealing as well as electrical annealing. Obviously, the crystallization rate of the 50 nm film is essentially decreased in comparison with the thicker films, which exhibit a distinct columnar structure. In order to improve the understanding of the underlying mechanisms for the considerable difference between crystallization process in thin and thick films, TEM investigations of partly and fully crystallized layers of different thicknesses are in progress.

### References

[1] A. Rogozin, N. Shevchenko, M. Vinnichenko, F. Prokert, A. Cantelli, A. Kolitsch, and W. Möller, Appl. Phys. Lett. **85,** 1 (2004).

[2] A. Rogozin, N. Shevchenko, M. Vinnichenko, M. Seidel, A. Kolitsch, and W. Möller, Appl. Phys. Lett. **89,** 061908 (2006).

| ROBL-CRG | **Experiment title:** **Pole figure measurements on coarse grained black tourmaline** | **Experiment number:** **20_02_633** |
|---|---|---|
| **Beamline:** BM 20 | **Date of experiment:** from: 14.12.2005 to: 17.12.2005 | **Date of report:** 06.12.2006 |
| **Shifts:** 9 | **Local contact(s):** Dr. Norbert Schell | *Received at ROBL:* *08.12.2006* |

**Names and affiliations of applicants** (* indicates experimentalists):

**K. Walther *, A. Frischbutter, and C. Scheffzük;**
GeoForschungsZentrum Potsdam, AB 5.3, Telegrafenberg, D-14773 Potsdam, Germany

**R. Hielscher, and H. Schaeben**
TU Bergakademie Freiberg, Inst. für Geologie, Bernhard-von-Cotta-Str. 2, D09596 Freiberg, Germany

**N. Schell**
Forschungszentrum Rossendorf, Dresden, Germany and ROBL-CRG, Grenob le, France

## Report

Black tourmaline (schörl) (ditrigonal-pyramidal) is a characteristic mineral formed during the pneumatolytic state of the consolidation of granitic intrusions into the Earth's crust. It may be concentrated like planar, mostly spotlike distributed occurrences on joint planes within granitic bodies, but never reaches concentrations in nature required for diffraction experiments using neutron radiation. Therefore, textural information on tourmaline may be of interest analysing the latest states of granitic magma consolidation or even states of its earliest deformation.

Tourmaline occurs in several modifications depending on its contents on iron, sodium and others. The tourmaline under investigation was proved to be the iron-rich mineral *schörl*.

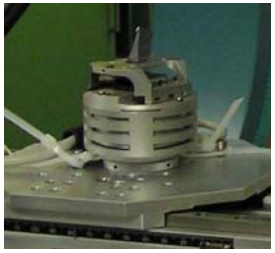

**Fig. 1:** Sample oszillator

With a powder sample it was verified that (0 5 $\bar{5}$ 1), (2 2 $\bar{4}$ 0), (0 1 $\bar{1}$ 2), (1 3 $\bar{4}$ 1), (1 2 $\bar{3}$ 2) and (2 1 $\bar{3}$ 1) were the strongest reflections. Measurements of pole figures of these lattice planes with a 5°x5°-grid, where the azimuthal angle varies from 0° till 355° and the polar angle from 0° till 70°, were performed at ROBL at a wavelength of 1.54 Å. Because the sample is coarse-grained a special sample oscillator (Huber 511.301) was used. The oscillation range was 10 mm and achieved by the movement of an excenter. In Fig. 1 is shown the sample oscillator. Thus increasing the number of crystallites which should be detected it was estimated to obtain smooth pole figures. The data analysis showed that the effect of the coarse grains remained. All ODF-programms we tried have refused working.

We tried some correction strategies:

- smoothing with binominals,
- smoothing with fast Fourier analysis,
- smoothing with cubic splines.

All these corrections work one-dimensional, i.e. for the same tilt (polar) angle for varying azimuthal angles. In the pole figures is this to be seen as "elongations" on circular traces. In Fig. 2 is shown a section of the (012)-pole figure for the polar angle $\psi = 5°$. Besides the background corrected experimental measured values there are shown 5-fold binominal smoothed data and data after fast Fourier smoothing.

Another correction concept was to develop the circles of the pole figures in Gaussians. Gaussians with halfwidth below 2° were regarded as "grains" and removed, i.e. replaced by the mean value of the neighbours. Removing a certain number of the strongest "grains" the remaining pole figure should be smoother and processable. But alas, this procedure was changing only the scale of the effect. The remaining pole figure show still coarse grains.

Further investigations are under their way to fix this problem with newly developed algorithms for sharp textures.

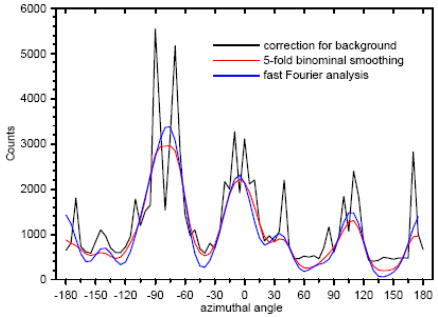


**Fig. 2:** Smoothing of pole figures. The black curve represents the background corrected original data, in red is shown the effect of binominal smoothing, the blue curve shows fast Fourier smoothing.

| ROBL-CRG | **Experiment title:**<br>**Nanophase formation in ZnO implanted with transition or rare earth metal ions** | **Experiment number:**<br>20-02-634 |
|---|---|---|
| **Beamline:**<br>BM 20 | **Date of experiment:**<br>from: 15.07.2006 to: 18.07.2006 | **Date of report:**<br>23.10.2006 |
| **Shifts:**<br>12 | **Local contact(s):**<br>Dr. Norbert Schell | *Received at ROBL:*<br>*24.10.2006* |

**Names and affiliations of applicants** (* indicates experimentalists):

**Shengqiang Zhou*, F. Eichhorn*, N. Schell*, K. Potzger**

Forschungszentrum Rossendorf, Institute of Ion Beam Physics and Materials Research, P.O.B. 510119, D-01314 Dresden, Germany

## Report:

Recently due to the potential application in spintronics, both magnetic/semiconductor hybrid heterostructure and diluted magnetic semiconductor (DMS) have attracted huge research attention [1]. In both research fields, GaAs is the most intensively studied material. Epitaxial MnAs and transition metal (e.g. Fe) were achieved on GaAs substrates due to their structure compatibility: i.e. Mn-based metallic compounds have common III/column atoms with GaAs, while Fe/GaAs has a cube-on-cube orientation with a small lattice mismatch of -1.4% [2, 3]. Room temperature spin injection was reported from MnAs [4] and Fe [5] into GaAs. In parallel, Mn doped GaAs has been demonstrated to be a DMS with a Curie temperature of 110 K [6]. Very recently, wide-band-gap semiconductors (GaN and ZnO) doped with transition metals were reported to be DMS with Curie temperatures above room temperature [7]. Nevertheless, the origin of the observed ferromagnetism is still controversial, e.g. ferromagnetic clusters [8]. In contrast, only a few investigations deal with epitaxial magnetic/ZnO(or GaN) heterostructures. This is partially due to the chemical incompatibility, the different crystal symmetry or the large lattice mismatch between the 3d-ferromagnet and ZnO. For instance, Fe is a bcc crystal, while hcp MnAs and Co have a very large lattice mismatch with ZnO (12% and 23%, respectively). In this paper, we made an extensive investigation on the structural and magnetic properties evolution of Fe implanted ZnO upon annealing, and demonstrate the possibility to form epitaxial magnetic Zn-ferrite embedded in ZnO. With respect to the crystal symmetry and lattice mismatch, our results suggest that other ferrites, which have been epitaxially grown onto MgO, $SrTiO_3$, and $Y_{0.15}Zr_{0.85}O_2$, and exhibit rich magnetic properties [9], could be epitaxially embedded inside or grown onto ZnO.

From the experiment we have reached two conclusions:

(1) By correlating the structural and magnetic properties of Fe-implanted ZnO, we found either bcc-Fe or partially inverted $ZnFe_2O_4$ nanocrystals are the origin of the observed ferromagnetism.

(2) We demonstrate the possibility to form epitaxial magnetic Zn-ferrite embedded in ZnO, and the epitaxial relationship is $ZnFe_2O_4$ (111)[110]//ZnO(0001)[11$\underline{2}$0].

Fig. 1 shows the SR-XRD patterns for the as-implanted and annealed samples. For the as-implanted sample, Fe nanoparticles were observed, and no other Fe-oxide ($Fe_2O_3$, $Fe_3O_4$, and $ZnFe_2O_4$) particles were detected. After 823 K and 15 min annealing, larger and more Fe nanoparticles are formed. After 1073 K and 15 min annealing, the Fe(110) peak almost disappeared and the sample already shows an indication for the presence of $ZnFe_2O_4$. After 3.5 hours annealing at 1073 K, crystalline and oriented $ZnFe_2O_4$ particles are clearly identified. The inset shows a zoom of the Fe(110) peak to show the development of Fe nanoparticles more clearly.

Fig. 2 shows the pole figure for $ZnFe_2O_4$(511) and $ZnFe_2O_4$(333). Both diffraction lines have the same Bragg angle in the cubic $ZnFe_2O_4$. The sample tilt, $\chi$, is the angle by which the surface is tilted out of the diffraction plane. The angle of rotation about the surface normal is denoted by $\varphi$, which ranges from -60° to 60°. The pole figure shows poles at $\chi$~39°, 56° and 70°, respectively, with sixfold symmetry and an indication of a tail from ZnO(11$\underline{2}$0). It is consistent with the theoretic $ZnFe_2O_4$(511) / (333) pole figure viewed along [111] with rotation twins. The in-plane orientation relationship is $ZnFe_2O_4$[110]//ZnO[11$\underline{2}$0].

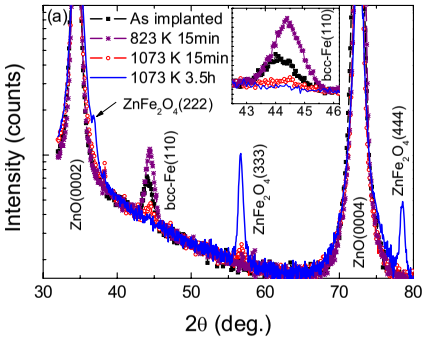


**Fig. 1:** SR-XRD patterns of Fe implanted ZnO reveal the second phase development (from bcc-Fe to $ZnFe_2O_4$) upon annealing.

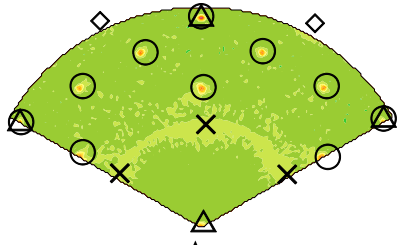


**Fig. 2:** Pole figure of $ZnFe_2O_4$(511) reveals the epitaxy of $ZnFe_2O_4$.

### References

1. H. Ohno, Semicond. Sci. Technol. **17**, 275 (2002).
2. M. Tanaka, et al., J. Appl. Phys. **76**, 6278 (1994).
3. A. K. Das, et al., Phys. Rev. Lett. **91**, 087203 (2003).
4. M. Ramsteiner, et al., Phys. Rev. B **66**, 081304 (2002).
5. H. J. Zhu, et al., Phys. Rev. Lett. **87**, 016601 (2001).
6. Y. Ohno, et al., Nature **402**, 790 (1999).
7. A review by A. H. MacDonald, et al., Nature Materials **4**, 195 (2005).
8. Shengqiang Zhou, et al., J. Appl. Phys. to be published (2006).
9. A review by Y. Suzuki, Annu. Rev. Mater. Res. **31**, 265 (2001).

| ROBL-CRG | **Experiment title:** **$L1_0$ ordering in FePt films designed for future magnetic memory materials** | **Experiment number:** **20_02_635** |
|---|---|---|
| **Beamline:** BM 20 | **Date of experiment:** from: 07.12.2005 to: 13.12.2005 | **Date of report:** 14.06.2006 |
| **Shifts:** 18 | **Local contact(s):** Dr. Norbert Schell | *Received at ROBL:* *04.07.06* |

**Names and affiliations of applicants** (* indicates experimentalists):
V. Cantelli* FZR, FWIS
Dr. J. von Borany* FZR, FWIS
Dr. N. Schell FZR, FWIS, ROBL-CRG

## REPORT

Due to its high magneto-crystalline anisotropy ($0.7\text{-}1\times10^8$ erg/cm$^3$) the $L1_0$ phase of FePt alloys belongs to the preferred materials for future magnetic recording media, with the potential to achieve a storage density above 1 Tbit/in$^2$ [1]. Unfortunately, FePt films deposited at room temperature (RT) exhibit only the face-centered cubic (fcc) A1-phase and a subsequent heat treatment is required to achieve the face-centered tetragonal (fct), ferromagnetic $L1_0$ phase.

In the present experiment, *in-situ* grazing incidence X-ray diffraction (GI-XRD, $\lambda = 1.54$ Å, $\alpha_i = 1°$) was used to characterize the A1 $\rightarrow$ $L1_0$ phase transition of dc-magnetron sputtered $Fe_xPt_{100-x}$ films [$x = (50 \pm 2)$] during post annealing treatments at $T_A \leq 350$°C in vacuum ($p < 5\times10^{-6}$ mbar). The FePt films of about 70 nm thickness were deposited at RT with a sputtering rate of $(0.54 \pm 0.03)$ Å/s from elemental targets [Fe (3.5N) / Pt (5N)] onto $SiO_2$(1.5 µm)/Si(111) substrates of $15 \times 15$ mm$^2$ size. Some specimens were irradiated with He-ions (50 keV, 0.1 - $30\times10^{16}$ cm$^{-2}$) at RT or at 250°C. This treatment should lower the disorder-order transformation temperature due to the creation of point defects and, therefore, decrease the activation energy for reordering[2].

Figure 1 shows GI-XRD patterns for FePt films during annealing. Already at 310°C the $L1_0$ phase starts to form. The A1$\rightarrow$$L1_0$ transformation is characterized by the appearance of the superstructure peaks [(001)/(110)] and by a peak splitting [(200)/(002)&(220)/(202)] due to the tetragonal distortion. At 325°C the $L1_0$ transition is almost complete which is confirmed by the long range order parameter S = 0.9 [3]. The mean grain size continuously increases with the annealing temperature, from 6 nm (as-deposited) to 11 nm (325°C). The films are non or only weakly textured.

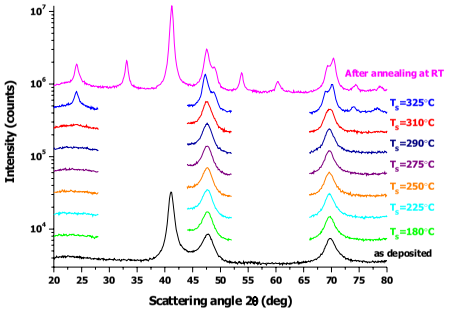


**Fig. 1:** GI-XRD patterns ($\alpha_i = 1°$) collected during vacuum annealing. The $L1_0$ contribution starts to be detected at 310°C by the splitting (200)/(002) and (220/(202).

Magnetic hysteresis loops (recorded by SQUID at RT) confirm the $L1_0$ ferromagnetic phase transition after annealing. As reported in Fig. 2, in both parallel and perpendicular hysteresis loops, the coercive field is 5 kOe. There is no easy and hard axis which is a proof for the random orientation of the grains and the magnetic domains.

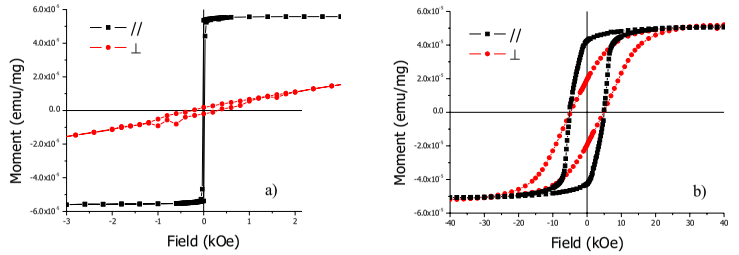


**Fig. 2:** Magnetic hystheresis loops of FePt films: a) before annealing; b) after annealing at 325°C.

As shown in Fig. 3, after $He^+$ irradiation (RT or 250°C) the films are still in the paramagnetic A1 phase and no decrease of the transition temperature has been found with respect to the not irradiated samples. In addition, the calculated long range order parameter and the average grain size do not differ significantly from the samples without He irradiation.

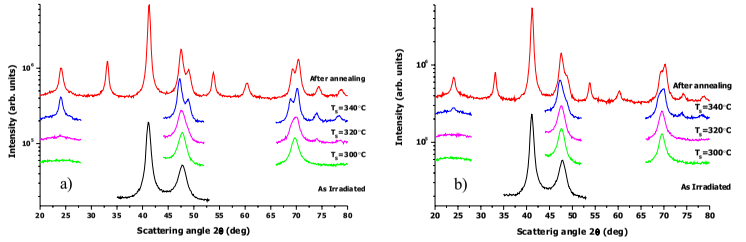


**Fig. 3:** GI-XRD patterns ($\alpha_i = 1°$) of ion-irradiated films ($He^+$, 50 keV, $3\times10^{16}$ cm$^{-2}$) collected during vacuum annealing a) irradiation at RT; b) irradiation at 250°C.

These results pointed out that the disorder-order transition is not effected by $He^+$ irradiation for films deposited by magnetron sputtering. Calculations reveal that for our deposition conditions ($p = 0.3$ Pa, $V_T \approx 400$ V, target-substrate distance: 10 cm) no thermalization of the sputtered atoms and reflected Ar neutrals (from the sputter gas) occurs. Thus, the atoms arriving on the substrate have hyperthermal (sputtered atoms) or much higher (reflected neutrals) energies leading to an increased surface adatom mobility or even vacancy formation. In particular, the Ar neutral, reflected by the Pt target, have energies which exceed the displacement energy of Fe, Pt atoms in the film. We suppose that the films exhibit a high density of point-defects (vacancies) already after deposition which explains the low A1$\rightarrow$$L1_0$ transition temperature as well as the insensitivity against further ion irradiation.

In conclusion, we succeded in the preparation of FePt layers by dual magnetron sputtering characterised by a very low transition temperature of about $(325 \pm 25)$°C.

**References:**

[1] M. Hanson, O. Kazakova, E.B. Svedberg, J. of Magn. and Magn. Mat. **272–276** (2004) 1359.

[2] D. Ravelosona, C. Chappert, V. Mathet, H. Bernas, Appl. Phys. Lett. **76** (2000) 236.

[3] B.E. Warren, *X-Ray Diffraction*, p. 208-216, Dover Publications, INC., New York (1990).

| ROBL-CRG | **Experiment title:**<br>***In-situ* x-ray diffraction during sputter deposition of Ti-Al-N MAX-phase thin films** | **Experiment number:**<br>**20_02_636** |
|---|---|---|
| **Beamline:**<br>BM 20 | **Date of experiment:**<br>from: 01.03.2006 to: 07.03.2006 | **Date of report:**<br>11.11.2006 |
| **Shifts:**<br>18 | **Local contact(s):**<br>Dr. Norbert Schell | *Received at ROBL:*<br>*28.11.06* |


**Names and affiliations of applicants (* indicates experimentalists):**

*M. Beckers, Forschungszentrum Rossendorf, Germany
*C. Höglund, J. Birch, Linköping University, Sweden
*N. Schell, *R.M.S. Martins, ROBL-CRG, France


## Report

### AIM:

Due to their combination of metallic and ceramic properties, the ***$M_{n+1}AX_n$ phases*** – ternary nitrides and carbides with M being a transition metal, A an A group element and X nitrogen or carbon – are subject of numerous studies. Also thin films of the $M_{n+1}AX_n$ carbides have been extensively studied, but only ***very recently*** the first results on nitride deposition in form of ***$Ti_2AlN$*** have been published [1, 2; compare Reports 20_02_608, part III + IV]. However, for ***$Ti_4AlN_3$*** and the proposed meta-stable modification ***$Ti_3AlN_2$, no experimental work*** on thin films has been reported up to now. Hence, during this experiment the **growth of $Ti_{n+1}AlN_n$ $M_{n+1}AX_n$ phase** compounds with n = 2 and 3 was studied ***in-situ***.

### EXPERIMENTAL:

A total of nine samples were deposited onto single crystal MgO(111) and $Al_2O_3$(0001) substrates by reactive magnetron co-sputtering from Ti and Al targets in an Ar/$N_2$ atmosphere at temperatures between 600 and 725°C. According to previous experiments [3] the $Ti_4AlN_3$ deposition parameters were set to target powers of Ti 83 W and Al 14 W with Ar/$N_2$ flux ratios of 7.82/0.6 sccm, leading to a working pressure of 0.8 Pa. Thin $(Ti_{0.63}Al_{0.37})N$ or $Ti_2AlN$ were used as seed layers, in order to improve $Ti_4AlN_3$ nucleation and prevent interfacial diffusion processes to the MgO substrate. A constant bias voltage of -30 V was applied for all depositions. Each sequential deposition step of seed layer and $Ti_4AlN_3$ was characterized in two different scattering geometries: (1) low angle specular reflectivity for thickness determination and (2) large angle x-ray diffraction (XRD) to determine phase formation and off-plane lattice parameters. The energy of the incident x-rays was monochromatized to 11.554 keV ($\lambda$ = 1.073 Å). Additional ex-situ techniques used were Rutherford backscattering spectrometry (RBS) to obtain the final film composition and high resolution transmission electron microscopy (HRTEM) to cross-check for local $M_{n+1}AX_n$ phase formation.

### RESULTS

Fig. 1 shows the XRD results for samples deposited onto $Al_2O_3$ at 600°C, 675°C, and 725°C substrate surface temperature. For 725°C and 625°C, prior to the $Ti_4AlN_3$, a thin $Ti_2AlN$ seed layer was deposited at 675°C, showing basal plane growth as displayed by the multiple (000$\ell$) diffraction peaks (see also [1]). Similar results as in Figure 1 have been obtained for $Ti_4AlN_3$ growth onto MgO(111) and/or using $(Ti_{0.63}Al_{0.37})N$ as a seed layer. For 675°C substrate temperature, as depicted in Figure 1(a), the deposition of 700 Å nominal $Ti_4AlN_3$ does not induce this phase, but an $Ti_2AlN$ growth with segregation of surplus Ti into cubic $(Ti_{1-x}Al_x)N$ with unknown Al concentration. This may be ascribed to an insufficient Al adatom mobility, which consistent

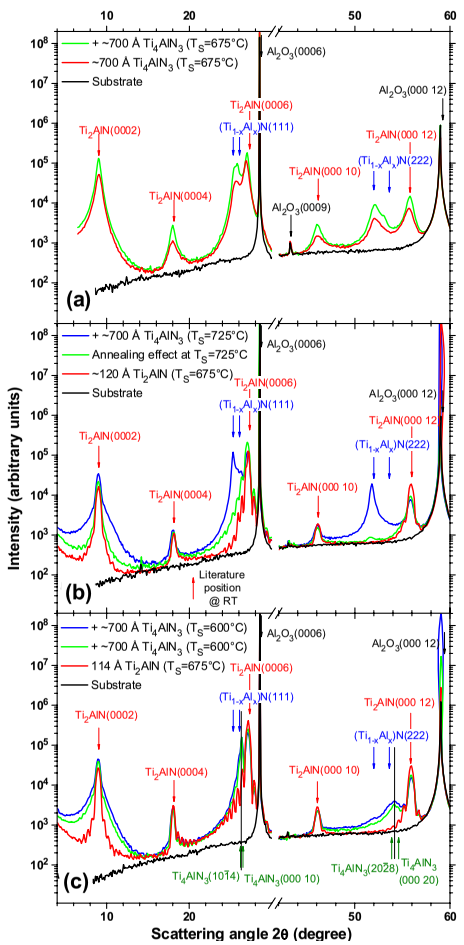


**Fig. 1**: *In-situ* XRD of nominal $Ti_4AlN_3$ deposition at different temperatures

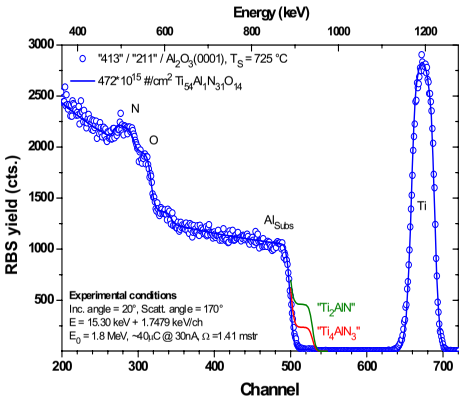


**Fig. 2**: *Ex-situ* RBS of nominal $Ti_4AlN_3$ deposited at 725°C, showing Al

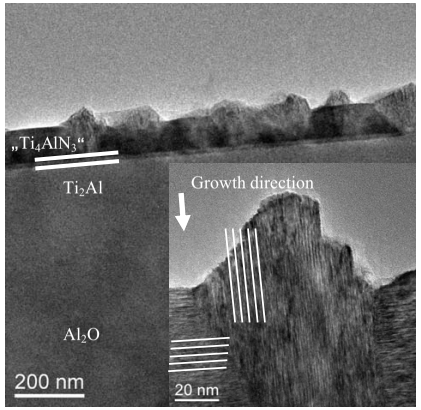


**Fig. 3**: *Ex-situ* HR-TEM micrograph of nominal $Ti_4AlN_3$ deposited at 600°C

with [2] should be overcome by higher temperature. However, when heating to 725°C the previously deposited $Ti_2AlN$ shows first traces of decomposition, as depicted in Fig. 1(b). Accordingly, nominal $Ti_4AlN_3$ deposition induces nucleation of a very low-mosaicity TiN, with no Al incorporation at all, as proven by ex-situ RBS shown in Fig. 2. Hence, the Al seems to act as a surfactant for TiN growth before desorption from the growth surface and evaporation into the vacuum. When depositing the nominal $Ti_4AlN_3$ at 600°C, the stoichiometry as proven by RBS (not shown here) is 4Ti:Al:3N, and the XRD shows peaks that may be attributed to a tilted $Ti_4AlN_3$ growth, as observed also for diffusion-limited $Ti_2AlN$ growth [1]. However, the HRTEM results depicted in Fig. 3 reveal hillocks and two competing alledged basal plane orientations with no evidence of a disctinct $Ti_4AlN_3$ phase, but a irregularly twinned structure stil that needs further investigations.

### REFERENCES


[1]: M. Beckers, N. Schell, *et al.:* Journal of Applied Physics **99**, 34902 (2006).
[2]: M. Beckers, N. Schell, *et al.:* Applied Physics Letters **89**, 074101 (2006).

| ROBL-CRG | **Experiment title:** ***In-situ* study of the preferential orientation of sputtered Ni-Ti thin films as a function of bias and substrate type** | **Experiment number:** **20_02_637** |
|---|---|---|
| **Beamline:** BM 20 | **Date of experiment:** from: 19.04.2006 to: 25.04.2006 | **Date of report:** 05.08.2006 |
| **Shifts:** 18 | **Local contact(s):** Dr. Norbert Schell | *Received at ROBL:* *25.08.06* |

**Names and affiliations of applicants** (* indicates experimentalists):

**Rui M.S. Martins*, N. Schell***: FZR, ROBL-CRG at ESRF, B.P. 220, F-38043, Grenoble, FRANCE

**F.M. Braz Fernandes***: CENIMAT-Centro de Investigação de Materiais, Campus da FCT/UNL, 2829-516 Monte de Caparica, Portugal

**Report:**

The preferential orientation of Ni-Ti thin films is a crucial factor in determining their shape memory behavior. The texture has a strong influence on the extent of the strain recovery. The relationship between structure and deposition parameters is of extreme importance for future device applications. Our approach is *in-situ* XRD *during* deposition carried out in a process chamber installed on the 6-circle-goniometer of ROBL [1]. Near-equiatomic films were co-sputtered from Ni-Ti and Ti targets. Substrate type and bias voltage play an important role for the preferred orientation.

## EXPERIMENTAL

For the deposition of the Ni-Ti films a 1-in Ni-Ti target (49 at% Ni – 51 at% Ti) and a 1-in Ti target (purity 99.99%) were inserted on the unbalanced magnetrons. The base pressure was about $2\times10^{-5}$ Pa, and the films were deposited under an Ar pressure of 0.42 Pa. The Ni-Ti and Ti magnetrons were driven at a power of 40 and 20 W, respectively, resulting in deposition rates of roughly 1 Å/s. For the deposition of the TiN buffer layer, the Ti target was run at a constant power of 80 W with an $Ar/N_2$ gas flow of 2/0.5 sccm. The deposition and annealing temperature was ≈ 470°C. The processing conditions of the samples studied are presented in Tab. 1. The scans were run in Bragg-Brentano geometry, using 0.675 Å radiation. Specular reflectivity (XRR) has been used for the growth rate calculation of the TiN buffer layer.

| *Sample* | *Substrate* | *Buffer layer* | *Substrate bias (V)* | | *Deposition (min.)* | | *Annealing (min.)* | |
|---|---|---|---|---|---|---|---|---|
| | | | *TiN deposition* | *Ni-Ti deposition* | *TiN* | *Ni-Ti* | *TiN* | *Ni-Ti* |
| S36 | $SiO_2^*$/Si(100) | - | - | 0 | - | 122 | - | 146 |
| S37 | Si(111) | - | - | 0 | - | 123 | - | 146 |
| S38 | $SiO_2^*$/Si(100) | TiN | -30 | 0 | - | 120 | 16 | 139 |
| S39 | Si(100) | - | - | -25 | 3 | 121 | - | 141 |
| S40 | MgO(110) | - | - | 0 | - | 122 | - | 148 |
| S41 | $SiO_2^*$/Si(100) | TiN | -30 | -45 | 3 | 122 | 94 | 138 |

** 1400 Å amorphous $SiO_2$ capping layer*

**Table 1.** - Deposition parameters for the various samples investigated.

## RESULTS AND DISCUSSION

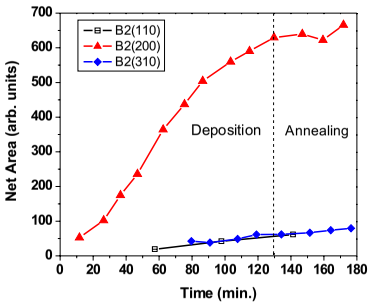


**Fig. 1.** – *Sample S36:* the integrated intensities of the Bragg-Brentano B2(110), B2(200) and B2(310) diffraction peaks as obtained from the positions of the respective peaks, recorded as a function of time after start of film growth.

For the Ni-Ti film **on thermally oxidized Si(100) without a substrate bias voltage** (*sample S36*), there is a strong preferential stacking on (h00) planes of B2 phase leading to a (100) fiber texture (Fig. 1) [2].

Figure 2 shows that the use of a **substrate bias voltage on naturally oxidized Si(100)** leads to a stacking with the {200} planes parallel to the surface and, when after approximately 40 min deposition the B2(110) is finally detected, the B2(200) intensity stays constant but the B2(110) intensity also doesn't increase [3]. An XRD scan in a larger range has shown the existence of grains with the (310) orientation parallel to the film surface (Fig. 3). Work is in progress to investigate the complete texture by the realization of pole figure measurements.

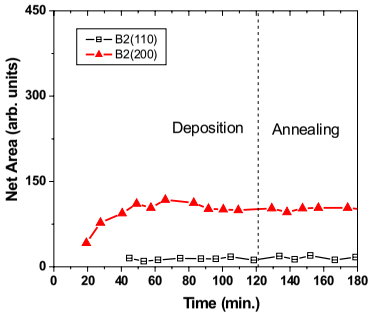


**Fig. 2.** – *Sample S39:* the integrated intensities of the Bragg-Brentano B2(110) and B2(200) diffraction peaks as obtained from the positions of the respective peaks, recorded as a function of time after start of film growth.

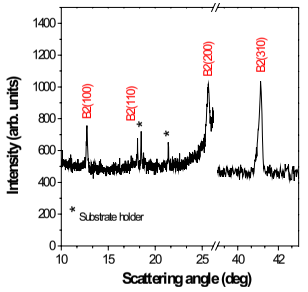


**Fig. 3.** – XRD diffractogram from the Ni-Ti *sample S39* during annealing after deposition stop at the same (deposition) temperature.

The behavior observed for *sample S40* by low angle time resolved XRR for the growing mode of the **first few monolayers on MgO(110)**, shows a good adaptation of the Ni-Ti structure to the substrate (Fig. 4). The intensity of the B2(110) peak is very high. However, contrary to the deposition on MgO(100) substrates where only the (100) orientation paralell to the substrate was detected [4], here not only the (110) but the (211) orientation of the B2 phase is also observed (Fig. 5), although not comparable in intensity.

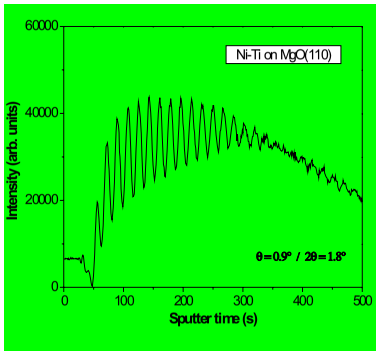


**Fig. 4.** – Time-dependent *in situ* XRR for the first minutes of deposition of the Ni-Ti film on MgO(110) substrate (*sample S40*).

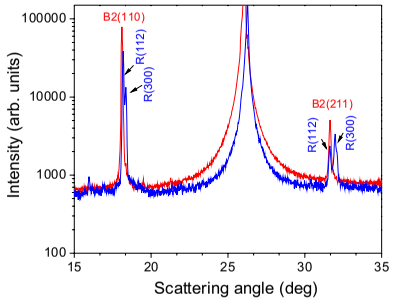


**Fig. 5.** – XRD diffractograms from *sample S40* during annealing after deposition stop at deposition temperature (top - red line) and room temperature (bottom – blue line).

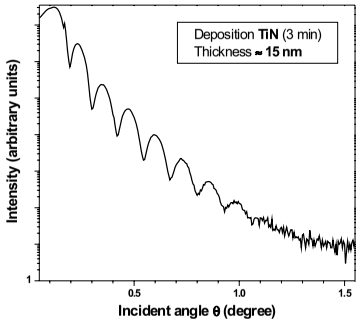


**Fig. 6.** – XRR spectra for a 3 min deposition of TiN (buffer layer of *sample S38*).

We have also been studying the effect of a **TiN layer deposited on top of the $SiO_2$/Si(100) substrate** prior to the deposition of the Ni-Ti films [5]. During this beamtime we could take profit of a new sputtering chamber with enlarged Be windows. This setup allowed to follow *in situ* also the B2(211) peak of the B2 phase. In this way it was possible to observe that a TiN buffer can be used to develop the (211) fiber texture of B2.

The effect of a TiN buffer layer with a thickness of about 15 nm (Fig. 6) was tested. For the *sample S38* <110> oriented grains of the Ni-Ti B2 phase dominate at small thicknesses while <211> oriented grains take over at larger thicknesses (Fig. 7a). Apparently, their TiN buffer layer has a considerable role in the appearance of the <211> oriented grains of the Ni-Ti B2 phase. Most likely, already since the beginning of the deposition, <211> oriented grains are present. An initial competitive growth between the <211> and <110> crystal orientations – competition between the orientation induced by the substrate and the one which minimizes surface energies – occurs. The <211> orientation gradually overgrows the <110> orientation.

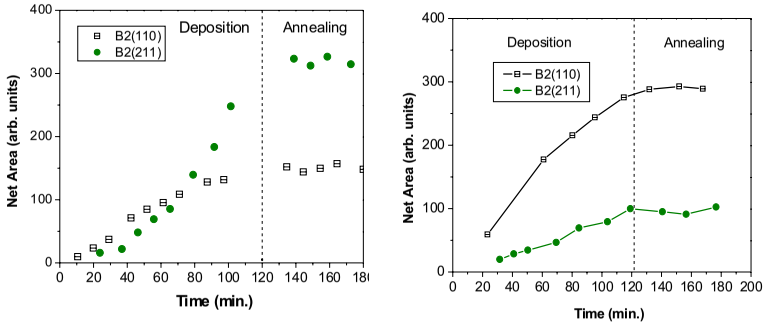


**Fig. 7.** – The integrated intensities of the Bragg-Brentano B2(110) and B2(211) diffraction peaks, recorded as a function of time after start of film growth. The Ni-Ti film was deposited on a TiN layer (≈ 15 nm) previously deposited on top of a $SiO_2$/Si(100) substrate: (a) *sample S38*, (b) *sample S41*.

The experiment with a substrate bias of -45 V (*sample S41* – Fig. 7b) has shown that the development of the (211) fiber texture is visibly reduced when compared to the one deposited without bias (*sample S38*) and the (110) fiber texture dominates since the beginning. The more energetic ion bombardment – due to the substrate bias – reduces the effect of the substrate.

## CONCLUSIONS

- An amorphous $SiO_2$ buffer layer induces the development of the (100) orientation of the B2 phase during deposition on heated substrates (≈ 470ºC).
- In previous studies it has been observed that on naturally oxidized Si(100) substrates the Ni-Ti B2 phase starts by stacking onto (h00) planes and then, very early in the deposition process, it changes to a (110) fiber texture [6-8]. During this beamtime, using a substrate bias voltage the same initial beavihour was observed but a (110) fiber texture was not detected. Instead, grains with the (310) orientation parallel to the film surface dominate.
- Using a MgO(110) substrate, a strong stacking of (110) planes of the B2 phase parallel to the film surface could be induced.
- Ni-Ti films were deposited on top of a TiN layer where a dominating orientation of TiN could not be identified (primarily <001> and <111> oriented grains nucleate and grow). Without substrate bias voltage, <110> grains of the Ni-Ti B2 phase dominate at small thicknesses while <211> oriented grains take over at larger thicknesses. A substrate bias (-45 V) reduces the development of the (211) fiber texture leading to a dominating (110) fiber texture.

## References

[1] W. Matz, N. Schell, W. Neumann, J. Bøttiger, J. Chevallier, *Rev. Sci. Instrum.* **72** (2001) 3344.
[2] R.M.S. Martins, N. Schell, M. Beckers, K.K. Mahesh, R.J.C. Silva, F.M. Braz Fernandes, *Appl. Phys. A* **84** (2006) 285.
[3] R.M.S. Martins, N. Schell, M. Beckers, A. Mücklich, H. Reuther, R.J.C. Silva, K.K. Mahesh, F.M.B. Fernandes, *Proceedings of SMST 2006* (*submitted*).
[4] R.M.S. Martins, N. Schell, M. Beckers, R.J.C. Silva, K.K. Mahesh, F.M. Braz Fernandes, *Mater. Sci. Eng. A* (*submitted*).
[5] R.M.S. Martins, N. Schell, R.J.C. Silva, L. Pereira, K.K. Mahesh, F.M. Braz Fernandes, *Sens. Actuators B (submitted)*.
[6] R.M.S. Martins, N. Schell, R.J.C. Silva, F.M. Braz Fernandes, *Nucl. Instr. & Methods Phys. Res. B* ***238*** (2005) 319.
[7] R.M.S. Martins, F.M. Braz Fernandes, R.J.C. Silva, M. Beckers, N. Schell, *Mater. Sci. Forum* ***514-516*** (2006) 1588.
[8] R.M.S. Martins, F.M. Braz Fernandes, R.J.C. Silva, M. Beckers, N. Schell, *Proceedings of SMST 2004* (2006) 421.

| ROBL-CRG | **Experiment title:**<br>**The influence of He ion irradiation on the texture development of thin films** | **Experiment number:**<br>**20_02_638** |
|---|---|---|
| **Beamline:**<br>BM 20 | **Date of experiment:**<br>from: 26.04.2006 to: 02.05.2006 | **Date of report:**<br>05.07.2006 |
| **Shifts:**<br>18 | **Local contact(s):**<br>Dr. Norbert Schell | *Received at ROBL:*<br>*05.07.06* |

**Names and affiliations of applicants** (* indicates experimentalists):

N. Schell* and J.v. Borany*

Forschungszentrum Rossendorf, Institute of Ion Beam Physics and Materials Research, P.O.B. 510119, 01314 Dresden, Germany

## Report:

Having tested the magnetron sputter deposition itself in an up-graded process chamber (see Experimental Report **20_02_608 *In-situ* x-ray diffraction during sputter deposition of $Ti_{1-x}Al_xN$ – Part IV: A new sputter chamber for MAX phase deposition**), the behaviour of the additional ion gun up to 6 keV and 10 µA allowing post-deposition ion irradiation with light atoms or energetic ion bombardment during sputter deposition was investigated by **off-sputtering of thin Pt films**.

**Fig. 1** shows the design study of the chamber from the beam entrance side with symmetric magnetrons, ion gun, viewport between Be entrance windows, one turbo pump (70 l/s) at a corner valve which can be used for throttling and substrate alignment and handling devices below. **Fig. 2** shows the schematic top-view geometry of the sample on the substrate holder.


**FIG. 1:** Design study of the depostion chamber.

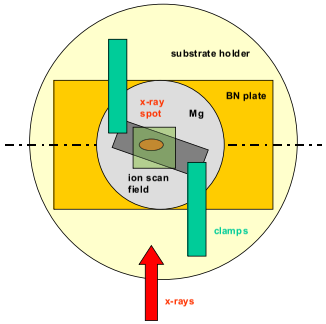


**FIG. 2:** Schematic top-view geometry.

The off-sputtering of the Pt films – 55 nm thick deposited on $SiO_2$(1.5 µm)/Si(100) – has been investigated by **XRD in Bragg-Brentano-geometry** ($\lambda = 1.54$ Å). The film was actually irradiated with **Ar ions of 5 keV** energy under an **incidence angle of 20°**; the total ion current of 2.72 µA within a scanning field of 4.2 x 4.2 $mm^2$ corresponds to an ion flux density of $9.6\times10^{13}$ ions/$cm^2$s. **Fig. 3** shows scans around the dominating Pt(111) peak recorded after consecutive sputtering steps as well as corresponding **TRIDYN code simulations** [1]. Three features are clearly observed: (i) the integrated peak area decreases as expected due to the film thickness reduction from sputtering, (ii) a second component appears at a lower scattering angle ($2\theta = 39.15°$) reflecting an expanded Pt lattice due to Ar incorporation, and (iii) at the end of the sputtering process the scan peaked with a very low intensity at the initial position ($2\theta = 39.60°$) which can be interpreted in terms of a very thin Pt film or even Pt islands (size <5 nm) with a relaxed lattice as Ar becomes volatile.

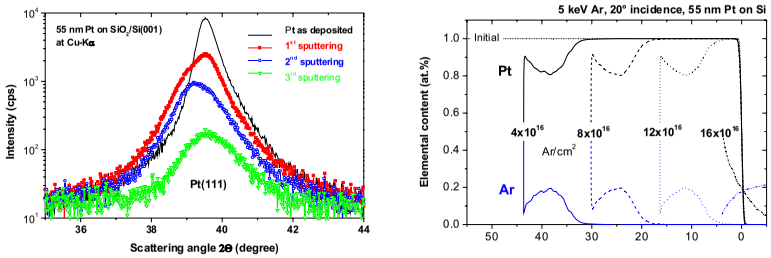


**FIG. 3:** XRD scans in Bragg-Brentano-geometry around the dominating Pt(111) peak after three consecutive off-sputtering steps lasting 13, 8, and 8 min, respectively (left); Pt off-sputtering and Ar incorporation into the residual film according to TRIDYN calculations for different Ar fluences (right): The reduction of the Pt film thickness with increasing Ar ion fluence is obvious, the sputter yield amounts to 2.8 at/ion. The calculated loss of the Pt areal density due to off-sputtering agrees quantitatively very well with the measured decrease of the integrated Pt(111) peak area. The Ar ions modify a near-surface region of the Pt films of approximately 10 nm; the maximum Ar content saturates at about 20 at.%.

## CONCLUSION

A process chamber with two magnetrons and one ion gun, heating and bias voltage, equipped with four Be windows for various x-ray scattering techniques off-plane and in-plane has been commissioned at ROBL-MR. First experiments demonstrate its possibilities for *in situ* x-ray investigations of the microstructural development during growth of thin films or their modification by additional ion bombardment [2]. Future experiments will be dedicated to study changes of film properties by ion irradiation *during* deposition. Energy and flux of the ions delivered from the gun can be varied independently from the ions and atoms from the magnetron targets.

### References:

[1] W. Möller and M. Posselt, Tridyn-FZR User Manual, Wiss.-Tech. Berichte, FZR-317, 2001.

[2] N. Schell, J.v. Borany, and J. Hauser, J., *A two magnetron sputter deposition chamber equipped with an additional ion gun for in situ observation of thin film growth and surface modification by synchrotron radiation scattering.* AIP Conference Proceedings (2006) for the 9th Intern. Conf. on Synchr. Rad. Instrum., SRI-2006, in Daegu, South Korea, 28 May – 02 June, 2006, *submitted.*

| ROBL-CRG | **Experiment title:** **Phase formation processes in nanoscale Nickel-alloy layers during heat treatment on SiGe substrates** | **Experiment number:** **20_02_617** **20_02_639** |
|---|---|---|
| **Beamline:** BM 20 | **Date of experiment:** from: 8.03.2006 to: 15.03.2006 | **Date of report:** 30.11.2006 |
| **Shifts:** 21 | **Local contact(s):** Dr. N. Schell | *Received at ROBL:* *5.12.2006* |

**Names and affiliations of applicants** (* indicates experimentalists):

**J. Rinderknecht*, I. Zienert*, H. Prinz***
AMD Saxony LLC & Co. KG, D-01277 Dresden, Germany

**N. Schell**
Forschungszentrum Rossendorf (FZR), Dresden and ROBL-CRG, Grenoble, France

## Report

The formation of Ni germanosilicides has been studied by XRD experiments using synchrotron radiation with an energy of 8.048 keV. A gracing incidence setup was chosen with a fixed angle of incidence of 0.5° to perform the large angle XRD detector scans. For thermal treatment, a Be-dome annealing chamber was used to investigate the phase formation and transition processes under quasi-statically conditions at elevated temperatures between RT and 800°C.

The investigated samples consisted of an SRAM area with a feature size of approx. 70 nm. Two different sets of samples where investigated. One set of samples possessed transistor gates, i.e. a dummy gate without polycrystalline Si, and one set did not. The deposited 10 nm thick metal layer were pure Ni, Ni with 5at.% of element A1 and Ni with 5at.% A1 plus 5at.% element A2. The alloying elements A1 & A2 were used to alter the thermal stability of the resulting monosilicide as well as to influence the texture thereof [1]. The areas which were to be silicidized consisted of single-crystal (001) silicon-germanium (22at.% Ge) substrate surrounded by silicon oxide.

The samples without dummy gate showed that the transition from Ni to $Me_2Si_{1-x}Ge_x$ is completed between 175°C and 200°C, i.e. the first silicidation step is completed at that temperature. For pure Ni samples the transition from $Me_2Si_{1-x}Ge_x$ to $MeSi_{1-x}Ge_x$ is finished at 325°C, the alloyed samples exhibit Me2Si1-xGex up to 425°C, which means that the alloying element(s) enhance the stability range of Me2Si1-xGex to higher temperatures.

On the samples with dummy gates, the pure Ni and NiA1 samples demonstrate a stability range of metallic Ni that is slightly increased to >200°C and >225°C, respectively. Also on pure Ni samples, the transition from $Me_2Si_{1-x}Ge_x$ to $MeSi_{1-x}Ge_x$ was completed at 400°C. The alloyed samples show $Me_2Si_{1-x}Ge_x$ only up to 300°C (NiA1) and 350°C (NiA1A2).

The comparison of the two sets of samples yields that on dummy gate samples the thermal stability of metallic Ni is enhanced slightly and that on pure Ni samples the thermal stability of $Me_2Si_{1-x}Ge_x$ was raised by 75 K due to the dummy gates. The dummy gates widen the stability range of $MeSi_{1-x}Ge_x$ to lower temperatures, i.e. the temperature where only $MeSi_{1-x}Ge_x$ can be found on alloyed samples is lowered by 75-125 K (NiA1A2 vs. NiA1) (see figure 1). However, no direct or indirect indication of $Me(Si_{1-x}Ge_x)_2$ formation could be found, opposed to previous investigations on pure Si substrates [2-4].

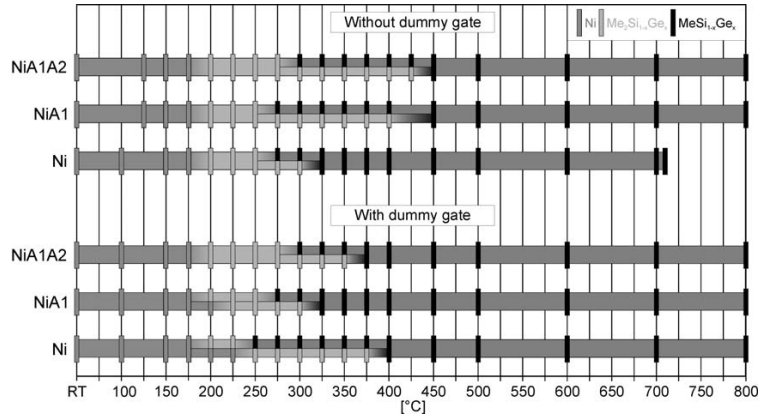


***Figure 1:*** *Summary of 109 SR-XRD results of 100 Å nickel samples with different alloying elements. High bars are actual measuring temperatures.*

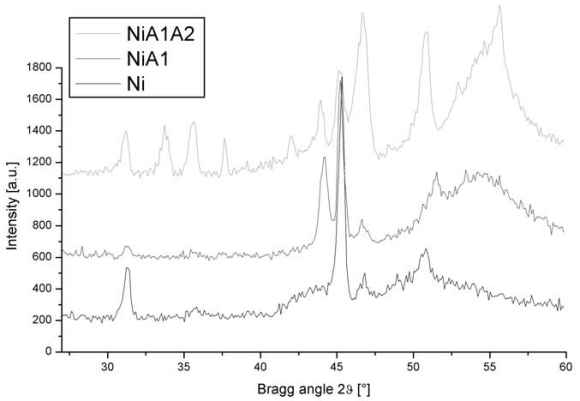


***Figure 2:*** *Comparison at 450°C of the sample set with gate structures.*

Figure 2 compares the diffraction pattern of 3 samples with gate structures at 450°C. The sample with alloying elements A1 and A2 exhibits the most "powder-like" distribution of the ratio between the different diffraction maxima. The sample with A1 shows a diffraction pattern between the pure Ni sample and the NiA1A2 sample. Whereas the pure Ni sample displays fewer diffraction maxima than the other two samples, which is due to a different texture, probably an axiotaxy like texture [1].

**References:**

[1] C. Detavernier et al., Nature **426** (2003) 641-645.
[2] J. Rinderknecht et al., Microelectronic Engineering **64** (2002) 143-149.
[3] J. Rinderknecht et al., Microelectronic Engineering **70** (2003) 226–232.
[4] J. Rinderknecht, Phase formation and size effects in nanoscale silicide layers for the sub-100 nm microprocessor technology, Ph.D thesis, TU Dresden, (2005), http://nbn-resolving.de/urn:nbn:de:swb:14-1126002535643-34479

| ROBL-CRG | **Experiment title:** *In-situ* x-ray diffraction during sputter deposition of Ti-Al-N MAX-phase thin films | **Experiment number:** 20_02_640 |
|---|---|---|
| **Beamline:** BM 20 | **Date of experiment:** from: 31.10.2006 to: 07.11.2006 | **Date of report:** 19.11.2006 |
| **Shifts:** 21 | **Local contact(s):** Dr. Johannes von Borany / Udo Strauch | *Received at ROBL:* *20.11.06* |

**Names and affiliations of applicants (* indicates experimentalists):**
*M. Beckers, *C. Höglund, Linköping University, Sweden
*N. Schell, GKSS at DESY, Hamburg, Germany
*J. von Borany, Forschungszentrum Rossendorf, Germany & ROBL-CRG, France

## Report

### AIM:

The ternary nitrides and carbides advertised under the name ***$M_{n+1}AX_n$ phases*** – with M being a transition metal, A an A group element and X nitrogen or carbon – show a unique combination of metallic and ceramic properties including good electrical conductivity, high temperature stability and machinability [1]. Due to these properties $M_{n+1}AX_n$ phase bulk samples as well as thin films have been extensively studied during the past years. Carbides have been deposited by DC sputtering from compound targets, from individual M and A targets with co-evaporated $C_{60,}$ and from three elemental targets at temperatures around 900°C. For the nitrides the only published thin film results so far concern $Ti_2AlN$, deposited ***by reactive sputtering*** in an $Ar/N_2$ gas mixture from a compound 2Ti:Al target at 830°C or ***from Ti and Al elemental targets at 670°C*** [2]. An alternative route of $M_{n+1}AX_n$ phase thin film growth could be by self-organized topotaxial solid-state-reaction between MX and A, alternatively between AX and M. Hence, during this experiment we investigated the possible ***formation of $Ti_2AlN$ during annealing of TiN/Al and AlN/Ti multilayer stacks.***

### EXPERIMENTAL:

A total of ***nine multilayer stacks*** were deposited onto single crystal MgO(111) and $Al_2O_3$(0001) substrates by reactive and non-reactive magnetron ***sputtering from Ti and Al targets*** in an $Ar/N_2$ atmosphere at substrate temperatures between 200 and 500°C. The deposition parameters for the Ti and Al metal layers were set to target powers of Ti and Al = 20 W with an Ar flux of 3.4 sccm and a working pressure of 0.5 Pa, leading to Ti and Al deposition rates of 0.21 and 0.32 Å/s, respectively. The deposition parameters for the TiN and AlN layers were set to target powers of Ti = 80W and Al = 27 W with an $Ar/N_2$ flux ratio of 2.16/0.66 sccm and a working pressure of 0.35 Pa, leading to Ti and Al deposition rates of 0.21 and 0.32 Å/s, respectively. Each sequential deposition step was characterized in two different scattering geometries: (1) low angle specular reflectivity (XRR), either time-resolved at a fixed angle to monitor each layer's growth mode, or angular-resolved for thickness and roughness determination. (2) Large angle x-ray diffraction (XRD) to determine phase formation and off-plane lattice parameters. Subsequent to deposition, some layers were ***annealed up to 650°C substrate temperature*** to check for ***possible $Ti_2AlN$ formation***. The energy of the incident x-rays was monochromatized to $\lambda = 1.053$ Å, i.e. 11774 ± 20 eV as estimated from single-crystal substrate peak shifts.

### RESULTS

Fig. 1 shows the *in-situ* data obtained for a 26 nm AlN / 10 nm TiN / 11 nm AlN / 20 nm Ti / 11 nm AlN stack on $Al_2O_3$ deposited at 200°C substrate temperature and subsequently annealed for about 2 h at 500°C. The XRD data in Fig. 1(a) reveal basal-plane heteroepitaxial growth of AlN(0001) and Ti(0001) onto

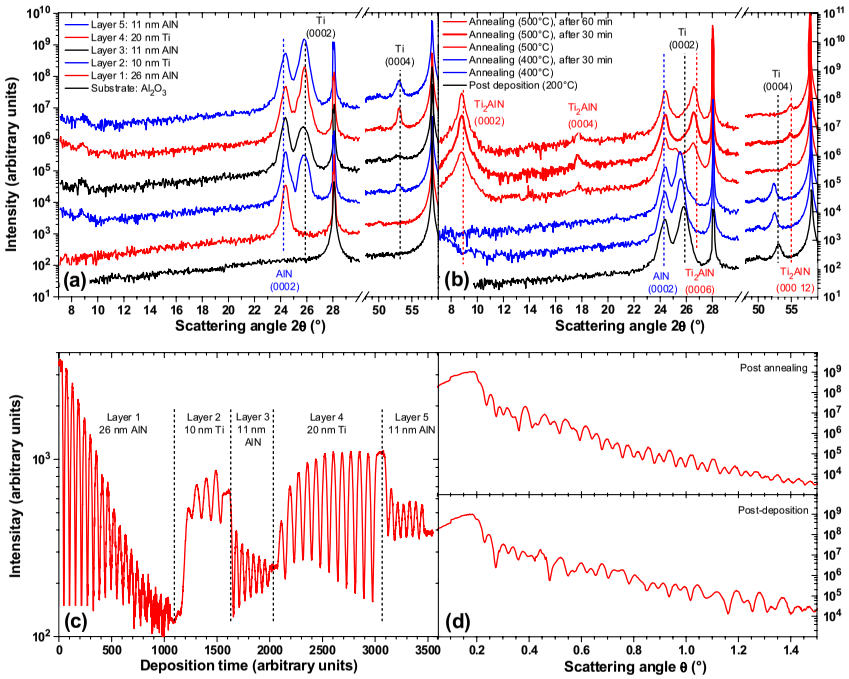


**Fig. 1**: *In-situ* results of a AlN/Ti multilayer stack: (a) sequential XRD results during deposition at 200°C, (b) XRD data during annealing up to 500°C, (c) time-resolved reflecivity of each deposition step (d) angular-resolved XRR data of the sample in the as-deposited and post-annealed state.

$Al_2O_3$(0001). The AlN(0002) signal shows lower intensity when compared to the yet thinner Ti layer, which can be understood by the growth oscillations in Fig. 1(c). Since the adatom mobility on AlN at 200°C is relatively low, the growth surface roughens and correspondingly the intensity oscillations for each AlN deposition show rapid exponential decay. Ti on the contrary has a higher electron density than AlN plus an increased adatom mobility, hence already during initial growth stages the reflectivity signal is increased, amplified by a significant surface smoothing, as can be deduced from the exponential growth of the intensity oscillations. In accordance to the smoother growth front a lower mosaicity of the Ti can be expected, and hence also an increased XRD signal. The oscillations were not recorded at the anti-bragg ½*$Q_d$ value, but could easily be fitted with a layer-by-layer growth model when taking the $Q_{meas}/Q_d$ value into account, where $Q_d$ denores the Q value corresponding to the c-axis value of Ti and AlN, respectively. During annealing, shown in Fig. 1(b), at 400°C the first stage of interfacial reaction seems to be AlN decomposition and nitrogen diffusion into Ti to form a $TiN_x$ compond as can be deduced from the shifting Ti peak, pointing towards lattice expansion. No further reaction takes place after holding 400°C for another 30 minutes. When increasing the temperature to 500°C, however, already after the ramping period of approx. 5 minutes $Ti_2AlN$ formation is evident by a $Ti_2AlN$(0002) peak. Accordingly the Ti(0002) intensity diminishes beyond the detection limit after a holding time of 60 minutes. The interfacial reaction can also be deduced from the XRR data shown in Fig. 1(c), where the single layer beating after annealing has vanished. The basal plane-oriented $Ti_2AlN$ formation occuring at 500°C reported is 170°C lower than temperatures reported in [2] and may open up low temperature $Ti_2AlN$ applications as well as $M_{n+1}AX_n$ phase formation by other AlN/M diffusion couples. No $Ti_2AlN$ formation at T ≤ 650°C has been found for TiN/Al couples (data not shown here).

### REFERENCES

[1]: M. W. Barsoum: Progress in Solid State Chemsitry **28**, 201 (2000).
[2]: M. Beckers, N. Schell, *et al.:* Applied physics letters **89**, 074101 (2006).

| ROBL-CRG | **Experiment title:** ***In situ* investigation of recrystallization of heavily damaged by ion bombardment ZnO thin films during thermal annealing** | **Experiment number:** **20_02_641** |
|---|---|---|
| **Beamline:** BM 20 | **Date of experiment:** from: 04.10.2006 to: 10.10.2006 | **Date of report:** 19.01.2007 |
| **Shifts:** 18 | **Local contact(s):** Mr. Udo Strauch | *Received at ROBL:* *22.01.2007* |


**Names and affiliations of applicants** (* indicates experimentalists):

**F. Eichhorn*, A. Rogozin*, N. Shevchenko*, M. Vinnichenko**

Forschungszentrum Dresden Rossendorf (FZD), Institute of Ion Beam Physics and Materials Research, D-01326 Dresden, Germany

**U. Strauch***

FZD and ROBL-CRG, Grenoble, France


## Report

A thorough understanding of damage accumulation and thermal stability of implantation-produced defects in ZnO is crucial for improvement of its electrical and optical properties. The aim of this experiment was to study the recrystallization process and related changes of electrical properties of the heavily damaged by ion bombardment ZnO thin films during thermal annealing in vacuum.

Undoped epitaxial ZnO films were deposited by reactive medium frequency pulsed magnetron sputtering at the base pressure of $3.4\times10^{-7}$ mbar using a mixture of Ar and $O_2$ (partial pressure of $1.0\times10^{-2}$ mbar and $1.4\times10^{-4}$ – $3.4\times10^{-3}$ mbar, correspondingly). The substrates where 10 mm x 10 mm x 1 mm pieces of (0001)-oriented $Al_2O_3$ single crystals, additionally cleaned in $O_2$ RF plasma for 5 min before the deposition. The ZnO films were implanted with arsenic ions at ion energy of 300 keV and fluences of $3\times10^{16}$ and $5\times10^{16}$ $As^+$ ions/cm$^2$.

The samples were characterized by *in situ* synchrotron XRD analysis at 8.045 keV and simultaneous four-point probe measurements during annealing in vacuum. The experiments are performed at non-isothermal (T-ramp: 10 K/min) and isothermal (temperature range of 700–850°C) annealing modes. *Ex-situ* measurements of pole figures of as-deposited epitaxial and annealed films were carried out.

The x-ray diffractograms of as-implanted ZnO film demonstrate only a broad peak around 32.2°, indicating XRD-amorphous or/ and nanostructural state of ZnO (Fig. 1). Annealing in vacuum leads to growth of the (002) peak, as shown on Fig.1. The *in situ* XRD experiments yield ZnO recrystallization temperature range and process rate at different annealing conditions. The XRD data evaluation and determination of the kinetic parameters of crystallization as well as the activation energy are in progress.

Figure 2 shows the integral intensity and FWHM of ZnO (002) peak as a function of annealing time. The peak integral intensity increased strongly during the first 10 min of annealing, and its enhancement slows down at further annealing. Probably, different mechanisms control the recrystallization during the initial and subsequent annealing period. Delay time and the recrystallization rate depend on annealing temperature as well as on the degree of damage of the implanted films (ion fluence).

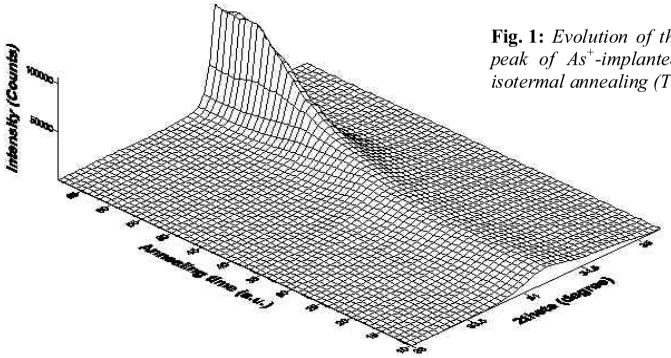


**Fig. 1:** *Evolution of the ZnO (002) diffraction peak of $As^+$-implanted samples during non-isotermal annealing (T-rate: 10 K/min).*

Figure 3 reveals an outset of structural changes at the temperature of ~ 500°C for ZnO implanted with fluence of $5\times10^{16}$ $As^+$/cm$^2$ and the temperature of ~ 600 °C for the sample implanted at $3\times10^{16}$ $As^+$/cm$^2$. To all appearance, the crystallization rate of the high-fluence implanted film is essentially lower in comparison with the sample implanted at $3\times10^{17}$ $As^+$/cm$^2$.

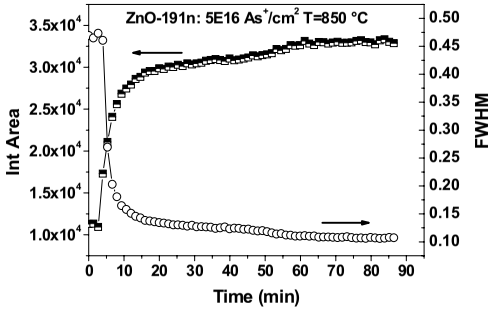


***Fig. 2:*** *Integral intensity of ZnO (002) peak recorded as a function of time during isothermal annealing at 850°C.*

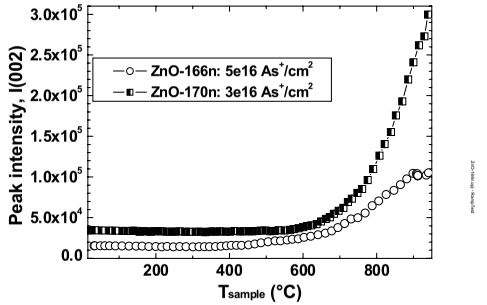


***Fig. 3:*** *Evolution of the ZnO (002) peak intensity of $As^+$-implanted samples during non-isotermal annealing (T-rate: 10 K/min).*

The pole figure measurements (not shown here) demonstrate that recrystallization of ZnO films heavily damaged by ion bombardment leads to a significant enhancement of in-plane and off-plane textures of annealed samples. The crystalline quality of annealed ZnO is only slightly lower than that of the undoped epitaxial as-deposited ZnO.

| ROBL-CRG | **Experiment title:** **Materials Characterization for Embedded DRAM-Trench-Technology** | **Experiment Number:** **20_02_643** |
|---|---|---|
| **Beamline:** BM 20 | **Date of experiment:** from: 23.09.2006 to: 25.09.2006 | **Date of report:** 15.01.2007 |
| **Shifts:** 9 | **Local contact(s):** Dr. J. von Borany | *Received at ROBL:* *19.01.2007* |

**Names and affiliations of applicants** (* indicates experimentalists):

**S. Teichert***
Qimonda Dresden GmbH & Co OHG, D-01079 Dresden, Germany

**F. Eichhorn*, J. von Borany***
Forschungszentrum Dresden-Rossendorf, Institute of Ion Beam Physics and Materials Research, D-01314 Dresden, Germany

## Report

The continuous size reduction in the DRAM technology requires the replacement of traditional materials, e.g. the classical gate $SiO_2$ films has to be substituted by insulators with significant higher dielectric constant κ, the so-called high-κ dielectrics. Doped $HfO_2$ layers are candidates for the application as dielectric in next generation trench capacitors [1]. The formation of different crystalline phases plays a crucial role for the dielectric properties. The equilibrium phase diagram of $HfO_2$ shows at ambient conditions a stable monoclinic phase. Tetragonal and cubic ($CaF_2$-type) or orthorhombic phases exist at high temperatures (T > 1600°C) or high pressures, respectively. Doping with e.g. Si can be used to stabilize the cubic/tetragonal/orthorhombic phase of $HfO_2$ in thin films [2]. Theoretical calculations showed that the dielectric constants of the cubic/tetragonal phases can possess significantly higher k values in comparison to the monoclinic phase [3]. The experimental data support these results for the correlation of structural and electrical properties [2,4].

In the experiment mixed $Hf_{0.92}Si_{0.08}O_2$ and nanolaminates ($HfO_2$-$SiO_2$ layer stacks) grown by atomic layer deposition (ALD) on Si(001) substrates have been analyzed by X-ray diffraction (XRD) at 8.045 keV. All layers (thickness = 10...15 nm) were annealed in an RTP process for 30 s in a $N_2$ atmosphere after the deposition process for variable temperatures in the range between 600 and 1000°C. Grazing incidence geometry (α = 0.5°) was performed to collect the diffraction pattern in a wide range of scattering angles (2θ = 15° – 92°).

The as-deposited $Hf_{0.92}Si_{0.08}O_2$ films are in the amorphous state. After annealing at temperatures > 600°C all mixed Hf-oxide films crystallize preferably into the cubic phase (fig. 1, left). It is interesting to note that the monoclinic phase is suppressed very efficient for an annealing treatment up to 1000°C. In addition to the cubic phase small traces of the orthorhombic phase may be present in the films. The polycrystalline films contain randomly oriented grains as proved by intensity ratio of the reflexes (see comparison with powder diffraction pattern in fig. 1, right).

In contrast, the GIXRD data of the nanolaminate (fig. 2) point to a texture of the film. The (111) pole figure reveals a fibre texture with components at χ = 15° and χ = 56° ... 58°. The component at χ = 15° may result from grains with {221} ‖ Si substrate (001). In $CaF_2$-type crystals this orientation is typically observed as a result of a twin formation by a rotation of 180° around the <111> axis of grains with {100} ‖ (001) Si substrate. Furthermore, these {100} oriented grains would explain the 2nd component of the (111) pole figure at χ = 56…58°. However, further measurements are needed to support this discussion.

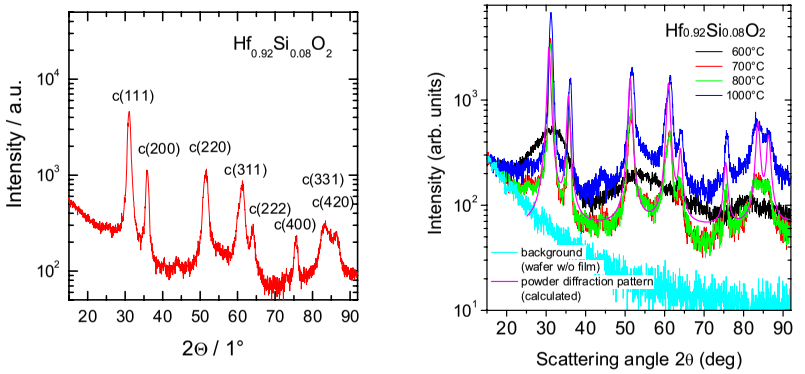


***Fig 1:*** *Examplary GIXRD scans for a mixed $Hf_{0.92}Si_{0.08}O_2$ film after annealing at 1000°C in $N_2$ (left) or in a sequence after different annealing treatments (right). Reflexes are indexed for the cubic phase of $HfO_2$.*

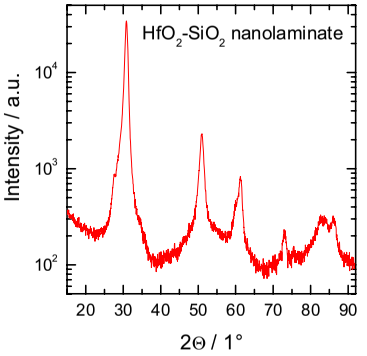


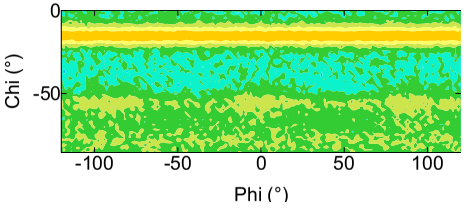


***Fig 3:*** *Pole figure for 2θ=30.9° near to the cubic $HfO_2$(111). Fibre Texture: 1st component at χ = 15°, 2nd component at χ = 56..58° with a partially preferential azimuthal orientation to the Si lattice.*

***Fig 2:*** *GIXRD scan for a $HfO_2$-$SiO_2$ nanolaminate film after annealing at 1000°C in $N_2$.*

## References

[1] W. Müller et al., IEDM, Dec 5-7, 2005 (Washington D.C.), 14.1.
[2] K. Tomida, K. Kita, A. Toriumi, Appl. Phys. Lett. **89** (2006) 142902.
[3] X. Zhao, d. Vanderbilt, Phys. Rev. **B65** (2002) 233106.
[4] K. Kita, K. Kyuno, A. Toriumi, Appl. Phys. Lett. **86** (2005) 102906.

| ROBL-CRG | **Experiment title:** **GISAXS Test at ROBL** | **Experiment Number:** **20_02_644** |
|---|---|---|
| **Beamline**: BM 20 | **Date of experiment**: from: 08.11.2006 to: 14.11.2006 | **Date of report**: 02.02.2007 |
| **Shifts:** 18 | **Local contact(s)**: Udo Strauch | *Received at ROBL:* *02.02.2007* |

**Names and affiliations of applicants** (* indicates experimentalists):

**F. Eichhorn* and J. Grenzer***

Forschungszentrum Dresden-Rossendorf, Institute of Ion Beam Physics and Materials Research, D-01314 Dresden, Germany

## Report:

We report on first grazing incidence small angle x-ray scattering test measurements at ROBL.

Grazing-incidence small-angle scattering (GISAXS) is an increasingly important structural characterization technique and finds its application in nanostructures and nanocomposites investigations at surfaces and interfaces. The GISAXS method can be used as a complementary method to conventional surface-sensitive tools such as scanning probe microscopy and electron microscopy. The GISAXS technique is, like any X-ray technique, a non-destructive one and therefore can be easily used in situ and in real time investigations to monitor the formation of the nanostructure or nanocomposite, that is a great advantage to understand the kinetics of nanoassembly processes. Moreover GISAXS can be used to investigate non-destructively structures just below a surface.

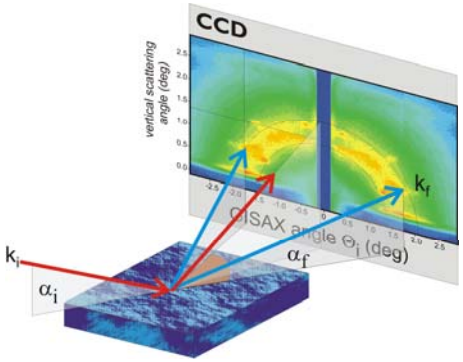


***Figure 1**:*
*Experimental GISAXS setup; for | | > 0 is the scattering vector almost parallel to the sample surface that allows determining the lateral structure. Using a 2D detector a $Q_{ip}$ (in-plane) and $Q_z$ reciprocal space map could be recorded at once.*

The aim of this test experiment was to expand the experimental capabilities of the ROBL beamline, especially in material research. Therefore, we conducted a series of tests to find out the experimental conditions to operate the beamline for an optimal GISAXS experiment. Figure 1 shows the principal setup of a GISAXS experiment. As a detector we used a MAR-CCD with a detector radius of 165 mm. The detector was placed 3 m behind the sample. To reduce air scattering, tests were carried out at an x-ray energy of 11 keV and a He filled flight tube was employed between the sample and detector.

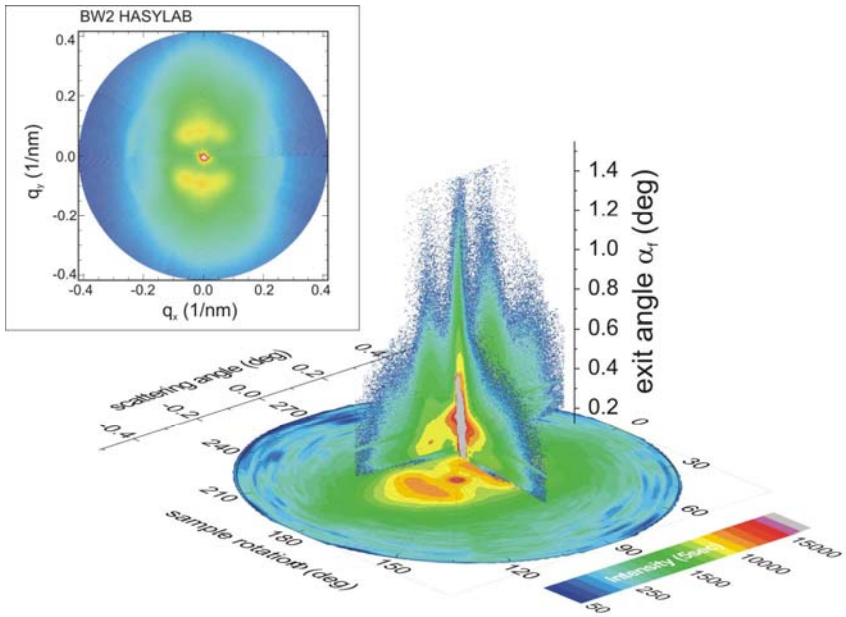


***Figure 2:***
*The GISAXS scattering pattern of a free standing InAs quantum dot sample was measured at an incidence angle of 0.3 degree; the out of plane intesity distribution is shown for a sample rotation angle of 0 and 90 degree; the in-plane patteren is composed of 36 scans and shown for an exit angle of 0.3 degree as well. The inset shows a similar in-plane pattern measured at the BW2 at HASYLAB.*

Figure 2 shows a GISAXS scattering pattern of a freestanding InAs quantum dot sample grown on a GaAs substrate. The sample was provided by M. Schmidbauer (Institut für Kristallzüchtung, Max-Born-Straße 2, D-12489 Berlin, Germany). The sample shows a clear one dimensional short range ordering with an average dot distance of about 80 nm. The inset shows the GISAXS scattering measured under similar conditions (E = 10keV) at the BW2 beamline at HASYLAB.

In conclusion, GISAXS measurements can be carried out at the ROBL beamline taking into account the synchrotron beam characteristics at a bending magnet, the need of a longer counting time and a higher sample - detector distance to increase resolution. For routine operations a double beam stop (for the direct and reflected beam) as well as an optimized flight tube should be installed.

| ROBL-CRG | **Experiment title:** **Real-time studies of the ITO film structure and resistivity behavior during annealing** | **Experiment number:** **IH-HC-777** |
|---|---|---|
| **Beamline:** BM 20 | **Date of experiment:** from: 21.09.2005 to: 24.09.2005 | **Date of report:** 02.06.2006 |
| **Shifts:** 9 | **Local contact(s):** Rui Martins | *Received at ROBL:* *09.06.06* |

**Names and affiliations of applicants** (* indicates experimentalists):

R. Martins*, FZ Rossendorf, IIM, Dresden, Germany

A. Rogozin*, FZ Rossendorf, IIM, Dresden, Germany

N. Shevchenko*, FZ Rossendorf, IIM, Dresden, Germany

M. Vinnichenko, FZ Rossendorf, IIM, Dresden, Germany

**Report:**

The present measurements are a continuation of experiment IH-SI-206 and were aimed to study the ***ITO thin film annealing by electric current in vacuum***. Compared to the isothermal annealing, the annealing process by electric current at equivalent temperatures is more efficient and shows sufficient reduction of the activation energy and a decrease of the kinetic exponent of the crystallization process. The mechanism of ITO crystallization enhancement by electric current has never been experimentally studied.

In this work the conventional isothermal and electric current annealing processes are investigated by real-time synchrotron XRD analysis and resistivity measurements. In order to better understand the crystallization mechanism during electric current annealing, amorphous ITO layers were produced (i) with different thicknesses, (ii) at different base pressure and (iii) with alloyed (Freiberger Ne-metal GmbH) and sintered (Kurt & Lesker) magnetron targets. The ITO films with thicknesses of 75, 145, 180, and 280 nm were deposited by middle frequency pulsed reactive magnetron sputtering at the base pressure of $8.6 \cdot 10^{-6}$ mbar. The set of ITO samples was prepared at the following base pressures: $3.4 \cdot 10^{-5}$, $2.5 \cdot 10^{-5}$, $1.4 \cdot 10^{-5}$, $8.6 \cdot 10^{-4}$, and $4.6 \cdot 10^{-4}$ mbar. The thickness of these ITO films is within the range of 170-180 nm.

The ITO crystallization temperature and delay time strongly depend on the type of the magnetron target used for ITO film deposition (Figs 1 and 2). At non-isothermal annealing (T-ramp: 5 K/min) the XRD data reveal a rapid crystallization at the temperature of ~250°C for ITO deposited with an alloy target and the crystallization temperature of ~330°C for the sintered target (Fig. 1). In the present experiment the high crystallization temperature ITO films are used.

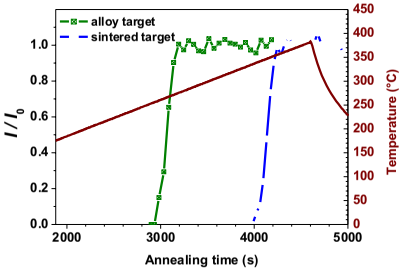


**Fig. 1:** Evolution of the normalized ITO film XRD peak integral intensity at non-isotermal annealing (T-rate: 5 K/min) .

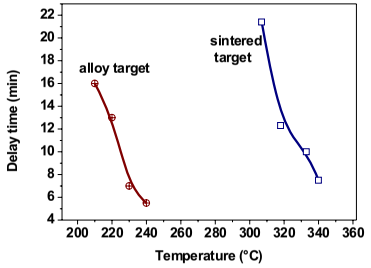


**Fig. 2:** Crystallization delay time *vs*. annealing temperature for ITO films produced with sinterd and alloy magnetron targets.

The deposition base pressure influences the crystallization onset *during* deposition, and finally regulates the initial crystalline degree of ITO films. However, the XRD data and resistivity behavior show that no influence of the base pressure parameter on the crystallization onset and the rate during the electric current annealing process. An effect of ITO film thickness on the crystallization onset at electric current annealing is not found. Possibly a slight enhancement of the crystallization rate for ITO films with higher thickness is present but the data could be statistically insignificant. Such experiments require more samples per experimental point as well as a comparison of the electric current annealing with the isothermal annealing.

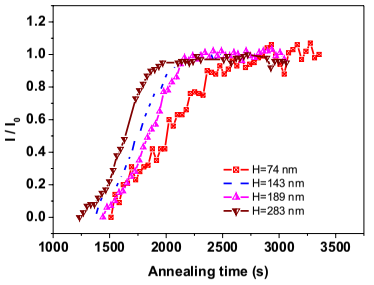


**Fig. 3:** Evolution of the normalized ITO XRD peak integral intensity at different film thicknesses during annealing by electric current.

| ROBL-CRG | **Experiment title:**<br>XRD test studies of implanted single crystals, magnetic MLs and sputter-deposited NiTi shape memory alloys<br>**Part II : Magnetic nanocrystals in a single crystalline matrix (preliminary studies)** | **Experiment number:**<br>**20_02_IH-MI387** |
|---|---|---|
| **Beamline:**<br>BM 20 | **Date of experiment:**<br>from: 23.08.2005 to: 27.08.2002 | **Date of report:**<br>05.10.2005 |
| **Shifts:**<br>12 | **Local contact(s):**<br>Dr. Norbert Schell | *Received at ROBL:*<br>*12.10.05* |

**Names and affiliations of applicants** (* indicates experimentalists):

F. Eichhorn*, N. Schell*, K. Potzger, Shengqiang Zhou

Forschungszentrum Rossendorf, Institute of Ion Beam Physics and Materials Research, P.O.B. 510119, 01314 Dresden, Germany

## Report:

Granular materials consisting of an insulating host material and embedded ferromagnetic nanoparticles are currently investigated due to their possible applications in ultra high density data storage [1], magneto-optics [2] and magneto-transport [3] as well as in basic research as model systems for fast magnetization switching [4] or electron holography [5]. Especially in the field of spintronics, diluted magnetic semiconductors (DMS) are worldwide under intense investigation. They are "conventional" semiconductors doped with transition metal (TM) ions which are diluted within the host matrix and ferromagnetically aligned *via* an indirect magnetic coupling [5]. Especially for ZnO doped with Fe, RT ferromagnetism has been confirmed experimentally [6, 7] and Bolduc *et al.* have achieved RT ferromagnetism of Si by Mn-ion implantation with Mn fluences of $1\times10^{15}$/cm$^2$ and $1\times10^{16}$/cm$^2$ [8]. However, the origin of the observed ferromagnetism is still controversial, i.e. DMS or secondary precipitates. In order to understand the origin of this ferromagnetism, it is necessary to correlate the measured magnetic properties with the material´s structure. Here, we would like to present first results characterizing epitaxially oriented Fe nanoparticles in ZnO(001) and Mn or $Mn_xSi_y$ in Si(001), respectively (both by the method of high temperature ion implantation).

### Results

Fig. 1 shows the diffractograms for Si(001) implanted with $5\times10^{16}$ cm$^{-2}$ Mn ions (300 keV) at 620 K. The measurement with symmetric beam path shows only the Si(004) diffraction line and a low intensity part of Si(002). Grazing incidence measurement results in a more complex diagram (black curve). The diffraction line positions of Si, $Mn_{27}Si_{47}$ and Mn are indicated.

From the experiment it may be concluded that

- the implantation process forms a *thin layer of polycrystalline Si* (maybe *via* amorphization and subsequent recrystallization);
- furthermore, the *surface layer contains one or two new crystalline phases*: $Mn_{27}Si_{47}$ and Mn;
- using the Scherrer formula, the crystal diameter of the new phases may be estimated. Unfortunately, the lines are strongly superimposed. Assigning the intensity at $2\theta = 79.0°$ to Mn a *diameter of 10 nm* is calculated. Asuming $Mn_{27}Si_{47}$ lines at $2\theta = 42.2°$ and 74.61° a *diameter of minimum 6 nm* may be calculated.

Fig. 2 shows the diffractograms for Zn(001) implanted with $4\times10^{16}$ cm$^{-2}$ Fe ions (180 keV) at 250 K. The diagrams measured with symmetric beam path show only the diffraction lines ZnO(002) and ZnO(004) at $2\theta = 34.4°$ and $2\theta = 72.6°$, respectively. Grazing incidence show the line ZnO(103) at $2\theta = 63°$. *No indication of any crystalline phase beyond ZnO is found.* However, the (002) and (004) lines have shoulders at the high angle slope suggesting a strained layer of ZnO: implanted Fe is distributed in a surface layer of ZnO like an alloying element. The assumed existence of a diluted magnetic semiconductor will be studied in the future.

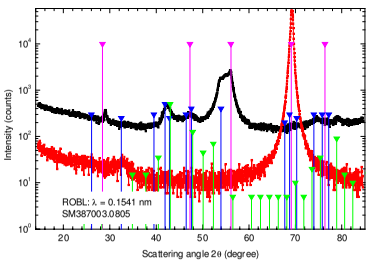


**Fig. 1**: Si(001) implanted with $5\times10^{16}$ cm$^{-2}$ Mn ions (300 keV) at 620 K :
red curve – symmetric beam path,
black curve – incidence angle 0.4°.
Diffraction lines are indicated in the colours
magenta – Si (PDF 27-1402)
green – Mn (PDF 32-0637)
blue – $Mn_{27}Si_{47}$ (PDF 26-1251).

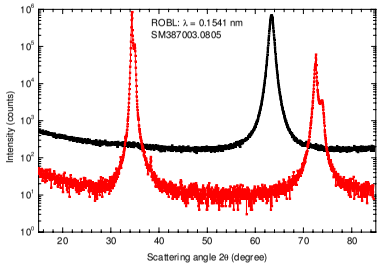


**Fig. 2**: Zn(001) implanted with $4\times10^{16}$ cm$^{-2}$ Fe ions (180 keV) at 250 K :
red curve – symmetric beam path,
black curve – incidence angle 0.4°.

### References

[1] C.W. White *et al.*, J. Appl. Phys. **93**, 5656 (2002).
[2] S. Honda *et al.*, Appl. Phys. Lett. **77**, 711 (2000).
[3] N. Hayashi *et al.*, Surf. Coat. Tech. **169-170**, 540 (2003).
[4] K.S. Buchanan *et al.*, Phys. Rev. B **70**, 174436 (2004).
[5] J. Biskupek *et al.*, J. Magn. Magn. Mater. **293**, 924 (2005).
[6] T. Dietl *et al.*, Science **287**, 1019 (2000).
[7] M. Venkatesan *et al.*, Phys. Rev. Lett. **93**, 177206 (2004).
[8] J.H. Shim *et al.*, Appl. Phys. Lett. **86**, 082503 (2005).
[9] M. Bolduc *et al.*, Phys. Rev. B **71**, 033302 (2005).

| ROBL-CRG | **Experiment title:** **Real-time studies of the ITO film structure and resistivity behavior during annealing** | **Experiment number:** **IH-SI-206** |
|---|---|---|
| **Beamline:** BM 20 | **Date of experiment:** from: 15.05.2005 to: 17.05.2005 | **Date of report:** 12.12.2005 |
| **Shifts:** 6 | **Local contact(s):** Mrs. Valentina Cantelli | *Received at ROBL:* *14.12.05* |

**Names and affiliations of applicants** (* indicates experimentalists):

V. Cantelli*, FZ Rossendorf, IIM, Dresden, Germany

A. Rogozin*, FZ Rossendorf, IIM, Dresden, Germany

N. Shevchenko*, FZ Rossendorf, IIM, Dresden, Germany

M. Vinnichenko, FZ Rossendorf, IIM, Dresden, Germany

**Report:**

Usually only thermal heating is used for annealing of the transparent conductive oxides (TCO). Treatment by electric current is a relatively well studied process for amorphous metallic alloys, however, it has never been experimentally exploited for TCO thin films. This method provides additional advantage because the Joule heat is released directly in the film and no external heater is required. Therefore, the aim of our work was to study the process of the ITO thin film annealing by electric current in vacuum, in particular a real-time *in-situ* investigation of the structure and resistivity.

The films were deposited by reactive middle frequency pulsed magnetron sputtering at the base pressure of $8.6 \cdot 10^{-4}$ Pa. Plates of Si(100) ($24 \times 12.5 \times 0.3$ mm$^3$) covered with 1 µm insulating $SiO_2$ layers were used as the substrates. Two aluminum stripes ($12 \times 2$ mm$^2$ and 1 µm thick) were predeposited at the ends of the plates atop of the $SiO_2$ layer. During ITO growth, a $12 \times 1.5$ mm$^2$ area of each stripe was screened from the deposition flow so that their open parts provided electrical contact to the film. The thickness of the amorphous ITO films is within the range of 170-180 nm.

Using two elastic cylindrical electrodes, direct electric current was put into the film. A special power supply providing a constant electric power under the variable resistance of the film was designed for the annealing experiment. The annealing parameters, electric power and potential drop on the sample are used to determine the real-time behavior of resistivity of the film with known geometric dimensions. Simultaneously the samples were characterized by *in-situ* synchrotron XRD analysis in Bragg-Brentano geometry using a multi-channel position sensitive detector.

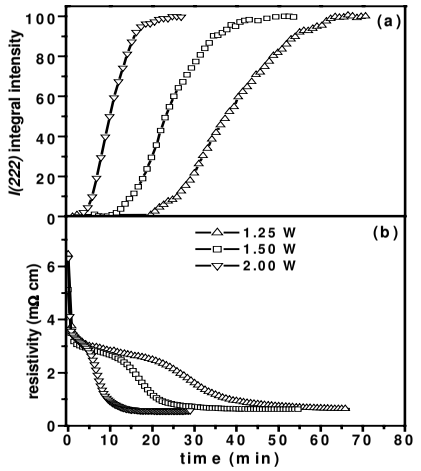


**Fig. 1:** **(a)** Evolution of the ITO film normalized XRD peak integral intensity and **(b)** evolution of the film resistivity during annealing by direct electric current.

The time dependences of the film resistivity and normalized integral intensity for different annealing powers are shown in Fig. 1. The resistivity decreases in two stages. During the first stage the sample remains amorphous. The commencement of the second stage coincides with the onset of the film crystallization for different electric powers. Independent of the power, the factor of the resistivity decrease remains approximately the same. Power enhancement (from 1.25 to 2.0 W) leads to an increase in the sample temperature (from 198 to 225°C), hastens the onset of the film crystallization and reduces the total time of the amorphous-to-crystalline transformation. The time dependence of the normalized integral intensity has s-like shape, which is typical for the crystallization process.

Compared to the isothermal annealing process, during annealing by electric current at equivalent temperatures the crystallization begins earlier and progresses faster. In this case the crystallization activation energy is lower (0.81±0.09 eV) than for isothermal treatment (1.44±0.18 eV).

The XRD data were analyzed to determine the kinetic parameters of crystallisation using the Kolmogorov–Johnson–Mehl-Avrami equation [$f \sim 1\text{-}exp(-kt^n)$]. Probably, n~2 reveals a two-dimensional crystallisation process with constant growth rate assuming site saturation mode.

| ESRF | **Experiment title:**<br>***In-situ* study during co-sputtering of TiNi-TiN nanocomposite thin films (cont.)** | **Experiment number:**<br>**MA-105** |
|---|---|---|
| **Beamline:**<br>BM 20 | **Date of experiment:**<br>from: 05.07.2006 to: 11.07.2006 | **Date of report:**<br>02.02.2007 |
| **Shifts:**<br>18 | **Local contact(s):**<br>Dr. Norbert Schell | *Received at ESRF:*<br>*06.02.07* |

**Names and affiliations of applicants** (* indicates experimentalists):

**F.M. Braz Fernandes*, Rui J. C. Silva*, Mahesh K. Koosappa***
CENIMAT-Centro de Investigação de Materiais, Campus da FCT/UNL, 2829-516 Monte de Caparica, PORTUGAL

**Rui M.S. Martins*, N. Schell***
Forschungszentrum Dresden-Rossendorf, Institute of Ion Beam Physics and Materials Research, D-01314 Dresden, GERMANY and ROBL-CRG at ESRF, F-38043, Grenoble, FRANCE

## REPORT

The effect of a TiN layer deposited on top of the $SiO_2$/Si(100) substrate prior to the deposition of the Ni-Ti films has been analysed in previous experiments [reports ME-1087 and 20_02_637]. Due to the promising results obtained concerning the manipulation of the preferential orientation of the Ni-Ti thin films through the deposition of a TiN buffer layer [1], complementary tests have been performed on this subject. During this beamtime there was also the opportunity to complete a series of methodical investigations on Si(100) substrates.

### EXPERIMENTAL

| *Sample #* | *Substrate* | *Buffer layer* | *Substrate bias (V)* | | *Deposition (min.)* | | *Annealing (min.)* | |
|---|---|---|---|---|---|---|---|---|
| | | | *TiN deposition* | *Ni-Ti deposition* | *TiN* | *Ni-Ti* | *TiN* | *Ni-Ti* |
| *S50* | $SiO_2$*/ Si(100) | TiN | -30 | 0 | 32 [1)] | 123 | 105 [1)] | 52 |
| *S51* | $SiO_2$*/ Si(100) | TiN | -30 | 0 | 3 | 118 | 120 | 58 |
| *S53* | MgO(100) | TiN | -30 | 0 | 3 | 120 | 80 | 54 |
| *S52* | $SiO_2$*/ Si(100) | – | – | 0 | – | 134 | – | 62 |
| *S54* | Si(100) | – | – | -45 | – | 122 | – | 60 |
| *S55* | Si(100) | – | – | 0 | – | 118 | – | 54 |

** 1400 Å amorphous $SiO_2$ capping layer* *[1)] at 600°C*

**Tab. 1:** Deposition parameters for the various samples investigated.

The Ni-Ti films and the TiN buffer layers were deposited by D.C. magnetron sputtering in a chamber especially designed for *in-situ* x-ray measurements [2]. Two unbalanced magnetrons, equipped with a 25.4 mm Ni-Ti target (51 at% Ni – 49 at% Ti) and a 25.4 mm Ti target (purity 99.99%), respectively, were positioned at a distance of 100 mm from the substrate. The base pressure at the deposition temperature of ≈ 470°C was $2\times10^{-5}$ Pa and the working pressure during deposition was 0.42 Pa. For the deposition of the TiN buffer layers, the Ti target was run at a constant power of 80 W with an $Ar/N_2$ gas flow of 2/0.5 sccm and for the Ni-Ti films the Ni-Ti and Ti magnetrons were driven at a power of 40 and 24 W, respectively.

The processing conditions of the samples studied are presented in Tab. 1. Scans were run in Bragg-Brentano geometry, using 0.675 Å (E = 18.37 keV) radiation, to reveal the type of preferential orientation during the deposition and annealing processes and to determine off-plane lattice parameters.

### RESULTS AND DISCUSSION

The TiN buffer layer of *sample S50* lead to a preferential growth of {110} Ni-Ti B2 planes parallel to the substrate from the beginning of the deposition with a constant growth rate during the whole deposition (Fig. 1). The diffraction peak B2(211) also appears and grows but with a much lesser intensity. In the case of the B2(200) peak, it was detected later (with low intensity) in contrast to what is observed when the Ni-Ti films are deposited directly on $SiO_2$/Si(100) substrates [3, 4].

Specular reflectivity (XRR) has been employed to characterize the TiN buffer layer of *#S51* (Fig. 2). The results did not show evidence of a structural change due to the annealing step. The XRR curves immediately after deposition and 90 min later are superposed.

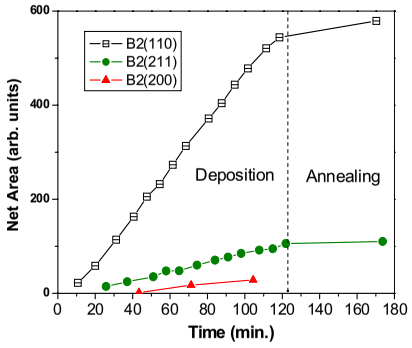


**Fig. 1:** *#S50:* the integrated intensities of the Bragg-Brentano B2(110), B2(211) and B2(200) diffraction peaks as obtained from the positions of the respective peaks, recorded as a function of time after start of film growth.

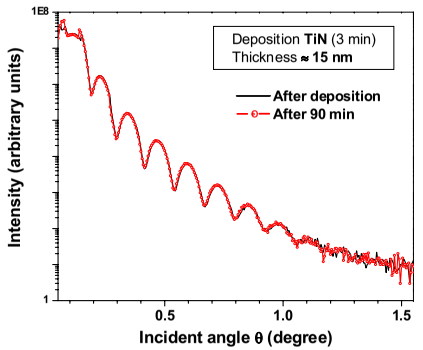


**Fig. 2:** XRR spectra obtained immediately after deposition and XRR spectra obtained 90 min after deposition of TiN (buffer layer of *#S51*).

Low angle specular reflectivity time resolved at a fixed incidence angle was as well very useful to determine the growth mode of the TiN buffer layer and the Ni-Ti film (first 9 min 30s) for the deposition on MgO(100) substrate (*#S53*, Fig. 3), revealing a layer-by-layer growth mode (with the decrease in oscillation amplitude, indicating that the surface becomes rougher during sputtering). A single orientation of Ni-Ti is grown during the 120 min of deposition, with (100) stacking parallel to the substrate. The first layers deposited on the TiN (100) are constrained (compressive planar stress state) and this deformation remains until the end of the deposition; later layers are having a gradually relaxed interplanar distance (smaller $d_{(200)}$ in the direction of the surface normal), indicating a gradual relaxation of the compressive stress constraint imposed at the interface Ni-Ti/TiN (Fig. 4).

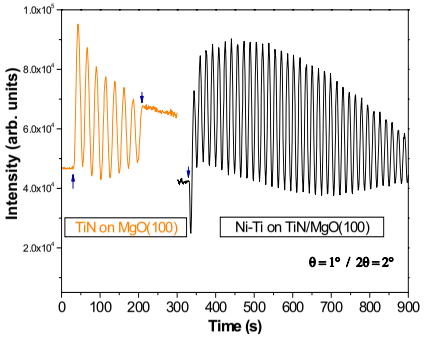


**Fig. 3:** Time-dependent *in situ* XRR for the TiN buffer layer and the first minutes of deposition of the Ni-Ti film on MgO(100) substrate (*#S53*).

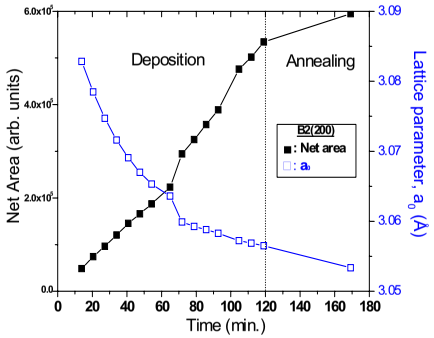


**Fig. 4:** The integrated intensities of the Bragg-Brentano B2(200) diffraction peak and the lattice parameter $a_0$ as obtained from the position of the peak, recorded as a function of time after start of Ni-Ti film growth (*#S53*).

The complementary tests on Si(100) substrates have shown that the use of a substrate bias voltage (-45 V) on naturally oxidized Si(100) (*#S54*) leads to a film growth where, at the beginning, the {200} planes are stacking parallel to the substrate like for depositions without bias voltage (*#S55)* [5-8]. However, after the stabilization of the B2(200) intensity there is the development of grains with the {310} planes parallel to the substrate in contrast to the B2(110) preferred orientation observed for depositions without bias. This result confirms the information obtained in a previous experiment using a substrate bias voltage of -25 V [*#S39*, report 20_02_637].

## CONCLUSIONS

- A preferential growth of {110} Ni-Ti B2 planes parallel to the substrate from the beginning of the deposition can be obtained using a TiN buffer layer. In this case the <100> orientation is greatly reduced with the appearance of the B2(200) peak only at a later stage of the Ni-Ti deposition.
- A single orientation of Ni-Ti (≈900 nm) with (100) stacking parallel to the substrate can be produced using a TiN(100) buffer layer. The experiments also show that the TiN layer acts as a diffusion barrier. In contrast to the Ni-Ti film deposited directly on MgO(100) (*sample S24*, [report ME-936]), here no peaks from interfacial reaction products were detected.
- The use of a bias voltage on naturally oxidized Si(100) substrates leads to a dominance of grains of the Ni-Ti B2 phase with the (310) orientation parallel to the substrate after an initial stacking of the B2 phase onto (h00) planes.

## REFERENCES

[1] R.M.S. Martins, N. Schell, R.J.C. Silva, L. Pereira, K.K. Mahesh, F.M. Braz Fernandes, *Sens. Actuators B (accept.)*
[2] W. Matz, N. Schell, W. Neumann, J. Bøttiger, J. Chevallier, *Rev. of Sci. Instrum.* **72** (2001) 3344.
[3] R.M.S. Martins, N. Schell, M. Beckers, K.K. Mahesh, R.J.C. Silva, F.M. Braz Fernandes, *Appl. Phys. A* **84** (2006) 285.
[4] R.M.S. Martins, N. Schell, M. Beckers, A. Mücklich, H. Reuther, R.J.C. Silva, K.K. Mahesh, F.M.B. Fernandes, *Proceedings of SMST 2006* (*accepted*).
[5] R.M.S. Martins, N. Schell, R.J.C. Silva, F.M. Braz Fernandes, *Nucl. Instr. & Methods Phys. Res. B* ***238*** (2005) 319.
[6] R.M.S. Martins, F.M. Braz Fernandes, R.J.C. Silva, M. Beckers, N. Schell, *Mater. Sci. Forum* ***514-516*** (2006) 1588.
[7] R.M.S. Martins, F.M. Braz Fernandes, R.J.C. Silva, M. Beckers, N. Schell, *Proceedings of SMST 2004* (2006) 421.
[8] R.M.S. Martins, N. Schell, M. Beckers, R.J.C. Silva, K.K. Mahesh, F.M. Braz Fernandes, *Mater. Sci. Eng. A* (*accepted*).

| ESRF | Experiment title: Effect of surface condition on the internal stresses in oxide layers on iron substrates | Experiment number: MA-106 |
|---|---|---|
| Beamline: BM 20 | Date of experiment: from: 21.06.2006 to: 27.06.2006 | Date of report: 29.01.2007 |
| Shifts: 18 | Local contact(s): Norbert Schell | *Received at ESRF: 29.01.2007* |

**Names and affiliations of applicants** (* indicates experimentalists):

**Haroldo Pinto, Pedro Augusto S. Silva, Federico Sket**

Max Planck Institut für Eisenforschung GmbH, Max-Planck-Straße 1,
40237 Düsseldorf, Germany

## Report:

### *Introduction*

Dense and adherent oxide layers protect metallic substrates by barring the diffusion between the corrosive environment and the reactant and, thus, by decreasing the corrosion rate [1, 2]. The integrity of protective oxide films is, however, strongly influenced by strain/stress generation in the oxides at high temperatures as well as at room temperature after cooling.

The Pilling-Bedworth-Ratio (PBR), which is the ratio between the volume of the oxide and of the metal necessary for the oxide formation, has been often used to estimate strains in oxide layers. However, not even a qualitative connection exists between the PBR and the internal stresses in oxide layers. This is due to other factors affecting the strain state, such as cation diffusion mechanisms, lattice misfit between substrate and oxide in epitaxial layers, the formation of new oxides and gradients in the oxide composition of the layer. After oxidation and cooling the strain/stress state is also modified by additional stresses formed as a result of differences in the thermal properties of the oxide layer and metallic substrate. These cooling stresses are usually related to oxide spalling. Since the influence of surface roughness on the structure and residual stresses in oxide layers are not clear, experimental investigations of mass gain, layer morphology, texture and residual stress state of oxide layers on polycrystalline iron are performed using thermogravimetry, microscopy and synchrotron X-ray diffraction.

### *Experimental Details*

Armco iron samples provided by REMAG, Mannheim were cut into disks of 8mm diameter and 1mm thickness. These samples were ground, some of them also polished and etched in order to produce surface with different roughness (Tab.1). The roughness of the samples was determined as average surface roughness $R_a$ using a surface roughness tester. All samples were oxidized for 10h in a thermo-gravimetric analyses instrument (TGA) at ambient pressure in laboratory air. The heating rate up to the oxidation temperature of 450°C was 1.88 K/s.

Diffraction experiments were performed on the oxidized samples using an X-ray energy of 6.9 keV. Average internal stresses within the oxide layers were determined using the $\sin^2\psi$ technique. Internal stress depth profiles were assessed in the oxide layer using the LIBAD method [3] with incidence angles of $\alpha$=5° and $\alpha$=10°.

### *Results*

Due to the weak intensity of the hematite reflections using the $\sin^2\psi$ -method residual stresses could only be analyzed in the magnetite. The magnetite in all of the 5 investigated samples contains compressive in-plane residual stresses (Tab.2). The magnitude of the average residual stresses in the magnetite of the oxide layers, regarding the experimental error margin, is almost the same and agrees well with earlier measurements. A relation between substrate roughness and compressive residual stress in the magnetite could not be found.

***Table 1:*** *Samples investigated*

| Samples | Surface Preparation | Roughness $R_a$ [µm] | Oxidation Temp. [°C] | Oxidation Time [h] |
|---|---|---|---|---|
| 142 | Ground, SiC180 | 0.31 ± 0.005 | 450 | 10 |
| 242 | Ground SiC2400 | 0.03 ± 0.005 | 450 | 10 |
| 342 | Polished, MgO | 0.02 ± 0.011 | 450 | 10 |
| 442 | Ground SiC2400, electrolyt. polished (Struers AC2) | 0.09 ± 0.025 | 450 | 10 |
| 542 | Polished MgO, etched (Nital) | 0.27 ± 0.020 | 450 | 10 |

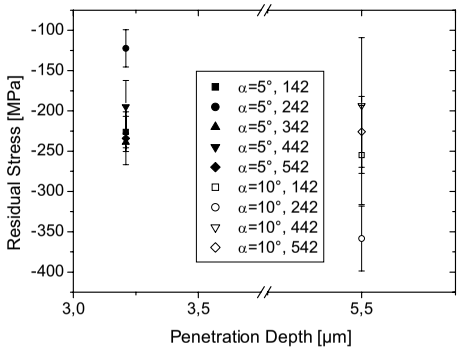


***Fig. 1:*** *Residual stress values obtained in different depths of the magnetite layer*

The LIBAD method allowed measurements of the residual stress values in different depths of the magnetite layer (Fig.1). These measurements also revealed compressive residual stresses within the magnetite. The magnitude of these compressive residual stresses shows a tendency to increase from the surface of the oxide layer towards the interface to the substrate. The residual stress gradient in the magnetite is presumably due to the growth defects at the interface between the oxide layer and the substrate as well as due to the strain misfit introduced by the differences in the thermal expansion of the oxide layer and the substrate during cooling. Similar to the average residual stress values obtained in the magnetite also the residual stress profiles determined in the layer do not show a correlation to substrate roughness.

***Table 2:*** *Residual stress in magnetite (731), penetration depth = 14.4 µm (at $\sin^2\psi$ = 0.3)*

| Sample | 142 | 242 | 342 | 442 | 542 |
|---|---|---|---|---|---|
| Residual Stress [MPa] | -206 +/- 19 | -184 +/- 12 | -212 +/- 19 | -255 +/- 18 | -215 +/- 14 |

Average microstrain values determined on several reflections of the magnetite using the Rietveld software MAUD [4] and Popa's model [5] show a tendency of increasing microstrains with increasing roughness of the ground respectively mechanically polished oxide layer. The increase of layer microstrains with increasing surface roughness presumably is due to the higher defect density near the mechanically coarse ground surface compared to the polished surface.

### *References*

[1] M. Schütze: Stresses and Decohesion of Oxide Scales, Mater. Sci. Technol. **4** (1988) 407 – 414

[2] S. Corkovic, A. Pyzalla: In-situ Stress Analyses during High Temperature Oxidation of Mild Steel and Grey Cast Iron, Materials and Corrosion, (2007, in print)

[3] K. van Acker: Internal Stress States in Cold Worked Metals and in Metal Matrix Composites, Dissertation, Katholieke Universiteit Leuven, Belgien (1996)

[4] L. Lutterotti, S. Matthies, D. Chateigner, S. Ferrari, J. Ricote : Mat. Sci. Forum, **408-412** II (2002), p. 1603.

[5] N.C. Popa: J. Appl. Cryst. **31** (1998) 176

| ESRF | **Experiment title:** ***In-situ* study during co-sputtering of NiTi-TiN nanocomposite thin films** | **Experiment number:** **ME-1087** |
|---|---|---|
| **Beamline:** BM 20 | **Date of experiment:** from: 12.04.2005 to: 19.04.2005 | **Date of report:** 24.08.2005 |
| **Shifts:** 21 | **Local contact(s):** **Rui M.S. Martins** | *Received at ESRF:* *24.08.05* |

**Names and affiliations of applicants** (* indicates experimentalists):

**F.M. Braz Fernandes***, **Rui J.C. Silva***, **Mahesh K. Koosappa***: CENIMAT – Centro de Investigação de Materiais, Campus da FCT/UNL, 2829-516 Monte de Caparica, PORTUGAL

**Rui M.S. Martins***, **N. Schell***, FZR, ROBL-CRG at ESRF, B.P. 220, F – 38043, Grenoble, FRANCE

**Report:**

The growth of near-equiatomic NiTi thin films on oxidized silicon wafers, deposited by magnetron co-sputtering from NiTi and Ti targets, has been studied *in situ*. Widening the scope of the previous experiments concerning the influence of the deposition parameters on the film structure [1-4], here the incorporation of TiN at different steps of the NiTi depositions was tested. TiN films grown by vapor phase deposition techniques usually have a preferred growth orientation that varies according to the growth conditions. Previous measurements performed by the ROBL staff were fundamental in choosing the deposition conditions for TiN [5].

**EXPERIMENTAL**

The samples were deposited in the sputter chamber installed on the 6-circle-goniometer of ROBL [6]. Pieces of size 15×15 $mm^2$, cut from Si(100) wafers with a 1400 Å amorphous $SiO_2$ capping layer, have been used as substrates. The magnetron with the NiTi alloy target (49 at% Ni – 51 at% Ti) was run at a dc power of 40 W. The magnetron with the pure Ti target (99.99 %) was run at 20 W for the NiTi depositions and at 80 W for the TiN (deposition pressure = $3.5\times10^{-3}$ mbar). The substrate temperature was kept at ≈ 470°C. The scans were run in Bragg-Brentano geometry, using 0.675 Å radiation.

| *Sample* | *TiN deposition: ratio Ar/$N_2$* | *Substrate bias (V)* | | *Deposition (min.)* | | | | | | *Annealing (min.)* | |
|---|---|---|---|---|---|---|---|---|---|---|---|
| | | *TiN deposition* | Ni-Ti *deposition* | *TiN (on top of Si wafer)* | *NiTi 1st layer* | *TiN 1st intermediate* | *NiTi 2nd layer* | *TiN 2nd intermediate* | *NiTi 3rd layer* | *TiN (on top of Si wafer)* | *After last deposition of NiTi* |
| S29 | - | - | -45 | - | 128 | - | - | - | - | - | 83 |
| S30 | 9.4/4.7 | -30 | 0 | 50 | 120 | - | - | - | - | 131 | 113 |
| S31 | 10/2.5 | -30 | 0 | 40 | 122 | - | - | - | - | 27 | 57 |
| S32 | 10/2.5 | -30 | 0 | 15 | 120 | - | - | - | - | 28 | 60 |
| S33 | 10/2.5 | -30 | 0 | 3 | 60 | 0.5 | 60 | - | - | 87 | 77 |
| S34 | 10/2.5 | -30 | 0 | 3 | 122 | - | - | - | - | 27 | 60 |
| S35 | 10/2.5 | -30 | 0 | 3 | 40 | 1 | 40 | 3 | 40 | 105 | 62 |

Deposition parameters for the various samples investigated.

**RESULTS**

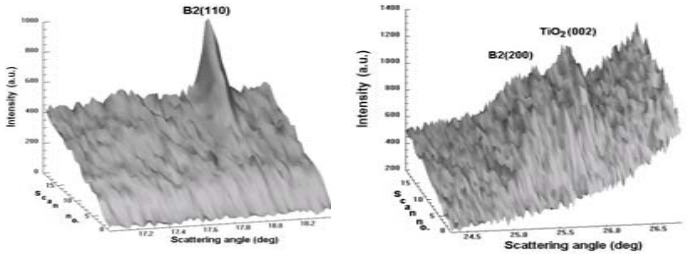


**Fig. 1:** XRD spectra with peak evolution during the deposition of sample S29.

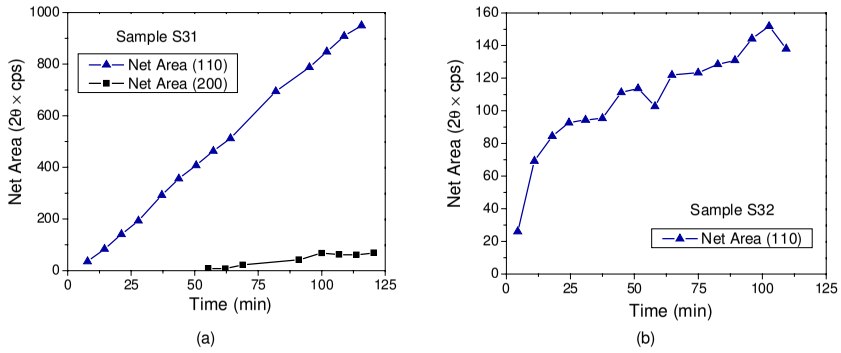


**Fig. 2:** Evolution of the net area of the diffraction peaks B2(110) and B2(200) for sample S31 (a), and for the diffraction peak B2(110) for sample S32 (b) during deposition.

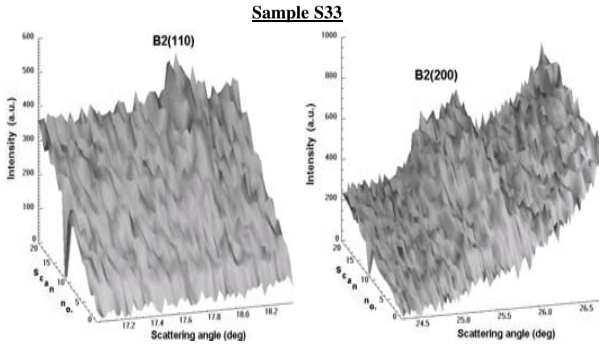


**Fig. 3:** 3D plots of the peak intensity of B2 phase [left: B2(110), right: B2(200)] of samples S33 (top part) and S34 (bottom part).

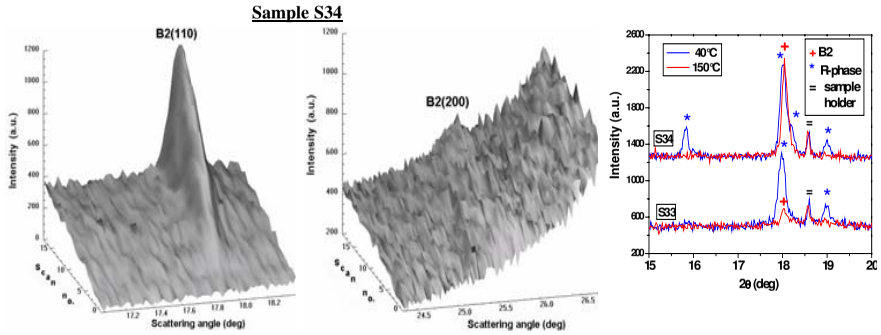


**Fig. 4:** Crystalline structure changes of NiTi films S33 (bottom) and S34 (top) at different temperatures. ∇

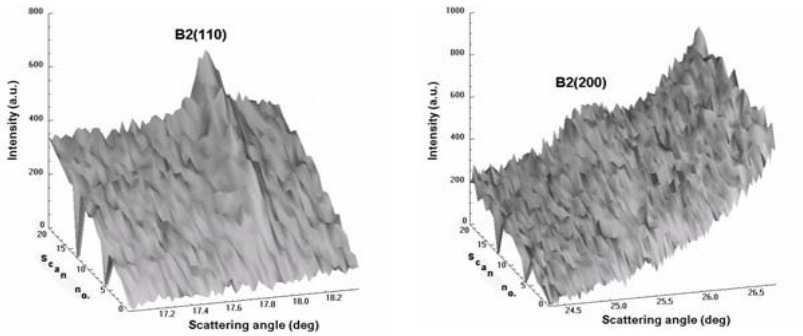


**Fig. 5:** 3D sequence of XRD patterns of sample S35 during deposition.

*Note:* The zero intensities are manually inserted into the graphs to mark the last scan during the deposition of NiTi before a deposition of an intermediate layer of TiN (scans during the deposition of TiN are not represented).

The type of substrate plays an important role for the preferential stacking of sputtered NiTi films. Previous experiments with deposition on Si(100) have put in evidence that B2 phase starts by stacking onto (100) planes and, as the thickness increases, the preferred orientation changes to (110) fiber texture. However, for NiTi films deposited on Si substrates at high temperatures, there exist interfacial diffusion and chemical interactions at the interface resulting in silicide formation. During experiment ME-936 a $SiO_2$ layer was used as an effective barrier. There, a preferential stacking of B2(100) was observed when using a Si oxidized substrate (*no* bias). We suggest that a stronger interfacial adsorption on the heated substrate promotes the preferential coverage by a first layer of Ti on top of the $SiO_2$/Si substrate. This leads to the preferential formation of the (h00)-oriented NiTi film since, in the B2 cubic austenite phase, the (h00) planes are alternately occupied by Ni and Ti atoms.

In the present experiments, the bias effect was studied (sample S29). During the deposition, the first deposited layers had a (100) orientation, later changing into (110) (Fig. 1). We consider that the more energetic ion bombardment of the growing film enhances the surface mobility of Ni and Ti adatoms, inducing the fiber texture (110), which is the more densely packed crystallographic plane. Apparently, due to the existence of a large amount of oxygen on the $SiO_2$ layer, Ti atoms arriving on the $SiO_2$ surface get oxidized, forming a thin interfacial layer of $TiO_2$. The deposition of TiN was then tested as a possible future tool to control the properties of this type of films to be used for the functional devices.

The results have shown that TiN acts not only as a diffusion barrier, but also induces different crystallographic orientations depending on the process conditions like deposition parameters or annealing time:

- in sample S31 (Fig. 2-a), the TiN layer induces the preferential growth of (110) plane parallel to the substrate from the beginning of the deposition, with a constant rate up to the end of the deposition; the diffraction peak (200) appears only at a later stage, always remaining very weak;
- for the sample S32, the diffraction peak (110) also appears since the beginning of the deposition (though much less intense); at the end of the deposition, still there is no evidence of the (200) diffraction peak (Fig. 2-b);
- samples S33-S35 (Figs 3-5) are characterized by different preferential orientations; Fig. 4 shows that, in the case of samples deposited on the top of an intermediate TiN layer, the R-phase transformation is detected while cooling.

## CONCLUSIONS

These experiments have proved the usefulness of the TiN layer as (i) an efficient diffusion barrier and (ii) to induce different preferential orientations of the growing film. Further studies are required to clarify the role of TiN deposited as an intermediate layer on top of a Si substrate or during the NiTi deposition. This will help to define the parameters in order to use TiN to manipulate the texture of NiTi films. This is very important because the recoverable strain depends on the texture and strong textures may lead to anisotropic shape memory behavior.

## REFERENCES

[1] N. Schell, R.M.S. Martins, F.M. Braz Fernandes, *Applied Physics A: Materials Science & Processing* (in press).
[2] R.M.S. Martins, F.M. Braz Fernandes, R.J.C. Silva, N. Schell, *Nuclear Instruments & Methods in Physics Research* (in press).
[3] R.M.S. Martins, F.M. Braz Fernandes, R.J.C. Silva, M. Beckers, N. Schell, *Materials Science Forum* (in press).
[4] R.M.S. Martins, F.M. Braz Fernandes, R.J.C. Silva, M. Beckers, N. Schell, *Proceedings of SMST 2004* (in press).
[5] N. Schell, W. Matz, J. Bøttiger, J. Chevallier, P. Kringhoj, Journal of Applied Physics **91** (2002) 2037.
[6] W. Matz, N. Schell, W. Neumann, J. Bøttiger, J. Chevallier, Review of Scientific Instruments **72** (2001) 3344.

| ESRF | **Experiment title:** ***In situ*** **study of the co-sputtering of ternary (Ni-Ti-X, X=Cu, Hf) SMA thin films** | **Experiment number:** **ME-1255** |
|---|---|---|
| **Beamline:** BM 20 | **Date of experiment:** from: 15.02.2006 to: 21.02.2006 | **Date of report:** 25.04.2006 |
| **Shifts:** 18 | **Local contact(s):** **Norbert Schell** | *Received at ESRF:* *02.05.06* |

**Names and affiliations of applicants** (* indicates experimentalists):

**F.M. Braz Fernandes***, **Rui J. C. Sila***, **Mahesh K. Koosappa***
CENIMAT – Centro de Investigação de Materiais, Campus da FCT/UNL, 2829-516 Monte de Caparica, PORTUGAL
**N. Schell***, **Rui M.S. Martins***
FZR, ROBL-CRG at ESRF, B.P. 220, F – 38043, Grenoble, FRANCE

## 1. OBJECTIVE

Taking into account previous results obtained concerning the effect of a TiN interlayer on the subsequent growth of NiTi thin films, we decided to focus this experiment on the ternary system Ni-Ti-Hf and to complement its study with some more experiments with TiN.

## 2. EXPERIMENTAL

**Table 1:** Deposition parameters for the various samples investigated.

| Sample | Intermediate layer | | | | Deposition | | | Remarks |
|---|---|---|---|---|---|---|---|---|
| | Layer / Substrate | Target (Power) | Bias (V) | Gas flow ( Ar / $N_2$ ) | Targets (Power) | Bias (V) | Ar Gas flow | |
| **S-42** | TiN / Si(100) | Ti (80 W) | -30 | 10.0 / 2.5 (sccm) | NiTi (40W) / Ti (20 W) | -45 | 4.7 (sccm) | effect of **TiN(111)** on the deposition of TiNi ***with*** **bias**; to be compared with **S31** (NiTi deposition ***without*** **bias)** |
| **S-43** | | | | | NiTi (40W) / Ti (20 W) | -90 | | effect of **TiN(111)** on the deposition of TiNi ***with*** **bias (90 V)**; to be compared with **S31** (NiTi deposition ***without*** **bias)** and S42 (bias = -45 V). |
| **S-44** | | | | | NiTi (40W) / Ti (20 W) + NiTi (40W) / Ti (25 W) | -45 | | effect of **TiN(111)** on the deposition of TiNi **with variable power (Ti target)**: **1 h (Ti, 20 W)+ 1 h (Ti, 25 W)** |
| **S-45** | HfN / Si(100) | Hf (80 W) | -30 | 10.0 / 2.5 (sccm) | NiTi (60W) / Hf (18 W) | -45 | 4.7 (sccm) | effect of **HfN(111)** on the deposition of TiNiHf: **TiNi (60 W) / Hf (18 W)**. |
| **S-46** | | | | | NiTi (60W) / Hf (8 W) | | | effect of **HfN(111)** on the deposition of TiNiHf: **TiNi (60 W) / Hf (8 W)**. |
| **S-47** | | | | | NiTi (60W) / Hf (13 W) | | | effect of **HfN(111)** on the deposition of TiNiHf: **TiNi (60 W) / Hf (13 W)**. |

## 3. RESULTS AND DISCUSSION

### 3.1 NiTi / TiN

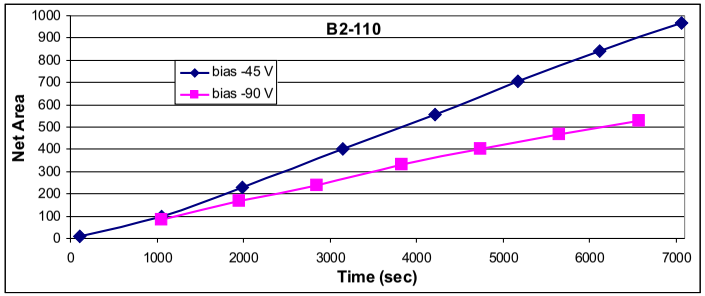


(a)

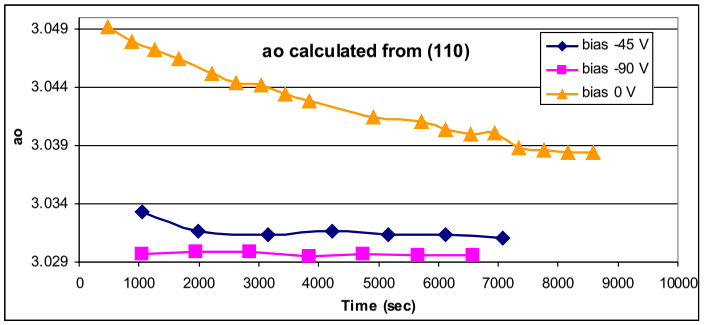


(b)

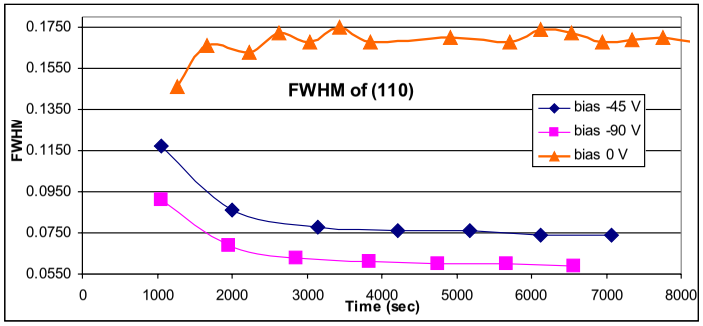


(c)

**Fig. 1:** Effect of the bias applied during NiTi deposition on (a) the B2(110) net area, (b) $a_0$ (calculated from 110) and (c) $FWHM_{(110)}$.

The NiTi / TiN experiments aimed to study the effect of the TiN intermediate layer on the growth of the NiTi film, for:

- 2 different bias voltage (-45 and -90 V) applied during NiTi deposition,
- 2 different power levels applied to the Ti target (20 W and 25 W).

***The bias increase from 45 to 90 V led to a significant decrease of the intensity of the B2(110) peak.***

This behavior is associated with the evolution noticed for a0, FWHM of B2(110), where:

- for the TiNi thin films, increasing the bias decreases the B2(110) intensity slightly,
- a0 is continuously decreasing during the deposition without bias (sample S31 from ME-1087, April 2005); the deposition with -45 V applied led to a slight decrease of a0 at the beginning, followed by a stabilisation; increasing the bias further to -90 V, leads to a practically constant value during all the deposition; it is clear that the a0 value is decreasing for increasing bias, approaching the equilibrium value of 3.03 Å for no bias applied; this trend may be interpreted as being associated with a relaxation of biaxial compressive stress states on the plane of the film;
- the decrease in the FWHM value as a funciton of the increase in the applied bias during deposition may be related to an overall trend of increasing coherence domain length with increasing bias applied during deposition,
- changing the Ti target power from 20 to 25 W made the TiNi thin film to be constituted by a lower half layer equiatomic and an upper half layer Ti-rich (presence of $Ti_2Ni$ precipitates).

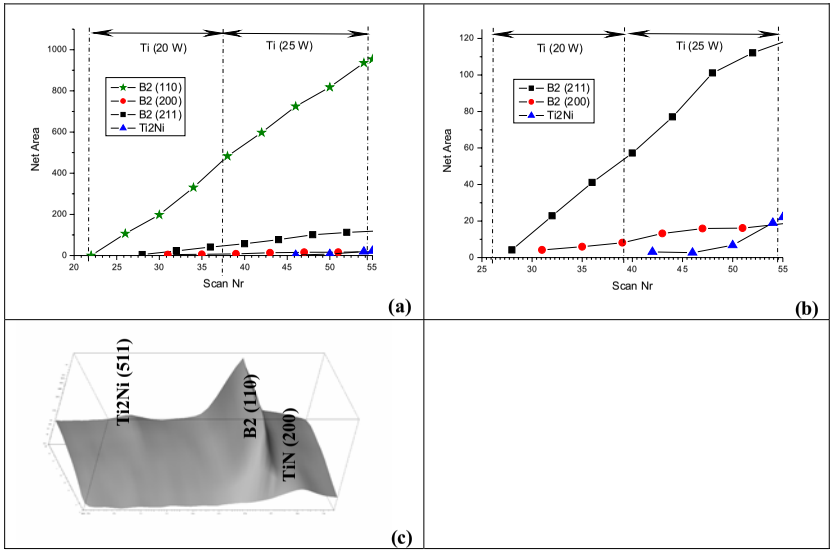


**Fig. 2:** XRD results from sample **S-44** (varying power of the Ti target).

(a) Variation of the net area of the diffraction peaks (110), (200) and (211) from B2 and (511) from $Ti_2Ni$.
(b) Zoom of the net area axis of (a).
(c) 3D representation of diffrcation peaks in the 2Θ scattering angle range from 16.9 to 19º.

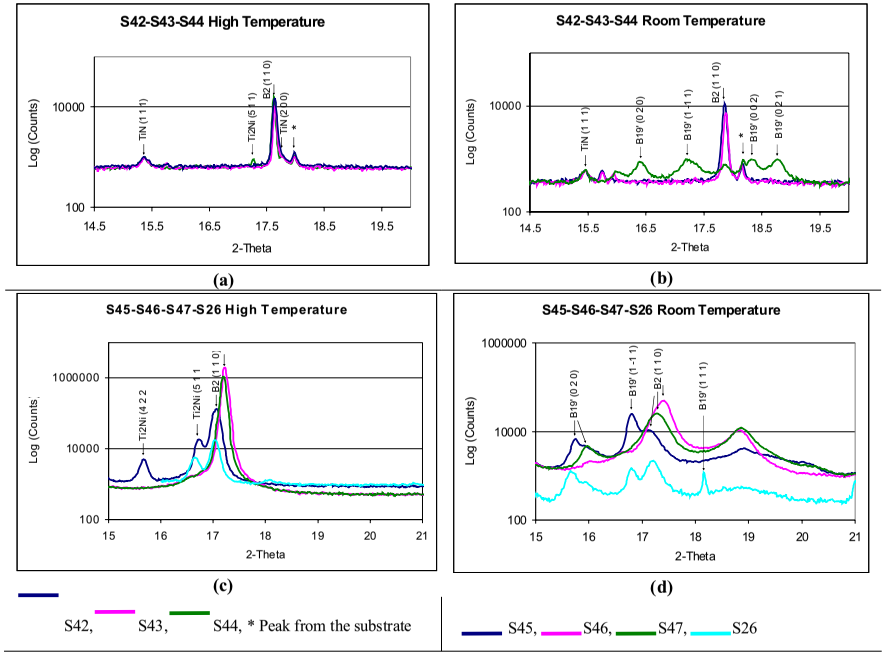


**Fig. 3:** XRD patterns of samples S-42–S-44 (a, b), and S-45–S-47 compared with S-26 (c, d).

(a) S-42, S-43 and S-44 at 470ºC (deposition temperature) with TiN as the intermediate layer.
(b) S-42, S-43 and S-44 at room temperature again with TiN as the intermediate layer.
(c) S-45, S-46, S-47, and S-26 at 470ºC (deposition temperature) with HfN as the intermediate layer.
(d) S-45, S-46, S-47, and S-26 at room temperature again with HfN as the intermediate layer.

### 3.2 NiTiHf / HfN

- the high-temperature transformation characteristics of the TiNiHf shape memory alloys give rise to a martensitic transformation during cooling close to 200ºC,
- the increasing amount of Hf incorporated in TiNiHf thin films shifts the B2(110) peak towards lower 2θ (higher d spacing) and decreases its intensity,
- the presence of $Ni_4(Ti,Hf)_3$ in the TiNiHf thin films was detected.

## 4. CONCLUSIONS

The results show that the *in-situ* study by XRD / XRR of the deposition of thin films, where important reactions (precipitation phenomena, phase transformations) take place, is a powerful tool for the development of these materials.

| ESRF | **Experiment title:** ***In-situ*** **XRD study of the co-sputtering of ternary (Ni-Ti-X, X = Cu, Hf) SMA thin films** | **Experiment number:** **ME-936** |
|---|---|---|
| **Beamline:** BM 20 | **Date of experiment:** from: 16.02.2005 to: 22.02.2005 | **Date of report:** 25.02.2005 |
| **Shifts:** 18 | **Local contact(s):** Dr. Norbert Schell | *Received at ESRF:* *25.02.05* |

**Names and affiliations of applicants** (* indicates experimentalists):

**F.M. Braz Fernandes***, **Rui J.C. Silva***, **Mahesh Karimbi Koosappa***: CENIMAT – Centro de Investigação de Materiais, Campus da FCT/UNL, 2829-516 Monte de Caparica, PORTUGAL

**N. Schell***, **Rui M.S. Martins***, FZR, ROBL-CRG at ESRF, B.P. 220, F – 38043, Grenoble, FRANCE

**Report:**

Previous experiments at ROBL were carried out using separate NiTi and Ti targets:
**- 20_02_608 and ME-584** where the power applied to each magnetron was kept constant
**- ME-814**., where the power was varied.
This new series of experiments was intended to make the *in-situ* study of the structural evolution during co-sputtering using NiTi and Ti/Hf/Cu targets, testing also the change of substrate: Si(100) oxidized, MgO(100) and MgO(111).

**EXPERIMENTAL**

The experimental conditions used are presented in the following table.

| *sample* | *Power applied to the 2nd magnetron (W)* | | | | *Substrate* | | | |
|---|---|---|---|---|---|---|---|---|
| | *NiTi* | *Ti* | *Hf* | *Cu* | Si oxydized | Si(100) | MgO(100) | MgO(111) |
| S23 | 40 | 20 | | | X | | | |
| S24 | 40 | 20 | | | | | X | |
| S25 | 40 | 20 | | | | | | X |
| S26 | 40 | | 15 | | | X | | |
| S27 | 40 | | 20 | | | X | | |
| S28 | 40 | | | 20 | | X | | |

**RESULTS**

The depositions performed using Ti as a second magnetron showed a strong influence of the substrate on the preferential stacking of NiTi sputtered. Previous experiments of the same type with deposition on Si(100) have put in evidence that the first layers were stacking preferentially on (100), changing later to (110) preferential orientation. Now, the experiments carried on using Ti as a 2nd substrate and using Si oxydized, MgO(100) and MgO(111) have shown:

- preferential stacking of (100) of B2, when using the substrates Si oxydized and MgO(100),
- preferential stacking of (110) of B2, when using the substrate MgO(111).

The preferential orientation of B2(100) // MgO(100) and B2(110) // MgO(111) were very strong and were kept as such until the end of the deposition, which lasted for 2 hours (circa 3500 Å thick film).

The experiments using the Hf and Cu targets allowed us to identify the 2θ ranges where the most relevant changes of the diffraction peaks shall appear along the deposition.

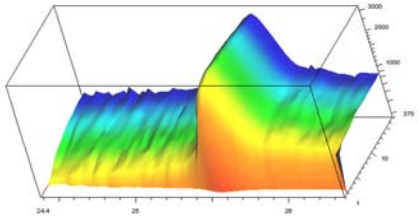

S23 during deposition

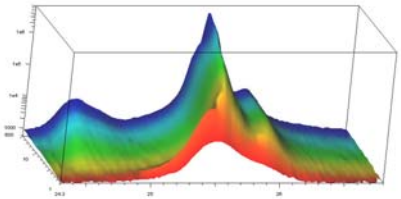

S24 during deposition

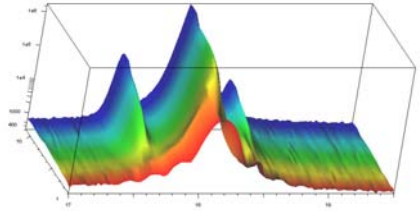

S25 during deposition

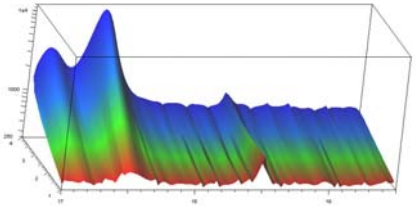

S26 during deposition

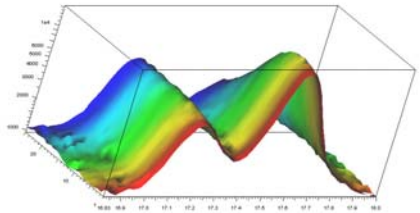

S26 during cooling

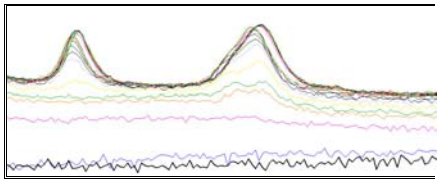

S27 (15.5 < 2θ < 18)

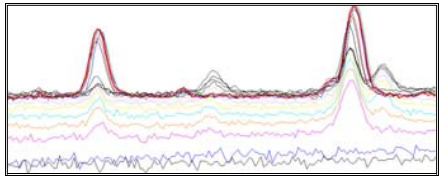

S28 (15.5 < 2θ < 18)

**CONCLUSIONS**

The additions of Cu and Hf can give deeper information concerning the stacking preference of NiTi-based thin films due to the different "preferences" of site occupations: while Cu tends to replace Ni, Hf tends to replace Ti positions. Further experiments are required to the effect of these site replacements on the type of preferential orientation of the sputtered films. These results should be coupled with the binary NiTi experiments on different substrates in order to give a better understanding of the structure of the sputtered thin films.

| ESRF | **Experiment title:** Determination of the chemical composition profile for III-N heterostructures containing ultra-thin layers | **Experiment number:** SI1261 |
|---|---|---|
| **Beamline:** BM 20 | **Date of experiment:** from: 09.02.2006 to: 14.02.2006 | **Date of report:** 22.02.2006 |
| **Shifts:** 15 | **Local contact(s):** Dr. Norbert Schell | *Received at ESRF:* *22.02.06* |

**Names and affiliations of applicants** (* indicates experimentalists):

J. Gaca* and M. Wójcik*, Institute of Electronic Materials Technology, Wolczynska 133, 01 919 Warsaw, Poland

**Report:**

The basic problem concerning epitaxial growth of III-N crystals is the shortage of bulk crystals to be used as substrates. III-nitride heterostructures are commonly grown on foreign ones, such as sapphire. However, the large mismatches of lattice constants and thermal expansion coefficients between substrate and epitaxial layer result in high defect density and poor crystallographic order in the layer. Attempts have been made to grow GaN films with reduced defect density. Since native substrates are not available, alternative methods have been investigated using various types of buffer layers for improved nucleation and reduced defect density. One of the most promising consists in applying multiple layers of quantum dots (QDs), which may be achieved by introducing very thin superlattices in the buffer. The aim of the experiment was to investigate the chemical composition profile of the buffer layer and to determine the dependence between this profile and the crystalline and chemical order of the III-nitride epilayer. To this end the following epitaxial systems grown on sapphire (001) oriented substrates were investigated: Each sample (except reference one) consisted of: 20 nm nucleation AlN layer, on top of it there was deposited either AlN/GaN or AlGaN/GaN superlatice, and finally some samples were covered by a GaN cup layer. Details of the samples are presented in table below.

| | Nucleation layer | Superlattice | Cup layer |
|---|---|---|---|
| 1 | AlN 20 nm | 30 x (10 nm AlN / 10 nmGaN) | GaN 1000nm |
| 2 | AlN 20 nm | 30 x (5 nm AlN / 5 nmGaN) | GaN 1000nm |
| 3 | AlN 20 nm | 15 x (5 nm AlN / 5 nmGaN) | GaN 1000nm |
| 4 | AlN 20 nm | 10 x (5 nm AlN / 5 nmGaN) | GaN 1000nm |
| 5 | AlN 20 nm | 5 x (5 nm AlN / 5 nmGaN) | GaN 1000nm |
| 6 | AlN 20 nm | 15 x (5 nm $Al_{0.5}$ $Ga_{0.5}$ N / 5 nmGaN) | GaN 1000nm |
| 7 | AlN 20 nm | 30 x (10 nm AlN / 10 nmGaN) | without |
| 8 | AlN 20 nm | 30 x (5 nm AlN / 5 nmGaN) | without |
| 9 | AlN 20 nm | 15 x (5 nm AlN / 5 nmGaN) | without |
| 10 | AlN 20 nm | 10 x (5 nm AlN / 5 nmGaN) | without |
| 11 | AlN 20 nm | 5 x (5 nm AlN / 5 nmGaN) | without |
| 12 | AlN 20 nm | 15 x (5 nm $Al_{0.5}$ $Ga_{0.5}$ N / 5 nmGaN) | without |
| 13 | AlN 20 nm | 30 x (10 nm AlN / 10 nmGaN) | GaN 100nm |
| 14 | AlN 20 nm | 15 x (5 nm AlN / 5 nmGaN) | GaN 100nm |
| 15 | AlN 20 nm | 15 x (5 nm $Al_{0.5}$ $Ga_{0.5}$ N / 5 nmGaN) | GaN 100nm |
| 16 | AlN 20 nm | 30 x (5 nm AlN / 5 nmGaN) | GaN 100nm |
| 17 | AlN 20 nm | GaN template | GaN 1000nm |
| 18 | AlN 20 nm | GaN template | GaN 1000nm |

**Table** of investigated samples.

The characterization of all structures was carried out using HRXRD and XRR. 1- and 2-dim. scans of the reciprocal space in the vicinity of 002 and 004 Bragg reflections and reciprocal-space maps of diffusely scattered intensity were performed. Samples of reciprocal-space maps are presented below: Figs 1-4 show intensity maps (iso-intensity levels in log-scale) from rough surfaces, and Fig. 5 shows the contour plot of a reciprocal space map near the 004 mean Bragg peak of 30 x GaN / AlN superlattice where a very week AlN nucleation layer peak can be discerned on the shoulder of the large AlN peak.

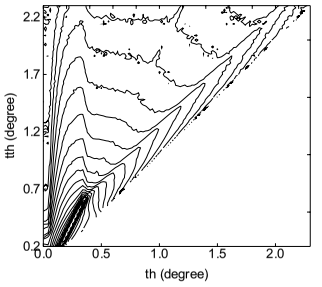


**Fig. 1:** 30 x GaN(10 nm) / AlN(10 nm) on 20 nm AlN nucleation layer *without* cup layer (# 996).

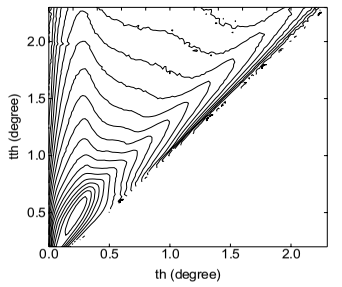


**Fig. 2:** 30 x GaN(10 nm) / AlN(10 nm) on 20 nm AlN nucleation layer *with* 1 μm GaN cup layer (# 997).

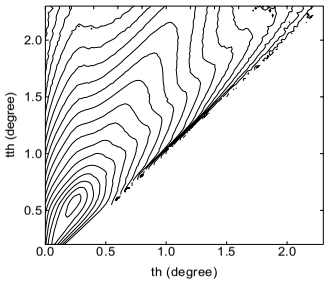


**Fig. 3:** 15 x GaN(5 nm) / AlN(5 nm) on 20 nm AlN nucleation layer *with* 1 μm GaN cup layer (# 1001).

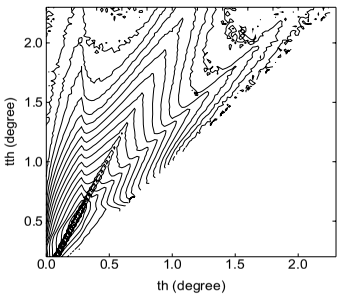


**Fig. 4:** 10 x GaN(5 nm) / AlN(5 nm) on 20 nm AlN nucleation layer *without* cup layer (# 1003).

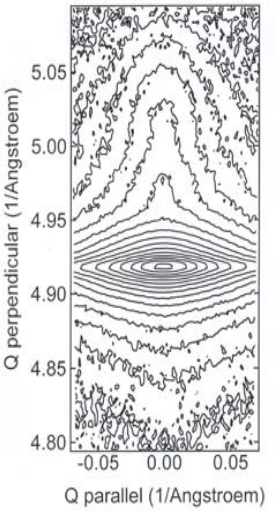


**Fig. 5:** 30 x GaN(10 nm) / AlN(10 nm) on 20 nm AlN nucleation layer *without* cup layer (# 996, as in Fig. 1).

| ESRF | **Experiment title:** **In-plane lattice parameter determination of Zn:$LiNbO_3$ thin films epitaxially grown on x-cut $LiNbO_3$ substrates using x-ray diffraction methods** | **Experiment number:** **SI-1346** |
|---|---|---|
| **Beamline:** BM 20 | **Date of experiment:** from: 12.07.2006 to: 15.07.2006 | **Date of report:** 28.08.2006 |
| **Shifts:** 9 | **Local contact(s):** Dr. Norbert Schell | *Received at ESRF:* *30.08.06* |

**Names and affiliations of applicants** (* indicates experimentalists):

Dr. J. Kräußlich *[1)]
Dr. O. Wehrhan *[1)]
PhD U. Zastrau *[1)]
Dr. C. Dubs [2)]
DP A. Lorenz [2)]
Prof. A. Tünnermann [2)]

Friedrich-Schiller-University of Jena
[1)] Institute for Optics and Quantum Electronics
[2)] Institute of Applied Physics
Max-Wien-Platz 1
07743 Jena
Gemany

**Report:**

The aim of the experiment has been to characterize Zn:$LiNbO_3$ thin films epitaxially grown on $LiNbO_3$ substrates by means of high resolution x-ray diffraction methods. Data concerning the characteristics of the epitaxial growth, the crystallographic orientation of the thin film in respect to the substrate as well as the numerical evaluation of the in-plane lattice parameters $\mathbf{c} = \mathbf{d}_{(000\ 0)}$ and $\mathbf{d}_{(01\text{-}1\ 0)}$ of the epitaxially grown $Li_{1-x}Zn_xNbO_3$ thin films are of special interest for the thin film producer to optimize the technological growth process.

$LiNbO_3$, due to its outstanding optical and electro-optical properties, is a suitable material to optical waveguide devices such as modulators and switches and to second-harmonic generation devices for integrated optical applications [1, 2, 3]. Optical waveguides demand a well-defined modification of the local refractive index $\Delta n$. For this purpose, Zn-substituted stoichiometric $Li_{1-x}Zn_xNbO_3$ thin films with a thickness until 4 µm were grown on conventional x-cut $LiNbO_3$ single crystal substrates by means of the liquid phase epitaxy (LPE) method [4, 5].

X-ray diffraction patterns taken up with symmetric reflexes in the Θ/2Θ-mode permit to determine the lattice parameter differences of the grown thin film in respect to the substrate only perpendicularly to the sample surface, however, with high precision ($\Delta d_\perp/d_\perp < 10^{-5}$) (Fig. 1).

It particularly results for the sample LNBV-1kt-2 (thin film without Zn):
$(\Delta d/d)_\perp = 8.3 \cdot 10^{-4} \pm 2 \cdot 10^{-5}$
$a_{\perp thin\ film} = 0.51478\ nm \pm 2 \cdot 10^{-5}\ nm$
with respect to $a_{\perp substrate} = 0.51522\ nm \pm 2 \cdot 10^{-5}\ nm$

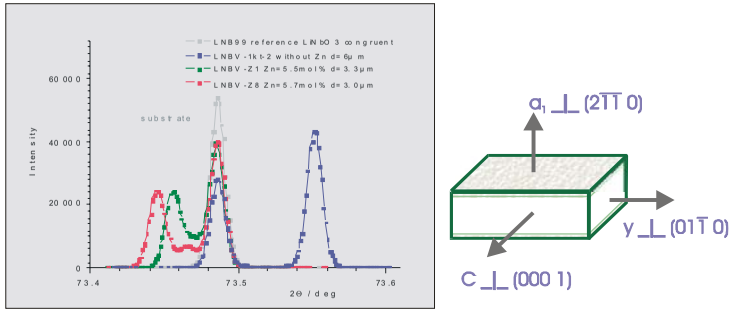


**Fig. 1**: Θ/2Θ-scan taken up with the symmetric 4-2-2 0 -reflection of the LiNbO3 thin film epitaxially grown on x-cut $LiNbO_3$ substrate.

From two-dimensional ´reciprocal space maps´ taken up by x-ray diffraction with asymmetric reflexes, data can be won both to the lateral and normal lattice parameters of the grown thin film in respect to the substrate, although with somewhat smaller precision ($\Delta d_{\shortparallel}/d_{\shortparallel} < 2 \cdot 10^{-4}$).

The rsm´s (Figs 2 and 3) reveal for the two different lateral directions c ⊥ (000 1) and y ⊥ (01-1 0) pseudomorphous growth of the thin film in respect to the substrate, despite the existing different crystallographic symmetry.

Using generalized Hooke' law in matrix way of writing, the relaxed lateral and normal lattice parameters as well as the deformation and tension components of the grown thin film can be computed.

$$\boldsymbol{\sigma_m = C_{mn}\varepsilon_n} \qquad m,n = 1,\ldots,6$$

with $\sigma_2 \neq 0;\ \sigma_3 \neq 0;\ \sigma_1 = \sigma_4 = \sigma_5 = \sigma_6 = 0;$
and $\varepsilon_1 \neq 0;\ \varepsilon_2 \neq 0;\ \varepsilon_3 \neq 0;\ \varepsilon_4 = \varepsilon_5 = \varepsilon_6 = 0;$

$\sigma_m$ - tension components
$\varepsilon_n$ - deformation components
$C_{mn}$ - elastic stiffnesses / $10^9$ Pa

$$\mathbf{0 = C_{11}\varepsilon_1 + C_{12}\varepsilon_2 + C_{13}\varepsilon_3}$$
$$\mathbf{\sigma_2 = C_{12}\varepsilon_1 + C_{11}\varepsilon_2 + C_{13}\varepsilon_3}$$
$$\mathbf{\sigma_3 = C_{13}\varepsilon_1 + C_{13}\varepsilon_2 + C_{13}\varepsilon_3}$$

and assuming that $\varepsilon_2 = \varepsilon_3$

$\varepsilon_1 = -(C_{12} + C_{13}) / C_{13}\varepsilon_2$
$\mathbf{\varepsilon_1 = -0.64\ \varepsilon_2}$ (← transversal contraction)

| $C_{11}$ [$10^9$ Pa] | $C_{12}$ [$10^9$ Pa] | $C_{13}$ [$10^9$ Pa] | $C_{14}$ [$10^9$ Pa] | $C_{33}$ [$10^9$ Pa] | $C_{44}$ [$10^9$ Pa] |
|---|---|---|---|---|---|
| 203 | 55 | 75 | 8.8 | 244 | 60 |

**Table 1**: Elastic stiffness modulus [6] of $LiNbO_3$.

From this follows the numerical calculation of the **relaxed lattice parameters $a_{relax}$ and $c_{relax}$** for the stoichiometric $LiNbO_3$ thin film coherently grown on congruent $LiNbO_3$ substrates

with the measured values
especially for the sample LNBV-1kt-2 (thin film without Zn):

$a_{\parallel} = 0.51522$ nm
$a_{\perp} = 0.51478$ nm
$c_{\parallel} = 1.3867$ nm

and with $(a_{\parallel} - a_{relax})/a_{relax} = \varepsilon_{\parallel} = \varepsilon_2$
$(a_{\perp} - a_{relax})/a_{relax} = \varepsilon_{\perp} = \varepsilon_1$
$\varepsilon_1 = -0.64\ \varepsilon_2$

$$a_{relax} = (a_{\parallel} - \varepsilon_2/\varepsilon_1 \bullet a_{\perp})/(1 - \varepsilon_2/\varepsilon_1) = 0.5149\ \text{nm} \pm 0.0005\ \text{nm}$$
$$\varepsilon_1 = -3.49(1) \cdot 10^{-4}$$
$$\varepsilon_2 = 5.45(1) \cdot 10^{-4}$$

and with $(c_{\parallel} - c_{relax})/c_{relax} = \varepsilon_{\parallel} = \varepsilon_3\ (= \varepsilon_2)$

$$c_{relax} = 1/(1 + \varepsilon_3) \bullet c_{\parallel} = 1.386\ \text{nm} \pm 0.002\ \text{nm}$$
$$\varepsilon_3 = 5.45(1) \cdot 10^{-4}$$

As final result arises now the ´in-plane´ tension components of the grown thin film, in direction of the lateral crystallographic axes y and c, respectively:

$$\sigma_2 = 1.32(1) \cdot 10^8\ \text{N/m}^2$$
$$\sigma_3 = 1.48(1) \cdot 10^8\ \text{N/m}^2$$

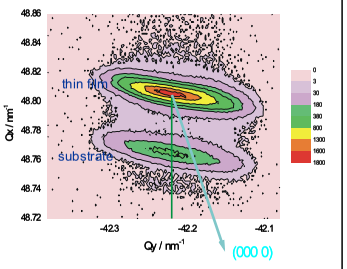


**Fig. 2**: rsm: asymmetric 4-51 0 reflection.

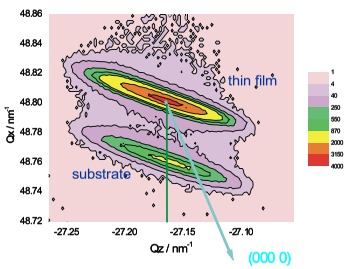


**Fig. 3**: rsm: asymmetric4-2-2 6 reflection.

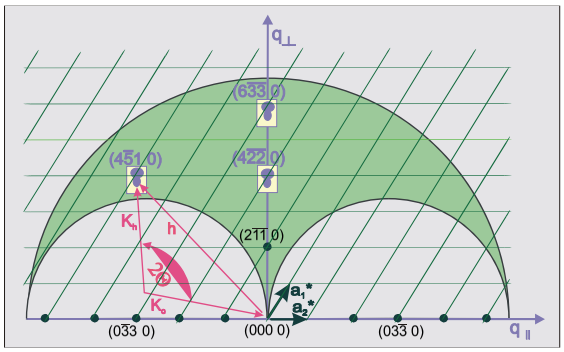


**Fig. 4**: Reciprocal lattice of $LiNbO_3$ in (000 1) cross-section projection for the two-dimensional taking up ´reciprocal space maps´ with asymmetric reflections to determine the lateral thin film lattice parameters in relation to the substrate.

We thank all members of the ROBL beamline team, especially Dr. Schell, for all the helpful support at the time of execution this experiment.

**References**

[1] J.-P. Ruske, B. Zeitner, and A. Tünnermann, A.S. Rasch: Electronics Letters **39** (2003) 1048
[2] J.-P. Ruske, A. Tünnermann, and Th. Fehn: Laser & Photonics June (2004) 34
[3] M. Iwai, T. Yoshino, S. Yamaguchi, M. Imaeda, N. Pavel, I. Shoji, and T. Taira: Appl. Phys. Lett. **83** (2003) 3659
[4] C. Dubs, A. Lorenz, J.-P. Ruske, J. Fuchs, and A. Tünnermann: Zeitschrift für Kristallographie, Supplement Issue **22** (2005) 52
[5] T. Kawaguchi, K. Mizuuchi, T. Yoshino, M. Imaeda, K. Yamamoto, and T. Fukuda: J Crystal Growth **203** (1999) 173
[6] R. S. Weise and T. K. Gaylord; Appl. Phys. A: Mater. Sci. Process **37**, 191 (1985)

**Forschungszentrum Dresden - Rossendorf**
P.O. Box 51 01 19 · 01314 Dresden / Germany

**The Rossendorf Beamline**
ESRF / sector 21 · BP 220 · F-38043 Grenoble / France
Phone: +33 (0)4.76.88.24.62
Fax: +33 (0)4.76.88.25.05
e-mail: scheinost@esrf.fr
www.fzd.de

Member of the Leibniz Association